

Synthesis and Electrochemical Characterization of Ternary Metal Oxides

by

Alexandria Rae Combs Bredar

A dissertation submitted to the Graduate Faculty of
Auburn University
in partial fulfillment of the
requirements for the Degree of
Doctor of Philosophy

Auburn, Alabama
May 1st, 2021

Keywords: delafossite, spinel, electrochemical impedance spectroscopy, oxygen reduction reaction, continuous-injection synthesis

Copyright 2021 by Alexandria R. C. Bredar

Approved by

Byron H. Farnum, Chair, Assistant Professor, Department of Chemistry and Biochemistry
Christian R. Goldsmith, Associate Professor, Department of Chemistry and Biochemistry
Christopher J. Easley, C. Harry Knowles Professor, Department of Chemistry and Biochemistry
Evangelos Miliordos, James E. Land Assistant Professor, Department of Chemistry and
Biochemistry
Ryan B. Comes, Assistant Professor, Department of Physics

Abstract

Metal oxides are an incredibly diverse class of materials that have found significant utility in the development of emerging solar conversion technologies. Their varied electronic properties allow them to function as charge transport materials, light absorbers, photocatalysts, and electrocatalysts, just to name a few. Many metal oxides consist of first row transition metals, which means they are cheap and abundant to use in these technologies. The structural diversity among metal oxides allows for the tuning of their electronic and optical properties, which is important for application of metal oxides in different devices. One particularly interesting way to tune metal oxide properties is to have two metal cations present in the material. These ternary metal oxides can be tuned in ways that binary oxides cannot.

This thesis focuses on the investigation of two different ternary metal oxide materials and their electrochemical properties towards hole transport and catalysis. Chapter 2 and 3 focuses on delafossite CuGaO_2 which has shown promise as a hole transport layer in p-type heterojunction solar devices. The properties of CuGaO_2 as a nanocrystalline mesoporous film were characterized using electrochemical techniques such as cyclic voltammetry and electrochemical impedance spectroscopy and found that depending on the pH at which the particles were synthesized, the hole density of the material changed, shifting from metallic to semiconductive. The hole density could also be controlled by post synthetic annealing under different environments, such as O_2 , Ar, and H_2 . Chapter 4 explores the electrocatalytic properties of single crystalline epitaxial spinel MnFe_2O_4 towards the oxygen reduction reaction (ORR), which is an important catalytic process for fuel cell technologies. These single crystalline films were grown via MBE on conductive substrates such that their electrochemical properties could be assessed. We find that MnFe_2O_4 has great selectivity for ORR but suffers from large overpotentials.

Lastly, the use of nanocrystalline materials in energy technologies has required significant investigation into different synthetic methods. Ternary metal oxides are more difficult to synthesize due to competition to form the individual binary oxide materials. While investigating a continuous injection nanocrystal synthesis for ternary metal oxide synthesis we discovered a unique pathway of metal oxide formation, where one metal precursor catalyzes the formation of the other binary oxide. Specifically, we found that Lewis acids, such as gallium and indium, can catalyze the formation of Cu_2O , which previously could not be accessed with the continuous injection synthesis. The investigation of this catalytic pathway has revealed an interesting method to study nanocrystalline reaction kinetics, as well as access metal oxides that could be difficult to synthesize.

Acknowledgments

The number of people I need to thank is frankly too great to list in this document. My support system throughout my education career has been devoted and steadfast in their expectations of my success. To my mom and dad, you will truly never understand how much I love and appreciate you. To Betty Burton, who has been a combination of mother, grandmother, aunt, and friend. To my twin sister Lucinda, who has been with me since (literally) day one. To my brother Chris and his wife Christina, who have been great sources of love and advice. To my in-laws, Bart and Radonna who have been a wonderful addition to my family and have been very supportive of my goals. To my sister-in-law, Ansley, for being such a beacon of positivity and love in my life. To my best friend, Molly Melillo, who has been a constant source of support and laughter ever since we met. All of you are the reason I am where I am today. Thank you.

My professors at Centre College were truly the first people to encourage me to pursue graduate school, and even since I've left Centre, they've been amazing sources of advice and comfort as I've pursued this dream. To Dr. Kari Young and Dr. Jeff Fieberg, for initiating my interests in inorganic and physical chemistry. I especially want to thank Dr. Lenny Demoranville, who has truly been my inspiration as a chemist. You were the first to mentor me and cultivate my love of chemistry, even when it still scared me. You have seen me at my personal and professional lows, as well as my highs. From the bottom of my heart, I cannot thank you enough for supporting me through every hard and easy decision I have made for the past 9 years.

My time in graduate school at Auburn has been fulfilling and rewarding, personally and intellectually. Thank you to all of my colleagues and peers who have ridden the waves of graduate school with me. To everyone I've met and worked with in the Farnum group: Chase, Motiur, Amanda, Javier, Alex, Andricus, Russel, Niharika, Humaira, and Nilave; it has been

incredibly fun to work alongside all of you and share this experience. I particularly want to thank Noah Gibson, who put a significant amount of his undergraduate research education in my hands. Your work ethic, intelligence, and disposition will take you so far in life, and I so appreciate that I had the opportunity to learn with you. To Jessica and Ethan, who have been the best workout/coffee/adventure friends. To Julie Niklas, who had the audacity to leave a year earlier than I could. I miss your constant presence in my lab every day, but I'm so thankful for your continued guidance and support from afar. To my committee members, Dr. Chris Goldsmith, Dr. Chris Easley, and Dr. Evangelos Miliordos, who have all been incredibly supportive and great sources of insight. To Dr. Ryan Comes and his graduate student Miles Blanchett for collaborating with me on projects and for the helpful scientific discussions. Last, but not least, none of this would have been possible without my advisor Dr. Byron Farnum. Thank you for trusting me to be the first person in your research group over four years ago. What ensued has been some of the most joyful, difficult, and rewarding years of my life. The enthusiasm with which you love science is infectious and reflects in your mentorship, and I am so thankful for all of the advice and lessons you've taught me as I begin the pursuit of my own independent career path.

My last thank you is reserved for the most important person in my life, my husband Garrett Bredar. Adventuring to Auburn 5 years ago with you was the best decision I could have made. Your support of my career goals, while simultaneously pursuing your own, has meant so much to me. I am so proud of everything we have achieved in our time at Auburn, and I can't wait to see what our future holds.

Table of Contents

Abstract.....	ii
Acknowledgments	iv
List of Tables	ix
List of Figures.....	x
List of Abbreviations	xiii
Chapter 1 Introduction	1
1.1 Solar Energy Conversion and Alternative Energy Sources	1
1.2 Metal Oxides for Energy Conversion Technologies	5
1.3 Synthesis of Metal Oxides	15
1.4 Metal Oxide Electrochemistry	19
1.5 Conclusion	55
Chapter 2 Evidence and Influence of Copper Vacancies in p-Type CuGaO ₂ Mesoporous Films	78
2.1 Introduction	78
2.2 Experimental	80
2.3 Results	82
2.4 Discussion	94
2.5 Conclusion	100
2.6 Appendix	101
2.7 References	116
Chapter 3 Influence of Synthesis pH and Post-Synthetic Annealing on the Hole Density of CuGaO ₂ Mesoporous Films	120

3.1 Introduction	120
3.2 Experimental	122
3.3 Results	125
3.4 Discussion	140
3.5 Conclusion	147
3.6 Appendix	148
3.7 References	155
Chapter 4 Epitaxially Grown Spinel MnFe_2O_4 and Its Ability to Perform the Oxygen Reduction Reaction	159
4.1 Introduction	159
4.2 Experimental	162
4.3 Results	164
4.4 Discussion	179
4.5 Conclusion	184
4.6 Appendix	184
4.7 References	192
Chapter 5 Group 13 Lewis Acid Catalyzed Synthesis of Cu_2O Nanocrystals via Hydroxide Transmetallation	197
5.1 Introduction	197
5.2 Experimental	200
5.3 Results and Discussion	203
5.4 Conclusion	225
5.5 Appendix	226

5.6 References 242

List of Tables

Table 1.1 Common Equivalent Circuits to Fit EIS Data	29
Table 2.1 Elemental Analysis of CuGaO ₂ Films from XPS	86
Table 3.1 P1 Dye Adsorption to CuGaO ₂	129
Table 4.1 Stoichiometry of MnFe ₂ O ₄ Films Determined from XPS	167
Table 4.2 Electron Transfer Numbers, Exchange Current Density and Rate Constants of MnFe ₂ O ₄ Films	175
Table 5.1 Cu ₂ O Nanocrystal Sizes.....	206
Table 5.2 Comparison of Catalysis Values	215

List of Figures

Figure 1.1 Diagram of a p-n junction	2
Figure 1.2 Fuel Cell Diagram	4
Figure 1.3 n-type vs p-type Heterojunction Solar Cell Diagram	6
Figure 1.4 Band Diagrams of n-type and p-type Metal Oxides	10
Figure 1.5 Delafossite CuGaO_2 Crystal Structure	13
Figure 1.6 Manganese Spinel Crystal Structures	15
Figure 1.7 CVs and TiO_2 nanotubes and NiO films	21
Figure 1.8 RDE and K-L Plot Examples using Pt/C Data	23
Figure 1.9 Simulated Nyquist and Bode Plot EIS Data	26
Figure 1.10 Simulated Capacitance vs Frequency Plot	27
Figure 1.11 Equivalent Circuit Models for TiO_2 at Different Potentials	33
Figure 1.12 Capacitance comparison of TiO_2 micron and nanoparticles	35
Figure 1.13 Potential Dependence of Capacitance and Transport Resistance of TiO_2 Nanotubes	39
Figure 1.14 Capacitance vs Frequency Measurements of PSCs with and without TiO_2	42
Figure 1.15 Capacitance and Mott-Schottky of ZnO nanowire	45
Figure 1.16 Electron recombination and extraction lifetimes calculated from EIS data for TiO_2 and ZnO	46
Figure 1.17 Nyquist and Bode plots comparing TiO_2 and SnO_2 QDSCs	49
Figure 1.18 Nyquist plots of SnO_2 DSSCs treated vs untreated with TiCl_4	50
Figure 1.19 Nyquist Plot of p-type NiO DSSC	53

Figure 1.20 Capacitance and DOS of NiO electrodes	54
Figure 1.21 Conductivity of undoped and Mg-doped CuGaO ₂	55
Figure 2.1 Delafossite crystal structure	79
Figure 2.2 SEM of CuGaO ₂ nanocrystals	83
Figure 2.3 Powder XRD of CuGaO ₂ nanocrystals	84
Figure 2.4 XPS of Cu 2p and O 1s region of CuGaO ₂ films	87
Figure 2.5 CV of CuGaO ₂ film in MeCN	88
Figure 2.6 Nyquist and Bode Phase plots of CuGaO ₂ films.....	90
Figure 2.7 Equivalent Circuit Mode and Bode Phase/Nyquist plots of CuGaO ₂ Films	91
Figure 2.8 Diffusion resistance and capacitance of CuGaO ₂ films	92
Figure 3.1 Powder XRD of pH 5 and 9 CuGaO ₂ powders and films	126
Figure 3.2 SEM of pH 5 and pH 9 CuGaO ₂ powders	127
Figure 3.3 Diffuse reflectance spectra of pH 5 and pH 9 CuGaO ₂	128
Figure 3.4 CV measurements pH 5 and pH 9 O ₂ , Ar, and H ₂ Annealed Films	131
Figure 3.5 Capacitance vs Frequency plots for pH 5 and pH 9 O ₂ , Ar, and H ₂ Annealed Films	133
Figure 3.6 Nyquist plots at 0 V of pH 5 and pH 9 O ₂ , Ar, and H ₂ annealed films	136
Figure 3.7 Nyquist plots showing diffusional resistance feature	137
Figure 3.8 Capacitance vs Frequency plots with Nyquist insets for films annealed multiple times	139
Figure 3.9 CVs and pH 5 and pH 9 O ₂ , Ar, and H ₂ annealed films in I ⁻ /I ₃ ⁻ electrolyte	140
Figure 4.1 Diagram of MBE electrode for ORR catalysis	162
Figure 4.2 RHEED and AFM analysis of MnFe ₂ O ₄ Films	166

Figure 4.3 XPS of Mn 2p and Fe 2p region of MnFe ₂ O ₄ Films	169
Figure 4.4 CVs of MnFe ₂ O ₄ Films	171
Figure 4.5 RDE and K-L Plots of MnFe ₂ O ₄ Films	176
Figure 4.6 Tafel Plots of MnFe ₂ O ₄ Films	178
Figure 5.1 PXRD and SEM of Synthesized Cu ₂ O Nanocrystals	204
Figure 5.1 PXRD and SEM of Synthesized Cu ₂ O Nanocrystals	204
Figure 5.2 UV-Vis of Post Reaction Solutions	207
Figure 5.3 FTIR of Post Reaction Solutions	209
Figure 5.4 FTIR Δ Absorbance Plots for 5 mol% Ga Catalyst	210
Figure 5.5 Precursor and Ester Absorbance vs Time Plots	212
Figure 5.6 FTIR Δ Absorbance for 100 mol% Ga ³⁺ and In ³⁺	221
Scheme 5.1 Reaction Scheme Comparing Previous Work and This Work	199
Scheme 5.2 Proposed Catalytic Mechanism for Cu ₂ O Synthesis	218

List of Abbreviations

DSSC	Dye-Sensitized Solar Cell
PSC	Perovskite Solar Cell
QDSC	Quantum Dot Solar Cell
OPV	Organic Photovoltaic
CV	Cyclic Voltammetry
EIS	Electrochemical Impedance Spectroscopy
RDE	Rotating Disk Electrochemistry
K-L	Koutecky-Levich
MBE	Molecular Beam Epitaxy
RHEED	Reflective High Energy Electron Diffraction
XPS	X-Ray Photoelectron Spectroscopy
PXRD	Powder X-Ray Diffraction
SEM	Scanning Electron Microscopy
TEM	Transmission Electron Microscopy
EDS	Energy Dispersive Spectroscopy
FTIR	Fourier-Transform Infrared Spectroscopy
NC	Nanocrystal
MeCN	Acetonitrile
ORR	Oxygen Reduction Reaction
GC	Glassy Carbon

Chapter 1

Introduction

*Portions of this chapter were reproduced from Bredar, A. R. C.; Chown, A. L.; Burton, A. R.; Farnum, B. H. *ACS Appl. Energy Mater.* **2020**, *3* (1), 66–98.

1.1 Solar Energy Conversion and Alternative Energy Sources

1.1.1 World energy consumption, fossil fuel use, and CO₂ production As the world energy demand continues to increase, the realization of carbon neutral and carbon free renewable energy sources is of vital importance. In 2016, the year I began my Ph.D., the world consumed 17.4 TW of energy.¹ The most recent publication of world energy consumption statistics shows that number has increased to almost 19 TW in 2019, and this number is expected to increase steadily for the next several decades.¹ From the resources used to consume this amount of energy, namely fossil fuels such as coal, oil, and gasoline, 34.2 billion tonnes of CO₂ were produced¹, which has been shown to have a direct effect on our changing climate.² To meet world energy requirements without exacerbating the growing problem of climate change, most of the world's energy supply needs to be generated from renewable resources. Of all the avenues of renewable energy to pursue, solar energy has pervaded as the obvious choice, as the amount of energy from the sun that strikes the earth in just over one hour surpasses the world's current yearly energy requirement.³ For successful solar energy application, sunlight needs to be efficiently captured and converted to a useful form. This can be accomplished with either solar-to-electric or solar-to-fuel methods.

1.1.2 Solar-to-Electric and Solar-to-Fuel Energy Conversion Solar-to-electric is commonly employed in the form of photovoltaics, which have the capability to significantly reduce our reliance on fossil fuels. The first successful practical photovoltaic developed was made from

silicon, doped with different elements to create a p-n junction.⁴ This junction allows the efficient separation of photogenerated electrons and holes to produce current (**Figure 1.1**).

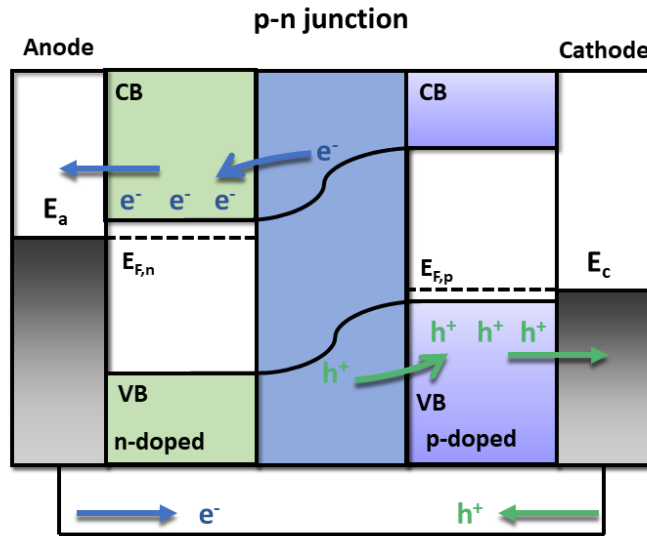


Figure 1.1: Diagram of a p-n junction created by doped Si, and the separation of photogenerated charges.

These photogenerated charges are derived from silicon's band gap of 1.1 eV, which allows for broad visible and UV light absorption ($\lambda < 1127$ nm). However, the success of any photovoltaic device is driven by its ability to separate charge over a large distance while minimizing recombination events. Silicon must be extremely pure to operate at its highest potential, and this makes widespread solar energy use from Si-based solar cell devices very expensive.³ Even at its maximum theoretical operating efficiency, a single junction Si-based device can only achieve 30% efficiency, based on the Shockley-Queisser Limit.^{5,6} This theoretical efficiency can be exceeded by the use of multi-junction photovoltaics, where multiple semiconductors are used to increase the number of useful photons captured from the solar spectrum.⁷ Many traditional main group semiconductors (i.e. IV, III-V semiconductors) still require high levels of purity for practical use. For this reason, alternative designs of photovoltaics have been heavily investigated,

which has opened a door of scientific exploration into new materials for better and more cost-effective solar energy capture and conversion to electricity.

Although the conversion of solar energy to electric energy is vitally important to alleviating the burden of fossil fuels on our planet, it cannot be the exclusive solution. The diffuse and intermittent nature of sunlight prevents it from being used consistently. However, the conversion of sunlight into molecules introduces a way to store solar energy in the form of chemical bonds. These bonds can then be broken to release the stored energy, allowing for more consistent and widespread use of the energy harnessed from the sun. This design is borrowed from nature, where plants utilize highly efficient photosynthetic pathways to convert H_2O and CO_2 into O_2 and carbohydrates. Mimicking nature has inspired scientists to study the processes of water oxidation and CO_2 reduction for decades. Many different catalysts, in the form of molecules or materials, have been explored to exploit the chemistry that nature seems to do with such ease. Effective design of devices that can do “artificial” photosynthesis require molecules and/or materials that can effectively and efficiently absorb light, separate charge, and catalyze the necessary oxidation and reduction reactions to produce chemical fuels, typically H_2 and O_2 . A particularly impressive breakthrough in solar-to-fuel conversion devices came in 2012 with the development of the “artificial leaf”.⁸ This device used Si as the scaffold and light absorber, a Co-based oxygen evolving complex (OEC), and a NiMoZn alloy as the proton reduction catalyst. While this device utilizes earth abundant materials for catalysis, a more cost-effective device design would utilize a cheaper and more earth abundant semiconductor scaffold as well.

1.1.3 Electrochemical Consumption of Solar Derived Fuels Once solar fuels such as H_2 and O_2 are photochemically produced they can be used directly to produce electricity in devices called fuel cells. While fuel cells are not powered by sunlight, their ability to use photogenerated

fuels, such as H₂ and O₂, to electrochemically produce electricity while only producing water as a byproduct make them great alternatives to power vehicles.⁹ Fuel cells, in their simplest design, have an anode (where H₂ or another fuel is oxidized to produce electrons), an electrolyte (for the diffusion of ions), and a cathode (where byproducts of oxidation at the anode can be reduced) (Figure 1.2).

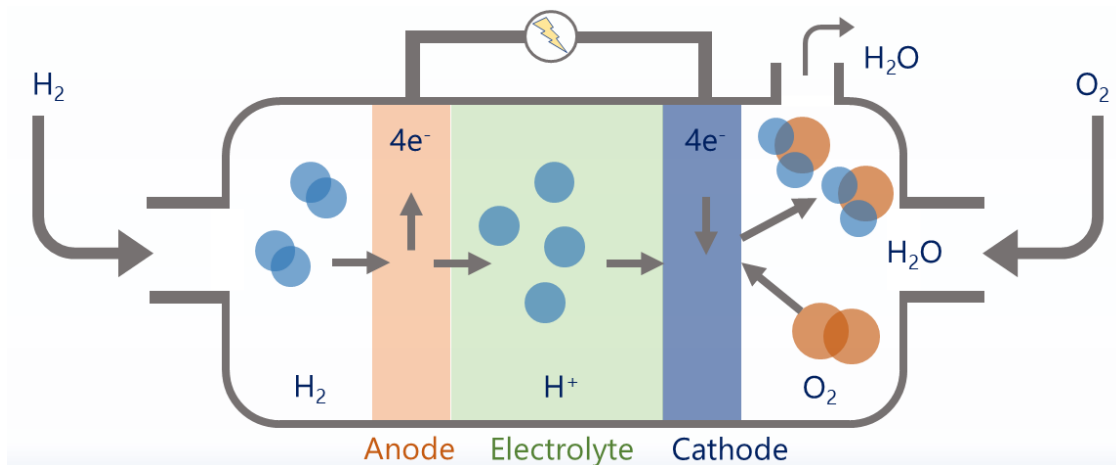
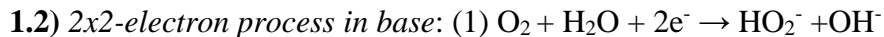
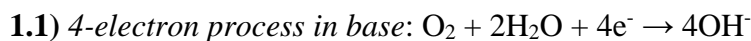
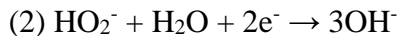


Figure 1.2: Fuel Cell diagram, showing the oxidation of H₂ as a fuel, followed by reduction of O₂ to form water as a byproduct.

The cathode of these devices is particularly interesting because of their necessity to reduce oxygen to form the byproducts of fuel oxidation. For example, H₂ oxidized at the anode produces protons (H⁺) which then travel to the cathode via the electrolyte. O₂ introduced into the system cannot effectively react until its double bond is broken. This specific reaction is called the oxygen reduction reaction (ORR) and is complicated by its multi-electron/multi-proton chemistry. ORR has two possible mechanisms, which change slightly depending on if the reaction is done in acid or base. The alkaline ORR mechanisms are the most relevant to this thesis and are shown in **Equations 1.1** and **1.2**.





The 4-electron process is preferable because it has fewer reaction steps and does not produce intermediates, such as the peroxy anion, that can be poisonous to catalytic activity.¹⁰ Currently the best catalyst for this reaction is Pt/C, which has high selectivity for the 4-electron mechanism, is stable in both acidic and basic media, and has the best onset potential for the reaction reported to date of ~0.9 V vs RHE.¹¹ However, the majority of the cost of fuel cell technology is due to the use of Pt as a catalyst, which is too costly for widespread use.¹² The effective implementation of fuel cell technology in our energy economy requires cheaper alternative catalysts that can effectively perform ORR.

The research dedicated to understanding the chemistry of the energy conversion technologies discussed above has done an excellent job highlighting the necessity of materials that are inexpensive, yet do not sacrifice efficiency. Metal oxides have proven highly efficient in this area, as well as cost effective in these technologies. The rest of this thesis will highlight work that seeks to understand how and why certain metal oxides function for potential application in these technologies.

1.2 Metal Oxides for Energy Conversion Technologies

1.2.1 Heterojunction Devices In 1991, Michael Graetzel and Brian O'Regan reported on the development of the first Dye-Sensitized Solar Cell (DSSC).¹³ This device differed from previous solar cell designs because it separated the processes of light absorption and charge separation, where electrons are generated by photon absorption via a light absorber (typically a molecular dye) anchored onto an electron transport material (ETM) (**Figure 1.3**). The ETM scavenges electrons produced from photoexcitation of the molecular dye, which is then regenerated by a

redox mediator in solution. The redox mediator is then reduced at the counter electrode of the device, completing the circuit. The first DSSC utilized TiO_2 , a wide bandgap n-type metal oxide semiconductor, as a scaffold metal oxide for electron harvesting, dyed with a ruthenium complex as a visible light absorber, sandwiched between two electrodes with iodide/triiodide (I^-/I_3^-) electrolyte as a redox mediator.¹³ This device can be described as an n-type DSSC, because of the use of an n-type metal oxides semiconductor as the ETM. p-Type DSSCs can be made as well, by using a p-type semiconductor as a hole transport material (HTM). In these devices, the hole generated in the ground state of the dye is moved through the valence band of the HTM to the cathode of the device. The electron in the excited state is transferred to the redox mediator in solution, which is then oxidized at the anode of the device (**Figure 1.3**).

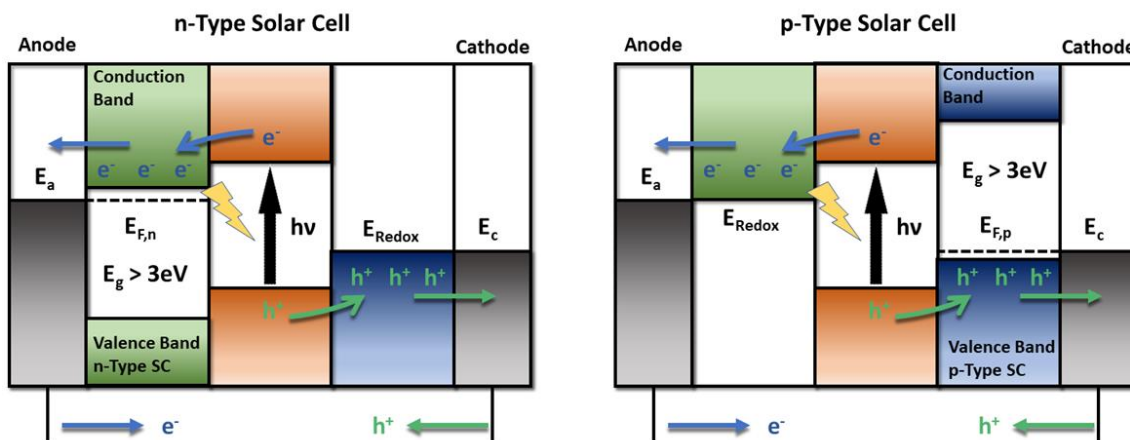


Figure 1.3: n-type vs p-type heterojunction solar cell construction.

An important aspect of this design was the utilization of nanocrystalline TiO_2 as a mesoporous film, generating a much higher surface area for dye coverage and electrolyte intercalation.¹⁴ More dye coverage translates to more photon absorption, which means more current is generated from the device. It also means more direct contact of the film with the redox mediator to ensure ease of charge passage between the electron transport layer and the redox mediator. In a Si-based photovoltaics, the voltage is determined by the band gap of Si. In the

DSSC described above, the voltage is determined by the energetic difference between the $E_{1/2}$ of the redox mediator and the Fermi level (E_{Fermi}) of the ETM. The DSSC was the first example of a heterojunction solar cell that did not use traditional semiconductor materials, and since its discovery a variety of heterojunction solar cell designs have been achieved by changing the ETM, light absorber, and redox mediator. Most prominently, heterojunction device research currently focuses on DSSCs, perovskite SCs, quantum dot SCs, and organic photovoltaics (OPVs), all of which can utilize metal oxides in their designs. There is also significant versatility in these designs, to achieve higher voltages, currents, and efficiencies. A similar device design has also been more recently developed to continue exploration of solar-to-fuel conversion. The Dye-Sensitized Photoelectrosynthesis Cell (DSPEC) is built much like a DSSC, but with the addition of a molecular catalyst that can perform water oxidation.¹⁵

The benefit of these devices is their use of the metal oxide semiconductor as a cheap and earth abundant material to perform the necessary electron transfer chemistry, which makes them a great alternative to devices that require highly crystalline and pure Si. Section 1.2.2 will discuss the important physical and electronic properties of metal oxide semiconductors that make them highly valuable for heterojunction devices.

1.2.2 Metal Oxides in Electrocatalysis As discussed in Section 1.1.3, the catalysis of ORR is very important to the widespread utilization of fuel cell technologies. Metal oxides that are metallic or semiconductor in nature have shown the ability to catalyze this reaction, and are excellent alternatives to Pt/C. Any catalyst that is utilized in these technologies needs to have high reactivity (low overpotential), high stability at different pH values, and high selectivity between the 2-electron and 4-electron process for ORR. Many studies that utilize metal oxides for ORR catalysis do so by alloying with Pt in order to reduce the amount of Pt needed, therefore

reducing the cost.¹⁶ This is also beneficial because many metal oxides have low stability in acidic conditions and this reduces that issue. However, finding ways to exclusively use metal oxides would be the most cost-effective solution.

It should be noted that the most utilized form of metal oxides in ORR catalysis are nanocrystalline/nanoparticle powders mixed with a high surface area conductive substrate, such as graphene, to improve conductivity. Providing a high surface area material for the reaction to occur is also important. Understanding the contribution of the crystal structure and electronics of transition metal oxides is crucial for discovering better catalysts for these important reactions. Some descriptors have been explored to understand metal oxide reactivity better. O₂ adsorption, for example, is particularly structure dependent, and even the same catalysts can give different activity based on its structure.¹⁰ The protonation of the oxygen to form water or hydroxide also needs to occur, and is compensated by reduction of the metal atom at the surface. Therefore understanding M-OH bond strength at the surface is important for understanding catalytic activity.¹⁰ These descriptors are particularly important for understanding if the 4-electron or the 2x2-electron will dominate at certain surfaces or reaction conditions.

The most investigated transition metal oxides for ORR catalysis have been Co, Mn, Fe, and Ni oxides, including combinations of these metals in various oxides.¹⁷ In particular, these materials with specifically the spinel crystal structure have found an immense amount of success in the field. Spinel metal oxides will be detailed more below in Section 1.2.6.

1.2.3 *n-Type vs p-Type Metal Oxide Semiconductors* In any application utilizing semiconductors, the electronic and optical properties are very important as they will determine how the material conducts charge. There are 3 main types of semiconductors: n-type, p-type and intrinsic, all of which have valence bands that consists of filled states, and a conduction band that

consists of empty states. n-Type semiconductors all have Fermi levels that lie much closer to the conduction band edge, as opposed to p-type semiconductors that have Fermi levels close to their valence bands. Intrinsic semiconductors, like Si, have a Fermi level that is perfectly between the valence and the conduction bands. The concentration of charge carriers is reflected by the position of the Fermi level, meaning that n-type semiconductors have electrons as a majority charge carrier and p-type semiconductors have holes as a majority charge carrier. The majority charge carrier of a semiconductor is an important aspect of their ability to function in energy conversion devices. Depending on the device application, the band gap can be important as well. For photocatalysis use of a narrow band gap semiconductor (1-2 eV) is preferable for more visible light absorption. Heterojunction devices can use metal oxides as visible light absorbers, but they can also be used as selective electron/hole contacts. Wide band gap semiconductors (>3 eV) can only absorb UV light, and therefore will not compete with a visible light absorber. n-Type metal oxides are used as electron selective contacts (ETMs) and p-type metal oxides are used as hole selective contacts (HTMs).

TiO₂, utilized by the DSSC described above, and other n-type wide band gap semiconductor metal oxides have been shown to have a large number of conduction band states, as well as large electron mobilities, leading to large conductivities.^{18,19} n-Type conductivity in a metal oxide derives from having electrons largely delocalized in the conduction band, typically due to overlap of the metal *s/d* orbitals, which lowers the effective mass of electrons and gives rise to high charge mobility.²⁰ The employment of TiO₂ in the first DSSC has seemed somewhat serendipitous, as no other wide band gap n-type metal oxide has been able to match its charge transport capabilities, while somewhat limiting recombination pathways. SnO₂ is too conductive as a result of n-type defects, making recombination pathways more energetically favorable²¹,

ZrO₂ has a conduction band minimum which is energetically unfavorable for electron injection from most dyes²², and ZnO, while similar energetically to TiO₂, suffers from poor injection of the electron from the molecular light absorber into the conduction band.²³

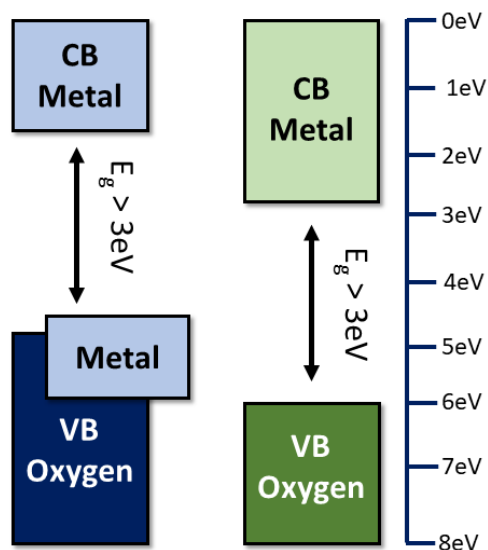


Figure 1.4: band diagrams of p-type (blue) and n-type (green) semiconductors and their contributing orbitals

As stated above, the research and development of most heterojunction solar cells has focused on using n-type semiconductors. However, to increase the maximum photovoltages and photocurrents for DSSCs, tandem devices need to be realized. This can only be accomplished by finding p-type semiconductor materials that can move holes as effectively as n-type semiconductors move electrons. These hole transport materials (HTMs) also need to be transparent to visible light. The obvious, yet complicated answer is to use p-type wide band gap metal oxide semiconductors. However, the band structure of metal oxides makes this inherently challenging. In p-type metal oxides, mobility of holes is dependent upon the delocalization of charge through the oxygen *2p* orbitals, which are highly localized orbitals.²⁴ Moving electrons through the highly delocalized conduction band is much simpler than moving holes through the

highly localized and electronegative oxygen-based orbitals that make up the valence band of metal oxides. However, some metals, such as late transition metals Ni and Cu, have *s* and *d* orbitals with the proper energetics such that they can overlap with the oxygen *2p* orbitals, helping delocalize the charge (**Figure 1.4**).²⁵ This improves hole conduction through the valence band significantly, allowing for holes to be the majority charge carrier.

NiO has been the most widely investigated p-type semiconductor for heterojunction device applications to date.²⁶ Originally chosen for its synthetic simplicity and wide band gap of 3.6 eV²⁷, devices utilizing NiO have been plagued with problems, mostly surrounding fast charge recombination.²⁶ Other issues that make NiO a less than ideal p-type wide band gap metal oxide are its unfavorable valence band edge position compared to typical redox mediators, decreasing the photovoltage, and absorption of visible light because of d-d transitions, decreasing the photocurrent by competing with productive light absorption of the dye.²⁶ The champion n-type DSSC using TiO₂ has an efficiency of 12.4%.²⁸ The champion p-type DSSC, which uses NiO, has only achieved an efficiency of 1.3%. This points to significant difficulty in charge transport, light absorption, or electron recombination that is less apparently in n-type DSSCs. To achieve a high functioning tandem DSSC the p-type side needs to work as effectively as the n-type side. Other heterojunction solar cells also benefit from an HTM, so diversifying the library of HTMs with p-type metal oxides is of value. For this reason, exploration of other p-type metal oxides can contribute greatly to the heterojunction solar cell community.

1.2.4 Binary versus Ternary Metal Oxides Before discussing the specific metal oxides that were researched for this dissertation, a discussion of binary vs ternary metal oxides is warranted. The metal oxide library is vast and diverse in terms of elemental composition, crystal structures, and electronic properties. Almost all transition metals have associated oxides, many with

multiple stoichiometric and crystal structure combinations. As an example, iron has 16 different possible stoichiometric combinations of Fe, O, and H giving rise to several iron oxides and oxyhydroxides, each with unique structure, electronic, and optical properties. Upon introduction of a second metal, the possible number of structures in which Fe can be found increases significantly. Perovskites, spinels, delafossites, and several silicate crystal structures can incorporate Fe, along with secondary metal ions, to create ternary metal oxide crystal structures.

In the metal chalcogenide literature, the introduction of metal ions to create ternary and quaternary structures is very common. The introduction of other metal ions significantly increases the structural and optoelectronic properties of these materials, and this behavior can also be found in the metal oxide literature. Cu_2O is an interesting example, where cuprite consists of a cubic lattice with linearly coordinated copper atoms and tetrahedrally coordinated oxygen atoms. Cu_2O has a 2.2 eV band gap, allowing for visible light absorption, but has stability issues in aqueous systems, making it difficult to use in some photocatalytic applications. Delafossite CuMO_2 on the other hand, have similar crystallographic arrangements of the atoms, (linearly coordinated copper and tetrahedrally coordinated oxygen), but the introduction of the second ion significantly increases the stability in aqueous media at most pH's. The second ion can also be used to tailor the band gap, giving variety in the optoelectronic properties of these materials.

Another reason for pursuing ternary metal oxides is the tailoring of chemical reactivity of the metal oxide. Different metals have different reactivities to all chemical processes based on their size, oxidation state, Lewis acidity, electron configuration, coordination environment, and numerous other reasons. In order to satisfy charge balance, ternary metal oxides can have metals in the same oxidation state or in different oxidation states. The metals can also occupy different

coordination sites, which can tailor reactivity. Spinel metal oxides are excellent examples of materials that display this capability.

1.2.5 Delafossite CuMO_2 Alternative metal oxides that have gained attention in recent years, are delafossite $\text{Cu}^{\text{I}}\text{M}^{\text{III}}\text{O}_2$.²⁶ Delafossite copper metal oxides are ternary metal oxides with the formula $\text{Cu}^{\text{I}}\text{M}^{\text{III}}\text{O}_2$, where M^{III} can be a variety of transition metals or group 13 cations. Depending on the M^{III} cation present, variability of the band gap can be achieved, which gives rise to a diverse array of applications for delafossite materials, particularly within the construct of heterojunction devices. CuCrO_2 , CuScO_2 , CuAlO_2 , and CuGaO_2 all have band gaps >3 eV²⁹, and have all been investigated as potential HTMs in heterojunction solar cells.³⁰⁻³⁷ If transition metals such as cobalt, iron, or manganese occupy the B cation site, then the band gap is ~ 1.5 eV which is appropriate for visible light absorption. For this reason, CuCoO_2 , CuFeO_2 , and CuMnO_2 have been investigated as photocatalysts for H^+/CO_2 reduction.³⁸⁻⁴¹ Several delafossites, including CuFeO_2 , CuRhO_2 , and CuCrO_2 have been investigated for water oxidation catalysis.⁴² The crystal structure consists of O-Cu-O layers alternating between MO_6 edge-shared octahedra, stacked in the c-direction (**Figure 1.5**).

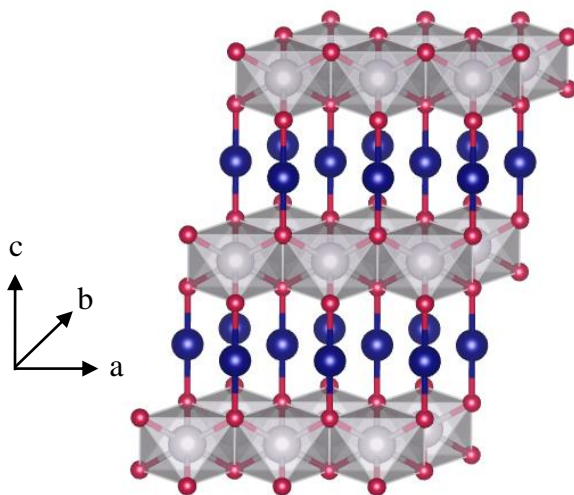


Figure 1.5: Delafossite CuGaO_2 as the 3R polymorph

The crystal structure has two possible polymorphs: the 2H and the 3R polymorph. The 3R polymorph is the most common crystallographic phase, but some CuMO_2 , such as CuScO_2 prefer the 2H phase.³⁷ The anisotropy of the crystal structure also gives rise to anisotropic charge transport, where it has been shown for CuAlO_2 that hole conduction is 25 times faster in the ab-plane (Cu^{I} atoms) than in the c-direction.⁴³

For application as a hole transport material in heterojunction solar cell devices, CuGaO_2 has emerged as a promising candidate. Compared to NiO , its optical transparency is significantly better due to copper in its 1+ oxidation state, giving it a d^{10} electron count and preventing absorption losses from $d-d$ transitions. Its valence band edge is also 200mV more positive than that of NiO , meaning it will give a larger photovoltage in device operations. While the increase in photovoltage has been observed experimentally in CuGaO_2 based devices, photocurrents remain poor. Chapters 2 and 3 are devoted to understanding more fully why this could be.

1.2.6 Spinel Transition Metal Oxides Spinels are among the most ubiquitous structures in materials chemistry, considering almost all transition metals have been observed in a spinel.⁴⁴ The diversity of elements that can take this composition lends significant diversity to their possible electronic and optical properties. Spinels are typically of the formula $\text{A}^{\text{II}}\text{B}^{\text{III}}_2\text{O}_4$, where the A sites are tetrahedrally coordinated and the B sites are octahedrally coordinated. In a normal spinel, all A cations occupy tetrahedral sites, and all B cations occupy octahedral sites. However, depending on the crystal field stabilization energy of the cations involved, some 2+ cations prefer the octahedral sites, pushing half of the 3+ cations into tetrahedral sites. This is called an inverse spinel and is typical for Ni containing spinels, due to the preference of Ni^{2+} for octahedral sites. The crystal structure of spinels is typically cubic, but tetragonal distortions can

occur when certain elements, such as Mn, occupy the octahedral site and cause a significant Jahn-Teller distortion.⁴⁵ The crystal structures of some common spinels are shown in **Figure 1.6**.

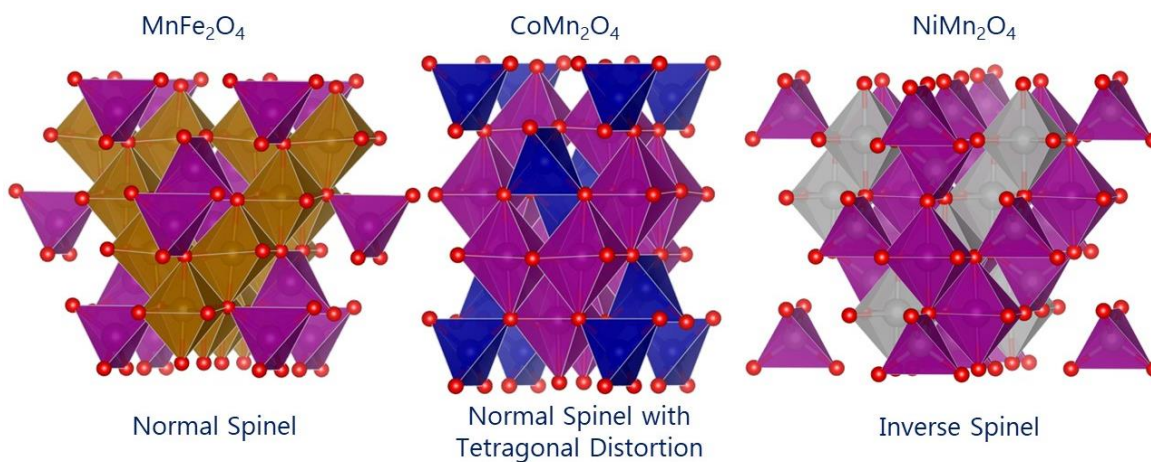


Figure 1.6: Manganese based spinels demonstrating the variations in structure type. A) MnFe₂O₄ is a normal spinel, b) CoMn₂O₄ is a normal spinel with a tetragonal distortion, and c) NiMn₂O₄ is an inverse spinel

The vastness of the spinel library and the toolkit to synthesize them, makes them excellent candidates for exploring their catalytic activity. Recently, Yang et. al. systematically synthesized and reported on the ORR capability of 16 different transition metal-based spinel oxides as nanocrystals on a carbon support.⁴⁶ This study is recent in a large list of spinel based ORR studies that have looked at nanocrystalline ORR activity as a function of defects, dopants, morphologies, etc. Little work has been done to understand ORR activity on single crystal spinel materials, and chapter 4 of this thesis will aim to shed light on this area, specifically with MnFe₂O₄ grown via molecular beam epitaxy.

1.3 Synthesis of Metal Oxides

This introduction would not be complete without a brief overview into the synthetic methods in which metal oxides can be produced. Metal oxides can be studied in a variety of forms,

including single crystalline, polycrystalline, and nanocrystalline. The morphology and size of the material can play a role in the properties of the material that are measured; therefore, it is important to understand how different synthesis methods can produce different forms of the metal oxide. The metal oxides studied for this thesis were mainly synthesized as nanocrystals, but the study of single crystalline spinels grown via molecular beam epitaxy (MBE) was done as well. An overview of nanocrystalline synthesis methods, mainly hydrothermal and continuous-injection, and the single-crystalline synthesis method MBE are discussed below.

1.3.1 Hydrothermal Synthesis Hydrothermal synthesis describes the synthesis of materials in aqueous conditions at elevated temperatures and greater than 1 atm of pressure.⁴⁷ To achieve these conditions, the reactions take place in Teflon-lined autoclave vessels. Hydrothermal synthesis can be used to synthesize many different and new materials, because the reaction conditions allow for the formation of supercritical water.⁴⁸ This changes the relative solubility of reactants and induces crystallization. Solvothermal synthesis works similarly, but with the exception that an organic solvent is used in place of water. Hydrothermal and solvothermal syntheses are extremely versatile synthetic techniques but have the downside of being a “black box” reaction, in the sense that the formation of products cannot be readily observed. Hydrothermal synthesis can also suffer from unregulated seed formation and growth phases that cause polydispersity in nanocrystal formation. For the reason, hydrothermal synthesis is usually reserved for materials that are difficult to form at ambient pressure, such as delafossite oxides.⁴⁹ Otherwise, nanocrystals are synthesized using methods that allow for significantly more control over the size, morphology, and phase of the desired material

1.3.2 Continuous Injection Synthesis Some of the most utilized synthetic methods in the inorganic nanocrystal synthesis are the hot-injection and heat-up synthetic methods, which have

been utilized for the synthesis of many binary, ternary, quaternary nanocrystal materials.^{50,51} Hot-injection synthesis involves the injection of a precursor material into a high boiling point solvent, which induces a fast nucleation event from supersaturation of the solution. This is then followed by a short-lived growth stage, where remaining monomer in solution contributes to the growth of the nanocrystals. This synthesis is particularly well-known for making well-defined nanocrystals, due to very distinct nucleation and growth phases. However, this method relies on uniform stirring and heating of the reaction solution, which makes scale up of the hot-injection reaction difficult. Heat-up synthesis, on the other hand, provides a great solution for scale up problems, as all the precursors are present in the reaction flask upon heating. The application of heat at a controlled rate allows for the controlled decomposition of precursors into monomer, which can then nucleate once supersaturation has been achieved. This instigates the growth phase, followed by completion of the reaction. This synthesis can be particularly great for making ternary or quaternary materials by precursor tailoring, which can be more challenging with the hot-injection synthesis. However, the heat-up synthesis does tend to have more issues with controlling particle size and morphology, as the rate of precursor decomposition can affect the initiation of nucleation and growth phases, which need to be well-separated. These syntheses are also not necessarily well-suited for metal oxide synthesis, as the oxygen in the crystal structure needs to come from a ligand in solution, typically through lysis of a carboxylic acid. This limits the range of precursor materials, which can be very important for synthetic tailoring.

This has led to the investigation of the continuous injection synthesis, which is a middle ground option between the hot-injection and heat-up synthetic methods.^{52,53} It involves the slow addition of precursor to a hot solvent solution, which allows for a highly controlled layer-by-layer addition of monomer to the nanocrystal surface. This extends the growth regime of the

synthesis and allows for significant variation of particle size, as well as doping and dopant location in the nanocrystal structure.^{54,55} This reaction is particularly well-suited to metal oxide nanocrystals, because metal oleate precursors can form the necessary M-OH monomer units via an esterification reaction, which is catalyzed by the metal precursor itself. This method has been shown to be applicable to the synthesis of first row transition metal binary oxides, as well as some ternary metal oxide species, such as doped metal oxides.^{52,55-57} We explored this synthesis for the development of a wider variety of ternary metal oxide synthesis and were enlightened by how reactivity of the individual metal components can influence the overall mechanistic pathway. This will be discussed significantly in Chapter 5.

1.3.3 Molecular Beam Epitaxy Pulsed-laser deposition (PLD), chemical vapor deposition (CVD), and molecular beam epitaxy (MBE) are the typical choices for the growth of single crystalline metal oxide films. What these methods have in common is the volatilization of metals to the gas phase, combined with oxygen to produce a layered deposition of material onto a substrate.⁵⁸ The difference between these methods is the way in which the metals are volatilized and deposited. For the purpose of this thesis only metal oxide MBE will be discussed.

MBE is a synthesis technique that has the capability to produce exceptionally pure, defect-free metal oxide materials.^{58,59} This is related to the way in which the metals are volatilized, which is done using effusion cells. Effusion cells are used to thermally generate atomic beams of the desired metal to be deposited on the substrate. Oxygen is also introduced to the system as either molecular oxygen (O_2) or ozone (O_3). The amount of oxygen introduced into the synthesis chamber is very important for the oxidation of the evaporated metal species and for stoichiometric balance to achieve the desired material. Once a proper mixture of metal cations and oxygen atoms has been achieved, growth of highly pure, single-crystalline materials by

deposition on a substrate. The growth of the film is monitored *in situ* using Reflection High-Energy Electron Diffraction (RHEED), which is a surface sensitive technique that scatters electrons based on the morphology and crystal structure of a material's surface. MBE has been the “gold standard” method for producing high quality semiconductor materials for decades and is one of the best techniques for investigating the intrinsic properties of materials.⁶⁰ This is particularly important for comparison to nanocrystalline materials, which have a higher defect tolerance that could impart different properties when studying materials.

1.4 Metal Oxide Electrochemistry

One of the best tools for studying the properties of metal oxides for energy applications is electrochemistry. The conductivity, surface area, defects, and band structures of metal oxides all have an electrochemical response when probed in an electrochemical cell, which allows for understanding of the contribution of all those properties to how a metal oxide would behave in a solar cell device. The library of electrochemical techniques is vast, and by far the most common technique is cyclic voltammetry (CV) which is typically used to study the electrochemical response of small molecules in solution. Metal oxides can be studied using cyclic voltammetry as well, where redox features related to oxidation and reduction of the metal centers can be observed. CV is particularly important for studying metal oxides used in electrocatalysis, because catalytic electrochemistry is well understood using cyclic voltammetry. For fundamental investigation of the metal oxide itself, the separation of faradaic vs non-faradaic current in metal oxide electrochemistry is more challenging due to large surface area of the electrodes and the inherent electrochemical response of a metal oxide. Therefore, electrochemical impedance spectroscopy (EIS) is a very powerful technique to study metal oxide films and is used

significantly in the metal oxide and solar cell literature. CV discussing the investigation of metal oxide electrodes, including for electrocatalytic studies, will be discussed in section 1.4.1, and EIS will be discussed in section 1.4.2.

1.4.1 Cyclic Voltammetry and Rotating Disk Electrochemistry

1.4.1.1 Cyclic Voltammetry on Mesoporous Films Cyclic Voltammetry is also a useful technique to study metal oxide nanocrystalline and single crystalline materials. While EIS can be useful for separating resistive and capacitive components in systems, it can be challenging to interpret without the necessary equivalent circuit model. It is also more complex and a less used technique. CV is the most common electrochemical technique, and while it is most commonly used on homogeneous systems, it can be very useful for heterogeneous systems as well. Techniques like scan rate dependence can be informative of surface bound or diffusion-controlled processes at the metal oxide surface. Experiments in different electrolytes can be informative of different redox processes at the metal oxide surface, depending on electrolyte diffusion based on cation size and charge balance at the surface. CV can even be informative of the presence of defect sites in materials based on redox features present in the voltammogram.

To highlight a few examples of the usefulness of CV in the metal oxide literature, we can look no further than TiO₂, which has been studied intensely due to its employment in heterojunction devices. Specifically, its electrochemistry as a nanoporous film in electrolyte has been of great interest because of the contribution of capacitance from the conduction band states, as well as faradaic processes associated with charge accumulation at the surface. In aqueous electrolyte at different pH's TiO₂ shows different behavior based on the proton concentration in solution.⁶¹ This study also shows difference in charge accumulation at the metal oxide interface as a function of scan rate.⁶¹ CV has also been used to understand the contribution of trap states in

electron transfer at the surface of nanocrystalline TiO_2 .^{62,63} Changes in capacitance of a metal oxide can also be observed in CV experiments, for example, in the case of doping of a metal oxide. True semiconductor behavior in a CV should have a sharp onset of current increase due to the onset of the band states being probed. No current should be passed at potentials in the band gap because there are no states there, except for monoenergetic or exponential trap states caused by defects. However, doping of a metal oxide can cause changes in CV, seen by significant non-faradaic current at potentials in the bandgap (**Figure 1.7a**).⁶⁴

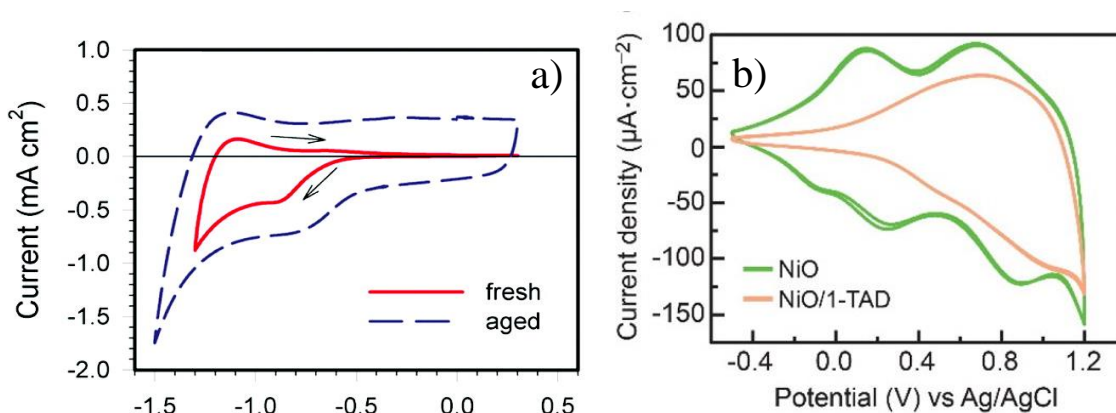


Figure 1.7: a) CV of TiO_2 nanotubes comparing a fresh film with a film aged by cycling in basic aqueous electrolyte. Cycling induces the formation of Ti^{3+} centers which dopes the material, changing the non-faradaic current observed. Reprinted with permission from the American Chemical Society.⁶⁴ b) CV of NiO before and after passivation of Ni vacancy defects using atomic layer deposition. Reprinted with permission from the American Chemical Society.⁶⁵

NiO is a p-type metal oxide that has also been studied significantly with CV and compared to TiO_2 has significantly more redox features that can be probed. These redox features have been assigned to $\text{Ni}^{\text{II/III}}$ and $\text{Ni}^{\text{III/IV}}$ redox events, specifically stabilized by hydroxides at the surface (**Figure 1.7b**).⁶⁶ These redox features are caused by defects, specifically Ni vacancies in the NiO material, and when remediated the voltammograms for this material can change significantly.⁶⁵ This can be explored even further by adding a redox active electrolyte to the electrochemical cell to probe the redox properties of the surface states.⁶⁷

These types of cyclic voltammetry studies were very useful in understanding the behavior of mesoporous CuGaO₂ films and will be discussed further in chapters 2 and 3.

1.4.1.2 Cyclic Voltammetry for Electrocatalysis CV is one of the most important techniques for understanding electrocatalytic processes, as it can be used to understand rate constants, numbers of e⁻ transferred, diffusion limits of substrate, etc. ORR, specifically, needs to be electrochemically evaluated while the working electrode is rotating, in an experiment called Rotating Disk Electrochemistry. This is due to the low solubility of O₂ in water, therefore the electrode needs to be rotated to improve mass transfer to the surface. This allows for analysis of the system under diffusion-limited conditions. An example of this data is shown in **Figure 1.8a** for Pt/C electrode.

Some important parameters that are derived from electrochemical analysis of heterogeneous catalysts are the E_{onset}, defined in most ORR literature as the potential at 10 μA cm⁻², E_{1/2}, defined as the potential when half the maximum current is passed, η_j, the overpotential defined at a specific current density, and j_d, the current density at diffusion-limiting conditions.⁶⁸ To really understand the activity of a catalyst under kinetic and diffusion controlled regimes, Koutecky-Levich analysis should be applied. The K-L equation relates the total current density achieved by a catalyst to the rotation of the electrode as follows:

$$1) \frac{1}{J} = \frac{1}{J_k} + \frac{1}{J_L} = \frac{1}{nFkC_0} + \frac{1}{0.62nFC_0(D_0)^{2/3}\nu^{-1/6}\omega^{1/2}}$$

Where J_k is the kinetic current density, J_L is the diffusion-limiting current density, n is the overall number of electrons transferred, F is Faraday's constant, k is the electron transfer rate constant, C₀ is the O₂ concentration in the electrolyte, D₀ is the diffusion coefficient of O₂ in the electrolyte, ν is the viscosity of the electrolyte, and ω is the angular velocity in units of rad s⁻¹.⁶⁹

From a K-L plot, where J⁻¹ is plotted versus ω^{-1/2}, the slope of the line is the number of e⁻

transferred and the intercept is the rate constant of for electron transfer. **Figure 1.8b** shows a K-L plot generated from the RDE data in **Figure 1.8a**.

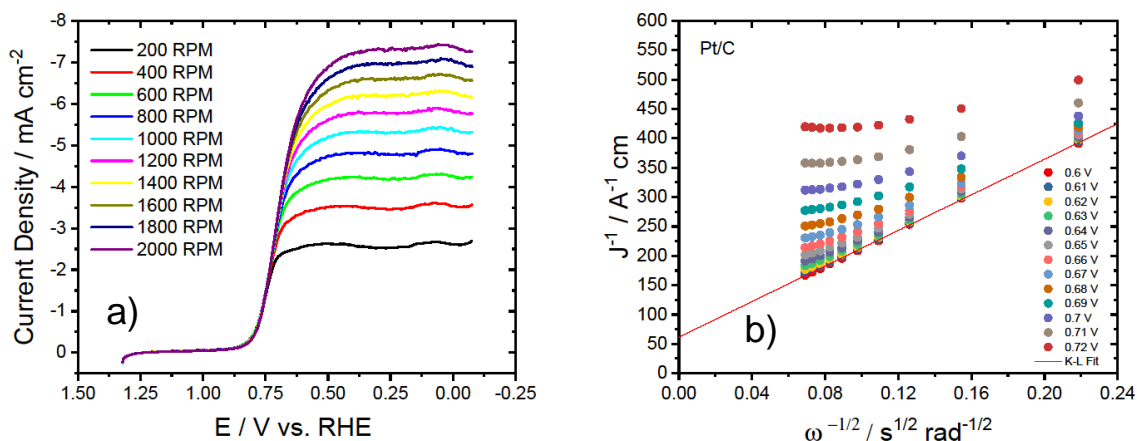


Figure 1.8: a) RDE experiment of O₂ reduction in 0.1 M KOH electrolyte using Pt/C as a catalyst. b) Koutecky-Levich plot of the data from the RDE experiment showing a linear relationship for J^- vs. $\omega^{-1/2}$. From the slope of the line and electron transfer number can be calculated, and the intercepts can be used to find the electron transfer rate constant.

Along with simple CV experiments, this analysis was applied to the study of single crystalline spinel MnFe₂O₄ films grown via molecular beam epitaxy (MBE), which will be discussed in more detail in Chapter 4.

1.4.2 Electrochemical Impedance Spectroscopy The importance of EIS in this thesis, particularly chapters 2 and 3, warrants an in-depth discussion on the technique and its use in studying metal oxide electrode materials. Electrochemical impedance spectroscopy (EIS) is a versatile technique for the study of electrode materials relevant to energy applications such as heterojunction solar cells, and electro/photocatalysis.^{70–75} For these energy applications, metal oxides with semiconductor and metallic properties are of most interest because of the need to conduct charge through an electrical device. These materials are therefore found ubiquitously throughout energy applications including solar-to-electrical and solar-to-fuel energy conversion

as well as energy storage in batteries and supercapacitors. As discussed in Section 1.2, wide band gap semiconductor metal oxides such as TiO₂, ZnO, and NiO have been heavily studied as n-type and p-type electrodes in heterojunction solar cells such as dye-sensitized solar cells (DSSCs), organic photovoltaics (OPV), quantum dot sensitized solar cells (QDSCs), and perovskite solar cells (PSCs).⁷⁶⁻⁸⁰

As an alternating current (AC) technique, EIS is capable of distinguishing between resistive and capacitive responses of metal oxide interfaces based on the frequency dependence of the observed current. Central to this is the fact that the impedance of a resistor does not depend on the frequency of the modulated voltage, however, the impedance of a capacitor is inversely proportional to this frequency.^{70,75,83} Therefore, EIS offers the ability to study these components independently over a selected voltage range based on a frequency dependent current response. By comparison, a direct current technique such as cyclic voltammetry (CV) shows capacitive and resistive features simultaneously, such that differentiating the two can sometimes be difficult.⁶¹

1.4.2.1 EIS Background EIS is fundamentally an AC technique in which an applied potential $E(t)$ is modulated over time with a small amplitude ($|E_o| \sim 5-10$ mV) at a controlled frequency (ω) according to **Equation 1.3**. Here, ω is an angular frequency defined by $\omega = 2\pi f$ and f is the frequency in Hz. The small perturbation in potential defined by $|E_o|$ is required to ensure linear behavior of the current following the Butler-Volmer model.⁶⁸ The measured current response $I(t)$ is matched in frequency but offset by a phase angle (ϕ) depending on the parameters of the electrochemical circuit, **Equation 1.4**. Impedance is defined as the AC analog to resistance and is thus related to the alternating potential and current through Ohm's law shown in **Equation 1.5** and is expressed in units of ohms (Ω).

$$1.3) E(t) = |E_o| \sin(\omega t)$$

$$1.4) I(t) = |I_0|\sin(\omega t + \varphi)$$

$$1.5) Z(\omega) = E(t)/I(t)$$

In a typical EIS experiment, the modulation frequency is sampled over a wide range (~ 1 mHz – 1 MHz) for a fixed applied potential (E_{app}) on top of which the small modulation amplitude $|E_0|$ is applied such that $E(t) = E_{app} + |E_0|\sin(\omega t)$. When the frequency range is completed, E_{app} is shifted to a new value and the process is repeated. For a single potential, experiments may take anywhere from a few seconds to tens of minutes depending on the frequency range of interest. Therefore, it is not uncommon for experiments to take many hours to fully collect EIS data over a wide potential range and/or with a small step size between applied potentials.

Collected data are then interpreted using a variety of plots. The most important is the Nyquist plot, in which impedance is plotted as a complex number ($j = \sqrt{-1}$) according to **Equation 1.6** with Z_{Im} (Z'') along the y-axis and Z_{Re} (Z') along the x-axis (**Figure 1.9**). The characteristic semicircle arc arises from the parallel combination of a resistor and capacitor described in **Figure 1.9**. Each data point in a Nyquist plot represents a different frequency with ω decreasing from left to right. At infinitely low frequencies, the applied potential is essentially constant, and this condition is considered the DC limit where $Z_{Re} = R_s + R_{ct}$. This condition is often relevant when relating EIS data to other DC electrochemical techniques such as cyclic voltammetry. For each frequency, the impedance is defined by a vector originating from the origin with magnitude $|Z|$ and phase angle φ . These two terms are defined with respect to Z_{Re} and Z_{Im} by **Equations 1.7-1.8** below.

$$1.6) Z(\omega) = |Z|(\cos(\varphi) - j\sin(\varphi)) = Z_{Re} - jZ_{Im}$$

$$1.7) |Z| = (Z_{Re}^2 + Z_{Im}^2)^{1/2}$$

$$1.8) \tan \varphi = Z_{Im}/Z_{Re}$$

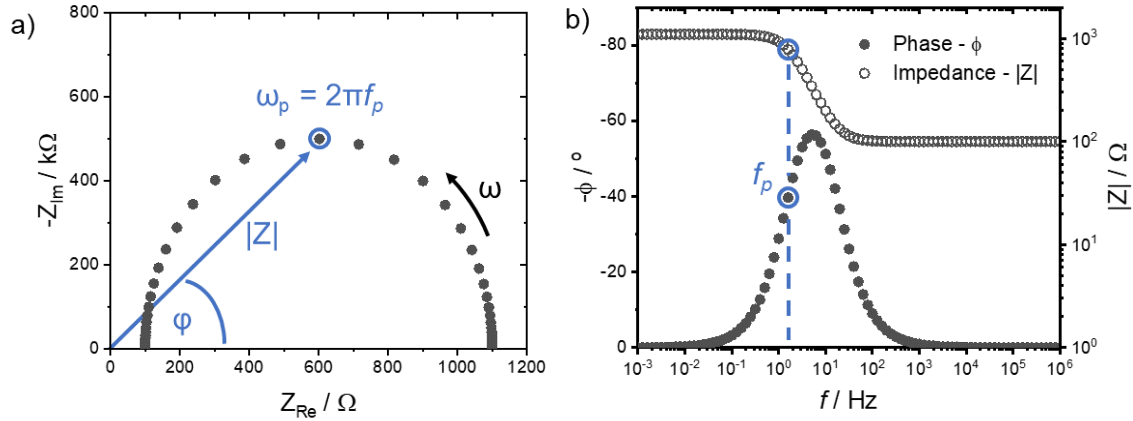


Figure 1.9: Simulated (a) Nyquist and (b) Bode plots representing the same EIS data ($R_s = 100 \Omega$, $R_{ct} = 1000 \Omega$, $C_{int} = 100 \mu\text{F}$). In the Nyquist plot, the modulus $|Z|$ and phase angle ϕ define the position of each frequency dependent data point in a complex plane. In the Bode plot, $|Z|$ and ϕ are plotted against the modulation frequency. The angular frequency associated with the $-Z_{Im}$ peak in the Nyquist plot is labeled ω_p and corresponds to points labeled f_p in the Bode plot.

Another method of graphing EIS data is the Bode plot, which is a combination of two plots that show the magnitude of impedance $|Z|$ and the phase angle ϕ on the y-axis and the modulation frequency f along the x-axis. Again, each data point represents a unique frequency which can now be correlated directly with $|Z|$ and ϕ . The Bode plot therefore allows for the frequency dependence of impedance to be more clearly observed than what is shown in the Nyquist plot. Sometimes, $|Z|$ and ϕ are combined into a single Bode plot with two different y-axes while at other times they are separated into Bode-Z and Bode-Phase plots. A simulated Bode plot is shown in **Figure 1.9** with the same parameters used in the Nyquist plot for comparison. Note that although the peak shape observed for ϕ results from the semicircle arc shown in the Nyquist plot, the frequencies associated with each peak are not identical. The peak in the Nyquist plot is directly related to R_{ct} and C_{int} at the electrode surface according to $f_p = 1/R_{ct}C_{int}$ where $R_{ct}C_{int}$ is known as the time constant for the parallel circuit. The peak in the Bode-Phase plot, however, does not correlate with f_p and can sometimes be difficult to interpret directly due the presence of additional circuit elements such as series resistance. We caution the

use of Bode plots to directly interpret EIS data and instead encourage all data to be fit according to a well-defined circuit model (discussed further below).

EIS data can also be interpreted in terms of frequency dependent and potential dependent capacitance. Just like impedance, capacitance can be defined as a complex number and determined from $Z(\omega)$ based on **Equation 1.9**. Plotting C_{Re} vs frequency reveals direct information about capacitance at the electrode surface. This method of analysis has become particularly useful in the area of PSCs where accumulation of mobile ions (*e.g.* iodide, methylammonium) in the perovskite material at the interface with metal oxide electrodes results in large capacitances at low-frequencies.^{84–88} **Figure 1.10** shows an example plot of C_{Re} vs frequency for the same data shown in **Figure 1.9**. Note that the plateau in capacitance occurs at $C_{Re} = 100 \mu\text{F} = C_{int}$, thus allowing for the interfacial capacitance to be obtained directly from the plot.

$$\mathbf{1.9)} C(\omega) = 1/j\omega Z(\omega) = C_{Re} - jC_{Im}$$

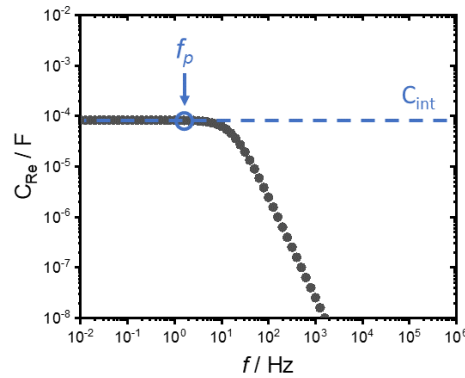
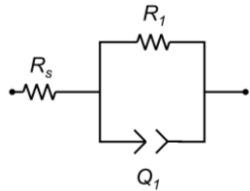
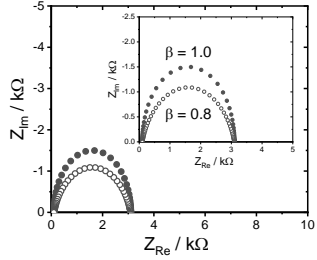
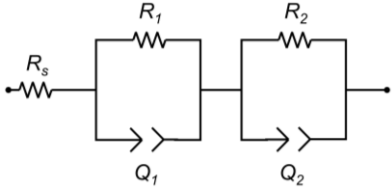
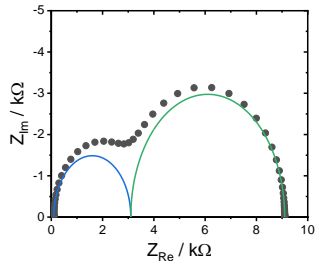
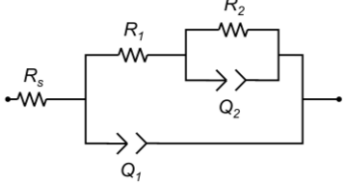
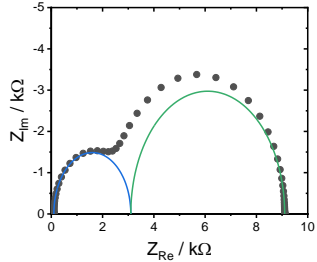
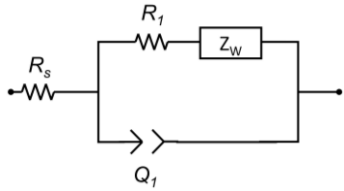
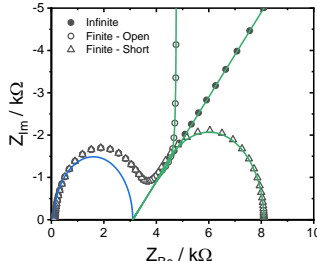
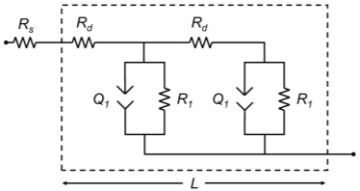
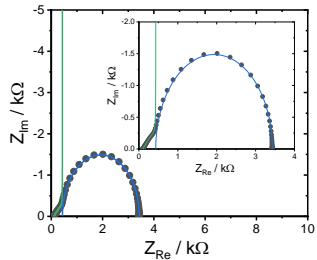


Figure 1.10: Capacitance vs frequency plot showing a plateau at $C_{int} = 100 \mu\text{F}$. C_{Re} was calculated from **Equation 1.9** based on the same data simulated in **Figure 1.9**. The peak frequency observed in the Nyquist plot is shown here for reference at f_p .

Another important aspect of interpreting EIS data is fitting of the data using equivalent circuit models. These models consist of resistors, capacitors (or constant phase elements), and inductors

to mimic the pathways through which current can flow in an electrochemical system. To briefly expand, resistors are used to model redox behavior and mobile charges in electrochemical systems, capacitors and constant phase elements are used to model the contributions of non-faradaic current, and inductors model electromagnetic fluxes, typically caused by proximity of electrodes. With these components five models have been identified of significance to the metal oxide community: a simple Randle's circuit (Model A), multiple Randle's circuits in series (Model B), the imbedded Randle's circuit (Model C), Randle's circuit with a Warburg diffusion term (Model D), and a more specialized model that describes diffusion of charges in a thin layer film (Model E). A graphic of these equivalent circuits and their corresponding Nyquist plots are shown in **Table 1.1**. The mathematical description of the circuit components as well as a more detailed explanation of these equivalent circuits is discussed in our review of EIS in metal oxide materials.⁸⁹

Table 1.1 Summary of common equivalent circuits for analyzing EIS data of metal oxide electrodes

Circuit	Simulated Data
<p>Model A</p> 	
<p>Model B</p> 	
<p>Model C</p> 	
<p>Model D</p> 	
<p>Model E</p> 	

$R_1 = 3 \text{ k}\Omega$, $R_2 = 6 \text{ k}\Omega$, $C_1 = 1 \text{ }\mu\text{F}$, $C_2 = 10 \text{ }\mu\text{F}$, $R_d = 1 \text{ k}\Omega$, $\sigma = 5 \text{ k}\Omega \text{ s}^{-1/2}$, $L/D^{1/2} = 1 \text{ s}^{1/2}$, $\beta = 1.0$ unless otherwise indicated. Blue lines show R_1 and Q_1 terms appear in the overall data. Green lines show R_2 , Q_2 , R_d , or Z_w terms appear in the data.

1.4.1.2 EIS of Metal Oxides for Heterojunction Devices The rest of this section will detail the use of EIS on metal oxide electrodes that are relevant to the study of heterojunction devices. Nanocrystalline, polycrystalline, and single crystalline metal oxide materials have been of great importance for their utilization in devices for solar-to-electric energy conversion.⁹⁰ As discussed in Section 1.2.1, n-type and p-type wide band gap oxides are used as selective contacts for electron and hole transport, respectively, between a light absorber and the external circuit. Oxides that have been utilized in heterojunction devices as charge transport layers include TiO₂,^{91–93} ZnO,^{94,95} SnO₂,^{96–98} Nb₂O₅,^{99–101} SrTiO₃,^{101–103} ZnSn₂O₄,^{104–106} CeO₂,^{107,108} NiO,^{109,110} and CuGaO₂.^{111,112} This list gives a small taste of the variety found in metal oxides; from using transition metals to lanthanides, from binary to ternary, and from n-type to p-type.

In some cases, the metal oxide facilitates charge separation from the light absorber at the metal oxide interface such as in dye-sensitized solar cells where a molecular chromophore is bound directly to the metal oxide surface.^{76,113} However, for heterojunction solar cells in which the light absorber is a semiconductor material of considerable thickness (e.g. quantum dot solar cells,^{77,78} organic photovoltaics,^{79,114} and perovskite solar cells^{80,84–88}), charge separation of e⁻ and h⁺ may occur within the semiconductor and the metal oxide serves only an electrode selective for e⁻ or h⁺. In the former case, the EIS data can be readily interpreted in terms of the electronic properties of the metal oxide because an electrolyte with a large Helmholtz capacitance is present at the interface. In the latter case, the significantly lower capacitance of the semiconductor makes interpretation of EIS data more challenging because the measured interfacial capacitance is a series combination of the semiconductor and metal oxide. This is perhaps why EIS studies focusing on metal oxides in the latter devices are not found often in the literature. Notable exceptions include studies on QDSCs which compare SnO₂ and TiO₂ where electron diffusion in

the metal oxide can be observed²¹ and PSCs where the nature of the metal oxide makes a significant difference in the magnitude of the interfacial capacitance observed at low frequencies.^{84–88}

EIS is a powerful tool to characterize metal oxide electrodes, either in simple electrochemical cells, or in the context of complete solar cells. While CV on heterogeneous systems is useful, EIS can provide distinction between specific interfaces such as the metal oxide/electrolyte and metal oxide/substrate interfaces as well as significant information on the band structure, density of states, number and type of charge carrier, and conductivity of the metal oxide electrode.⁷⁵ In this section we describe metal oxides used for solar-to-electric energy conversion, the results of their EIS data, and the models that have been used to understand their properties. The understanding of heterogeneous electrochemistry using EIS is significant in the literature for TiO₂, ZnO, and SnO₂ for electron transport (n-type), and NiO and CuGaO₂ for hole transport (p-type). In most cases, a metal oxide/electrolyte interface is specifically studied, however, a discussion of metal oxide/semiconductor interfaces is also included in the section on TiO₂ as it relates to recent work in the area of PSCs. The specific resistors and capacitors discussed in this section are related to the resistance to charge diffusion/transport (R_d , R_t , or Z_w) through the metal oxide, resistance to charge transfer (R_{ct}) or charge recombination (R_{rec}) at the metal oxide interface, and the chemical capacitance (C_{μ}) of the metal oxide. Importantly, C_{μ} can also be represented as a density of states (DOS) of the metal oxide, which gives insight into the distribution of defect/trap states at the metal oxide interface. Metal oxide morphology and doping are also shown to influence C_{μ} , due to surface area changes, exposure of surface states, and changes in conductivity/introduction of defects.

1.4.1.2.1 n-type metal oxides: TiO₂: The most significant use of EIS to study a metal oxide in the context of heterojunction solar cells has been done on TiO₂ because of its use in the original Grätzel cell.¹¹⁵ Bisquert and coworkers, in particular, have published a significant body of work on mesoporous films of TiO₂ nanocrystals, as they are the most relevant in the context of dye-sensitized solar cells for their high surface area.^{61,116-119}

Bisquert has shown that depending on the applied potential to a bare TiO₂ electrode in a three-electrode set-up, different models can be used to understand the electronic properties of the metal oxide.¹¹⁷ Specifically, the electrode can behave as an insulator at potentials very positive of the conduction band edge, and as a metal at potentials very negative of the conduction band edge. In these regimes, the equivalent circuits are simplified as shown in **Figure 1.11**. The corresponding Nyquist plots next to each circuit demonstrate that the impedance at positive potentials resembled a Randles circuit with an infinitely large R_{ct} , due to low level of electronic states in the band gap. As the potentials became more negative and conduction band states began to be populated by electrons, R_{ct} decreased and a semicircle arc was observed at low frequencies. At these conditions, the resistance for electron diffusion through the film could be observed, shown by the linear behavior at high frequencies, and the capacitance associated with conduction band states could be estimated. The transmission line equivalent circuit shown as Model E was developed to model EIS data such as this for TiO₂ mesoporous films. As the applied potential was pushed further negative, the diffusional resistance decreased such that the linear feature was no longer observed. The capacitance of the metal oxide also increased such that the full semicircle arc was not fully resolved over the frequency range. These changes were explained by an exponential increase in the density of conduction band states in TiO₂. As these states were populated at more negative potentials, the diffusional resistance decreased based on its inverse

relationship with conductivity and the capacitance increased as the concentration of charges went up. Overall, this work demonstrated the ability of impedance to differentiate insulator, semiconductor, and metallic behavior in metal oxide films, while considering the unique contributions of the mesoporous structure.

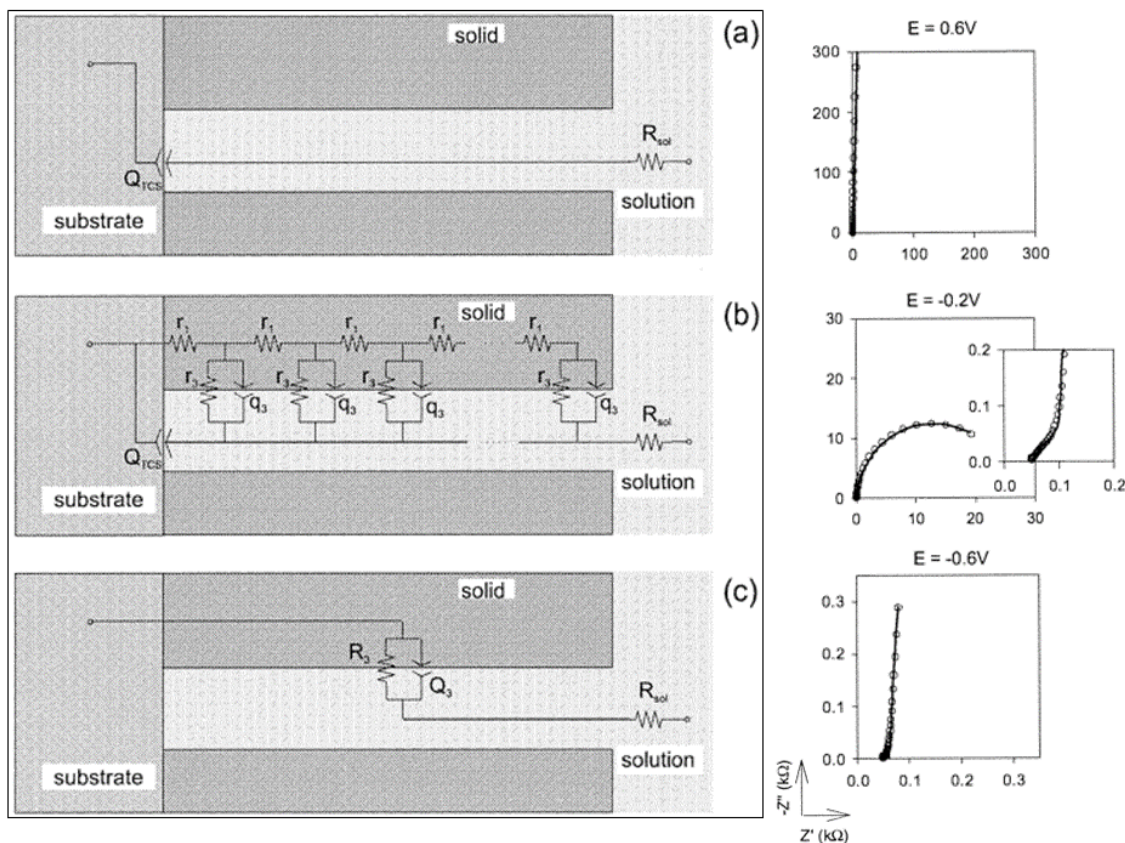


Figure 1.11: (left) Equivalent circuit models used to analyze EIS data for mesoporous TiO_2 electrodes as a function of applied potential. Going from positive to negative potentials, TiO_2 is modeled as an insulator (a), semiconductor (b), and metal (c). (right) Nyquist plots obtained at different applied potentials to show the behavior of each equivalent circuit. Reprinted with permission from the American Chemical Society.¹¹⁷

Bisquert and coworkers have also modified the transmission line model from above to include interfaces specific to DSSCs. Features were added that take into account the unique properties of electrolyte diffusion, charge recombination at the metal oxide/electrolyte interface,

and the electrolyte/counter electrode interface.¹¹⁹ Other models have been proposed that are specific to DSSCs in other operating conditions.^{120,121} Prior to Bisquert, Kern et. al. derived a model that allowed for elucidation of EIS behavior for DSSCs at open circuit conditions under illumination where the modeling of electron diffusion and recombination was done with differential equations, as opposed to RC circuit elements.¹²² It was later elucidated by Adachi et. al. that despite the different physical assumptions made by Kern and Bisquert for their models, they are each mathematically the same.¹²³

One aspect of TiO₂ that researchers have sought to understand is the presence and distribution of trap/surface states present at potentials below the conduction band edge. The presence of these states influences the measured chemical capacitance and the charge transfer/recombination events that take place at the metal oxide surface. A study by Mora-Sero and Bisquert showed that the Fermi-level of electrons in surface states was distinct from the Fermi-level of free electrons in the conduction band of TiO₂.¹²⁴ Due to recombination of the electrons in the surface state with the electrolyte, the Fermi-level of the surface states is always below that of the bulk Fermi-level. The charge transfer resistance was measured by EIS and plotted vs the Fermi-level energy of the surface states and the bulk. It was revealed that surface state recombination is dominant due to low concentration of conduction band electrons when the Fermi-level of the surface state is below that of the surface state energy and conduction band energy. As the Fermi-level of the surface state surpasses the energy level of the surface state, and the bulk Fermi-level approaches the conduction band, conduction band recombination becomes the dominant pathway.

Results of EIS investigations of nanoparticle TiO₂ mesoporous films in many studies have indicated the presence of such surface/trap states.^{62,125–130} Gimenez et. al. studied surface states

for a bare TiO₂ electrode in aqueous electrolyte by modeling the charge transfer resistance and chemical capacitance using the transmission line model (Model E).¹²⁷ A monoenergetic trapping model was developed in the paper and was validated by simulations and experimental data. EIS data showed an exponential increase in C_{μ} as the monoenergetic trap state was approached (around -0.85 V vs Ag/AgCl) followed by a decrease at more negative potentials, then an exponential increase at the trap state tail. The opposite trend was observed for R_{ct} where recombination resistance decreased as the trap states were populated with electrons. Illumination of the electrode resulted in similar behavior for C_{μ} , but R_{ct} was constant over the applied potential range. This was explained by a saturation of recombination events from photogenerated charges. EIS has also been used to differentiate between monoenergetic trap states and exponential trap states. Bertoluzzi et al. elucidated the contribution of exponential and monoenergetic trap states to the total chemical capacitance by comparing nanoparticle TiO₂ with submicron TiO₂, which had more defined crystal facets to expose the surface states (**Figure 1.12**).⁶²

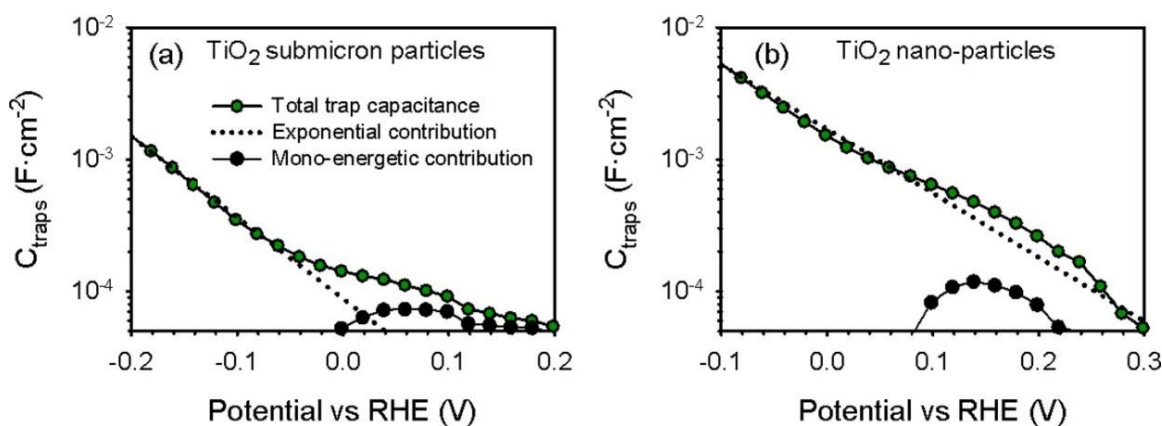


Figure 1.12: Total capacitance of trap states measured via EIS for **(left)** submicron TiO₂ and **(right)** nanoparticle TiO₂. The contribution of monoenergetic traps was confirmed by the peak feature in the capacitance as a function of potential. The contribution of exponential trap states is shown by the dashed line. Reprinted with permission from the American Chemical Society.⁶²

Other studies have shown that passivation of trap/surface states can be achieved by adding blocking layers.^{129,131–134} Blocking layers are a standard component of heterojunction solar cells because of their ability to limit charge recombination. Pascoe et. al. showed with EIS that atomic layer deposition of Al₂O₃ improved recombination by increasing R_{ct}, while C_μ stayed consistent.¹²⁹ However, it was also shown the conduction band states were being suppressed by the blocking layer treatment. Góse et al. used EIS to understand the improvements and limitations of blocking layers in DSSCs.¹³³

The desire to change the charge transport properties and surface area of TiO₂ electrodes has led to an exploration of different nanocrystalline morphologies. There are two notable aspects to the areas which have been investigated. The first is exploration of different crystal phases of TiO₂, such as anatase, rutile, and brookite to understand the relationship between crystal structure and charge transport. The most studied of these phases is anatase TiO₂ because of its larger band gap and higher conductivity,¹³⁵ but interest in rutile and brookite have been reported in the literature.^{135–144} EIS has been used to understand the fundamental charge transport properties of rutile and anatase crystal phases directly,^{145,146} as well as in solar cells.^{147–150} Growth of the rutile phase thermodynamically favors nanorods and can be seen in a study by Kim et al. to function well as a scaffold for perovskite nanocrystals in solid state PSCs.¹⁴⁹ Using EIS the authors determined the effect of rutile nanorod length on device performance. Under both an applied potential and illumination, it was determined that the impedance fitting could be simplified from the transmission line model (Model E) to a simple two-arc model (Model B), because the mid-frequency Nyquist arc did not have a linear feature indicating diffusion limited charge transport, believed to be due to the large, applied potential. The mid frequency arc was the result of the recombination resistance and the chemical capacitance. The authors showed that

nanorod length had little effect on the chemical capacitance or recombination resistance in these devices, as neither of these parameters were changing significantly with applied potential, which was consistent with previously reported rutile PSC measurements. However, the photocurrent and photovoltage decreased in devices with increasing nanorod length.

Brookite solar cells have typically shown lower efficiencies than anatase TiO₂, but have had large open circuit potential (V_{oc}).^{143,144,147,148,151} Pourjafari et al. used EIS to study anatase TiO₂ and brookite samples synthesized under acidic and basic conditions to compare how morphology and surface structure affected electron injection into TiO₂.¹⁴⁷ EIS was measured at the open circuit potential under illumination and Nyquist plots were fit to the transmission line model (Model E). Synthesis and nanoparticle treatment both showed an effect on the measured chemical capacitance, recombination resistance, and electron lifetime in the TiO₂ electrodes. C_{μ} showed exponential dependence on V_{oc} for each sample, consistent with surface states, but base-synthesized brookite C_{μ} was considerably lower than anatase TiO₂. R_{rec} for brookite DSSCs was lower than anatase, but acid treatment increased R_{rec} in brookite DSSCs. Base-treated brookite also had the shortest electron lifetime, consistent with a small R_{rec} .

Kusamawait et. al. had previously done a similar study on brookite TiO₂ photoelectrodes and showed high V_{oc} for brookite devices.¹⁴⁸ They also showed a higher recombination resistance and slower charge transport. The same EIS model was used in both studies (Model E). Hsiao et. al. also explored the effect of brookite and rutile defects in anatase TiO₂ with EIS in a DSSC.¹⁵⁰ The authors emphasize that the presence of trap states in TiO₂ has been tied to crystal defects, and intentionally adding those defects helps study the influence of trap states on charge transport. Measured EIS of pure and defect-rich anatase reveal an increased C_{μ} for defect-rich anatase, which is consistent with the surface traps acting as electron sinks.

The second aspect of morphological studies of TiO₂ using EIS has focused on changing the shape of the nanocrystal.^{152,153} By exploring different particle shapes, control over electron transport and surface area can be achieved. Morphologies that have been explored for TiO₂ with EIS include: nanoparticles,^{62,116,117,119–123,125–128,150,154–161} nanowires/nanotubes/nanorods,^{63,64,153,162–171} and other irregular shapes.^{130,172} Several of these morphologies have been studied in conjunction with synthetic, photochemical, and electrochemical doping. The most popular structure, besides nanoparticles, in the literature is the nanowire/nanotube/nanorod structure. To briefly differentiate these structures, nanorods are solid particles oriented specifically on the substrate, nanotubes are also oriented specifically but are hollow, and nanowires are solid but do not have a specific orientation. Their popularity is due to the idea that electron flow in a metal oxide could potentially be directed vectorially toward the conductive substrate for improved charge transport and extraction from the solar cell.¹⁶⁴ For this reason, one-dimensional TiO₂ nanostructures have been investigated in solar cell devices.^{153,162,167,168} Wu et. al. used EIS to measure and deconvolute every aspect of a nanotube DSSC, including resistances associated with diffusion, electron, and charge transfer, as well as capacitances associated with the double-layer, contact, and chemical capacitances in the device.¹⁶⁸

One of the first studies of TiO₂ nanotubes by Fabregat-Santiago et al. used EIS to compare the charge transport properties and chemical capacitance to that of TiO₂ nanoparticles.⁶⁴ Whereas TiO₂ nanoparticles typically show low charge carrier densities with a Fermi-level that is well below the conduction band edge, different morphologies of TiO₂ can display more metallic behavior (i.e. high carrier density). To explore if this phenomenon is observed in TiO₂, nanotubes were synthesized with widths of 20 nm, reflective of the size of TiO₂ nanoparticles

synthesized for films but had variable lengths from 200-1000 nm. The Nyquist plots display a single arc at low frequency with a high frequency linear feature, indicative of electron diffusion through the TiO₂ nanotube. The widths of these TiO₂ nanotubes did not show a depletion capacitance consistent with band bending, which is the same behavior observed in nanoparticles.

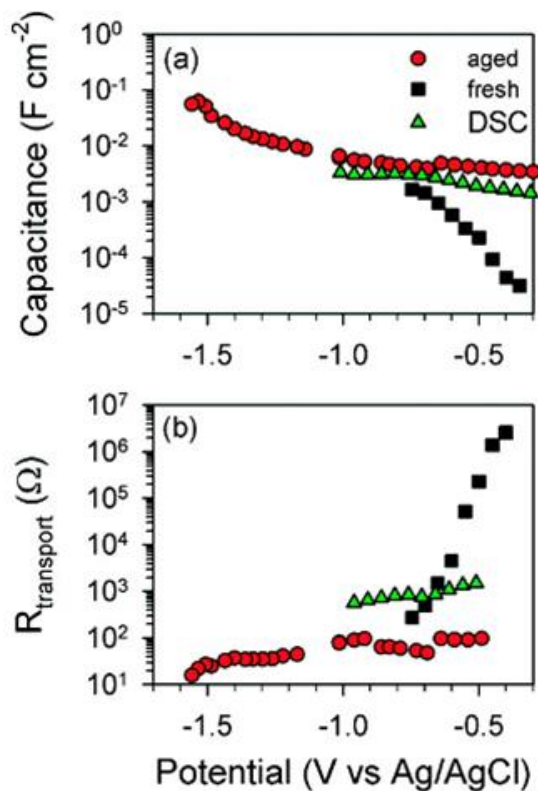


Figure 1.13: Potential dependence of capacitance and transport resistance for TiO₂ nanotubes measured by EIS as a function of applied potential. The “aged” nanotube electrode showed a large, uniform C_{μ} and low R_t , indicating that H⁺ intercalation into the TiO₂ electrode had occurred. Reprinted with permission from the American Chemical Society.⁶⁴

Furthermore, it was demonstrated in the study by Fabregat-Santiago et al. that the nanotubes were susceptible to electrochemical doping, when exposed to an extremely negative potential for an extended time in basic media. This caused a significant change in the chemical capacitance and transport resistance. **Figure 1.13** shows that in the “fresh” nanotubes, the transport resistance measured by EIS exhibited an exponential dependence on applied potential,

indicative of a low number of charge carriers when the applied potential is far from the conduction band edge. A similar trend was observed for the chemical capacitance, consistent with an increase in electronic states as the conduction band edge was approached (**Figure 1.13**). TiO₂ nanotubes that were “aged” by long exposure to an applied negative potential showed a significant decrease in transport resistance and increase in capacitance that varied less with applied potential. This indicated an increase in charge carriers in the nanotubes resulting in Fermi-level pinning near the conduction band edge. The increased carrier concentration was attributed to reduction of Ti⁴⁺ sites coupled to intercalation of H⁺ into the TiO₂ lattice. It was also demonstrated that the capacitance measured was variable with the length of the TiO₂ nanotube, indicating the role of surface area in proton intercalation. Comparative studies of nanotubes in acidic media showed R_t and C_μ values similar to “aged” samples in basic solution. Thus, a high concentration of protons immediately induced the reduction of TiO₂ and increased carrier density. Interestingly, studies of TiO₂ nanoparticles in acidic media did not demonstrate this intercalation behavior, which demonstrated that nanotube morphology was an important factor for proton intercalation.

Doping is a very common way to control defects and electronic properties of metal oxide electrodes.¹⁷³ EIS studies on TiO₂ electrodes have revealed a wide range of changes in charge transport resistance and chemical capacitance based on the chemical nature of the dopant and the method with which the dopant is introduced (e.g. photoinduced^{165,166} or electrochemically⁶⁴ induced). Niobium, tantalum, cerium and tin have each been doped into TiO₂ and the resulting effects studied with EIS.^{174–177} Collectively, these studies point to the same result where increased concentration of dopant atoms led to decreased charge transport resistances due to the higher concentration of free carriers in the TiO₂ conduction band.

Discussion up to this point has focused on TiO₂/electrolyte interfaces where the interfacial capacitance is directly related to the chemical capacitance of the TiO₂ electrode. However, when these electrodes are used as electron transport layers in lead halide perovskite solar cells, the capacitance at the metal oxide/semiconductor interface is more closely related to that of the perovskite material due to the formation of a depletion layer.^{84–88} Nonetheless, the nature of the metal oxide in contact with the perovskite has been shown to influence the presence of an ionic capacitance at the metal oxide/perovskite interface.^{178,179} This “extra” capacitance is due to mobile ions within the perovskite such as iodide and methylammonium which accumulate at the interface. This ionic capacitance is also problematic in PSCs as it leads to a hysteresis in photoinduced current-voltage measurements which are used to determine solar-to-electrical conversion efficiency, leading to uncertainty in these measurements.¹⁸⁰ Kim et al. has provided direct evidence for this assignment by examining the capacitance vs frequency data collected by EIS for PSCs with a TiO₂ electron transport layer in the “normal” configuration (electrons directed toward the transparent conductive oxide (TCO)) and with an organic electron transport layer in the “inverted” configuration (electrons directed away from the TCO).¹⁸¹ **Figure 1.14** shows that the TiO₂/perovskite interface results in significant capacitance in the low frequency region due to the accumulation of ions at the interface. The use of the organic electron transport layer removes much of this capacitance and yields a more reproducible current voltage curve. Studies have shown the use of SnO₂ as an n-type selective contact and/or NiO as a p-type selective contact can also decrease this low frequency ionic capacitance, although the physical origin of the metal oxide dependence is not yet fully understood.^{178,181}

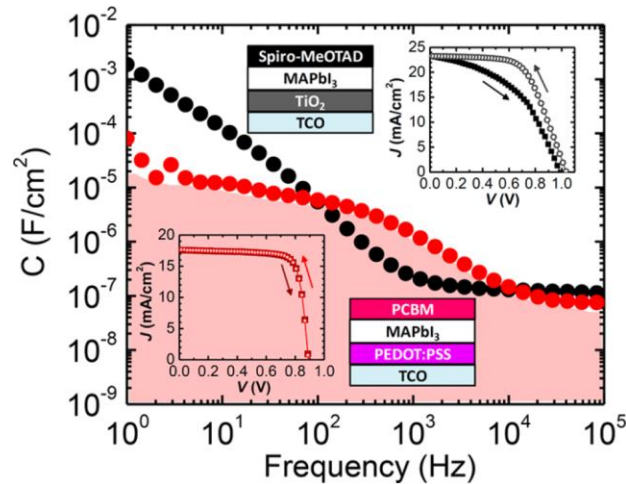


Figure 1.14: Capacitance vs frequency measured for PSCs with (black) and without (red) a TiO₂ electron transport layer. The inclusion of the TiO₂ layer results in ionic capacitance at low frequencies which results in hysteresis in the illuminated J-V curve (inset). The use of an organic electron transport layer, PCBM, does not show this ionic capacitance and therefore no hysteresis in the J-V curve. Reprinted with permission from ref __. Copyright 2015 American Chemical Society.

Figure 1.14 also highlights an important aspect of understanding capacitance at metal oxide interfaces. The frequency dependence shows that the ionic capacitance occurs in the low frequency region while the bulk capacitance of the perovskite occurs at high frequency. Therefore, in order to obtain meaningful information about the depletion layer capacitance of the perovskite, a high frequency can be used to isolate this feature from the ionic capacitance. Almora et al. have highlighted this technique in distinguishing true depletion layer capacitance using Mott-Schottky analysis from erroneous assignments due to the influence of the ionic term.¹⁸²

ZnO: Zinc oxide was one of the first metal oxides employed in heterojunction solar cells,^{183,184} but never surpassed the efficiencies of TiO₂ solar cells. In comparison studies of TiO₂ and ZnO solar cells, the TiO₂ devices typically have better performance.^{185–187} Interest in ZnO has been maintained because of the ease with which different morphologies of ZnO can be

synthesized.^{188,189} While different morphologies have been explored in TiO₂, the crystal structure of ZnO gives rise to synthetic simplicity and a large level of variability to explore many unique structures. EIS has been used to study ZnO nanoparticles, but nanorods/nanotubes are the main ZnO structures studied with EIS, for the same reasons stated above for TiO₂.

Before different ZnO morphologies are discussed, it is useful to compare ZnO systems that are similar to TiO₂ to understand if they can, electrochemically, be treated the same. A study by Guillén et al. addressed the issue of transport resistance measurement in ZnO nanoparticulate DSSCs, that did not show the diffusion feature in their Nyquist data.¹⁹⁰ By combining time constants measured with IMPS and capacitance values measured from EIS the authors used the relationship $\tau_{rt} \gamma = R_t C_{\mu}$, where gamma is an illumination factor, to calculate R_t. EIS measurements were performed at short-circuit conditions, as to be comparable to the IMPS data, and was then converted to R_t from the given relationship. To check their method, the R_t values obtained from EIS + IMPS were compared to data collected using EIS only, and the values are comparable until high Fermi-level conditions are reached, as expected.

An early EIS study on a ZnO nanowire array demonstrated that EIS could characterize the film by mathematically modeling the nanowire.¹⁹¹ First, via Mott-Schottky measurements, Mora-Sero et al. demonstrated that by appropriately defining the particle geometry of the ZnO nanowires, band bending was demonstrated at their surface (**Figure 1.15**). This has not been observed in anatase TiO₂ nanoparticles or nanotubes. The Mott-Schottky equation predicts a linear trend between C⁻² and the applied potential (E_{app}) when band bending at the semiconductor/solution interface is present, **Equation 1.10**. Here, ϵ is the relative dielectric constant of the semiconductor, ϵ_0 is vacuum permittivity, A is surface area of the interface, e is the fundamental charge, N is the doping density, k_B is Boltzmann's constant, and T is

temperature. If a linear trend is observed, then the measured capacitance is that of the depletion layer formed at the metal oxide interface and the flat band (E_{fb}) and doping density of the semiconductor may be determined. The small linear slope observed in the Mott-Schottky data indicated a high density of charges (N) in the nanowires, behavior that was attributed to the synthetic method. A decrease in charge density and capacitance was observed when nanowires were annealed under air at 450 °C, which indicated a remediation of defects that resulted in surface states. The change in capacitance with annealing was also seen in a study by Tena-Zaera et al. where ZnO nanowires were synthesized via electrodeposition and the same EIS model (Model A) was used.¹⁹²

$$\mathbf{1.10) \quad C^{-2} = (2/\epsilon\epsilon_0 A^2 e N)(E_{app} - E_{fb} - k_B T/e)}$$

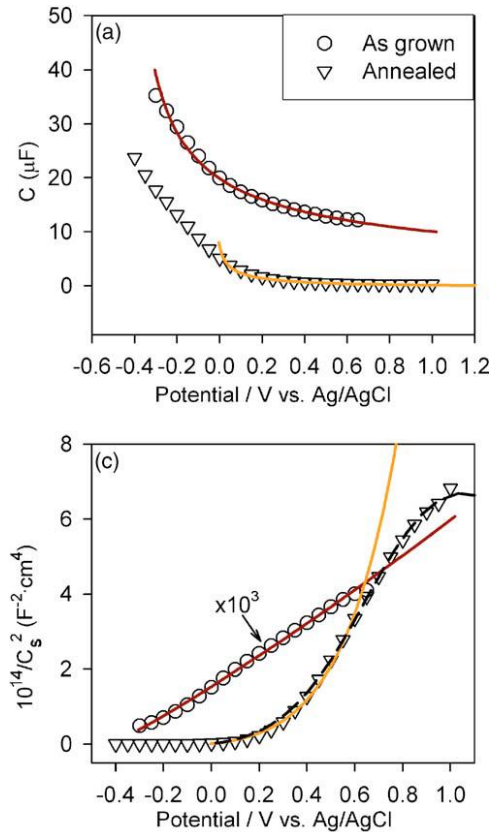


Figure 1.15: (top) Capacitance measured by EIS for a ZnO nanowire arrow before and after annealing at 450 °C in air. **(bottom)** Mott-Schottky representation of capacitance showing linear behavior for the as grown ZnO nanowire electrode. Reprinted with permission from AIP Publishing.¹⁹¹

Characterization of ZnO nanorod DSSCs using EIS has also been reported. Martinson et al. used the transmission line model (Model E) to measure the chemical capacitance and charge transfer resistance, as well as charge lifetimes and charge extraction time.¹⁹³ Briefly, charge lifetime is defined as the amount of time the photogenerated charge survives before recombination with the electrolyte and is calculated from the relationship $\tau_n = R_{\text{rec}}C_{\mu}$. Charge extraction time is the amount of time it take for the photogenerated charge to be collected in the external circuit, and is calculated from the relationship $\tau_d = R_t C_{\mu}$. EIS of the film was measured in the dark, with a bias such that the charge transport resistance feature is visible in the Nyquist plot. Conductivity is elucidated from the charge transport resistance and shows significantly

lower conductivity compared to nanoparticle TiO_2 . The ZnO nanorod film also shows lower capacitance and charge transfer resistance (**Figure 1.16**). However, the charge extraction time for the ZnO nanotube DSSC is two orders of magnitude shorter than for nanoparticle TiO_2 , displaying the influence of morphology on charge transport. EIS of a ZnO nanorod DSSC has also been studied under illumination and elucidates the contribution of trap states to the device performance.¹⁹⁴ Fit to Model E, the chemical capacitance under illumination showed exponential dependence at low bias potentials, consistent with a tail of surface trap states. At high bias potentials, the capacitance shows no dependence on illumination, which the authors attribute to a depletion layer capacitance related to the geometry of the electrode. R_{ct} also loses its linearity upon the bias potential reaching the onset of trap states tail, indicating a contribution of the surface states to recombination. R_t remained consistent, regardless of whether the EIS was measured in the dark or under illumination. The authors state this is consistent with electron transport occurring within the nanorod core.

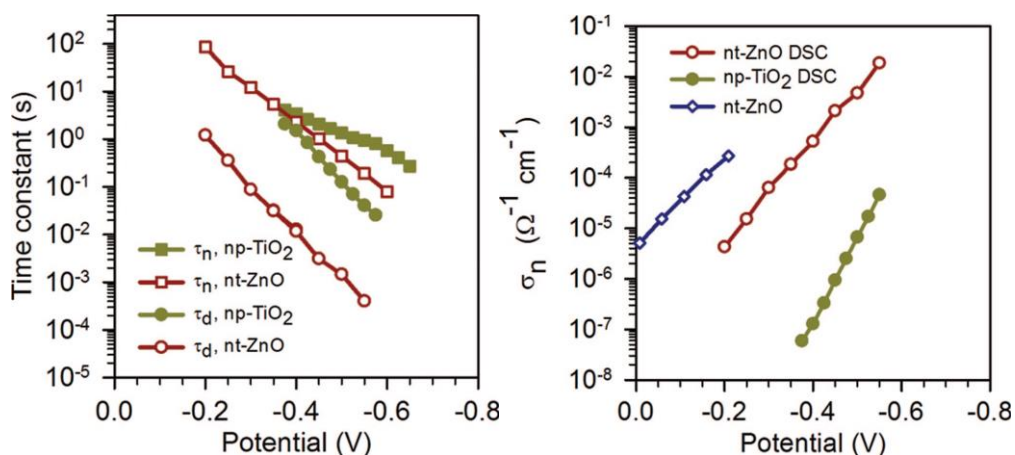


Figure 1.16: (left) Electron recombination lifetimes (τ_n) and extraction lifetimes (τ_d) calculated from resistance and capacitance values measured by EIS for DSSCs assembled from a nanoparticle TiO_2 electrode and a nanotube ZnO electrode. (right) Conductivity of a nanoparticle TiO_2 DSSC, a nanotube ZnO DSSC, and of the bare ZnO nanotube array electrode as a function of applied potential. Reprinted with permission from the American Chemical Society.¹⁹³

EIS has been used to compare the size and morphological aspects on the electronic behavior of other ZnO structures.^{195–206} To briefly highlight some unusual structures, ZnO aggregates made from sintered nanowires showed a relationship between sintering temperature and charge transport resistance, elucidated from EIS.²⁰⁵ Parthasarathay et al. used EIS to show surface state-mediated electron transfer in ZnO multipods.¹⁹⁶ Hosni et. al. investigated the electrochemical properties of ZnO electron transport layers when made of nanospheres or nanorods.²⁰⁶ Three different nanosphere sizes and one size of nanorod were studied with EIS. The smallest ZnO nanospheres had the highest capacitance and the largest density of trap states. The other nanospheres and the nanorods had a similar C_{μ} and trap state density. The capacitance measurements correlated with the measured R_{ct} , as the smallest nanospheres had the lowest charge transfer resistance, consistent with have the highest trap state density. The other nanoparticle morphologies had very similar R_{ct} values.

Like TiO_2 , the effects of defects and doping have been studied in ZnO using EIS.^{207–215} The contribution of native defects in ZnO on its electrochemical performance was assessed by Das et al., where they showed remediation of defects after post-synthetic annealing.²¹³ Cations doped into ZnO vary from alkali and alkaline earth metals to transition metals. Co-doped ZnO has been studied using EIS to assess the change in the dielectric of the material,²¹⁰ and has also been shown to change the morphology of ZnO depending on doping level, which lowered recombination resistance and increased the charge lifetime.²¹⁶ EIS was used to explore the effect of tin doping on ZnO particle grain boundaries and the resulting electronic properties.²¹² Li is one of the most well studied metal oxide dopants. In a study by Cheng et. al., ZnO doped at 5% and 20% was used as an electron transport layer in an inverted OPV.²¹⁴ Data was fit with Model C, and 5% Li-ZnO showed the largest recombination resistance and an electron lifetime that was

over two times longer than 20% Li-ZnO. Li doped ZnO has also been used as an electron transport layer in perovskite solar cells.²¹⁵ The authors acknowledge that Li^+ is more likely to interstitially dope in the ZnO structure as opposed to substituting into Zn sites in the structure. Mott-Schottky measurements show a positive shift in the conduction band edge compared to the undoped device. Nyquist plots fit with Model B showed that recombination resistance is higher and charge transport resistance is lower for the doped solar cell.

SnO₂: Along with TiO_2 and ZnO, SnO_2 is a heavily investigated metal oxide for heterojunction solar cells. However, its device efficiencies are consistently lower than those measured for devices utilizing TiO_2 .²¹⁷ Relative to TiO_2 , it has been shown that SnO_2 has faster electron transport, which is good for charge transport to the external circuit, but suffers from fast recombination with the oxidized chromophores and redox mediators.²¹⁸ EIS has been used to explore these challenges to further improve devices using SnO_2 .

Hossain et al. studied QDSCs with SnO_2 and compared them directly to the same device architecture using TiO_2 .²¹ **Figure 1.17** shows a comparison of Bode and Nyquist plots for these devices. An important feature of these data was the lack of Warburg diffusion in the SnO_2 electrodes, as seen by the inset Nyquist plots where a linear increase in impedance is observed in the mid-frequency range for TiO_2 and no such feature is observed for SnO_2 . Analysis of the TiO_2 data required a transmission line model (Model E) whereas SnO_2 data was analyzed using series of two parallel $\text{R}||\text{C}$ elements (Model B). This behavior is consistent with other literature on SnO_2 where rapid charge transport properties have been observed, thus R_d is small and not a major factor in the EIS data.^{219,220} The chemical capacitance and charge transfer resistance were also shown to be higher for SnO_2 than TiO_2 over the same potential range. Efforts to visualize R_t

for SnO₂ were unsuccessful, but the authors used the transport time of the device cathode to make a rough estimate of the diffusion length of the device. In a similar study of QDSCs with SnO₂, EIS was used to determine the contribution of the nanoparticle film structure to recombination and capacitance by changing the porosity of the electrode.²²¹ As expected, the more porous structure had a higher capacitance and a lower recombination resistance, explained by increased recombination via surface trap sites.

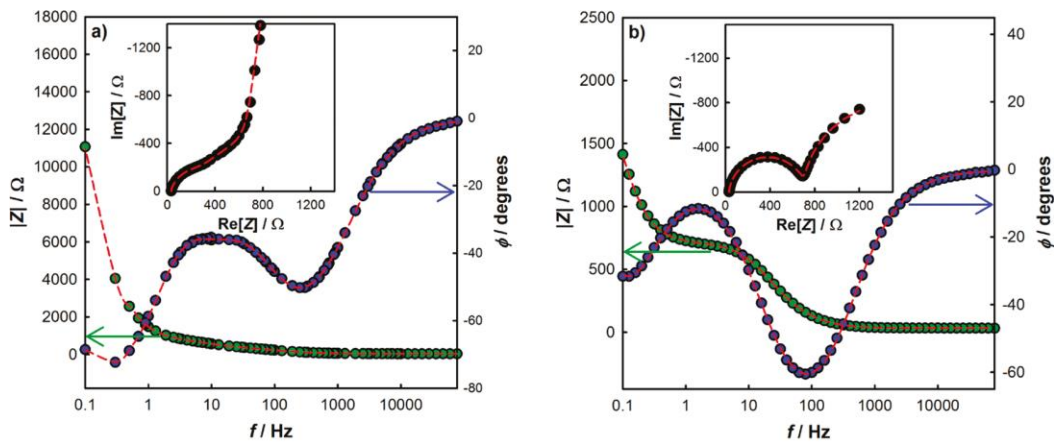


Figure 1.17: Nyquist and Bode plots for **(left)** TiO₂ and **(right)** SnO₂ QDSCs measured at their respective V_{oc} and 1 sun illumination. SnO₂ does not display the Warburg diffusion feature seen in the mid-frequency range for TiO₂ indicating rapid transport of electrons in the SnO₂ electrode. Reprinted with permission from Springer Nature.²¹

As with every metal oxide discussed thus far, the role of surface states has also been investigated for SnO₂. Huang et. al. investigated the effect of surface states on the function of QDSCs employing SnO₂ and compared with TiO₂.²²² As with the study discussed above, Warburg diffusion was found to be present for TiO₂ whereas it was absent in the case of SnO₂. Treatment of SnO₂ with TiCl₄ was shown to decrease the contribution of surface states to the C_{μ} of the electrode, which in turn led to an increase in R_{rec} . This was attributed to formation of a passivation layer, thus blocking surface states from participating in recombination reactions. EIS has also been used to explore blocking layer treatment of SnO₂ in DSSCs with similar results.²²³

SnO₂ electrodes were treated with either TiO_x or TiCl₄ and the EIS data compared with an untreated electrode. All treated solar cells showed a larger mid-frequency arc in the Nyquist plots than the untreated cell (**Figure 1.18**), indicative of increased recombination resistance at the SnO₂/chromophore/electrolyte interface. The smaller arc at low frequency was assigned the cathode/electrolyte interface. When R_{rec} is plotted over the entire applied potential range, it was shown the treatment increased R_{rec} universally for both treatment methods.

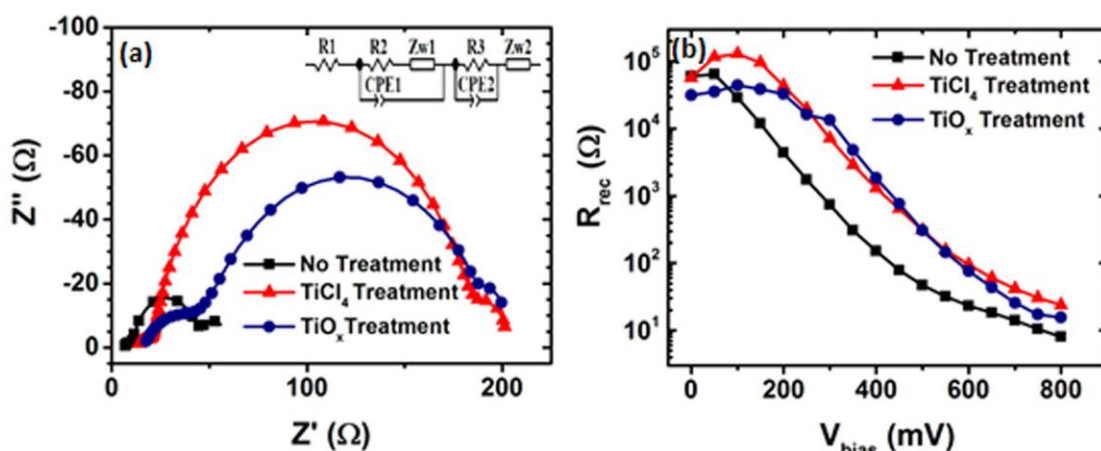


Figure 1.18: (left) Nyquist plots obtained at the open circuit condition for DSSCs assembled with SnO₂ electrodes which were untreated, treated with TiCl₄, and treated with TiO_x to determine the impact of blocking layers on R_{rec}. The equivalent circuit used to fit the data is shown as an inset. An increase in the mid frequency arc was consistent with an increase in R_{rec} following TiCl₄ and TiO_x treatment (**right**). Reprinted with permission from Springer Nature.²²³

Morphological changes of SnO₂ electrodes have been investigated in similar ways to TiO₂ and ZnO. Along with one-dimensional nanostructures (e.g. nanorods), hierarchical structures (e.g. nanoflowers), and nanofibers have been investigated in SnO₂ containing solar cells using EIS.^{224–228} Elumalai et al. and Kumar et al. investigated the charge transport properties of SnO₂ nanoflowers and nanofibers in DSSCs.^{224,225} In both studies, R_{rec} was larger for the nanoflowers compared to the nanofiber DSSCs. Interestingly, a higher capacitance was also seen for the

nanoflowers, which usually leads to a lower R_{rec} . This indicates a larger surface area for the nanoflowers, but a lower contribution of trap states to the recombination process.

Regardless of the inherent high conductivity of SnO_2 , doping has still shown interesting effects on its electrochemical properties.²²⁹⁻²³⁴ A study by Dou et. al. studied SnO_2 nanoflowers doped with Zn in DSSCs.²²⁹ They also studied the effect of a blocking layer on their devices and all of their data was compared to TiO_2 nanoparticles. The chemical capacitance is lower for Zn- SnO_2 compared to TiO_2 , but upon TiCl_4 treatment the Zn- SnO_2 nanoflowers and TiO_2 have a similar capacitance, due to the increase in surface states from the treatment. Charge recombination is also increased upon TiCl_4 treatment for the SnO_2 films and surpasses the recombination resistance for TiO_2 . Bisquert has pointed out that charge recombination can be affected by variations in the conduction band at different carrier concentrations,²³⁵ so to compensate the authors also plotted R_{rec} vs C_{μ} , which has been shown to allow for comparison of R_{rec} at the same density of states. The plot revealed significant inhibition of recombination events upon TiCl_4 treatment in the Zn- SnO_2 nanoflowers. An increase in electron lifetime was also observed in the treated nanoflowers. It should also be noted that charge transport resistance was very similar in each film, which revealed that doping had a larger impact on transport than morphology.

1.3.1.2.2 p-type metal oxides Metal oxides discussed up to this point behave as n-type semiconductors, however, in order to expand the range of heterojunction solar cell devices, p-type metal oxides have also been explored. The challenge of p-type oxides is the movement of charge (i.e. holes) through the valence band, which consists mainly of oxygen p-orbitals that are not highly delocalized, resulting in a large effective mass for holes.²³⁶ Therefore the best p-type

metal oxides consist of metals that have 3d orbitals that can energetically overlap with the oxygen 2p orbitals, helping with delocalization and charge transport.

NiO: Nickel oxide is the most heavily explored p-type metal oxide used as a hole transport material in heterojunction solar cells.¹⁰⁹ A great deal of electrochemical properties of NiO has been elucidated from EIS, including charge transport, interfacial recombination, and density of states.^{237–246} Huang et al. measured the impedance of a NiO based DSSC and compared those results to a TiO₂ electrode to demonstrate the differences between p-type and n-type devices.²³⁸ Nyquist data for the p-type device showed only two semicircles arcs, assigned to the NiO/electrolyte interface at low frequency and counter electrode/electrolyte interface, with no signs of Warburg diffusion. This was attributed to the low thickness of the NiO electrode. Comparing the two solar cells at the same potential showed a smaller recombination resistance for NiO than TiO₂. This result indicated that recombination events are more significant at the NiO/electrolyte interface.

In order to study the charge transport through the NiO electrode, Huang et al. did a follow up study with a thicker NiO nanocrystalline film. The net result was that a Warburg diffusion feature could now reasonably be observed in the mid-frequency range, although it was somewhat masked by the semicircle arc assigned to the counter electrode/electrolyte interface at high frequency (**Figure 1.19**).²⁴² This required fitting of their data using the transmission line model (Model E). When EIS was measured under illumination of the solar cell, R_t and C_μ showed a mild exponential dependence on the measured open circuit potential. The authors tied this behavior to a hopping mechanism for the charge transport, where the holes are localized between Ni²⁺ and Ni³⁺ atoms. Consistent with their previous study, the authors also showed that

illumination greatly affected R_{rec} , decreasing with higher light intensity and higher open circuit potential. **Figure 1.19b** shows a comparison of these data with data collected from intensity modulated photocurrent spectroscopy (IMPS) and intensity modulated photovoltage spectroscopy (IMVS) to show similar lifetimes for hole recombination ($\tau_{\text{h}} = R_{\text{rec}}C_{\mu}$) and hole transport ($\tau_{\text{tr}} = R_{\text{t}}C_{\mu}$).

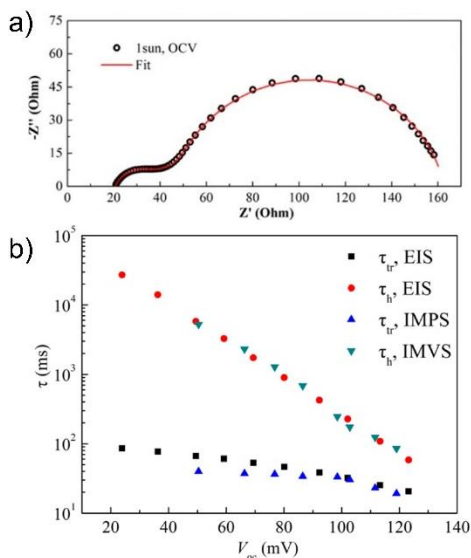
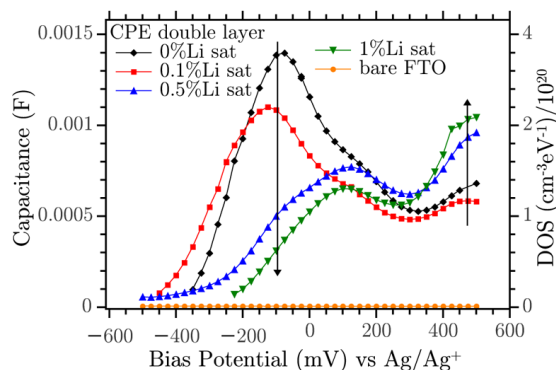


Figure 1.19. (a) Nyquist plot of a p-type NiO DSSC measured at open circuit potential under 1 sun illumination. (b) Hole lifetimes (τ_{h}) and hole extraction times (τ_{tr}) calculated from resistance and capacitance data measured from EIS compared to lifetimes measured from IMPS and IMVS. Reproduced with permission from ref 189. Copyright 2012 American Chemical Society.

There have been quite a few studies done on NiO doping, but only a few have used EIS to study the results.^{247–250} One in-depth study of a Li-doped NiO electrode using EIS was performed by D’Amario et al.²⁴⁹ Their exploration was inspired by the fast charge recombination lifetimes measured in previous studies, which indicated a high conductivity for NiO and/or high density of surface states that contribute to this recombination. The goal of this study was to shift the position of the valence band edge using Li^+ doping and thereby achieve a higher open circuit potential for the p-type solar cell. EIS results indicated a strong dependence of charge diffusion and chemical capacitance on the percent Li^+ concentration present during synthesis of NiO

nanoparticles. In terms of capacitance, NiO synthesized with 0% Li⁺ displayed a prominent peak at potentials near the valence band edge assigned to defect states in the NiO lattice. However, when NiO was synthesized with 1% Li⁺ this peak was dramatically smaller, and the overall capacitance was shifted to more positive potentials (**Figure 1.20**). The authors proposed that the inclusion of Li⁺ results in passivation of defect states, thus a lower contribution to the overall chemical capacitance is observed. P-type DSSC measurements supported these results by showing an increase in the open circuit potential from 60 mV (0% Li⁺) to 115 mV (1% Li⁺).



(b) Double layer capacitance vs V

Figure 1.20: Capacitance and density of states (DOS) of NiO electrodes measured by EIS over a range of applied potentials. The effect of Li-doping NiO is readily seen by the decrease in defect states near -100 mV vs Ag/Ag⁺. Reprinted with permission from the American Chemical Society.²⁴⁹

CuGaO₂: Delafossite copper metal oxides (Cu^IM^{III}O₂) have also been investigated as hole transport layers in p-type heterojunction solar cells due to their wide bandgaps and large hole mobilities.^{251,252} The first EIS study on CuGaO₂ nanoparticles was used to show that these mesoporous electrodes could behave in a semiconductor or metallic manner.²⁵³ Data was analyzed using a modified transmission line model (Model E) with the addition of a contact resistance between the CuGaO₂ electrode and the conductive substrate. This feature was important due to the plate-like morphology of the nanoparticles. The nanoparticles showed low

conductivities (σ), calculated from charge transport resistance, that increased moderately as the applied potential was stepped positive toward the valence band edge (**Figure 1.21**). CuGaO_2 nanoparticles were then doped with Mg^{2+} , which resulted in an order of magnitude increase in conductivity. Mott-Schottky analysis of the measured chemical capacitance allowed for the hole carrier density the Mg-doped CuGaO_2 to be measured at 10^{19} cm^{-3} compared with 10^{17} cm^{-3} for undoped nanoparticles.

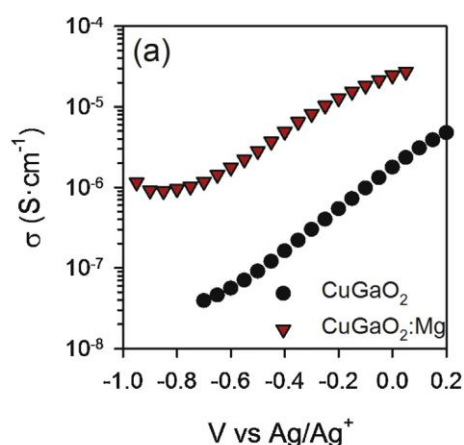


Figure 1.21: Conductivity (σ) of undoped and Mg-doped CuGaO_2 electrodes plotted vs applied potential showing the increase in conductivity with doping. Conductivity was calculated from the equation $\sigma = L(R_t A(1-p))^{-1}$, where L is the film thickness, A is geometric area of the film, and p is porosity (assumed to be 50% for a mesoporous film). Reprinted with permission from Elsevier.²⁵³

Chapters 2 and 3 of this dissertation will focus on our work with CuGaO_2 mesoporous films, which were studied heavily using EIS and other electrochemical techniques.

1.5 Conclusion

Our changing energy needs are driving some of the most important chemical research of the last several decades. The development of new materials for energy conversion devices will

continue to help our understanding of the fascinating electrochemical properties of different metal oxides.

The next few chapters will discuss electrochemical, catalytic, and synthetic studies of metal oxides. Chapter 2 discusses the effect of annealing temperature on the mesoporous film properties of CuGaO_2 synthesized at pH 9. This study found that CuGaO_2 behaves as a highly doped semiconductor, demonstrated by a large hole concentration and chemical capacitance measured from EIS. Chapter 3 expands on this work, finding that the prevalence of holes seems highly dependent on synthetic condition, as CuGaO_2 particles synthesized at pH 9 and pH 5 are compared. Post-synthetic annealing under different atmospheres (O_2 , Ar, H_2) was also found to influence the concentration of holes in the material. Chapter 4 discusses the study of epitaxially grown spinel oxide films, and their electrocatalytic efficiency towards the oxygen reduction reaction. These films were grown via molecular beam epitaxy and film characterization with XPS, as well as electrochemical characterization and evaluation of these single crystalline films as ORR catalysts will be discussed. Lastly, Chapter 5 discusses a new synthetic mechanism for metal oxide nanocrystal synthesis, namely Lewis-acid catalyzed formation of Cu_2O . The formation of ternary metal oxides phases is significantly more complicated than the formation of binary phases, due to competition of the precursors to form their own binary oxide. We highlight a particularly interesting pathway, where one metal precursor catalyzed the binary oxide formation of the other precursor, which formed less efficiently on its own.

1.6 References

- (1) Bp Statistical Review of World Energy 2020. **2020**, 68.
- (2) *Fundamentals of Materials for Energy and Environmental Sustainability*; Ginley, D. S., Cahen, D., Eds.; Cambridge University Press: Cambridge, 2011. <https://doi.org/10.1017/CBO9780511718786>.
- (3) Lewis, N. S.; Nocera, D. G. Powering the Planet: Chemical Challenges in Solar Energy Utilization. *Proc. Natl. Acad. Sci.* **2006**, *103* (43), 15729–15735. <https://doi.org/10.1073/pnas.0603395103>.
- (4) This Month in Physics History <http://www.aps.org/publications/apsnews/200904/physicshistory.cfm> (accessed Jan 27, 2021).
- (5) Shockley, W.; Queisser, H. J. Detailed Balance Limit of Efficiency of P-n Junction Solar Cells. *J. Appl. Phys.* **1961**, *32* (3), 510–519. <https://doi.org/10.1063/1.1736034>.
- (6) Rühle, S. Tabulated Values of the Shockley–Queisser Limit for Single Junction Solar Cells. *Sol. Energy* **2016**, *130*, 139–147. <https://doi.org/10.1016/j.solener.2016.02.015>.
- (7) Green, M. *Third Generation Photovoltaics: Advanced Solar Energy Conversion*; Springer Series in Photonics; Springer-Verlag: Berlin Heidelberg, 2003. <https://doi.org/10.1007/b137807>.
- (8) Nocera, D. G. The Artificial Leaf. *Acc. Chem. Res.* **2012**, *45* (5), 767–776. <https://doi.org/10.1021/ar2003013>.
- (9) Wagner, F. T.; Lakshmanan, B.; Mathias, M. F. Electrochemistry and the Future of the Automobile. *J. Phys. Chem. Lett.* **2010**, *1* (14), 2204–2219. <https://doi.org/10.1021/jz100553m>.
- (10) Cheng, F.; Chen, J. Metal–Air Batteries: From Oxygen Reduction Electrochemistry to Cathode Catalysts. *Chem. Soc. Rev.* **2012**, *41* (6), 2172–2192. <https://doi.org/10.1039/C1CS15228A>.
- (11) Coleman, E. J.; Chowdhury, M. H.; Co, A. C. Insights Into the Oxygen Reduction Reaction Activity of Pt/C and PtCu/C Catalysts. *ACS Catal.* **2015**, *5* (2), 1245–1253. <https://doi.org/10.1021/cs501762g>.
- (12) Gasteiger, H. A.; Kocha, S. S.; Sompalli, B.; Wagner, F. T. Activity Benchmarks and Requirements for Pt, Pt-Alloy, and Non-Pt Oxygen Reduction Catalysts for PEMFCs. *Appl. Catal. B Environ.* **2005**, *56* (1), 9–35. <https://doi.org/10.1016/j.apcatb.2004.06.021>.
- (13) O'Regan, B.; Grätzel, M. A Low-Cost, High-Efficiency Solar Cell Based on Dye-Sensitized Colloidal TiO₂ Films. *Nature* **1991**, *353* (6346), 737–740. <https://doi.org/10.1038/353737a0>.
- (14) Grätzel, M. Photoelectrochemical cells <https://www.nature.com/articles/35104607> (accessed Sep 30, 2018). <https://doi.org/10.1038/35104607>.
- (15) Brennaman, M. K.; Dillon, R. J.; Alibabaei, L.; Gish, M. K.; Dares, C. J.; Ashford, D. L.; House, R. L.; Meyer, G. J.; Papanikolas, J. M.; Meyer, T. J. Finding the Way to Solar Fuels

- with Dye-Sensitized Photoelectrosynthesis Cells. *J. Am. Chem. Soc.* **2016**, *138* (40), 13085–13102. <https://doi.org/10.1021/jacs.6b06466>.
- (16) Zhang, Z.; Liu, J.; Gu, J.; Su, L.; Cheng, L. An Overview of Metal Oxide Materials as Electrocatalysts and Supports for Polymer Electrolyte Fuel Cells. *Energy Environ. Sci.* **2014**, *7* (8), 2535–2558. <https://doi.org/10.1039/C3EE43886D>.
- (17) Xue, Y.; Sun, S.; Wang, Q.; Dong, Z.; Liu, Z. Transition Metal Oxide-Based Oxygen Reduction Reaction Electrocatalysts for Energy Conversion Systems with Aqueous Electrolytes. *J. Mater. Chem. A* **2018**, *6* (23), 10595–10626. <https://doi.org/10.1039/C7TA10569J>.
- (18) Mora-Seró, I.; Bisquert, J. Fermi Level of Surface States in TiO₂ Nanoparticles. *Nano Lett.* **2003**, *3* (7), 945–949. <https://doi.org/10.1021/nl0342390>.
- (19) Abayev, I.; Zaban, A.; Fabregat-Santiago, F.; Bisquert, J. Electronic Conductivity in Nanostructured TiO₂ Films Permeated with Electrolyte. *Phys. Status Solidi A* **2003**, *196* (1), R4–R6. <https://doi.org/10.1002/pssa.200306430>.
- (20) Hautier, G.; Miglio, A.; Waroquiers, D.; Rignanese, G.-M.; Gonze, X. How Does Chemistry Influence Electron Effective Mass in Oxides? A High-Throughput Computational Analysis. *Chem. Mater.* **2014**, *26* (19), 5447–5458. <https://doi.org/10.1021/cm404079a>.
- (21) Hossain, Md. A.; Jennings, J. R.; Koh, Z. Y.; Wang, Q. Carrier Generation and Collection in CdS/CdSe-Sensitized SnO₂ Solar Cells Exhibiting Unprecedented Photocurrent Densities. *ACS Nano* **2011**, *5* (4), 3172–3181. <https://doi.org/10.1021/nn200315b>.
- (22) Rochford, J.; Galoppini, E. Zinc(II) Tetraarylporphyrins Anchored to TiO₂, ZnO, and ZrO₂ Nanoparticle Films through Rigid-Rod Linkers. *Langmuir* **2008**, *24* (10), 5366–5374. <https://doi.org/10.1021/la703845u>.
- (23) Quintana, M.; Edvinsson, T.; Hagfeldt, A.; Boschloo, G. Comparison of Dye-Sensitized ZnO and TiO₂ Solar Cells: Studies of Charge Transport and Carrier Lifetime. *J. Phys. Chem. C* **2007**, *111* (2), 1035–1041. <https://doi.org/10.1021/jp065948f>.
- (24) Hautier, G.; Miglio, A.; Ceder, G.; Rignanese, G.-M.; Gonze, X. Identification and Design Principles of Low Hole Effective Mass *p*-Type Transparent Conducting Oxides. *Nat. Commun.* **2013**, *4*, 2292. <https://doi.org/10.1038/ncomms3292>.
- (25) Wang, Z.; Nayak, P. K.; Caraveo-Frescas, J. A.; Alshareef, H. N. Recent Developments in *p*-Type Oxide Semiconductor Materials and Devices. *Adv. Mater.* **2016**, *28* (20), 3831–3892. <https://doi.org/10.1002/adma.201503080>.
- (26) Odobel, F.; Pellegrin, Y. Recent Advances in the Sensitization of Wide-Band-Gap Nanostructured *p*-Type Semiconductors. Photovoltaic and Photocatalytic Applications. *J. Phys. Chem. Lett.* **2013**, *4* (15), 2551–2564. <https://doi.org/10.1021/jz400861v>.
- (27) Odobel, F.; Le Pleux, L.; Pellegrin, Y.; Blart, E. New Photovoltaic Devices Based on the Sensitization of *p*-Type Semiconductors: Challenges and Opportunities. *Acc. Chem. Res.* **2010**, *43* (8), 1063–1071. <https://doi.org/10.1021/ar900275b>.
- (28) Yella, A.; Lee, H.-W.; Tsao, H. N.; Yi, C.; Chandiran, A. K.; Nazeeruddin, M. K.; Diao, E. W.-G.; Yeh, C.-Y.; Zakeeruddin, S. M.; Grätzel, M. Porphyrin-Sensitized Solar Cells with

- Cobalt (II/III)-Based Redox Electrolyte Exceed 12 Percent Efficiency. *Science* **2011**, 334 (6056), 629–634. <https://doi.org/10.1126/science.1209688>.
- (29) Ueda, K.; Hase, T.; Yanagi, H.; Kawazoe, H.; Hosono, H.; Ohta, H.; Orita, M.; Hirano, M. Epitaxial Growth of Transparent P-Type Conducting CuGaO₂ Thin Films on Sapphire (001) Substrates by Pulsed Laser Deposition. *J. Appl. Phys.* **2001**, 89 (3), 1790–1793. <https://doi.org/10.1063/1.1337587>.
- (30) Renaud, A.; Cario, L.; Deniard, P.; Gautron, E.; Rocquefelte, X.; Pellegrin, Y.; Blart, E.; Odobel, F.; Jobic, S. Impact of Mg Doping on Performances of CuGaO₂ Based P-Type Dye-Sensitized Solar Cells. *J. Phys. Chem. C* **2014**, 118 (1), 54–59. <https://doi.org/10.1021/jp407233k>.
- (31) Xiong, D.; Xu, Z.; Zeng, X.; Zhang, W.; Chen, W.; Xu, X.; Wang, M.; Cheng, Y.-B. Hydrothermal Synthesis of Ultrasmall CuCrO₂ Nanocrystal Alternatives to NiO Nanoparticles in Efficient P-Type Dye-Sensitized Solar Cells. *J. Mater. Chem.* **2012**, 22 (47), 24760–24768. <https://doi.org/10.1039/C2JM35101C>.
- (32) Renaud, A.; Chavillon, B.; Pleux, L. L.; Pellegrin, Y.; Blart, E.; Boujtita, M.; Pauporté, T.; Cario, L.; Jobic, S.; Odobel, F. CuGaO₂: A Promising Alternative for NiO in p-Type Dye Solar Cells. *J. Mater. Chem.* **2012**, 22 (29), 14353–14356. <https://doi.org/10.1039/C2JM31908J>.
- (33) Yu, M.; Natu, G.; Ji, Z.; Wu, Y. P-Type Dye-Sensitized Solar Cells Based on Delafossite CuGaO₂ Nanoplates with Saturation Photovoltages Exceeding 460 mV. *J. Phys. Chem. Lett.* **2012**, 3 (9), 1074–1078. <https://doi.org/10.1021/jz3003603>.
- (34) Xu, Z.; Xiong, D.; Wang, H.; Zhang, W.; Zeng, X.; Ming, L.; Chen, W.; Xu, X.; Cui, J.; Wang, M.; Powar, S.; Bach, U.; Cheng, Y.-B. Remarkable Photocurrent of P-Type Dye-Sensitized Solar Cell Achieved by Size Controlled CuGaO₂ Nanoplates. *J. Mater. Chem. A* **2014**, 2 (9), 2968–2976. <https://doi.org/10.1039/C3TA14072E>.
- (35) Xiong, D.; Zhang, W.; Zeng, X.; Xu, Z.; Chen, W.; Cui, J.; Wang, M.; Sun, L.; Cheng, Y.-B. Enhanced Performance of P-Type Dye-Sensitized Solar Cells Based on Ultrasmall Mg-Doped CuCrO₂ Nanocrystals. *ChemSusChem* **2013**, 6 (8), 1432–1437. <https://doi.org/10.1002/cssc.201300265>.
- (36) Yu, M.; I. Draskovic, T.; Wu, Y. Cu(i)-Based Delafossite Compounds as Photocathodes in p-Type Dye-Sensitized Solar Cells. *Phys. Chem. Chem. Phys.* **2014**, 16 (11), 5026–5033. <https://doi.org/10.1039/C3CP55457K>.
- (37) Draskovic, T. I.; Yu, M.; Wu, Y. 2H-CuScO₂ Prepared by Low-Temperature Hydrothermal Methods and Post-Annealing Effects on Optical and Photoelectrochemical Properties. *Inorg. Chem.* **2015**, 54 (11), 5519–5526. <https://doi.org/10.1021/acs.inorgchem.5b00575>.
- (38) Prévot, M. S.; Jeanbourquin, X. A.; Bourée, W. S.; Abdi, F.; Friedrich, D.; van de Krol, R.; Guijarro, N.; Le Formal, F.; Sivula, K. Evaluating Charge Carrier Transport and Surface States in CuFeO₂ Photocathodes. *Chem. Mater.* **2017**, 29 (11), 4952–4962. <https://doi.org/10.1021/acs.chemmater.7b01284>.
- (39) Jang, Y. J.; Park, Y. B.; Kim, H. E.; Choi, Y. H.; Choi, S. H.; Lee, J. S. Oxygen-Intercalated CuFeO₂ Photocathode Fabricated by Hybrid Microwave Annealing for

- Efficient Solar Hydrogen Production. *Chem. Mater.* **2016**, 28 (17), 6054–6061. <https://doi.org/10.1021/acs.chemmater.6b00460>.
- (40) Gu, J.; Yan, Y.; Krizan, J. W.; Gibson, Q. D.; Detweiler, Z. M.; Cava, R. J.; Bocarsly, A. B. P-Type CuRhO₂ as a Self-Healing Photoelectrode for Water Reduction under Visible Light. *J. Am. Chem. Soc.* **2014**, 136 (3), 830–833. <https://doi.org/10.1021/ja408876k>.
- (41) Gu, J.; Wuttig, A.; Krizan, J. W.; Hu, Y.; Detweiler, Z. M.; Cava, R. J.; Bocarsly, A. B. Mg-Doped CuFeO₂ Photocathodes for Photoelectrochemical Reduction of Carbon Dioxide. *J. Phys. Chem. C* **2013**, 117 (24), 12415–12422. <https://doi.org/10.1021/jp402007z>.
- (42) Toyoda, K.; Hinogami, R.; Miyata, N.; Aizawa, M. Calculated Descriptors of Catalytic Activity for Water Electrolysis Anode: Application to Delafossite Oxides. *J. Phys. Chem. C* **2015**, 119 (12), 6495–6501. <https://doi.org/10.1021/jp5092398>.
- (43) Tate, J.; Ju, H. L.; Moon, J. C.; Zakutayev, A.; Richard, A. P.; Russell, J.; McIntyre, D. H. Origin of P-Type Conduction in Single-Crystal CuAlO₂. *Phys. Rev. B* **2009**, 80 (16), 165206. <https://doi.org/10.1103/PhysRevB.80.165206>.
- (44) Zhao, Q.; Yan, Z.; Chen, C.; Chen, J. Spinels: Controlled Preparation, Oxygen Reduction/Evolution Reaction Application, and Beyond. *Chem. Rev.* **2017**, 117 (15), 10121–10211. <https://doi.org/10.1021/acs.chemrev.7b00051>.
- (45) Shoemaker, D. P.; Li, J.; Seshadri, R. Unraveling Atomic Positions in an Oxide Spinel with Two Jahn–Teller Ions: Local Structure Investigation of CuMn₂O₄. *J. Am. Chem. Soc.* **2009**, 131 (32), 11450–11457. <https://doi.org/10.1021/ja902096h>.
- (46) Yang, Y.; Xiong, Y.; Holtz, M. E.; Feng, X.; Zeng, R.; Chen, G.; DiSalvo, F. J.; Muller, D. A.; Abruña, H. D. Octahedral Spinel Electrocatalysts for Alkaline Fuel Cells. *Proc. Natl. Acad. Sci.* **2019**, 116 (49), 24425–24432. <https://doi.org/10.1073/pnas.1906570116>.
- (47) Feng, S.-H.; Li, G.-H. Chapter 4 - Hydrothermal and Solvothermal Syntheses. In *Modern Inorganic Synthetic Chemistry (Second Edition)*; Xu, R., Xu, Y., Eds.; Elsevier: Amsterdam, 2017; pp 73–104. <https://doi.org/10.1016/B978-0-444-63591-4.00004-5>.
- (48) Adschiri, T.; Hakuta, Y.; Sue, K.; Arai, K. Hydrothermal Synthesis of Metal Oxide Nanoparticles at Supercritical Conditions. *J. Nanoparticle Res.* **2001**, 3 (2), 227–235. <https://doi.org/10.1023/A:1017541705569>.
- (49) Sheets, W. C.; Mugnier, E.; Barnabé, A.; Marks, T. J.; Poepelmeier, K. R. Hydrothermal Synthesis of Delafossite-Type Oxides. *Chem. Mater.* **2006**, 18 (1), 7–20. <https://doi.org/10.1021/cm051791c>.
- (50) van Embden, J.; Chesman, A. S. R.; Jasieniak, J. J. The Heat-Up Synthesis of Colloidal Nanocrystals. *Chem. Mater.* **2015**, 27 (7), 2246–2285. <https://doi.org/10.1021/cm5028964>.
- (51) Agrawal, A.; Cho, S. H.; Zandi, O.; Ghosh, S.; Johns, R. W.; Milliron, D. J. Localized Surface Plasmon Resonance in Semiconductor Nanocrystals. *Chem. Rev.* **2018**, 118 (6), 3121–3207. <https://doi.org/10.1021/acs.chemrev.7b00613>.
- (52) Ito, D.; Yokoyama, S.; Zaikova, T.; Masuko, K.; Hutchison, J. E. Synthesis of Ligand-Stabilized Metal Oxide Nanocrystals and Epitaxial Core/Shell Nanocrystals via a Lower-Temperature Esterification Process. *ACS Nano* **2014**, 8 (1), 64–75. <https://doi.org/10.1021/nn401888h>.

- (53) Jansons, A. W.; Plummer, L. K.; Hutchison, J. E. Living Nanocrystals. *Chem. Mater.* **2017**, *29* (13), 5415–5425. <https://doi.org/10.1021/acs.chemmater.7b00899>.
- (54) Jansons, A. W.; Hutchison, J. E. Continuous Growth of Metal Oxide Nanocrystals: Enhanced Control of Nanocrystal Size and Radial Dopant Distribution. *ACS Nano* **2016**, *10* (7), 6942–6951. <https://doi.org/10.1021/acs.nano.6b02796>.
- (55) Jansons, A. W.; Koskela, K. M.; Crockett, B. M.; Hutchison, J. E. Transition Metal-Doped Metal Oxide Nanocrystals: Efficient Substitutional Doping through a Continuous Growth Process. *Chem. Mater.* **2017**, *29* (19), 8167–8176. <https://doi.org/10.1021/acs.chemmater.7b02176>.
- (56) Cooper, S. R.; Plummer, L. K.; Cosby, A. G.; Lenox, P.; Jander, A.; Dhagat, P.; Hutchison, J. E. Insights into the Magnetic Properties of Sub-10 Nm Iron Oxide Nanocrystals through the Use of a Continuous Growth Synthesis. *Chem. Mater.* **2018**, *30* (17), 6053–6062. <https://doi.org/10.1021/acs.chemmater.8b02389>.
- (57) Plummer, L. K.; Hutchison, J. E. Understanding the Effects of Iron Precursor Ligation and Oxidation State Leads to Improved Synthetic Control for Spinel Iron Oxide Nanocrystals. *Inorg. Chem.* **2020**, *59* (20), 15074–15087. <https://doi.org/10.1021/acs.inorgchem.0c02040>.
- (58) Chambers, S. A. Epitaxial Growth and Properties of Doped Transition Metal and Complex Oxide Films. *Adv. Mater.* **2010**, *22* (2), 219–248. <https://doi.org/10.1002/adma.200901867>.
- (59) Doolittle, W. A.; Carver, A. G.; Henderson, W. Molecular Beam Epitaxy of Complex Metal-Oxides: Where Have We Come, Where Are We Going, and How Are We Going to Get There? *J. Vac. Sci. Technol. B Microelectron. Nanometer Struct. Process. Meas. Phenom.* **2005**, *23* (3), 1272–1276. <https://doi.org/10.1116/1.1926294>.
- (60) Schlom, D. G. Perspective: Oxide Molecular-Beam Epitaxy Rocks! *APL Mater.* **2015**, *3* (6), 062403. <https://doi.org/10.1063/1.4919763>.
- (61) Fabregat-Santiago, F.; Mora-Seró, I.; Garcia-Belmonte, G.; Bisquert, J. Cyclic Voltammetry Studies of Nanoporous Semiconductors. Capacitive and Reactive Properties of Nanocrystalline TiO₂ Electrodes in Aqueous Electrolyte. *J. Phys. Chem. B* **2003**, *107* (3), 758–768. <https://doi.org/10.1021/jp0265182>.
- (62) Bertoluzzi, L.; Herraiz-Cardona, I.; Gottesman, R.; Zaban, A.; Bisquert, J. Relaxation of Electron Carriers in the Density of States of Nanocrystalline TiO₂. *J. Phys. Chem. Lett.* **2014**, *5* (4), 689–694. <https://doi.org/10.1021/jz4027584>.
- (63) Zhang, Q.; Celorrio, V.; Bradley, K.; Eisner, F.; Cherns, D.; Yan, W.; Fermín, D. J. Density of Deep Trap States in Oriented TiO₂ Nanotube Arrays. *J. Phys. Chem. C* **2014**, *118* (31), 18207–18213. <https://doi.org/10.1021/jp505091t>.
- (64) Fabregat-Santiago, F.; Barea, E. M.; Bisquert, J.; Mor, G. K.; Shankar, K.; Grimes, C. A. High Carrier Density and Capacitance in TiO₂ Nanotube Arrays Induced by Electrochemical Doping. *J. Am. Chem. Soc.* **2008**, *130* (34), 11312–11316. <https://doi.org/10.1021/ja710899q>.
- (65) Flynn, C. J.; McCullough, S. M.; Oh, E.; Li, L.; Mercado, C. C.; Farnum, B. H.; Li, W.; Donley, C. L.; You, W.; Nozik, A. J.; McBride, J. R.; Meyer, T. J.; Kanai, Y.; Cahoon, J. F. Site-Selective Passivation of Defects in NiO Solar Photocathodes by Targeted Atomic

- Deposition. *ACS Appl. Mater. Interfaces* **2016**, *8* (7), 4754–4761. <https://doi.org/10.1021/acsami.6b01090>.
- (66) Boschloo, G.; Hagfeldt, A. Spectroelectrochemistry of Nanostructured NiO. *J. Phys. Chem. B* **2001**, *105* (15), 3039–3044. <https://doi.org/10.1021/jp003499s>.
- (67) Tian, L.; Tyburski, R.; Wen, C.; Sun, R.; Abdellah, M.; Huang, J.; D’Amario, L.; Boschloo, G.; Hammarström, L.; Tian, H. Understanding the Role of Surface States on Mesoporous NiO Films. *J. Am. Chem. Soc.* **2020**. <https://doi.org/10.1021/jacs.0c08886>.
- (68) Bard, A. J.; Faulkner, L. R. *Electrochemical Methods: Fundamentals and Applications, 2nd Ed.*; 2001.
- (69) Bard, A. J.; Faulkner, L. R. *Electrochemical Methods: Fundamentals and Applications*; Wiley: New York, 1980.
- (70) Bisquert, J.; Fabregat-Santiago, F. Impedance Spectroscopy: A General Introduction and Application to Dye-Sensitized Solar Cells. In *Dye-sensitized Solar Cells*; EPFL Press, 2010.
- (71) Klahr, B.; Gimenez, S.; Fabregat-Santiago, F.; Hamann, T.; Bisquert, J. Water Oxidation at Hematite Photoelectrodes: The Role of Surface States. *J. Am. Chem. Soc.* **2012**, *134* (9), 4294–4302. <https://doi.org/10.1021/ja210755h>.
- (72) Thomas, M. G. S. R.; Bruce, P. G.; Goodenough, J. B. AC Impedance Analysis of Polycrystalline Insertion Electrodes: Application to $\text{Li}_{1-x}\text{CoO}_2$. *J. Electrochem. Soc.* **1985**, *132* (7), 1521–1528. <https://doi.org/10.1149/1.2114158>.
- (73) Aurbach, D. Review of Selected Electrode–Solution Interactions Which Determine the Performance of Li and Li Ion Batteries. *J. Power Sources* **2000**, *89* (2), 206–218. [https://doi.org/10.1016/S0378-7753\(00\)00431-6](https://doi.org/10.1016/S0378-7753(00)00431-6).
- (74) Klahr, B.; Gimenez, S.; Fabregat-Santiago, F.; Bisquert, J.; Hamann, T. W. Photoelectrochemical and Impedance Spectroscopic Investigation of Water Oxidation with “Co–Pi”-Coated Hematite Electrodes. *J. Am. Chem. Soc.* **2012**, *134* (40), 16693–16700. <https://doi.org/10.1021/ja306427f>.
- (75) von Hauff, E. Impedance Spectroscopy for Emerging Photovoltaics. *J. Phys. Chem. C* **2019**, *123* (18), 11329–11346. <https://doi.org/10.1021/acs.jpcc.9b00892>.
- (76) Hagfeldt, A.; Boschloo, G.; Sun, L.; Kloo, L.; Pettersson, H. Dye-Sensitized Solar Cells. *Chem. Rev.* **2010**, *110* (11), 6595–6663. <https://doi.org/10.1021/cr900356p>.
- (77) Carey, G. H.; Abdelhady, A. L.; Ning, Z.; Thon, S. M.; Bakr, O. M.; Sargent, E. H. Colloidal Quantum Dot Solar Cells. *Chem. Rev.* **2015**, *115* (23), 12732–12763. <https://doi.org/10.1021/acs.chemrev.5b00063>.
- (78) Kim, M. R.; Ma, D. Quantum-Dot-Based Solar Cells: Recent Advances, Strategies, and Challenges. *J. Phys. Chem. Lett.* **2015**, *6* (1), 85–99. <https://doi.org/10.1021/jz502227h>.
- (79) Clarke, T. M.; Durrant, J. R. Charge Photogeneration in Organic Solar Cells. *Chem. Rev.* **2010**, *110* (11), 6736–6767. <https://doi.org/10.1021/cr900271s>.
- (80) Snaith, H. J. Perovskites: The Emergence of a New Era for Low-Cost, High-Efficiency Solar Cells. *J. Phys. Chem. Lett.* **2013**, *4* (21), 3623–3630. <https://doi.org/10.1021/jz4020162>.

- (81) Hamann, T. W. Splitting Water with Rust: Hematite Photoelectrochemistry. *Dalton Trans.* **2012**, *41* (26), 7830–7834. <https://doi.org/10.1039/c2dt30340j>.
- (82) Prévot, M. S.; Jeanbourquin, X. A.; Bourée, W. S.; Abdi, F.; Friedrich, D.; van de Krol, R.; Guijarro, N.; Le Formal, F.; Sivula, K. Evaluating Charge Carrier Transport and Surface States in CuFeO₂ Photocathodes. *Chem. Mater.* **2017**, *29* (11), 4952–4962. <https://doi.org/10.1021/acs.chemmater.7b01284>.
- (83) Cesiulis, H.; Tsyntsaru, N.; Ramanavicius, A.; Ragoisha, G. The Study of Thin Films by Electrochemical Impedance Spectroscopy. In *Nanostructures and Thin Films for Multifunctional Applications*; Tiginyanu, I., Topala, P., Ursaki, V., Eds.; Springer International Publishing: Cham, 2016; pp 3–42. https://doi.org/10.1007/978-3-319-30198-3_1.
- (84) Wang, H.; Guerrero, A.; Bou, A.; Al-Mayouf, A. M.; Bisquert, J. Kinetic and Material Properties of Interfaces Governing Slow Response and Long Timescale Phenomena in Perovskite Solar Cells. *Energy Environ. Sci.* **2019**, *12* (7), 2054–2079. <https://doi.org/10.1039/C9EE00802K>.
- (85) Almora, O.; García-Batlle, M.; Garcia-Belmonte, G. Utilization of Temperature-Sweeping Capacitive Techniques to Evaluate Band Gap Defect Densities in Photovoltaic Perovskites. *J. Phys. Chem. Lett.* **2019**, *10* (13), 3661–3669. <https://doi.org/10.1021/acs.jpcllett.9b00601>.
- (86) Fischer, M.; Tvingstedt, K.; Baumann, A.; Dyakonov, V. Doping Profile in Planar Hybrid Perovskite Solar Cells Identifying Mobile Ions. *ACS Appl. Energy Mater.* **2018**, *1* (10), 5129–5134. <https://doi.org/10.1021/acsaem.8b01119>.
- (87) Garcia-Belmonte, G.; Bisquert, J. Distinction between Capacitive and Noncapacitive Hysteretic Currents in Operation and Degradation of Perovskite Solar Cells. *ACS Energy Lett.* **2016**, *1* (4), 683–688. <https://doi.org/10.1021/acseenergylett.6b00293>.
- (88) Almora, O.; Aranda, C.; Mas-Marzá, E.; Garcia-Belmonte, G. On Mott-Schottky Analysis Interpretation of Capacitance Measurements in Organometal Perovskite Solar Cells. *Appl. Phys. Lett.* **2016**, *109* (17), 173903. <https://doi.org/10.1063/1.4966127>.
- (89) Bredar, A. R. C.; Chown, A. L.; Burton, A. R.; Farnum, B. H. Electrochemical Impedance Spectroscopy of Metal Oxide Electrodes for Energy Applications. *ACS Appl. Energy Mater.* **2020**, *3* (1), 66–98. <https://doi.org/10.1021/acsaem.9b01965>.
- (90) Rühle, S.; Anderson, A. Y.; Barad, H.-N.; Kupfer, B.; Bouhadana, Y.; Rosh-Hodesh, E.; Zaban, A. All-Oxide Photovoltaics. *J. Phys. Chem. Lett.* **2012**, *3* (24), 3755–3764. <https://doi.org/10.1021/jz3017039>.
- (91) Toyoda, T.; Shen, Q. Quantum-Dot-Sensitized Solar Cells: Effect of Nanostructured TiO₂ Morphologies on Photovoltaic Properties. *J. Phys. Chem. Lett.* **2012**, *3* (14), 1885–1893. <https://doi.org/10.1021/jz3004602>.
- (92) Bai, Y.; Mora-Seró, I.; De Angelis, F.; Bisquert, J.; Wang, P. Titanium Dioxide Nanomaterials for Photovoltaic Applications. *Chem. Rev.* **2014**, *114* (19), 10095–10130. <https://doi.org/10.1021/cr400606n>.

- (93) Zhen, C.; Wu, T.; Chen, R.; Wang, L.; Liu, G.; Cheng, H.-M. Strategies for Modifying TiO₂ Based Electron Transport Layers to Boost Perovskite Solar Cells. *ACS Sustain. Chem. Eng.* **2019**, *7* (5), 4586–4618. <https://doi.org/10.1021/acssuschemeng.8b06580>.
- (94) Huang, J.; Yin, Z.; Zheng, Q. Applications of ZnO in Organic and Hybrid Solar Cells. *Energy Environ. Sci.* **2011**, *4* (10), 3861–3877. <https://doi.org/10.1039/C1EE01873F>.
- (95) Anta, J. A.; Guillén, E.; Tena-Zaera, R. ZnO-Based Dye-Sensitized Solar Cells. *J. Phys. Chem. C* **2012**, *116* (21), 11413–11425. <https://doi.org/10.1021/jp3010025>.
- (96) Chappel, S.; Chen, S.-G.; Zaban, A. TiO₂-Coated Nanoporous SnO₂ Electrodes for Dye-Sensitized Solar Cells. *Langmuir* **2002**, *18* (8), 3336–3342. <https://doi.org/10.1021/la015536s>.
- (97) Ramasamy, E.; Lee, J. Ordered Mesoporous SnO₂-Based Photoanodes for High-Performance Dye-Sensitized Solar Cells. *J. Phys. Chem. C* **2010**, *114* (50), 22032–22037. <https://doi.org/10.1021/jp1074797>.
- (98) Tiwana, P.; Docampo, P.; Johnston, M. B.; Snaith, H. J.; Herz, L. M. Electron Mobility and Injection Dynamics in Mesoporous ZnO, SnO₂, and TiO₂ Films Used in Dye-Sensitized Solar Cells. *ACS Nano* **2011**, *5* (6), 5158–5166. <https://doi.org/10.1021/nn201243y>.
- (99) Sayama, K.; Sugihara, H.; Arakawa, H. Photoelectrochemical Properties of a Porous Nb₂O₅ Electrode Sensitized by a Ruthenium Dye. *Chem. Mater.* **1998**, *10* (12), 3825–3832. <https://doi.org/10.1021/cm980111l>.
- (100) Ling, X.; Yuan, J.; Liu, D.; Wang, Y.; Zhang, Y.; Chen, S.; Wu, H.; Jin, F.; Wu, F.; Shi, G.; Tang, X.; Zheng, J.; Liu, S. (Frank); Liu, Z.; Ma, W. Room-Temperature Processed Nb₂O₅ as the Electron-Transporting Layer for Efficient Planar Perovskite Solar Cells. *ACS Appl. Mater. Interfaces* **2017**, *9* (27), 23181–23188. <https://doi.org/10.1021/acsami.7b05113>.
- (101) Lenzmann, F.; Krueger, J.; Burnside, S.; Brooks, K.; Grätzel, M.; Gal, D.; Rühle, S.; Cahen, D. Surface Photovoltage Spectroscopy of Dye-Sensitized Solar Cells with TiO₂, Nb₂O₅, and SrTiO₃ Nanocrystalline Photoanodes: Indication for Electron Injection from Higher Excited Dye States. *J. Phys. Chem. B* **2001**, *105* (27), 6347–6352. <https://doi.org/10.1021/jp010380q>.
- (102) Yang, S.; Kou, H.; Wang, J.; Xue, H.; Han, H. Tunability of the Band Energetics of Nanostructured SrTiO₃ Electrodes for Dye-Sensitized Solar Cells. *J. Phys. Chem. C* **2010**, *114* (9), 4245–4249. <https://doi.org/10.1021/jp9117979>.
- (103) Bera, A.; Wu, K.; Sheikh, A.; Alarousu, E.; Mohammed, O. F.; Wu, T. Perovskite Oxide SrTiO₃ as an Efficient Electron Transporter for Hybrid Perovskite Solar Cells. *J. Phys. Chem. C* **2014**, *118* (49), 28494–28501. <https://doi.org/10.1021/jp509753p>.
- (104) Lana-Villarreal, T.; Boschloo, G.; Hagfeldt, A. Nanostructured Zinc Stannate as Semiconductor Working Electrodes for Dye-Sensitized Solar Cells. *J. Phys. Chem. C* **2007**, *111* (14), 5549–5556. <https://doi.org/10.1021/jp0678756>.
- (105) Tan, B.; Toman, E.; Li, Y.; Wu, Y. Zinc Stannate (Zn₂SnO₄) Dye-Sensitized Solar Cells. *J. Am. Chem. Soc.* **2007**, *129* (14), 4162–4163. <https://doi.org/10.1021/ja070804f>.

- (106) Mali, S. S.; Su Shim, C.; Kook Hong, C. Highly Porous Zinc Stannate (Zn_2SnO_4) Nanofibers Scaffold Photoelectrodes for Efficient Methyl Ammonium Halide Perovskite Solar Cells. *Sci. Rep.* **2015**, *5*, 11424. <https://doi.org/10.1038/srep11424>.
- (107) Corma, A.; Atienzar, P.; García, H.; Chane-Ching, J.-Y. Hierarchically Mesostructured Doped CeO₂ with Potential for Solar-Cell Use. *Nat. Mater.* **2004**, *3* (6), 394–397. <https://doi.org/10.1038/nmat1129>.
- (108) Song, W.; Gong, Y.; Tian, J.; Cao, G.; Zhao, H.; Sun, C. Novel Photoanode for Dye-Sensitized Solar Cells with Enhanced Light-Harvesting and Electron-Collection Efficiency. *ACS Appl. Mater. Interfaces* **2016**, *8* (21), 13418–13425. <https://doi.org/10.1021/acsami.6b02887>.
- (109) He, J.; Lindström, H.; Hagfeldt, A.; Lindquist, S.-E. Dye-Sensitized Nanostructured p-Type Nickel Oxide Film as a Photocathode for a Solar Cell. *J. Phys. Chem. B* **1999**, *103* (42), 8940–8943. <https://doi.org/10.1021/jp991681r>.
- (110) Hu, L.; Peng, J.; Wang, W.; Xia, Z.; Yuan, J.; Lu, J.; Huang, X.; Ma, W.; Song, H.; Chen, W.; Cheng, Y.-B.; Tang, J. Sequential Deposition of CH₃NH₃PbI₃ on Planar NiO Film for Efficient Planar Perovskite Solar Cells. *ACS Photonics* **2014**, *1* (7), 547–553. <https://doi.org/10.1021/ph5000067>.
- (111) Yu, M.; Natu, G.; Ji, Z.; Wu, Y. P-Type Dye-Sensitized Solar Cells Based on Delafossite CuGaO₂ Nanoplates with Saturation Photovoltages Exceeding 460 mV. *J. Phys. Chem. Lett.* **2012**, *3* (9), 1074–1078. <https://doi.org/10.1021/jz3003603>.
- (112) Zhang, H.; Wang, H.; Chen, W.; Jen, A. K.-Y. CuGaO₂: A Promising Inorganic Hole-Transporting Material for Highly Efficient and Stable Perovskite Solar Cells. *Adv. Mater.* **2017**, *29* (8), 1604984. <https://doi.org/10.1002/adma.201604984>.
- (113) O'Regan, B.; Grätzel, M. A Low-Cost, High-Efficiency Solar Cell Based on Dye-Sensitized Colloidal TiO₂ Films. *Nature* **1991**, *353*, 737–740.
- (114) Lu, L.; Zheng, T.; Wu, Q.; Schneider, A. M.; Zhao, D.; Yu, L. Recent Advances in Bulk Heterojunction Polymer Solar Cells. *Chem. Rev.* **2015**, *115* (23), 12666–12731. <https://doi.org/10.1021/acs.chemrev.5b00098>.
- (115) O'Regan, B.; Grätzel, M. A Low-Cost, High-Efficiency Solar Cell Based on Dye-Sensitized Colloidal TiO₂ Films. *Nature* **1991**, *353* (6346), 737–740. <https://doi.org/10.1038/353737a0>.
- (116) Bisquert, J.; Garcia-Belmonte, G.; Fabregat-Santiago, F.; Ferriols, N. S.; Bogdanoff, P.; Pereira, E. C. Doubling Exponent Models for the Analysis of Porous Film Electrodes by Impedance. Relaxation of TiO₂ Nanoporous in Aqueous Solution. *J. Phys. Chem. B* **2000**, *104* (10), 2287–2298. <https://doi.org/10.1021/jp993148h>.
- (117) Fabregat-Santiago, F.; Garcia-Belmonte, G.; Bisquert, J.; Zaban, A.; Salvador, P. Decoupling of Transport, Charge Storage, and Interfacial Charge Transfer in the Nanocrystalline TiO₂/Electrolyte System by Impedance Methods. *J. Phys. Chem. B* **2002**, *106* (2), 334–339. <https://doi.org/10.1021/jp0119429>.

- (118) Bisquert, J. Chemical Capacitance of Nanostructured Semiconductors: Its Origin and Significance for Nanocomposite Solar Cells. *Phys. Chem. Chem. Phys.* **2003**, *5* (24), 5360–5364. <https://doi.org/10.1039/B310907K>.
- (119) Fabregat-Santiago, F.; Bisquert, J.; Garcia-Belmonte, G.; Boschloo, G.; Hagfeldt, A. Influence of Electrolyte in Transport and Recombination in Dye-Sensitized Solar Cells Studied by Impedance Spectroscopy. *Sol. Energy Mater. Sol. Cells* **2005**, *87* (1), 117–131. <https://doi.org/10.1016/j.solmat.2004.07.017>.
- (120) Wang, Q.; Moser, J.-E.; Grätzel, M. Electrochemical Impedance Spectroscopic Analysis of Dye-Sensitized Solar Cells. *J. Phys. Chem. B* **2005**, *109* (31), 14945–14953. <https://doi.org/10.1021/jp052768h>.
- (121) Li, X.; Lin, H.; Li, J.; Li, X.; Cui, B.; Zhang, L. A Numerical Simulation and Impedance Study of the Electron Transport and Recombination in Binder-Free TiO₂ Film for Flexible Dye-Sensitized Solar Cells. *J. Phys. Chem. C* **2008**, *112* (35), 13744–13753. <https://doi.org/10.1021/jp800023z>.
- (122) Kern, R.; Sastrawan, R.; Ferber, J.; Stangl, R.; Luther, J. Modeling and Interpretation of Electrical Impedance Spectra of Dye Solar Cells Operated under Open-Circuit Conditions. *Electrochimica Acta* **2002**, *47* (26), 4213–4225. [https://doi.org/10.1016/S0013-4686\(02\)00444-9](https://doi.org/10.1016/S0013-4686(02)00444-9).
- (123) Adachi, M.; Sakamoto, M.; Jiu, J.; Ogata, Y.; Isoda, S. Determination of Parameters of Electron Transport in Dye-Sensitized Solar Cells Using Electrochemical Impedance Spectroscopy. *J. Phys. Chem. B* **2006**, *110* (28), 13872–13880. <https://doi.org/10.1021/jp061693u>.
- (124) Mora-Seró, I.; Bisquert, J. Fermi Level of Surface States in TiO₂ Nanoparticles. *Nano Lett.* **2003**, *3* (7), 945–949. <https://doi.org/10.1021/nl0342390>.
- (125) He, C.; Zhao, L.; Zheng, Z.; Lu, F. Determination of Electron Diffusion Coefficient and Lifetime in Dye-Sensitized Solar Cells by Electrochemical Impedance Spectroscopy at High Fermi Level Conditions. *J. Phys. Chem. C* **2008**, *112* (48), 18730–18733. <https://doi.org/10.1021/jp8085733>.
- (126) Hsu, C.-P.; Lee, K.-M.; Huang, J. T.-W.; Lin, C.-Y.; Lee, C.-H.; Wang, L.-P.; Tsai, S.-Y.; Ho, K.-C. EIS Analysis on Low Temperature Fabrication of TiO₂ Porous Films for Dye-Sensitized Solar Cells. *Electrochimica Acta* **2008**, *53* (25), 7514–7522. <https://doi.org/10.1016/j.electacta.2008.01.104>.
- (127) Gimenez, S.; Dunn, H. K.; Rodenas, P.; Fabregat-Santiago, F.; Miralles, S. G.; Barea, E. M.; Trevisan, R.; Guerrero, A.; Bisquert, J. Carrier Density and Interfacial Kinetics of Mesoporous TiO₂ in Aqueous Electrolyte Determined by Impedance Spectroscopy. *J. Electroanal. Chem.* **2012**, *668*, 119–125. <https://doi.org/10.1016/j.jelechem.2011.12.019>.
- (128) Park, K.; Zhang, Q.; Myers, D.; Cao, G. Charge Transport Properties in TiO₂ Network with Different Particle Sizes for Dye Sensitized Solar Cells. *ACS Appl. Mater. Interfaces* **2013**, *5* (3), 1044–1052. <https://doi.org/10.1021/am302781b>.
- (129) Pascoe, A. R.; Bourgeois, L.; Duffy, N. W.; Xiang, W.; Cheng, Y.-B. Surface State Recombination and Passivation in Nanocrystalline TiO₂ Dye-Sensitized Solar Cells. *J. Phys. Chem. C* **2013**, *117* (47), 25118–25126. <https://doi.org/10.1021/jp408055g>.

- (130) Park, K.; Zhang, Q.; Xi, J.; Cao, G. Enhanced Charge Transport Properties by Strengthened Necks between TiO₂ Aggregates for Dye Sensitized Solar Cells. *Thin Solid Films* **2015**, *588*, 19–25. <https://doi.org/10.1016/j.tsf.2015.04.054>.
- (131) Zhao, K.; Pan, Z.; Zhong, X. Charge Recombination Control for High Efficiency Quantum Dot Sensitized Solar Cells. *J. Phys. Chem. Lett.* **2016**, *7* (3), 406–417. <https://doi.org/10.1021/acs.jpcclett.5b02153>.
- (132) Cameron, P. J.; Peter, L. M. Characterization of Titanium Dioxide Blocking Layers in Dye-Sensitized Nanocrystalline Solar Cells. *J. Phys. Chem. B* **2003**, *107* (51), 14394–14400. <https://doi.org/10.1021/jp030790+>.
- (133) Góes, M. S.; Joanni, E.; Muniz, E. C.; Savu, R.; Habeck, T. R.; Bueno, P. R.; Fabregat-Santiago, F. Impedance Spectroscopy Analysis of the Effect of TiO₂ Blocking Layers on the Efficiency of Dye Sensitized Solar Cells. *J. Phys. Chem. C* **2012**, *116* (23), 12415–12421. <https://doi.org/10.1021/jp301694r>.
- (134) Elbohy, H.; Thapa, A.; Poudel, P.; Adhikary, N.; Venkatesan, S.; Qiao, Q. Vanadium Oxide as New Charge Recombination Blocking Layer for High Efficiency Dye-Sensitized Solar Cells. *Nano Energy* **2015**, *13*, 368–375. <https://doi.org/10.1016/j.nanoen.2014.09.008>.
- (135) Park, N.-G.; van de Lagemaat, J.; Frank, A. J. Comparison of Dye-Sensitized Rutile- and Anatase-Based TiO₂ Solar Cells. *J. Phys. Chem. B* **2000**, *104* (38), 8989–8994. <https://doi.org/10.1021/jp9943651>.
- (136) Lancelle-Beltran, E.; Prené, P.; Boscher, C.; Belleville, P.; Buvat, P.; Sanchez, C. All-Solid-State Dye-Sensitized Nanoporous TiO₂ Hybrid Solar Cells with High Energy-Conversion Efficiency. *Adv. Mater.* **2006**, *18* (19), 2579–2582. <https://doi.org/10.1002/adma.200502023>.
- (137) Liu, B.; Aydil, E. S. Growth of Oriented Single-Crystalline Rutile TiO₂ Nanorods on Transparent Conducting Substrates for Dye-Sensitized Solar Cells. *J. Am. Chem. Soc.* **2009**, *131* (11), 3985–3990. <https://doi.org/10.1021/ja8078972>.
- (138) Kumar, A.; Madaria, A. R.; Zhou, C. Growth of Aligned Single-Crystalline Rutile TiO₂ Nanowires on Arbitrary Substrates and Their Application in Dye-Sensitized Solar Cells. *J. Phys. Chem. C* **2010**, *114* (17), 7787–7792. <https://doi.org/10.1021/jp100491h>.
- (139) Wang, H.; Miyauchi, M.; Ishikawa, Y.; Pyatenko, A.; Koshizaki, N.; Li, Y.; Li, L.; Li, X.; Bando, Y.; Golberg, D. Single-Crystalline Rutile TiO₂ Hollow Spheres: Room-Temperature Synthesis, Tailored Visible-Light-Extinction, and Effective Scattering Layer for Quantum Dot-Sensitized Solar Cells. *J. Am. Chem. Soc.* **2011**, *133* (47), 19102–19109. <https://doi.org/10.1021/ja2049463>.
- (140) Wang, H.; Bai, Y.; Wu, Q.; Zhou, W.; Zhang, H.; Li, J.; Guo, L. Rutile TiO₂ Nano-Branched Arrays on FTO for Dye -Sensitized Solar Cells. *Phys. Chem. Chem. Phys.* **2011**, *13* (15), 7008–7013. <https://doi.org/10.1039/C1CP20351G>.
- (141) Feng, X.; Zhu, K.; Frank, A. J.; Grimes, C. A.; Mallouk, T. E. Rapid Charge Transport in Dye-Sensitized Solar Cells Made from Vertically Aligned Single-Crystal Rutile TiO₂ Nanowires. *Angew. Chem. Int. Ed.* **2012**, *51* (11), 2727–2730. <https://doi.org/10.1002/anie.201108076>.

- (142) Guo, W.; Xu, C.; Wang, X.; Wang, S.; Pan, C.; Lin, C.; Wang, Z. L. Rectangular Bunched Rutile TiO₂ Nanorod Arrays Grown on Carbon Fiber for Dye-Sensitized Solar Cells. *J. Am. Chem. Soc.* **2012**, *134* (9), 4437–4441. <https://doi.org/10.1021/ja2120585>.
- (143) Kogo, A.; Sanehira, Y.; Numata, Y.; Ikegami, M.; Miyasaka, T. Amorphous Metal Oxide Blocking Layers for Highly Efficient Low-Temperature Brookite TiO₂-Based Perovskite Solar Cells. *ACS Appl. Mater. Interfaces* **2018**, *10* (3), 2224–2229. <https://doi.org/10.1021/acsami.7b16662>.
- (144) Shahiduzzaman, Md.; Visal, S.; Kuniyoshi, M.; Kaneko, T.; Umezu, S.; Katsumata, T.; Iwamori, S.; Kakihana, M.; Taima, T.; Isomura, M.; Tomita, K. Low-Temperature-Processed Brookite-Based TiO₂ Heterophase Junction Enhances Performance of Planar Perovskite Solar Cells. *Nano Lett.* **2019**, *19* (1), 598–604. <https://doi.org/10.1021/acs.nanolett.8b04744>.
- (145) Dolata, M.; Kedzierzawski, P.; Augustynski, J. Comparative Impedance Spectroscopy Study of Rutile and Anatase TiO₂ Film Electrodes. *Electrochimica Acta* **1996**, *41* (7), 1287–1293. [https://doi.org/10.1016/0013-4686\(95\)00449-1](https://doi.org/10.1016/0013-4686(95)00449-1).
- (146) Weibel, A.; Bouchet, R.; Knauth, P. Electrical Properties and Defect Chemistry of Anatase (TiO₂). *Solid State Ion.* **2006**, *177* (3), 229–236. <https://doi.org/10.1016/j.ssi.2005.11.002>.
- (147) Pourjafari, D.; Reyes-Coronado, D.; Vega-Poot, A.; Escalante, R.; Kirkconnell-Reyes, D.; García-Rodríguez, R.; Anta, J. A.; Oskam, G. Brookite-Based Dye-Sensitized Solar Cells: Influence of Morphology and Surface Chemistry on Cell Performance. *J. Phys. Chem. C* **2018**, *122* (26), 14277–14288. <https://doi.org/10.1021/acs.jpcc.8b02384>.
- (148) Kusumawati, Y.; Hosni, M.; Martoprawiro, M. A.; Cassaignon, S.; Pauporté, Th. Charge Transport and Recombination in TiO₂ Brookite-Based Photoelectrodes. *J. Phys. Chem. C* **2014**, *118* (41), 23459–23467. <https://doi.org/10.1021/jp5047479>.
- (149) Kim, H.-S.; Lee, J.-W.; Yantara, N.; Boix, P. P.; Kulkarni, S. A.; Mhaisalkar, S.; Grätzel, M.; Park, N.-G. High Efficiency Solid-State Sensitized Solar Cell-Based on Submicrometer Rutile TiO₂ Nanorod and CH₃NH₃PbI₃ Perovskite Sensitizer. *Nano Lett.* **2013**, *13* (6), 2412–2417. <https://doi.org/10.1021/nl400286w>.
- (150) Hsiao, P.-T.; Tung, Y.-L.; Teng, H. Electron Transport Patterns in TiO₂ Nanocrystalline Films of Dye-Sensitized Solar Cells. *J. Phys. Chem. C* **2010**, *114* (14), 6762–6769. <https://doi.org/10.1021/jp1006457>.
- (151) Magne, C.; Cassaignon, S.; Lancel, G.; Pauporté, T. Brookite TiO₂ Nanoparticle Films for Dye-Sensitized Solar Cells. *ChemPhysChem* **2011**, *12* (13), 2461–2467. <https://doi.org/10.1002/cphc.201100194>.
- (152) Liao, J.-Y.; He, J.-W.; Xu, H.; Kuang, D.-B.; Su, C.-Y. Effect of TiO₂ Morphology on Photovoltaic Performance of Dye-Sensitized Solar Cells: Nanoparticles, Nanofibers, Hierarchical Spheres and Ellipsoid Spheres. *J. Mater. Chem.* **2012**, *22* (16), 7910–7918. <https://doi.org/10.1039/C2JM16148F>.
- (153) Lee, K.; Mazare, A.; Schmuki, P. One-Dimensional Titanium Dioxide Nanomaterials: Nanotubes. *Chem. Rev.* **2014**, *114* (19), 9385–9454. <https://doi.org/10.1021/cr500061m>.

- (154) Abayev, I.; Zaban, A.; Fabregat-Santiago, F.; Bisquert, J. Electronic Conductivity in Nanostructured TiO₂ Films Permeated with Electrolyte. *Phys. Status Solidi A* **2003**, *196* (1), R4–R6. <https://doi.org/10.1002/pssa.200306430>.
- (155) van de Lagemaat, J.; Park, N.-G.; Frank, A. J. Influence of Electrical Potential Distribution, Charge Transport, and Recombination on the Photopotential and Photocurrent Conversion Efficiency of Dye-Sensitized Nanocrystalline TiO₂ Solar Cells: A Study by Electrical Impedance and Optical Modulation Techniques. *J. Phys. Chem. B* **2000**, *104* (9), 2044–2052. <https://doi.org/10.1021/jp993172v>.
- (156) Frank, A.; Kopidakis, N.; Lagemaat, J. van de. Electrons in Nanostructured TiO₂ Solar Cells: Transport, Recombination and Photovoltaic Properties. *Coord. Chem. Rev.* **2004**, *248* (13), 1165–1179. <https://doi.org/10.1016/j.ccr.2004.03.015>.
- (157) Peter, L. M. Characterization and Modeling of Dye-Sensitized Solar Cells. *J. Phys. Chem. C* **2007**, *111* (18), 6601–6612. <https://doi.org/10.1021/jp069058b>.
- (158) Fabregat-Santiago, F.; Bisquert, J.; Cevey, L.; Chen, P.; Wang, M.; Zakeeruddin, S. M.; Grätzel, M. Electron Transport and Recombination in Solid-State Dye Solar Cell with Spiro-OMeTAD as Hole Conductor. *J. Am. Chem. Soc.* **2009**, *131* (2), 558–562. <https://doi.org/10.1021/ja805850q>.
- (159) Shin, I.; Seo, H.; Son, M.-K.; Kim, J.-K.; Prabakar, K.; Kim, H.-J. Analysis of TiO₂ Thickness Effect on Characteristic of a Dye-Sensitized Solar Cell by Using Electrochemical Impedance Spectroscopy. *Curr. Appl. Phys.* **2010**, *10* (3, Supplement), S422–S424. <https://doi.org/10.1016/j.cap.2009.12.039>.
- (160) Muniz, E. C.; Góes, M. S.; Silva, J. J.; Varela, J. A.; Joanni, E.; Parra, R.; Bueno, P. R. Synthesis and Characterization of Mesoporous TiO₂ Nanostructured Films Prepared by a Modified Sol–Gel Method for Application in Dye Solar Cells. *Ceram. Int.* **2011**, *37* (3), 1017–1024. <https://doi.org/10.1016/j.ceramint.2010.11.014>.
- (161) Boix, P. P.; Lee, Y. H.; Fabregat-Santiago, F.; Im, S. H.; Mora-Sero, I.; Bisquert, J.; Seok, S. I. From Flat to Nanostructured Photovoltaics: Balance between Thickness of the Absorber and Charge Screening in Sensitized Solar Cells. *ACS Nano* **2012**, *6* (1), 873–880. <https://doi.org/10.1021/nn204382k>.
- (162) Li, X.; Dai, S.-M.; Zhu, P.; Deng, L.-L.; Xie, S.-Y.; Cui, Q.; Chen, H.; Wang, N.; Lin, H. Efficient Perovskite Solar Cells Depending on TiO₂ Nanorod Arrays. *ACS Appl. Mater. Interfaces* **2016**, *8* (33), 21358–21365. <https://doi.org/10.1021/acsami.6b05971>.
- (163) Taveira, L. V.; Sagüés, A. A.; Macak, J. M.; Schmuki, P. Impedance Behavior of TiO₂ Nanotubes Formed by Anodization in NaF Electrolytes. *J. Electrochem. Soc.* **2008**, *155* (6), C293–C302. <https://doi.org/10.1149/1.2898503>.
- (164) Jose, R.; Thavasi, V.; Ramakrishna, S. Metal Oxides for Dye-Sensitized Solar Cells. *J. Am. Ceram. Soc.* **2009**, *92* (2), 289–301. <https://doi.org/10.1111/j.1551-2916.2008.02870.x>.
- (165) Spagnol, V.; Sutter, E.; Debiemme-Chouvy, C.; Cachet, H.; Baroux, B. EIS Study of Photo-Induced Modifications of Nano-Columnar TiO₂ Films. *Electrochimica Acta* **2009**, *54* (4), 1228–1232. <https://doi.org/10.1016/j.electacta.2008.08.070>.

- (166) Pu, P.; Cachet, H.; Sutter, E. M. M. Electrochemical Impedance Spectroscopy to Study Photo - Induced Effects on Self-Organized TiO₂ Nanotube Arrays. *Electrochimica Acta* **2010**, *55* (20), 5938–5946. <https://doi.org/10.1016/j.electacta.2010.05.048>.
- (167) Zhong, P.; Que, W.; Zhang, J.; Jia, Q.; Wang, W.; Liao, Y.; Hu, X. Charge Transport and Recombination in Dye-Sensitized Solar Cells Based on Hybrid Films of TiO₂ Particles/TiO₂ Nanotubes. *J. Alloys Compd.* **2011**, *509* (29), 7808–7813. <https://doi.org/10.1016/j.jallcom.2011.05.028>.
- (168) Ping Wu, H.; Lin Li, L.; Chon Chen, C.; Guang Diao, E. W. Anodic TiO₂ Nanotube Arrays for Dye-Sensitized Solar Cells Characterized by Electrochemical Impedance Spectroscopy. *Ceram. Int.* **2012**, *38* (8), 6253–6266. <https://doi.org/10.1016/j.ceramint.2012.04.079>.
- (169) Kapilashrami, M.; Zhang, Y.; Liu, Y.-S.; Hagfeldt, A.; Guo, J. Probing the Optical Property and Electronic Structure of TiO₂ Nanomaterials for Renewable Energy Applications. *Chem. Rev.* **2014**, *114* (19), 9662–9707. <https://doi.org/10.1021/cr5000893>.
- (170) Sudhagar, P.; Jung, J. H.; Park, S.; Sathyamoorthy, R.; Ahn, H.; Kang, Y. S. Self-Assembled CdS Quantum Dots-Sensitized TiO₂ Nanospheroidal Solar Cells: Structural and Charge Transport Analysis. *Electrochimica Acta* **2009**, *55* (1), 113–117. <https://doi.org/10.1016/j.electacta.2009.08.015>.
- (171) Kim, Y. J.; Lee, M. H.; Kim, H. J.; Lim, G.; Choi, Y. S.; Park, N.-G.; Kim, K.; Lee, W. I. Formation of Highly Efficient Dye-Sensitized Solar Cells by Hierarchical Pore Generation with Nanoporous TiO₂ Spheres. *Adv. Mater.* **2009**, *21* (36), 3668–3673. <https://doi.org/10.1002/adma.200900294>.
- (172) Kim, C. W.; Choi, M. J.; Lee, S.; Park, H.; Moon, B.; Kang, Y. S.; Kang, Y. S. Crystalline Matrix of Mesoporous TiO₂ Framework for Dye-Sensitized Solar Cell Application. *J. Phys. Chem. C* **2015**, *119* (44), 24902–24909. <https://doi.org/10.1021/acs.jpcc.5b08639>.
- (173) Berglund, S. P.; Hoang, S.; Minter, R. L.; Fullon, R. R.; Mullins, C. B. Investigation of 35 Elements as Single Metal Oxides, Mixed Metal Oxides, or Dopants for Titanium Dioxide for Dye-Sensitized Solar Cells. *J. Phys. Chem. C* **2013**, *117* (48), 25248–25258. <https://doi.org/10.1021/jp4073747>.
- (174) Archana, P. S.; Jose, R.; Yusoff, M. M.; Ramakrishna, S. Near Band-Edge Electron Diffusion in Electrospun Nb-Doped Anatase TiO₂ Nanofibers Probed by Electrochemical Impedance Spectroscopy. *Appl. Phys. Lett.* **2011**, *98* (15), 152106. <https://doi.org/10.1063/1.3579194>.
- (175) Zhang, J.; Peng, W.; Chen, Z.; Chen, H.; Han, L. Effect of Cerium Doping in the TiO₂ Photoanode on the Electron Transport of Dye-Sensitized Solar Cells. *J. Phys. Chem. C* **2012**, *116* (36), 19182–19190. <https://doi.org/10.1021/jp3060735>.
- (176) Ghosh, R.; Hara, Y.; Alibabaei, L.; Hanson, K.; Rangan, S.; Bartynski, R.; Meyer, T. J.; Lopez, R. Increasing Photocurrents in Dye Sensitized Solar Cells with Tantalum-Doped Titanium Oxide Photoanodes Obtained by Laser Ablation. *ACS Appl. Mater. Interfaces* **2012**, *4* (9), 4566–4570. <https://doi.org/10.1021/am300938g>.

- (177) Dorman, J. A.; Weickert, J.; Reindl, J. B.; Putnik, M.; Wisnet, A.; Noebels, M.; Scheu, C.; Schmidt-Mende, L. Control of Recombination Pathways in TiO₂ Nanowire Hybrid Solar Cells Using Sn⁴⁺ Dopants. *J. Phys. Chem. C* **2014**, *118* (30), 16672–16679. <https://doi.org/10.1021/jp412650r>.
- (178) Guerrero, A.; Garcia-Belmonte, G.; Mora-Sero, I.; Bisquert, J.; Kang, Y. S.; Jacobsson, T. J.; Correa-Baena, J.-P.; Hagfeldt, A. Properties of Contact and Bulk Impedances in Hybrid Lead Halide Perovskite Solar Cells Including Inductive Loop Elements. *J. Phys. Chem. C* **2016**, *120* (15), 8023–8032. <https://doi.org/10.1021/acs.jpcc.6b01728>.
- (179) Kim, H.-S.; Jang, I.-H.; Ahn, N.; Choi, M.; Guerrero, A.; Bisquert, J.; Park, N.-G. Control of I–V Hysteresis in CH₃NH₃PbI₃ Perovskite Solar Cell. *J. Phys. Chem. Lett.* **2015**, *6* (22), 4633–4639. <https://doi.org/10.1021/acs.jpcclett.5b02273>.
- (180) Garcia-Belmonte, G.; Bisquert, J. Distinction between Capacitive and Noncapacitive Hysteretic Currents in Operation and Degradation of Perovskite Solar Cells. *ACS Energy Lett.* **2016**, *1* (4), 683–688. <https://doi.org/10.1021/acsenergylett.6b00293>.
- (181) Kim, H.-S.; Jang, I.-H.; Ahn, N.; Choi, M.; Guerrero, A.; Bisquert, J.; Park, N.-G. Control of I–V Hysteresis in CH₃NH₃PbI₃ Perovskite Solar Cell. *J. Phys. Chem. Lett.* **2015**, *6* (22), 4633–4639. <https://doi.org/10.1021/acs.jpcclett.5b02273>.
- (182) Almora, O.; Aranda, C.; Mas-Marzá, E.; Garcia-Belmonte, G. On Mott-Schottky Analysis Interpretation of Capacitance Measurements in Organometal Perovskite Solar Cells. *Appl. Phys. Lett.* **2016**, *109* (17), 173903. <https://doi.org/10.1063/1.4966127>.
- (183) Redmond, G.; Fitzmaurice, D.; Graetzel, M. Visible Light Sensitization by Cis-Bis(Thiocyanato)Bis(2,2'-Bipyridyl-4,4'-Dicarboxylato)Ruthenium(II) of a Transparent Nanocrystalline ZnO Film Prepared by Sol-Gel Techniques. *Chem. Mater.* **1994**, *6* (5), 686–691. <https://doi.org/10.1021/cm00041a020>.
- (184) Rensmo, H.; Keis, K.; Lindström, H.; Södergren, S.; Solbrand, A.; Hagfeldt, A.; Lindquist, S.-E.; Wang, L. N.; Muhammed, M. High Light-to-Energy Conversion Efficiencies for Solar Cells Based on Nanostructured ZnO Electrodes. *J. Phys. Chem. B* **1997**, *101* (14), 2598–2601. <https://doi.org/10.1021/jp962918b>.
- (185) Quintana, M.; Edvinsson, T.; Hagfeldt, A.; Boschloo, G. Comparison of Dye-Sensitized ZnO and TiO₂ Solar Cells: Studies of Charge Transport and Carrier Lifetime. *J. Phys. Chem. C* **2007**, *111* (2), 1035–1041. <https://doi.org/10.1021/jp065948f>.
- (186) Mani, A.; Huisman, C.; Goossens, A.; Schoonman, J. Mott–Schottky Analysis and Impedance Spectroscopy of TiO₂/6T and ZnO/6T Devices. *J. Phys. Chem. B* **2008**, *112* (33), 10086–10091. <https://doi.org/10.1021/jp8013964>.
- (187) Chandiran, A. K.; Abdi-Jalebi, M.; Nazeeruddin, M. K.; Grätzel, M. Analysis of Electron Transfer Properties of ZnO and TiO₂ Photoanodes for Dye-Sensitized Solar Cells. *ACS Nano* **2014**, *8* (3), 2261–2268. <https://doi.org/10.1021/nn405535j>.
- (188) Wang, Z. L. Nanostructures of Zinc Oxide. *Mater. Today* **2004**, *7* (6), 26–33. [https://doi.org/10.1016/S1369-7021\(04\)00286-X](https://doi.org/10.1016/S1369-7021(04)00286-X).

- (189) Djurišić, A. B.; Chen, X.; Leung, Y. H.; Ng, A. M. C. ZnO Nanostructures: Growth, Properties and Applications. *J. Mater. Chem.* **2012**, *22* (14), 6526–6535. <https://doi.org/10.1039/C2JM15548F>.
- (190) Guillén, E.; Peter, L. M.; Anta, J. A. Electron Transport and Recombination in ZnO-Based Dye-Sensitized Solar Cells. *J. Phys. Chem. C* **2011**, *115* (45), 22622–22632. <https://doi.org/10.1021/jp206698t>.
- (191) Mora-Seró, I.; Fabregat-Santiago, F.; Denier, B.; Bisquert, J.; Tena-Zaera, R.; Elias, J.; Lévy-Clément, C. Determination of Carrier Density of ZnO Nanowires by Electrochemical Techniques. *Appl. Phys. Lett.* **2006**, *89* (20), 203117. <https://doi.org/10.1063/1.2390667>.
- (192) Tena-Zaera, R.; Elias, J.; Lévy-Clément, C.; Mora-Seró, I.; Luo, Y.; Bisquert, J. Electrodeposition and Impedance Spectroscopy Characterization of ZnO Nanowire Arrays. *Phys. Status Solidi A* **2008**, *205* (10), 2345–2350. <https://doi.org/10.1002/pssa.200779426>.
- (193) Martinson, A. B. F.; Góes, M. S.; Fabregat-Santiago, F.; Bisquert, J.; Pellin, M. J.; Hupp, J. T. Electron Transport in Dye-Sensitized Solar Cells Based on ZnO Nanotubes: Evidence for Highly Efficient Charge Collection and Exceptionally Rapid Dynamics. *J. Phys. Chem. A* **2009**, *113* (16), 4015–4021. <https://doi.org/10.1021/jp810406q>.
- (194) He, C.; Zheng, Z.; Tang, H.; Zhao, L.; Lu, F. Electrochemical Impedance Spectroscopy Characterization of Electron Transport and Recombination in ZnO Nanorod Dye-Sensitized Solar Cells. *J. Phys. Chem. C* **2009**, *113* (24), 10322–10325. <https://doi.org/10.1021/jp902523c>.
- (195) Ku, C.-H.; Wu, J.-J. Electron Transport Properties in ZnO Nanowire Array/Nanoparticle Composite Dye-Sensitized Solar Cells. *Appl. Phys. Lett.* **2007**, *91* (9), 093117. <https://doi.org/10.1063/1.2778454>.
- (196) Parthasarathy, M.; Ramgir, N. S.; Sathe, B. R.; Mulla, I. S.; Pillai, V. K. Surface-State-Mediated Electron Transfer at Nanostructured ZnO Multipod/Electrolyte Interfaces. *J. Phys. Chem. C* **2007**, *111* (35), 13092–13102. <https://doi.org/10.1021/jp072695x>.
- (197) Liu, H.; Piret, G.; Sieber, B.; Laureyns, J.; Roussel, P.; Xu, W.; Boukherroub, R.; Szunerits, S. Electrochemical Impedance Spectroscopy of ZnO Nanostructures. *Electrochem. Commun.* **2009**, *11* (5), 945–949. <https://doi.org/10.1016/j.elecom.2009.02.019>.
- (198) Dupuy, L.; Haller, S.; Rousset, J.; Donsanti, F.; Guillemoles, J.-F.; Lincot, D.; Decker, F. Impedance Measurements of Nanoporosity in Electrodeposited ZnO Films for DSSC. *Electrochem. Commun.* **2010**, *12* (5), 697–699. <https://doi.org/10.1016/j.elecom.2010.03.009>.
- (199) Lai, Y.-H.; Lin, C.-Y.; Chen, H.-W.; Chen, J.-G.; Kung, C.-W.; Vittal, R.; Ho, K.-C. Fabrication of a ZnO Film with a Mosaic Structure for a High Efficient Dye -Sensitized Solar Cell. *J. Mater. Chem.* **2010**, *20* (42), 9379–9385. <https://doi.org/10.1039/C0JM01787F>.
- (200) Lu, L.; Li, R.; Fan, K.; Peng, T. Effects of Annealing Conditions on the Photoelectrochemical Properties of Dye-Sensitized Solar Cells Made with ZnO Nanoparticles. *Sol. Energy* **2010**, *84* (5), 844–853. <https://doi.org/10.1016/j.solener.2010.02.010>.

- (201) Sudhagar, P.; Kumar, R. S.; Jung, J. H.; Cho, W.; Sathyamoorthy, R.; Won, J.; Kang, Y. S. Facile Synthesis of Highly Branched Jacks-like ZnO Nanorods and Their Applications in Dye-Sensitized Solar Cells. *Mater. Res. Bull.* **2011**, *46* (9), 1473–1479. <https://doi.org/10.1016/j.materresbull.2011.04.027>.
- (202) Puyoo, E.; Rey, G.; Appert, E.; Consonni, V.; Bellet, D. Efficient Dye-Sensitized Solar Cells Made from ZnO Nanostructure Composites. *J. Phys. Chem. C* **2012**, *116* (34), 18117–18123. <https://doi.org/10.1021/jp306174f>.
- (203) Sacco, A.; Lamberti, A.; Gazia, R.; Bianco, S.; Manfredi, D.; Shahzad, N.; Cappelluti, F.; Ma, S.; Tresso, E. High Efficiency Dye -Sensitized Solar Cells Exploiting Sponge-like ZnO Nanostructures. *Phys. Chem. Chem. Phys.* **2012**, *14* (47), 16203–16208. <https://doi.org/10.1039/C2CP42705B>.
- (204) Magne, C.; Moehl, T.; Urien, M.; Grätzel, M.; Pauporté, T. Effects of ZnO Film Growth Route and Nanostructure on Electron Transport and Recombination in Dye -Sensitized Solar Cells. *J. Mater. Chem. A* **2013**, *1* (6), 2079–2088. <https://doi.org/10.1039/C2TA00674J>.
- (205) Park, K.; Xi, J.; Zhang, Q.; Cao, G. Charge Transport Properties of ZnO Nanorod Aggregate Photoelectrodes for DSCs. *J. Phys. Chem. C* **2011**, *115* (43), 20992–20999. <https://doi.org/10.1021/jp2067292>.
- (206) Hosni, M.; Kusumawati, Y.; Farhat, S.; Jouini, N.; Pauporté, Th. Effects of Oxide Nanoparticle Size and Shape on Electronic Structure, Charge Transport, and Recombination in Dye-Sensitized Solar Cell Photoelectrodes. *J. Phys. Chem. C* **2014**, *118* (30), 16791–16798. <https://doi.org/10.1021/jp412772b>.
- (207) Wu, J.-J.; Wong, D. K.-P. Fabrication and Impedance Analysis of N-ZnO Nanorod/p-Si Heterojunctions to Investigate Carrier Concentrations in Zn/O Source- Ratio-Tuned ZnO Nanorod Arrays. *Adv. Mater.* **2007**, *19* (15), 2015–2019. <https://doi.org/10.1002/adma.200602052>.
- (208) Lee, S.-H.; Han, S.-H.; Jung, H. S.; Shin, H.; Lee, J.; Noh, J.-H.; Lee, S.; Cho, I.-S.; Lee, J.-K.; Kim, J.; Shin, H. Al-Doped ZnO Thin Film: A New Transparent Conducting Layer for ZnO Nanowire-Based Dye-Sensitized Solar Cells. *J. Phys. Chem. C* **2010**, *114* (15), 7185–7189. <https://doi.org/10.1021/jp1008412>.
- (209) Wong, K. K.; Ng, A.; Chen, X. Y.; Ng, Y. H.; Leung, Y. H.; Ho, K. H.; Djurišić, A. B.; Ng, A. M. C.; Chan, W. K.; Yu, L.; Phillips, D. L. Effect of ZnO Nanoparticle Properties on Dye-Sensitized Solar Cell Performance. *ACS Appl. Mater. Interfaces* **2012**, *4* (3), 1254–1261. <https://doi.org/10.1021/am201424d>.
- (210) Arshad, M.; Ahmed, A. S.; Azam, A.; Naqvi, A. H. Exploring the Dielectric Behavior of Co Doped ZnO Nanoparticles Synthesized by Wet Chemical Route Using Impedance Spectroscopy. *J. Alloys Compd.* **2013**, *577*, 469–474. <https://doi.org/10.1016/j.jallcom.2013.06.035>.
- (211) Raj, C. J.; Prabakar, K.; Karthick, S. N.; Hemalatha, K. V.; Son, M.-K.; Kim, H.-J. Banyan Root Structured Mg-Doped ZnO Photoanode Dye-Sensitized Solar Cells. *J. Phys. Chem. C* **2013**, *117* (6), 2600–2607. <https://doi.org/10.1021/jp308847g>.

- (212) Shinde, S. S.; Korade, A. P.; Bhosale, C. H.; Rajpure, K. Y. Influence of Tin Doping onto Structural, Morphological, Optoelectronic and Impedance Properties of Sprayed ZnO Thin Films. *J. Alloys Compd.* **2013**, *551*, 688–693. <https://doi.org/10.1016/j.jallcom.2012.11.057>.
- (213) Das, P. P.; Agarkar, S. A.; Mukhopadhyay, S.; Manju, U.; Ogale, S. B.; Devi, P. S. Defects in Chemically Synthesized and Thermally Processed ZnO Nanorods: Implications for Active Layer Properties in Dye-Sensitized Solar Cells. *Inorg. Chem.* **2014**, *53* (8), 3961–3972. <https://doi.org/10.1021/ic500279q>.
- (214) Cheng, W.-H.; Chiou, J.-W.; Tsai, M.-Y.; Jeng, J.-S.; Chen, J.-S.; Hsu, S. L.-C.; Chou, W.-Y. Lithium-Induced Defect Levels in ZnO Nanoparticles To Facilitate Electron Transport in Inverted Organic Photovoltaics. *J. Phys. Chem. C* **2016**, *120* (28), 15035–15041. <https://doi.org/10.1021/acs.jpcc.6b03656>.
- (215) Mahmud, M. A.; Elumalai, N. K.; Upama, M. B.; Wang, D.; Soufiani, A. M.; Wright, M.; Xu, C.; Haque, F.; Uddin, A. Solution-Processed Lithium-Doped ZnO Electron Transport Layer for Efficient Triple Cation (Rb, MA, FA) Perovskite Solar Cells. *ACS Appl. Mater. Interfaces* **2017**, *9* (39), 33841–33854. <https://doi.org/10.1021/acsami.7b09153>.
- (216) Krishnapriya, R.; Praneetha, S.; Kannan, S.; Vadivel Murugan, A. Unveiling the Co²⁺ Ion Doping-Induced Hierarchical Shape Evolution of ZnO: In Correlation with Magnetic and Photovoltaic Performance. *ACS Sustain. Chem. Eng.* **2017**, *5* (11), 9981–9992. <https://doi.org/10.1021/acssuschemeng.7b01918>.
- (217) Kay, A.; Grätzel, M. Dye-Sensitized Core–Shell Nanocrystals: Improved Efficiency of Mesoporous Tin Oxide Electrodes Coated with a Thin Layer of an Insulating Oxide. *Chem. Mater.* **2002**, *14* (7), 2930–2935. <https://doi.org/10.1021/cm0115968>.
- (218) Green, A. N. M.; Palomares, E.; Haque, S. A.; Kroon, J. M.; Durrant, J. R. Charge Transport versus Recombination in Dye-Sensitized Solar Cells Employing Nanocrystalline TiO₂ and SnO₂ Films. *J. Phys. Chem. B* **2005**, *109* (25), 12525–12533. <https://doi.org/10.1021/jp050145y>.
- (219) Kim, J.-Y.; Kim, J. Y.; Lee, D.-K.; Kim, B.; Kim, H.; Ko, M. J. Importance of 4-Tert-Butylpyridine in Electrolyte for Dye-Sensitized Solar Cells Employing SnO₂ Electrode. *J. Phys. Chem. C* **2012**, *116* (43), 22759–22766. <https://doi.org/10.1021/jp307783q>.
- (220) Ulfa, M.; Wang, P.; Zhang, J.; Liu, J.; de Marcillac, W. D.; Coolen, L.; Peralta, S.; Pauporté, T. Charge Injection and Electrical Response in Low-Temperature SnO₂-Based Efficient Perovskite Solar Cells. *ACS Appl. Mater. Interfaces* **2018**, *10* (41), 35118–35128. <https://doi.org/10.1021/acsami.8b10979>.
- (221) Xiao, J.; Huang, Q.; Xu, J.; Li, C.; Chen, G.; Luo, Y.; Li, D.; Meng, Q. CdS/CdSe Co-Sensitized Solar Cells Based on a New SnO₂ Photoanode with a Three-Dimensionally Interconnected Ordered Porous Structure. *J. Phys. Chem. C* **2014**, *118* (8), 4007–4015. <https://doi.org/10.1021/jp411922e>.
- (222) Huang, Q.; Li, F.; Gong, Y.; Luo, J.; Yang, S.; Luo, Y.; Li, D.; Bai, X.; Meng, Q. Recombination in SnO₂-Based Quantum Dots Sensitized Solar Cells: The Role of Surface States. *J. Phys. Chem. C* **2013**, *117* (21), 10965–10973. <https://doi.org/10.1021/jp402601v>.

- (223) Basu, K.; Benetti, D.; Zhao, H.; Jin, L.; Vetrone, F.; Vomiero, A.; Rosei, F. Enhanced Photovoltaic Properties in Dye Sensitized Solar Cells by Surface Treatment of SnO₂ Photoanodes. *Sci. Rep.* **2016**, *6*, 23312. <https://doi.org/10.1038/srep23312>.
- (224) Elumalai, N. K.; Jose, R.; Archana, P. S.; Chellappan, V.; Ramakrishna, S. Charge Transport through Electrospun SnO₂ Nanoflowers and Nanofibers: Role of Surface Trap Density on Electron Transport Dynamics. *J. Phys. Chem. C* **2012**, *116* (42), 22112–22120. <https://doi.org/10.1021/jp304876j>.
- (225) Naveen Kumar, E.; Jose, R.; S. Archana, P.; Vijila, C.; M. Yusoff, M.; Ramakrishna, S. High Performance Dye -Sensitized Solar Cells with Record Open Circuit Voltage Using Tin Oxide Nanoflowers Developed by Electrospinning. *Energy Environ. Sci.* **2012**, *5* (1), 5401–5407. <https://doi.org/10.1039/C1EE02703D>.
- (226) Wijeratne, K.; Akilavasan, J.; Thelakkat, M.; Bandara, J. Enhancing the Solar Cell Efficiency through Pristine 1-Dimensional SnO₂ Nanostructures: Comparison of Charge Transport and Carrier Lifetime of SnO₂ Particles vs. Nanorods. *Electrochimica Acta* **2012**, *72*, 192–198. <https://doi.org/10.1016/j.electacta.2012.04.016>.
- (227) Sigdel, S.; Elbohy, H.; Gong, J.; Adhikari, N.; Sumathy, K.; Qiao, H.; Wei, Q.; Sayyad, M. H.; Zai, J.; Qian, X.; Qiao, Q. Dye-Sensitized Solar Cells Based on Porous Hollow Tin Oxide Nanofibers. *IEEE Trans. Electron Devices* **2015**, *62* (6), 2027–2032. <https://doi.org/10.1109/TED.2015.2421475>.
- (228) Wang, D.; Liu, S.; Shao, M.; Li, Q.; Gu, Y.; Zhao, J.; Zhang, X.; Zhao, J.; Fang, Y. Aqueous Solution-Processed Multifunctional SnO₂ Aggregates for Highly Efficient Dye-Sensitized Solar Cells. *Ind. Eng. Chem. Res.* **2018**, *57* (21), 7136–7145. <https://doi.org/10.1021/acs.iecr.8b00039>.
- (229) Dou, X.; Sabba, D.; Mathews, N.; Wong, L. H.; Lam, Y. M.; Mhaisalkar, S. Hydrothermal Synthesis of High Electron Mobility Zn-Doped SnO₂ Nanoflowers as Photoanode Material for Efficient Dye-Sensitized Solar Cells. *Chem. Mater.* **2011**, *23* (17), 3938–3945. <https://doi.org/10.1021/cm201366z>.
- (230) Azam, A.; Ahmed, A. S.; Chaman, M.; Naqvi, A. H. Investigation of Electrical Properties of Mn Doped Tin Oxide Nanoparticles Using Impedance Spectroscopy. *J. Appl. Phys.* **2010**, *108* (9), 094329. <https://doi.org/10.1063/1.3506691>.
- (231) Teh, J. J.; Ting, S. L.; Leong, K. C.; Li, J.; Chen, P. Gallium-Doped Tin Oxide Nano-Cuboids for Improved Dye Sensitized Solar Cell. *ACS Appl. Mater. Interfaces* **2013**, *5* (21), 11377–11382. <https://doi.org/10.1021/am403640s>.
- (232) Shalan, A. E.; Rasly, M.; Osama, I.; Rashad, M. M.; Ibrahim, I. A. Photocurrent Enhancement by Ni²⁺ and Zn²⁺ Ion Doped in SnO₂ Nanoparticles in Highly Porous Dye-Sensitized Solar Cells. *Ceram. Int.* **2014**, *40* (8, Part A), 11619–11626. <https://doi.org/10.1016/j.ceramint.2014.03.152>.
- (233) Jim, W. Y.; Liu, X.; Yiu, W. K.; Leung, Y. H.; Djurišić, A. B.; Chan, W. K.; Liao, C.; Shih, K.; Surya, C. The Effect of Different Dopants on the Performance of SnO₂-Based Dye-Sensitized Solar Cells. *Phys. Status Solidi B* **2015**, *252* (3), 553–557. <https://doi.org/10.1002/pssb.201451256>.

- (234) Ben Haj Othmen, W.; Sdiri, N.; Elhouichet, H.; Férid, M. Study of Charge Transport in Fe-Doped SnO₂ Nanoparticles Prepared by Hydrothermal Method. *Mater. Sci. Semicond. Process.* **2016**, *52*, 46–54. <https://doi.org/10.1016/j.mssp.2016.05.010>.
- (235) Fabregat-Santiago, F.; Garcia-Belmonte, G.; Mora-Seró, I.; Bisquert, J. Characterization of Nanostructured Hybrid and Organic Solar Cells by Impedance Spectroscopy. *Phys. Chem. Chem. Phys.* **2011**, *13* (20), 9083–9118. <https://doi.org/10.1039/C0CP02249G>.
- (236) Hautier, G.; Miglio, A.; Ceder, G.; Rignanese, G.-M.; Gonze, X. Identification and Design Principles of Low Hole Effective Mass *p*-Type Transparent Conducting Oxides. *Nat. Commun.* **2013**, *4*, 2292. <https://doi.org/10.1038/ncomms3292>.
- (237) Xia, X. H.; Tu, J. P.; Zhang, J.; Wang, X. L.; Zhang, W. K.; Huang, H. Morphology Effect on the Electrochromic and Electrochemical Performances of NiO Thin Films. *Electrochimica Acta* **2008**, *53* (18), 5721–5724. <https://doi.org/10.1016/j.electacta.2008.03.047>.
- (238) Huang, Z.; Natu, G.; Ji, Z.; Hasin, P.; Wu, Y. P-Type Dye-Sensitized NiO Solar Cells: A Study by Electrochemical Impedance Spectroscopy. *J. Phys. Chem. C* **2011**, *115* (50), 25109–25114. <https://doi.org/10.1021/jp205306g>.
- (239) Yang, H.; Guai, G. H.; Guo, C.; Song, Q.; Jiang, S. P.; Wang, Y.; Zhang, W.; Li, C. M. NiO/Graphene Composite for Enhanced Charge Separation and Collection in *p*-Type Dye Sensitized Solar Cell. *J. Phys. Chem. C* **2011**, *115* (24), 12209–12215. <https://doi.org/10.1021/jp201178a>.
- (240) Feihl, S.; D. Costa, R.; Pflöck, S.; Schmidt, C.; Schönamsgruber, J.; Backes, S.; Hirsch, A.; M. Guldi, D. Nickel Oxide Nanostructured Electrodes towards Perylenediimide-Based Dye -Sensitized Solar Cells. *RSC Adv.* **2012**, *2* (30), 11495–11503. <https://doi.org/10.1039/C2RA22206J>.
- (241) Hsu, C.-Y.; Chen, W.-T.; Chen, Y.-C.; Wei, H.-Y.; Yen, Y.-S.; Huang, K.-C.; Ho, K.-C.; Chu, C.-W.; Lin, J. T. Charge Transporting Enhancement of NiO Photocathodes for *p*-Type Dye-Sensitized Solar Cells. *Electrochimica Acta* **2012**, *66*, 210–215. <https://doi.org/10.1016/j.electacta.2012.01.081>.
- (242) Huang, Z.; Natu, G.; Ji, Z.; He, M.; Yu, M.; Wu, Y. Probing the Low Fill Factor of NiO *p*-Type Dye-Sensitized Solar Cells. *J. Phys. Chem. C* **2012**, *116* (50), 26239–26246. <https://doi.org/10.1021/jp310053f>.
- (243) Barceló, I.; Guillén, E.; Lana-Villarreal, T.; Gómez, R. Preparation and Characterization of Nickel Oxide Photocathodes Sensitized with Colloidal Cadmium Selenide Quantum Dots. *J. Phys. Chem. C* **2013**, *117* (44), 22509–22517. <https://doi.org/10.1021/jp406989v>.
- (244) Hod, I.; Tachan, Z.; Shalom, M.; Zaban, A. Characterization and Control of the Electronic Properties of a NiO Based Dye Sensitized Photocathode. *Phys. Chem. Chem. Phys.* **2013**, *15* (17), 6339–6343. <https://doi.org/10.1039/C3CP50242B>.
- (245) Peiris, T. A. N.; Sagu, J. S.; Wijayantha, K. G. U.; García-Cañadas, J. Electrochemical Determination of the Density of States of Nanostructured NiO Films. *ACS Appl. Mater. Interfaces* **2014**, *6* (17), 14988–14993. <https://doi.org/10.1021/am502827z>.

- (246) Kang, J. S.; Kim, J.; Kim, J. S.; Nam, K.; Jo, H.; Son, Y. J.; Kang, J.; Jeong, J.; Choe, H.; Kwon, T.-H.; Sung, Y.-E. Electrochemically Synthesized Mesoscopic Nickel Oxide Films as Photocathodes for Dye-Sensitized Solar Cells. *ACS Appl. Energy Mater.* **2018**, *1* (8), 4178–4185. <https://doi.org/10.1021/acsaem.8b00834>.
- (247) Guai, G. H.; Leiw, M. Y.; Ng, C. M.; Li, C. M. Sulfur-Doped Nickel Oxide Thin Film as an Alternative to Pt for Dye-Sensitized Solar Cell Counter Electrodes. *Adv. Energy Mater.* **2012**, *2* (3), 334–338. <https://doi.org/10.1002/aenm.201100582>.
- (248) Natu, G.; Hasin, P.; Huang, Z.; Ji, Z.; He, M.; Wu, Y. Valence Band-Edge Engineering of Nickel Oxide Nanoparticles via Cobalt Doping for Application in p-Type Dye-Sensitized Solar Cells. *ACS Appl. Mater. Interfaces* **2012**, *4* (11), 5922–5929. <https://doi.org/10.1021/am301565j>.
- (249) D'Amario, L.; Boschloo, G.; Hagfeldt, A.; Hammarström, L. Tuning of Conductivity and Density of States of NiO Mesoporous Films Used in P-Type DSSCs. *J. Phys. Chem. C* **2014**, *118* (34), 19556–19564. <https://doi.org/10.1021/jp504551v>.
- (250) Jung, J. W.; Chueh, C.-C.; Jen, A. K.-Y. A Low-Temperature, Solution-Processable, Cu-Doped Nickel Oxide Hole-Transporting Layer via the Combustion Method for High-Performance Thin-Film Perovskite Solar Cells. *Adv. Mater.* **2015**, *27* (47), 7874–7880. <https://doi.org/10.1002/adma.201503298>.
- (251) Kawazoe, H.; Yasukawa, M.; Hyodo, H.; Kurita, M.; Yanagi, H.; Hosono, H. P-Type Electrical Conduction in Transparent Thin Films of CuAlO₂. *Nature* **1997**, *389* (6654), 939–942. <https://doi.org/10.1038/40087>.
- (252) Renaud, A.; Chavillon, B.; Pleux, L. L.; Pellegrin, Y.; Blart, E.; Boujtita, M.; Pauporté, T.; Cario, L.; Jobic, S.; Odobel, F. CuGaO₂: A Promising Alternative for NiO in p-Type Dye Solar Cells. *J. Mater. Chem.* **2012**, *22* (29), 14353–14356. <https://doi.org/10.1039/C2JM31908J>.
- (253) Herraiz-Cardona, I.; Fabregat-Santiago, F.; Renaud, A.; Julián-López, B.; Odobel, F.; Cario, L.; Jobic, S.; Giménez, S. Hole Conductivity and Acceptor Density of P-Type CuGaO₂ Nanoparticles Determined by Impedance Spectroscopy: The Effect of Mg Doping. *Electrochimica Acta* **2013**, *113*, 570–574. <https://doi.org/10.1016/j.electacta.2013.09.129>.

Chapter 2

Evidence and Influence of Copper Vacancies in p-Type CuGaO₂ Mesoporous Films

*This chapter was reproduced from the Bredar, A. R. C.; Blanchet, M. D.; Comes, R. B.; Farnum, B. H. *ACS Appl. Energy Mater.* **2019**, 2 (1), 19–28

2.1 Introduction

Delafossite Cu^IM^{III}O₂ materials have gained much attention over the past decade as p-type metal oxides capable of serving as hole transport layers (HTL) in a wide range of heterojunction solar cells^{1–15}, photocathodes for direct reduction of H⁺/CO₂^{16–21}, and electrocatalysts for oxidation of H₂O.²² Interest in these materials comes from the variability of the M^{III} atom and the layered delafossite crystal structure that is known to facilitate hole (h^+) diffusion through the valence band.^{23,24} For example, oxides such as CuAlO₂, CuScO₂, CuCrO₂, and CuGaO₂ are wide band gap materials that have been investigated as HTLs in combination with appropriate light absorbers and molecular catalysts to achieve solar-to-electrical^{1,2,4–8,10–15} and solar-to-fuel energy conversion.^{3,9} Likewise, visible band gap materials such as CuFeO₂, CuRhO₂, and CuMnO₂ have been shown to perform direct photocatalytic H⁺/CO₂ reduction via band gap excitation.^{17–21} More recently, CuCoO₂, CuRhO₂, CuFeO₂, CuCrO₂, and CuMnO₂ have all been shown to possess electrocatalytic properties toward water oxidation.²²

The layered delafossite structure is also a key aspect of their scientific interest. **Figure 2.1** shows the delafossite lattice as the 3R polymorph where alternating layers of Cu^I atoms and edge-shared MO₆ octahedra stack in the *c*-direction. Orbital mixing of Cu-3d and O-2p orbitals delocalizes the valence band and results in p-type conductivity. Charge transport, however, is highly anisotropic with faster hole diffusion occurring through the Cu^I layer vs across alternating Cu^I/MO₆ layers. For example, experimental measurements have shown that the hole mobility of CuAlO₂ in the [100] and [010] direction is 25 times faster than transport in the [001] direction.²⁴

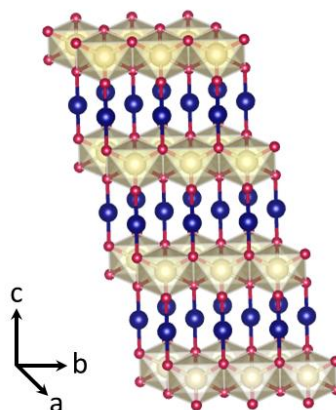


Figure 2.1: CuGaO₂ delafossite (3R) crystal structure where copper atoms (blue) lie in the *ab*-plane and stack alternately with edge-shared gallium oxide layers in the *c*-direction.

This chapter describe the investigation of the the structural and electrochemical properties of CuGaO₂ nanocrystalline mesoporous films in acetonitrile solution. CuGaO₂ has been studied previously as HTLs for dye-sensitized solar cells (DSSCs)^{2,6,7,10,14,25}, perovskite solar cells¹¹, organic photovoltaics (OPVs)¹, and for CO₂ reduction with molecular chromophore-catalyst assemblies.⁹ Previous results have noted that Mg-doping and thermal oxidation of CuGaO₂ can improve solar cell performance in DSSCs² and OPVs¹, respectively. In these examples, improved solar cell efficiency was attributed to a greater conductivity of holes throughout the nanocrystalline films due to a larger hole density (n_{h+}). Here, we show that a large n_{h+} , induced by copper vacancies in the delafossite lattice, can result in surface defects and give rise to characteristic electrochemical features. CuGaO₂ films also display large conductivities on the order of $10^{-5} \Omega^{-1} \text{ cm}^{-1}$, attributed to the high concentration of holes and a preferred orientation of nanocrystals in the film structure.

2.2 Experimental

2.2.1 Nanocrystal Synthesis CuGaO₂ nanocrystals were synthesized via a hydrothermal preparation, adapted from previously reported syntheses by Popplemeier, Jobic, and Cheng.^{8,10,26} Copper (II) nitrate hemipentahydrate (Cu(NO₃)₃•2.5H₂O, Acros Organics, 98%+) and gallium(III) nitrate (Ga(NO₃)₃•H₂O, Alfa Aesar, 99.99%) (5mmol each) were dissolved in deionized water (15 mL, 18 MΩ cm, Milli-Q). The solution was chilled in an ice bath and stirred continuously for 1 hour. Ethylene glycol (5mL, VWR) was then added to the mixture as a reducing agent, and the pH of the solution was adjusted to ~9 using a 2.5 M KOH solution in 1 mL increments. The final solution was stirred for 1 hour before transfer into a 45 mL Teflon-lined autoclave (Parr) for hydrothermal reaction at 190 °C for 24 hours in a box furnace (Lindberg Blue M). The resulting particles were washed overnight with ammonium hydroxide (NH₄OH, 28 vol%, BDH) to remove CuO and Cu₂O side products and then centrifuged and washed with deionized water 3 times. The particles were finally washed with acetone and dried in a vacuum oven (Lindberg Blue M) to result in a final yield of 60%.

2.2.2 Film Preparation A CuGaO₂ nanocrystal paste was prepared by adding deionized water (3.3 mL, 18 MΩ cm, Milli-Q), adjusted to pH 1 using nitric acid (20μL, HNO₃, VWR, 70%), and polyethylene glycol (0.25 g, PEG, MW 20,000, Millipore Sigma) to dry CuGaO₂ powder (0.5 g). The final composition of the paste was 15 wt% CuGaO₂ and 7.5 wt% PEG. The paste was sonicated using an ultrasonication horn (Branson 150) for 30 seconds to improve particle dispersity. CuGaO₂ mesoporous thin films were prepared by doctor blading the nanocrystal paste onto conductive FTO glass (SnO₂:F, 15 Ω/cm², Hartford Glass, Inc.). Films were then annealed in a tube furnace (Lindberg Blue M) under an oxygen atmosphere (99.999 %, Airgas) at

temperatures between 50-500 °C for 30 minutes (400 ft/min) followed by a second step under an argon atmosphere (99.999 %, Airgas) at 500 °C for 30 minutes (400 ft/min).

2.2.3 Characterization A range of characterization techniques were employed to study CuGaO₂ films before and after annealing. Attenuated total reflectance Fourier-transform infrared spectroscopy (ATR-IR) was performed using a Nicolet iS-50 spectrometer with a built-in ATR. UV-Vis-near IR transmittance and reflectance spectra were collected using a Cary 5000 spectrophotometer with an integrating sphere accessory. Kubelka-Munk analysis was performed directly with the Cary Win-UV software. Scanning electron microscopy (SEM) was performed using a Jeol JSM-7000F Field Emission Scanning Electron Microscope with energy dispersive spectroscopy (EDS, INCA). For a given CuGaO₂ films, elemental analysis using EDS was performed on three different regions with the same area (~300 μm x 300 μm) to obtain an average and standard deviation for elemental composition. Elemental peaks were calibrated using INCA software and a copper standard. Powder x-ray diffraction (PXRD) data were collected on a Bruker D8 Discover diffractometer (Cu K α source) with a Vantec 2000 two-dimensional area detector.

X-ray photoelectron spectroscopy was performed using a Physical Electronics (PHI) 5400 system with a monochromatic Al K α source. High resolution scans of the O 1s, Cu 2p, and Ga 2p peaks were performed with a pass energy of 36 eV and a step size of 0.05 eV. A neutralizing electron flood gun was used to prevent charging of the samples during measurement. The Casa XPS fitting software was used for all data analysis and fitting. Voigt function peaks for each element were constrained such that the full-width at half-maximum for each core-level peak were equal. The data were aligned such that the metal-oxide peak in the O 1s core level had a binding energy of 530.5 eV, which matches previous literature.¹

2.2.4 Electrochemistry Cyclic voltammetry (CV) experiments were performed with a Gamry 1010E potentiostat. Data were collected using a three-electrode setup where the working electrode was the CuGaO₂ film on FTO, the counter electrode was Pt mesh, and the reference was an aqueous Ag/AgCl electrode (satd. KCl). All experiments were performed in acetonitrile (MeCN, BDH) with 0.1 M LiClO₄ (99.99%, Millipore Sigma) electrolyte at a scan rate of 50 mV/s unless otherwise indicated. All reference potentials were calibrated before and after experiments using ferrocene (Fc⁺⁰). The $E_{1/2}(\text{Fc}^{+/0})$ was consistently measured to be 0.4 V vs Ag/AgCl in MeCN with 0.1 M LiClO₄. This value was used to adjust all potentials to the ferrocene reference.

Electrochemical impedance spectroscopy (EIS) was performed using the same potentiostat and three-electrode cell setup as the CV experiments. Data was collected over the potential range -0.9 to 1.1 V vs Fc⁺⁰, with a frequency range of 250 kHz – 100 mHz with 0.1 V steps and a modulation potential of 5 mV. Data were fit using Gamry Analyst software using an equivalent circuit model described further in the text.

2.3 Results

2.3.1 Synthesis and Characterization CuGaO₂ nanocrystals were synthesized by a hydrothermal method based on previous literature reports.^{8,10,26} SEM measurements of powder samples showed nanocrystals of a plate-like morphology with widths of ~200 nm and thicknesses of ~40 nm (**Figure 2.2**). EDS measurements revealed a Cu:Ga ratio of 0.96 ± 0.02 (**Table A2.1**), indicating an average $4 \pm 2\%$ deficiency of copper atoms in the lattice. Nanocrystals were combined with polyethylene glycol (PEG) and water to form a viscous paste which was used to doctor blade 4 μm thick films onto conductive FTO glass. CuGaO₂ films were

then annealed in a tube furnace under pure O₂ from 50-500 °C followed by under Ar at 500 °C. SEM images of annealed films showed no significant change in nanocrystal size or morphology with respect to powder samples.

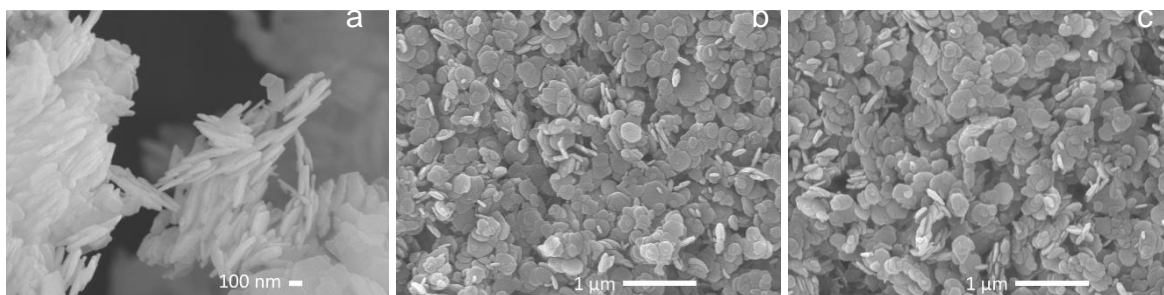


Figure 2.2: SEM images of CuGaO₂ nanocrystals: (left) powder, (middle) film annealed at 200 °C O₂, and (right) film annealed at 200 °C O₂ / 500 °C Ar.

Figure 2.3a shows a comparison of x-ray diffraction patterns collected for CuGaO₂ powder and thin film samples. The powder sample shows diffraction peaks consistent with the delafossite phase in the 3R rhombohedral polymorph.^{8,10,11,26,27} Upon deposition of CuGaO₂ nanocrystals as a thin film, an enhancement of the (00*l*) peaks was clearly observed, indicating a preferred orientation of nanocrystals with the (00*l*) planes parallel to the FTO substrate. **Figure 2.3b-c** shows the two-dimensional XRD pattern for a thin film annealed at 300 °C O₂ / 500 °C Ar where higher peak intensities were centered around $\chi = 90^\circ$. The χ angle refers to the tilt of the diffraction plane with respect to the sample stage. Films annealed under O₂ showed no change in the diffraction pattern from 50 - 450 °C. Decomposition to the oxidized CuGa₂O₄ spinel phase was observed at 500 °C (**Figure A2.1**). Treatment of films under an Ar environment at 500 °C showed no change in the delafossite phase.

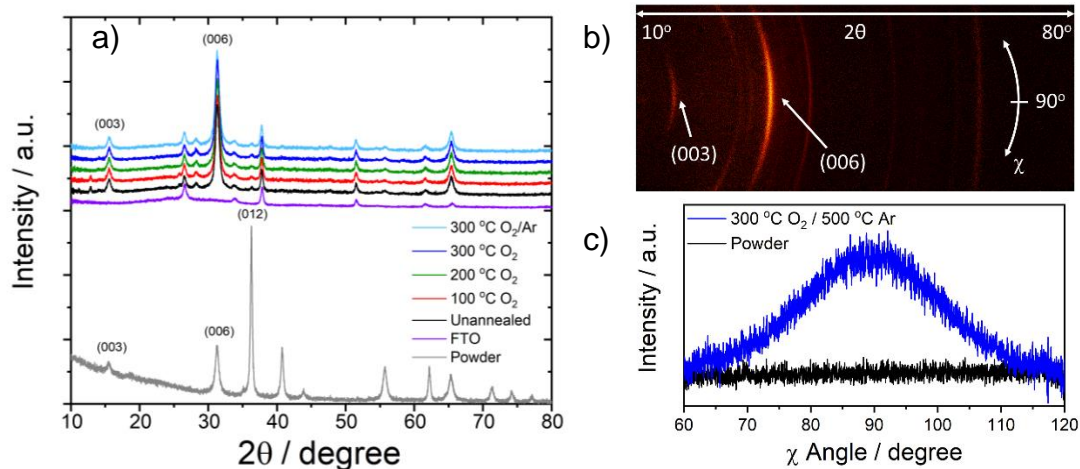


Figure 2.3: a) Powder X-ray diffractograms collected for CuGaO_2 powder and thin films annealed over a range of temperatures and atmospheric conditions. b) Two-dimensional (2θ , χ) XRD frame showing a preferred orientation of (003) and (006) peaks. c) Integration of the (006) peak intensity in the χ -direction for a powder sample and a thin film annealed at 300 °C O_2 / 500 °C Ar.

ATR-IR experiments were performed to assess the extent of PEG removal from the thin films as a function of annealing temperature and atmospheric conditions. ATR-IR spectra of CuGaO_2 films showed vibrational modes associated with PEG were removed at $T \geq 200$ °C under an O_2 environment, **Figure A2.2**. Continued annealing under an Ar atmosphere at 500 °C also showed removal of PEG for films initially annealed at $T < 200$ °C O_2 .

CuGaO_2 films under all annealing conditions were found to exhibit high scattering of visible light, consistent with the >100 nm size of nanocrystals and 4 μm film thickness. **Figure A2.3** shows UV-Vis-near IR transmittance and reflectance data of films annealed at the 200 °C O_2 and 200 °C O_2 / 500 °C Ar conditions where the reflectance reached a peaked of 25-30% in the visible range. A Kubelka-Munk analysis of reflectance data is shown in **Figure A2.3** where a sharp increase in the $F(R)$ function at $\lambda < 380$ nm is consistent with a wide band gap ($E_g \sim 3.3$ eV) for CuGaO_2 , consistent with previous reports in the literature.²⁸

XPS data collected for CuGaO₂ films as a function of annealing condition are shown in **Table 2.1**. All films clearly indicated the presence of both Cu^I (932.7 eV) and Cu^{II} (935.3 eV) at the nanocrystal surface, as shown by the Cu 2p_{3/2} spectra in **Figure 2.4a**.^{1,29-31} Satellite peaks in the 940-948 eV range were also observed, typical for the presence of Cu^{II}. The Cu^{II} peak at 935.3 eV is further assigned to Cu^{II} atoms associated with surface OH groups as opposed to lattice bound Cu^{II} atoms, which would give rise to a peak in the 933-934 eV range.²⁹ Furthermore, this distinction is made based on the concomitant presence of surface hydroxide (OH_{surf}) and surface water (H₂O_{surf}) detected in the O 1s region, **Figure 2.4b**. These peaks were observed at 531.8 and 533.1 eV, respectively, with lattice bound oxygen atoms giving rise to a peak at 530.5 eV, consistent with previous literature reports.¹ Based on these assignments, unannealed films clearly contained a large amount of OH_{surf} and H₂O_{surf} molecules due to the presence of PEG and water from the doctor bladed paste. Annealing under an O₂ atmosphere is shown to remove most of these peaks and yield a consistent peak shape for temperatures ≥200 °C, which features a main peak for lattice oxygen and shoulder peaks for OH_{surf} and H₂O_{surf}. The Cu^{II} peak at 935.3 eV was found to decrease over the same temperature range concurrent with a rise in the Cu^I peak at 932.7 eV, indicating that Cu^{II} is stabilized by the presence of OH_{surf} and/or H₂O_{surf}. Given the oxidizing annealing conditions, we believe this decrease in Cu^{II} is due to either migration of holes from surface copper sites to bulk copper sites or atomic migration of Cu^{II} atoms from the surface to bulk. Further annealing at 500 °C Ar showed a small but continued decrease of Cu^{II} peaks, consistent with the reducing environment of the atmosphere (**Figure A2.5**).

Table 2.1. Elemental analysis (at%) of CuGaO₂ film surfaces obtained from XPS

	Cu ^I	Cu ^{II}	Ga	O	Cu ^{II} /Cu ^I	Cu/Ga ^b
Unannealed	5.4	14.0	29.9	50.7	2.6	0.65
100 °C O ₂	7.0	11.2	30.7	51.7	1.6	0.60
200 °C O ₂	12.3	5.0	32.7	50.2	0.4	0.52
300 °C O ₂	12.1	4.1	33.9	49.9	0.3	0.48
100 °C O ₂ /Ar ^a	17.3	1.0	35.3	46.4	0.1	0.52
200 °C O ₂ /Ar ^a	14.8	2.0	36.5	46.9	0.1	0.46
300 °C O ₂ /Ar ^a	10.1	3.3	32.4	54.2	0.3	0.41

^aAr refers to annealing at 500 °C Ar after the O₂ step; ^bCu = (Cu^I + Cu^{II})

The Ga 2p_{3/2} peak was detected at 1118.5 eV (**Figure A2.4**), consistent with a +3 oxidation state.¹ The ratio of total copper (Cu^I + Cu^{II}) to Ga^{III} at the CuGaO₂ surface averaged 0.52 ± 0.08 for all samples. This could suggest formation of oxidized CuGa₂O₄ spinel at the surface, however, we note that no lattice bound Cu^{II} peaks were detected. Based on EDS results suggesting copper vacancies to be on the order of 4 ± 2% overall, the copper deficiency observed by XPS is believed to be due to concentration of copper vacancies defects at the surface.

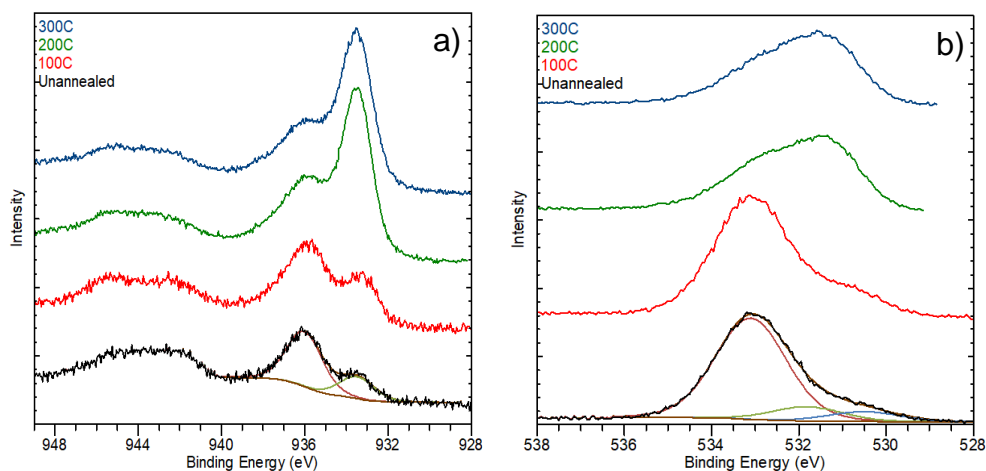


Figure 2.4: XPS data collected for CuGaO₂ films showing a) the Cu 2p_{3/2} region and b) the O 1s region as a function of annealing temperature under an O₂ atmosphere. Fitted lines are shown for the unannealed condition with peaks at 932.7 eV (green - Cu^I) and 935.3 eV (red - Cu^{II}) in the Cu 2p_{3/2} spectra and 530.5 eV (blue - lattice O), 531.8 eV (green - OH_{surf}), and 533.1 eV (red - H₂O_{surf}) in the O 1s spectra.

2.3.2 Electrochemistry - Electrochemical analysis of CuGaO₂ films was performed using cyclic voltammetry (CV) and electrochemical impedance spectroscopy (EIS) in acetonitrile (MeCN) solvent. In all cases, the CuGaO₂ films deposited on conductive FTO glass were used as the working electrode in a three-electrode setup with 0.1 M LiClO₄ electrolyte.

Figure 2.5 shows a comparison of CV data measured for films annealed at 100 °C O₂ and 300 °C O₂ followed by 500 °C Ar. Two observations of these data are readily evident. First, films annealed at 100 °C O₂ exhibited a small non-faradaic current (~5 μA) compared to 300 °C O₂ (~100 μA). A closer investigation revealed a dramatic increase in non-faradaic current as the annealing temperature jumped from 175 °C to 200 °C under O₂ atmosphere (**Figure A2.6**). This large change in background current is assigned to removal of the PEG polymer from the film structure, thus causing an increase in the internal surface area of the CuGaO₂ electrode. Second, films annealed under all conditions displayed a quasi-reversible redox feature with $E_{1/2} \sim 0.1$ V vs Fc⁺⁰ followed by an irreversible oxidation near 0.8 V. The quasi-reversible feature can be

seen most clearly for the 100 °C O₂ sample in **Figure 2.5a** (inset). However, as the annealing temperature was increased, the magnitude of the non-faradaic background made it more difficult to directly observe this feature. The second annealing step at 500 °C Ar was found to increase current associated with both redox features while the non-faradaic current remained nearly constant.

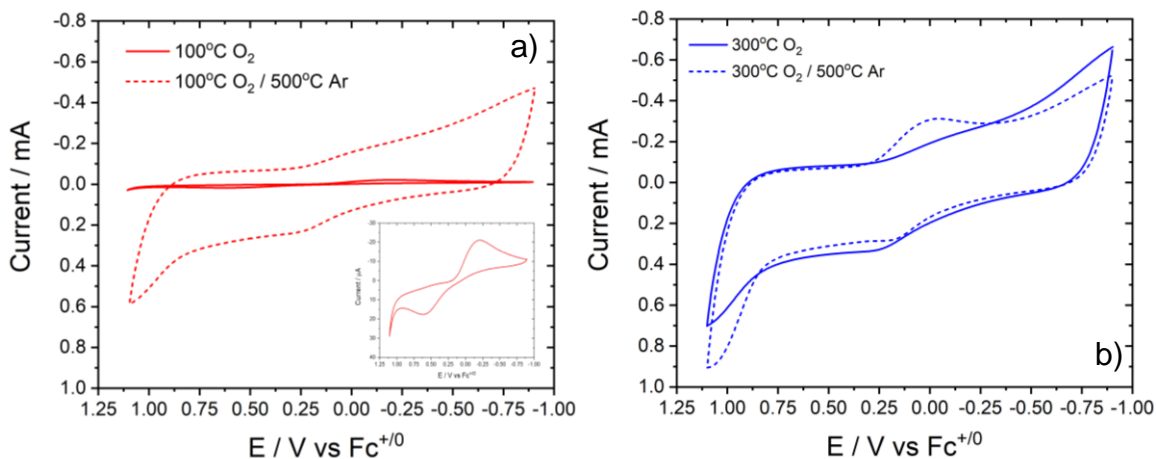


Figure 2.5: CV data of CuGaO₂ films measured in MeCN with 0.1 M LiClO₄ at a scan rate of 50 mV/s. a) 100 °C O₂ b) 300 °C O₂.

Electrochemical impedance spectroscopy was used to help further characterize the electrochemical properties of CuGaO₂ films. This technique is especially useful for differentiating multiple features such as double layer charging, charge transfer at the solid/solution interface, and charge transport through mesoporous films based on their frequency dependent responses.^{32–34} EIS data were collected over a range of applied potentials from -0.9 to 1.1 V vs Fc^{+/0} with a voltage modulation amplitude of 5 mV. The modulation frequency was varied from 250 kHz to 100 mHz. From this data, the diffusion resistance and CuGaO₂ film capacitance can be isolated and measured as a function of applied potential and annealing conditions.

Figure 2.6 shows a comparison of Nyquist and Bode-Phase plots obtained at an applied potential of 0 V as a function of annealing conditions. EIS data collected over all applied potentials and annealing conditions are shown in the Supporting Information. Nyquist plots display the imaginary (Z_{Im}) and real (Z_{Re}) components of the frequency dependent total impedance (Z) while the Bode-Phase plots display the phase angle defined by the expression $\theta = \tan^{-1}(Z_{\text{Im}}/Z_{\text{Re}})$. Multiple arcs can be observed in the Nyquist plots for any given annealing condition, corresponding with multiple peaks in the Bode-Phase plots. These arcs are indicative of distinct solid/liquid or solid/solid interfaces within the working electrode such as $\text{CuGaO}_2/\text{electrolyte}$ and $\text{FTO}/\text{CuGaO}_2$.

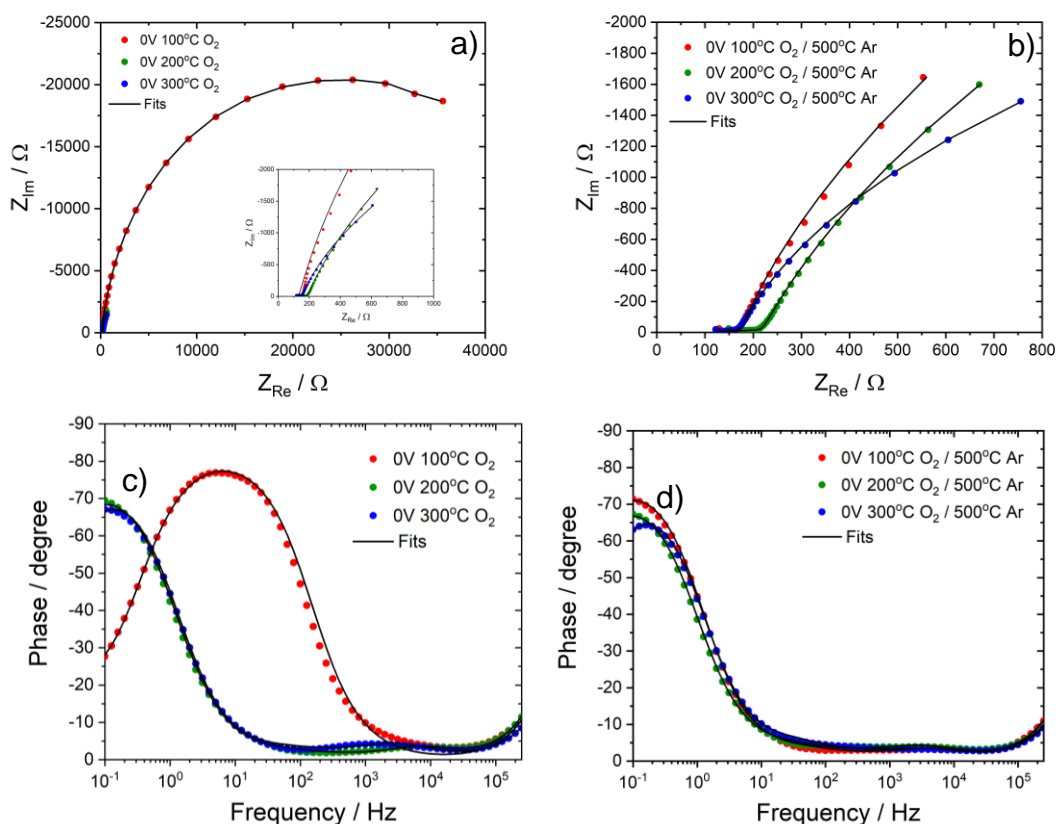


Figure 2.6: Nyquist (a-b) and Bode-Phase (c-d) plots for CuGaO₂ films measured in MeCN with 0.1 M LiClO₄. Applied potentials are referenced to ferrocene. Overlaid fits were generated using the equivalent circuit models shown in **Figure 2.7a** and **Figure A2.7**.

EIS data were fit to the equivalent circuit model shown in **Figure 2.7a** to extract quantitative values for the interfacial charge transfer resistances and capacitances. This model has been used previously to describe EIS data collected for mesoporous metal oxides films including CuGaO₂. The model features a transmission line circuit element developed by Bisquet to describe both the metal oxide/electrolyte interface (R_{film}/C_{film}) and charge diffusion (R_d) as distributed elements throughout the nanocrystalline film.^{33,34} A contact resistance (R_{con}) was also included to describe the resistance for charge transfer across the FTO/CuGaO₂ interface. The FTO/electrolyte interface was modeled as a single capacitor in parallel with the CuGaO₂/electrolyte interface since current may be passed through either surface. A series resistor (R_s) and a parallel R_0C_0

element were used to account for resistive losses in the external circuit and the interface of the electrolyte and reference/counter electrodes, respectively. Further details related to this model are given in the Supporting Information.

All capacitors were modeled as constant phase elements (CPE) to account for non-ideality using the expression $Z_{CPE} = 1/(Q(i\omega)^\beta)$ where Q has units of $F s^{\beta-1}$, ω is the angular modulation frequency ($2\pi f$), and β is an ideality factor which ranges from 1 to 0, with 1 representing an ideal capacitor. Ideality factors from the fitting analysis were found to be $\beta_{ref} = 0.95 \pm 0.03$, $\beta_{FTO} = 0.86 \pm 0.05$, and $\beta_{film} = 0.90 \pm 0.01$. Based on these values, the magnitude of Q was treated directly as the magnitude of the capacitance for each respective interface. All annealing conditions were found to fit the equivalent circuit shown in **Figure 2.7a** except for 100 °C O₂. This sample was best fit to a simplified model which substituted the transmission line circuit element with a simple parallel RC circuit to model the CuGaO₂/electrolyte interface, **Figure A2.7**. Summary tables of fitting constants for all measured data are given in the Supporting Information.

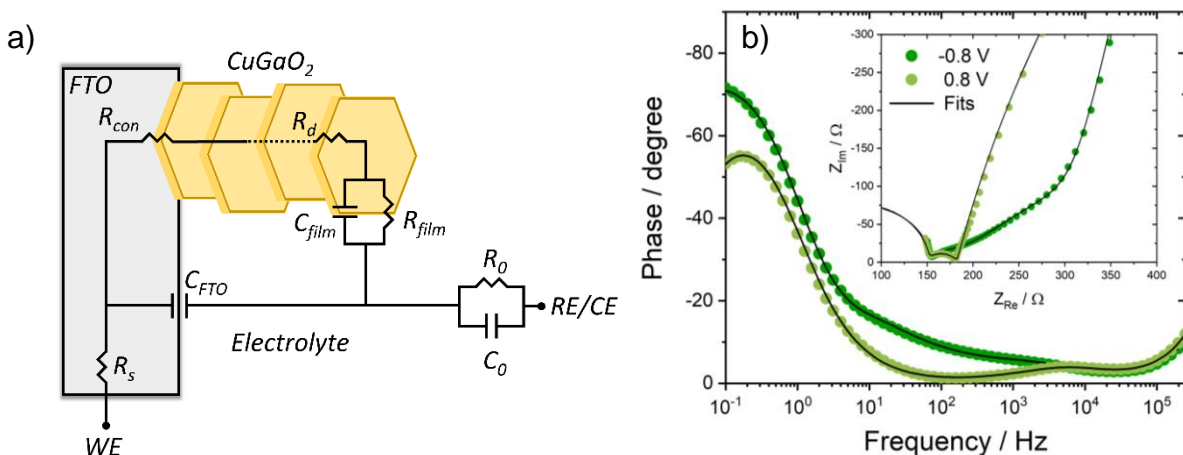


Figure 2.7: a) Equivalent circuit model used to fit EIS data. b) Bode-Phase and Nyquist (inset) plots for 200 °C O₂ film for two different applied potentials. The overlaid fits highlight the effect of R_d and R_{con} on the fitting analysis.

Figure 2.7b shows EIS data for the 200 °C O₂ annealing condition as a function of applied potential. Overlaid lines represent fits from the equivalent circuit which highlight certain aspects of the model at different frequency regions. The high frequency feature ($>10^5$ Hz) was modeled by the parallel R_0C_0 circuit element and was found to be invariant from sample to sample with $R_0 = 124 \pm 21 \Omega$ and $C_0 = 1.2 \pm 0.4$ nF. The mid frequency feature (10^1 - 10^4 Hz) was characteristic of R_d , R_{con} , and C_{FTO} . Here, the diffusion resistance R_d was modeled by the stretched tail feature shown in the Bode-Phase plot and linear region between 200-300 Ω in the Nyquist plot at -0.8 V. As the potential was stepped positive, the magnitude of R_d decreased as shown for the 0.8 V data. This decrease is consistent with CuGaO₂ behaving as a p-type material where the density of hole carriers was increased at more positive potentials, resulting in a smaller diffusion resistance.

Figure 2.8a shows a plot of R_d as a function of applied potential for different annealing conditions. Overall, the magnitude of R_d was similar across annealing conditions and decreased from $\sim 100 \Omega$ to $\sim 10 \Omega$ over a 1.8 V range in applied potential.

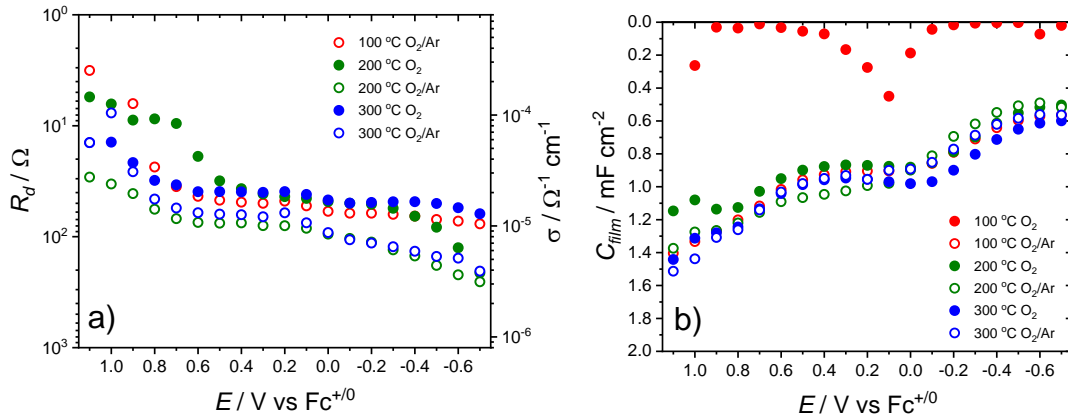


Figure 2.8: a) Diffusional resistance (R_d) and b) CuGaO₂/electrolyte interfacial capacitance (C_{film}) obtained from EIS modeling plotted as a function of applied potential. Capacitances were normalized to the 1 cm² geometric area of the CuGaO₂ films.

The parallel combination of R_{con} and C_{FTO} yielded a peak feature near 10^4 Hz in the Bode-Phase plot of **Figure 2.7**. This feature was difficult to directly observe when R_d was large but was more easily identified at positive applied potentials when R_d was smaller. The magnitude of the contact resistance was constant ($R_{con} = 23 \pm 7 \Omega$) and invariant with applied potential for all annealing conditions except for 100 °C O₂. This condition instead showed an extremely large $R_{con} > 10,000 \Omega$ which varied as a function of applied potential, **Figure A2.8**. This resistance resulted in the large peak feature observed in **Figure 2.6c** around 10^1 Hz. The large R_{con} values were assigned to a combination of incomplete sintering of nanocrystals to the FTO surface and the remaining presence of PEG inside the film pores. Poor contact at the CuGaO₂/FTO interface for 100 °C O₂ samples was also observed by delamination of the film after extended electrochemical experiments. The capacitance of the FTO/electrolyte interface was found to be constant over all samples with $C_{FTO} = 11 \pm 4 \mu\text{F cm}^{-2}$, consistent with other estimates from the literature.²⁵

Finally, the high frequency range ($>10^1$ Hz) was modeled by the CuGaO₂/electrolyte interface represented by the parallel $R_{film}C_{film}$ component of the transmission line circuit element. Due to the fact that no electroactive species were present in solution, R_{film} was always greater than 1000 Ω , **Figure A2.8**. A plot of C_{film} as a function of applied potential for different annealing conditions is shown in **Figure 2.8b**. For the 100 °C O₂ film, the capacitance displayed a peaked feature near 0.1 V vs Fc⁺⁰, similar to the quasi-reversible feature observed from cyclic voltammetry. All other annealing conditions displayed capacitance curves that were nearly identical to each other, showing a relatively large capacitance ($\sim 0.5 \text{ mF cm}^{-2}$) at the negative limit of applied potentials with a nominal increase to $\sim 1.5 \text{ mF cm}^{-2}$ at positive potentials. A small

peak in the capacitance was reproducibly observed near 0 V, again matching the observations from CV data.

2.4 Discussion

Delafossite CuGaO₂ nanocrystals were synthesized as hexagonal plates ~200 nm wide and ~40 nm thick. This anisotropic morphology is commonly observed for delafossites and is a consequence of their layered crystal structure.^{8,35} The large difference in width and thickness results in stacking of adjacent nanocrystals in the *c*-direction, as observed by SEM. Dispersion of nanocrystals into a thin film structure shows an enhancement of this stacking feature, indicating a preferred orientation of nanocrystals with respect to the FTO substrate. This is supported by SEM as well as two-dimensional XRD data where diffraction from the (003) and (006) planes were greatly enhanced upon thin film deposition. Furthermore, integration of the two-dimensional (006) peak with respect to the χ direction shows that nanocrystals were relatively flat (*i.e.* parallel with the FTO substrate) with signal intensity peaking at 90°.

It is possible that the polymer present in the film upon deposition could be directing the orientation of nanocrystals. Incorporation of polymer additives such as PEG, ethyl cellulose, and terpineol to nanocrystal suspensions is a standard method of controlling particle dispersion and increasing porosity for a wide range of mesoporous metal oxide films.^{5,7,36,37} However, based on the morphology of CuGaO₂ nanocrystals and the SEM images of powder samples which also show particle stacking, we believe the high orientation within thin films to be mostly controlled by the nanocrystalline dimensions. Indeed, other studies of CuGaO₂ films in the literature have also suggested oriented stacking from SEM^{10,11}, yet here we show this behavior more clearly via two-dimensional powder XRD measurements.

The electrochemistry of CuGaO₂ films can reveal a great deal of information about its capacitance and conductivity. These two terms are important in the context of solar energy conversion as CuGaO₂ is used as a hole transport layer in many solar cell architectures.^{1,2,6,7,10,11,14} The capacitance of the film in the region of the valence band is indicative of its ability to accept photogenerated holes while the conductivity is a measure of how quickly those holes may be transported to the external circuit. Capacitance measurements can also yield information about defect states present at the surface of CuGaO₂ nanocrystals.

In the present data, CV experiments revealed a quasi-reversible redox feature at 0.1 V vs Fc⁺⁰ which was supported by a capacitance peak near 0 V obtained from EIS data. A similar quasi-reversible feature in the range of 0 to 0.4 V vs SCE (-0.39 to 0.01 V vs Fc⁺⁰) has been observed for CuO supercapacitors and has been assigned to a Cu^{II}/Cu^I redox couple involving surface hydroxides.²⁹⁻³¹ We believe the quasi-reversible feature observed here for CuGaO₂ electrodes is also due to a Cu^{II}/Cu^I redox couple facilitated by Cu^{II} surface defects in contact with hydroxides at the nanocrystal surface. The presence of such defects is supported by XPS measurements where the largest fraction of Cu^{II} surface defects observed for annealed CuGaO₂ films was for the 100 °C O₂ condition. This condition also showed the most prominent quasi-reversible feature in CV measurements.

The conductivity of CuGaO₂ films could be estimated from the diffusion resistance (R_d) measured by EIS using the expression $\sigma = L/(R_d A(1-p))$ where σ is conductivity ($\Omega^{-1} \text{ cm}^{-1}$), L is the film thickness (cm), A is the geometric area of the film (cm^2), and p is porosity.^{25,33} **Figure 8a** shows conductivities calculated using $L = 4 \times 10^{-4} \text{ cm}$, $A = 1 \text{ cm}^2$, and the basic assumption of $p = 0.5$. The magnitude of conductivities for all samples (excluding 100 °C O₂) generally fell around $10^{-5} \Omega^{-1} \text{ cm}^{-1}$ and showed a mild increase as the applied potential was shifted in a positive

direction over a 1.8 V window. These data are in contrast with a study by Giménez which showed that the conductivity of CuGaO₂ films measured by EIS methods can be controlled with Mg-doping.²⁵ This method increases the density of holes (n_{h+}) and improves the conductivity according to the expression $\sigma = qn_{h+}\mu_{h+}$ where q is the elementary charge and μ_{h+} is the effective hole mobility through the mesoporous film. Mg-doped(1%) CuGaO₂ exhibited changes in conductivity over an order of magnitude from 10⁻⁶ to 10⁻⁵ Ω⁻¹ cm⁻¹ within a 1 V range of applied potentials whereas undoped CuGaO₂ displayed values in the range of 10⁻⁷ to 10⁻⁶ Ω⁻¹ cm⁻¹. Large changes in conductivity with applied potential is a clear indication of electrochemical oxidation of valence band states thus also increasing n_{h+} . In the present study, the increase in conductivity with positive applied potentials is consistent with CuGaO₂ being a p-type material, however, the small change in magnitude over a wide voltage range suggests that a large density of holes is already present within the oxide, thus limiting its capacity to increase n_{h+} further.

Hsu has also shown that chemical oxidation of CuGaO₂ films in the presence of UV/Ozone can result in higher n_{h+} and thus higher σ .¹ Here, the difference in conductivity between O₂ and Ar annealing steps also suggests that the hole density can be marginally affected by annealing conditions. XPS data shows a small reduction in the ratio of Cu^{II}:Cu^I peaks under Ar and in general, films annealed under O₂ are slightly more conductive than films annealed under the second Ar step. However, the effect is again relatively small with conductivity only changing by a factor of 3 for the 300 °C O₂ films measured at -0.4 V.

The high conductivity of CuGaO₂ films may also be aided by the preferred orientation of the nanocrystals on the FTO substrate. Stacking of nanocrystals could improve the degree of interparticle contacts, especially in such anisotropic structures, and lead to a reduction of carrier scattering at CuGaO₂/CuGaO₂ interfaces. This affect has been observed previously for mesoscale

NiO nanocrystals that also adopt hexagonal nanoplate structures.³⁸ Delafossites are known to possess large hole mobilities, however, mobility in the [100] and [010] directions (*i.e.* the copper plane) is much faster than in the [001] direction.²⁴ The orientation of nanocrystals in the CuGaO₂ film indicates that charge diffusion must occur in the [001] direction to be measured by the external circuit. Therefore, particle stacking may be helping to improve the effective hole mobility in this direction.

The origin of a large hole density in the present study is believed to be due to the presence of copper vacancies (V_{Cu}) and/or interstitial oxygen atoms (O_i) in the delafossite lattice.^{39,40} When copper vacancies are present, a hole must be introduced to compensate charge. Most likely, this hole takes the form of a Cu^{II} atom in the lattice. EDS results for CuGaO₂ films studied here revealed a copper deficiency on the order of $4 \pm 2\%$ overall while XPS results showed this deficiency to be on the order of $48 \pm 8\%$ at the surface. Copper vacancies have been observed previously in Mg-doped CuGaO₂ and have been estimated to have a low energy of formation for the delafossite structure based on theoretical calculations.^{2,41}

Interstitial oxygen atoms in the delafossite lattice could also play a role in p-type conductivity. Defects of this type are most prominent when the M^{III} atom is larger than Sc^{III} while smaller cations such as Al^{III} limit their formation due to a small *a*-lattice parameter.^{39,42–45} Unique phases incorporating interstitial oxygens have even been observed in the case of CuLaO_{2.66} and other lanthanides. The mild dependence of conductivity on O₂ annealing environment suggests that O_i defects may be present in CuGaO₂, however, a larger change in conductivity would be expected if they were the main defect type. Determining the percentage of such defects is also difficult due to the known presence of OH_{surf} and $\text{H}_2\text{O}_{\text{surf}}$ molecules which cloud the exact determination of oxygen content in the lattice via XPS.

Assuming only copper vacancies contribute to the density of holes, we can estimate $n_{h^+} \sim 10^{21}$ cm^{-3} based on the 4 % estimate for V_{Cu} , the density of copper atoms in CuGaO_2 , and assuming a 1:1 $V_{\text{Cu}}:h^+$ ratio. This value is on the order of electron densities found in n-type transparent conductive oxides such as $\text{Sn:In}_2\text{O}_3$ (ITO) and F:SnO_2 (FTO).⁴⁶ Indeed, copper delafossites such as CuAlO_2 and CuGaO_2 have been touted as p-type transparent conductive oxides themselves.^{28,47,48} Given the large hole density induced by copper vacancies, it is likely that the Fermi level of the present CuGaO_2 films is pinned with respect to the valence band edge. The flat-band potential (E_{fb}) of CuGaO_2 has been measured by Jobic and Odobel at 0.49 V vs SCE in water with 0.1 M LiClO_4 .⁶ Conversion of this value to the ferrocene reference in MeCN yields $E_{fb} = 0.10$ V vs $\text{Fc}^{+/0}$.⁴⁹ If the initial hole density were small, the capacitance of CuGaO_2 films would be expected to be large for $E > 0.1$ V and very small at $E < 0.1$ V (*i.e.* in the band gap). The present data instead shows a nearly uniform capacitance across all measured potentials as seen in both CV and EIS data. The capacitance at $E < 0.1$ V was also significant with $C_{film} \sim 0.5$ mF cm^{-2} . These data collectively point to a material which is more metallic than semiconductive with behavior that is similar to that of mesoporous transparent conductive oxides.

The origin of copper vacancies in CuGaO_2 nanocrystals is believed to be related to the synthetic conditions for their preparation. Multiple studies have shown that solution pH is one of the largest factors controlling the growth of CuGaO_2 nanocrystals. Reactions performed near the isoelectric point of pH 6.7 have been shown to make micron sized particles with smaller particles being produced at slightly acidic or basic conditions.²⁷ Here, we have used a pH 9 solution to synthesize our nanocrystals. Basic conditions are also known to produce CuO and Cu_2O side products which must be removed by washing with NH_4OH .^{8,10} The production of copper oxide side products in the synthesis could certainly account for a deficiency of copper atoms in

CuGaO₂. The NH₄OH washing step may also be responsible for inducing copper vacancies post-synthesis by leaching copper atoms from edge sites of the nanocrystals. Studies investigating the dependence of copper vacancies on synthetic procedure are currently underway in our laboratory.

In the context of solar-to-electrical and solar-to-fuel energy conversion strategies, CuGaO₂ represents one of only a handful of p-type metal oxides able to serve as hole transport layers.^{4,14} It is therefore critical to further understand its band structure, density of defect states, and hole diffusion for the successful development of these technologies. Understanding the energy and density of valence band states can better direct the synthesis of light absorbing molecules to achieve higher injection yields of photogenerated holes while understanding the exact nature of defect states in these materials can help decipher the effect they may have on electron-hole recombination at the CuGaO₂/solution interface or their role in hole transport through the material. Copper vacancies observed here was found to enhance the conductivity of CuGaO₂ films, however, they are also expected to act as recombination centers for photogenerated holes and electron donors, thus limiting solar energy conversion efficiency. For example, nickel vacancies in p-type NiO also display quasi-reversible redox features and passivation of these defects has led to improved device performance.^{36,50} Passivation of copper vacancies in CuGaO₂ may offer a means of achieving large hole conductivities without surface recombination. Likewise, the synthesis of smaller, isotropic CuGaO₂ nanocrystals that do not preferentially stack could remove the need for large hole densities by taking advantage of faster hole diffusion through Cu^I layers.

2.5 Conclusions

In this chapter the evidence for copper vacancies and Cu^{II} surface defects in CuGaO₂ nanocrystals was described. The density of holes induced by copper vacancies is estimated as an upper limit of $n_{h^+} \sim 10^{21} \text{ cm}^{-3}$. The impact of this high concentration of holes is manifested by large conductivities for hole diffusion measured by electrochemical impedance spectroscopy and the presence of Cu^{II} surface defects measured by x-ray photoelectron spectroscopy and cyclic voltammetry. Applications of CuGaO₂ nanocrystals as hole transport layers in a wide range of solar energy conversion strategies, including both solar-to-electrical and solar-to-fuel, is predicated on the ability to control this hole density. The origin of copper vacancies in the present study is proposed to be due to the basic pH conditions for the synthesis of CuGaO₂ nanocrystals which suggests the possibility of tuning the density of holes based on the synthetic conditions. Further understanding of the impact of synthesis and annealing on the hole density is described in Chapter 3.

2.6 Appendix

Table A2.1. EDS Measurements

Annealing Condition	Atomic%			Cu/Ga Ratio
	O	Cu	Ga	
100°C O ₂	59.3±1.4	19.9±0.7	20.8±0.7	0.96±0.05
200°C O ₂	49.9±0.2	24.3±0.1	25.72±0.3	0.95±0.01
300°C O ₂	49.0±0.5	24.9±0.3	25.8±0.3	0.97±0.02
100°C O ₂ /Ar	49.3±0.3	25.1±0.4	25.9±0.1	0.97±0.02
200°C O ₂ /Ar	49.0±0.4	24.8±0.1	26.13±0.3	0.95±0.01
300°C O ₂ /Ar	48.8±0.3	25.2±0.4	26.3±0.2	0.96±0.02
All Samples ^a	49.2±0.5	24.9±0.4	26.0±0.3	0.96±0.02

^aAll samples excluding 100°C O₂ because values are skewed by the presence of polymer in the sample

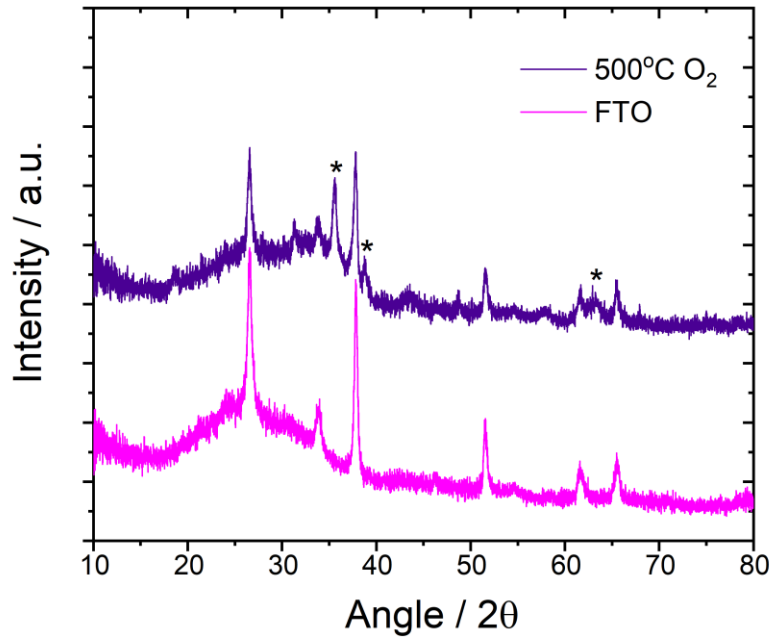


Figure A2.1: Powder XRD at 500 °C showing formation of CuGa₂O₄ spinel (*peaks)

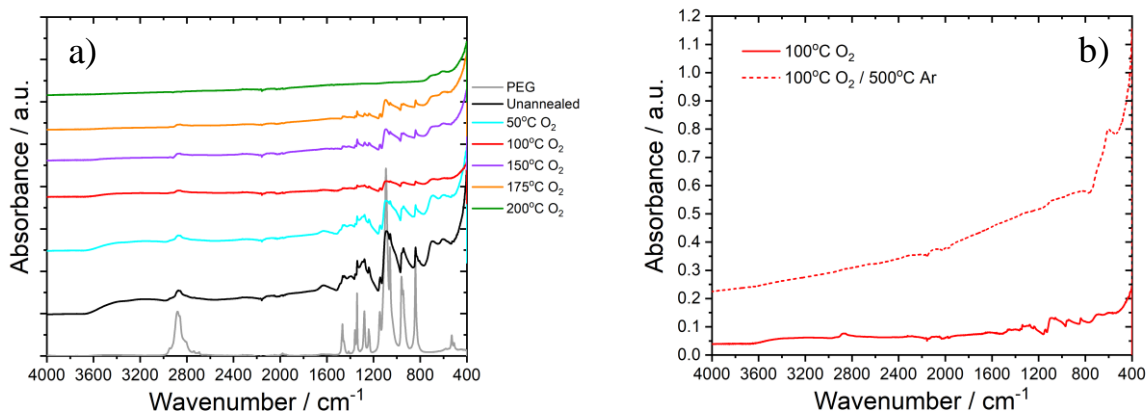


Figure A2.2. FTIR spectra of a) CuGaO_2 films annealed under O_2 from 50-200 °C and b) CuGaO_2 films annealed at 100°C under O_2 and with a subsequent Ar step.

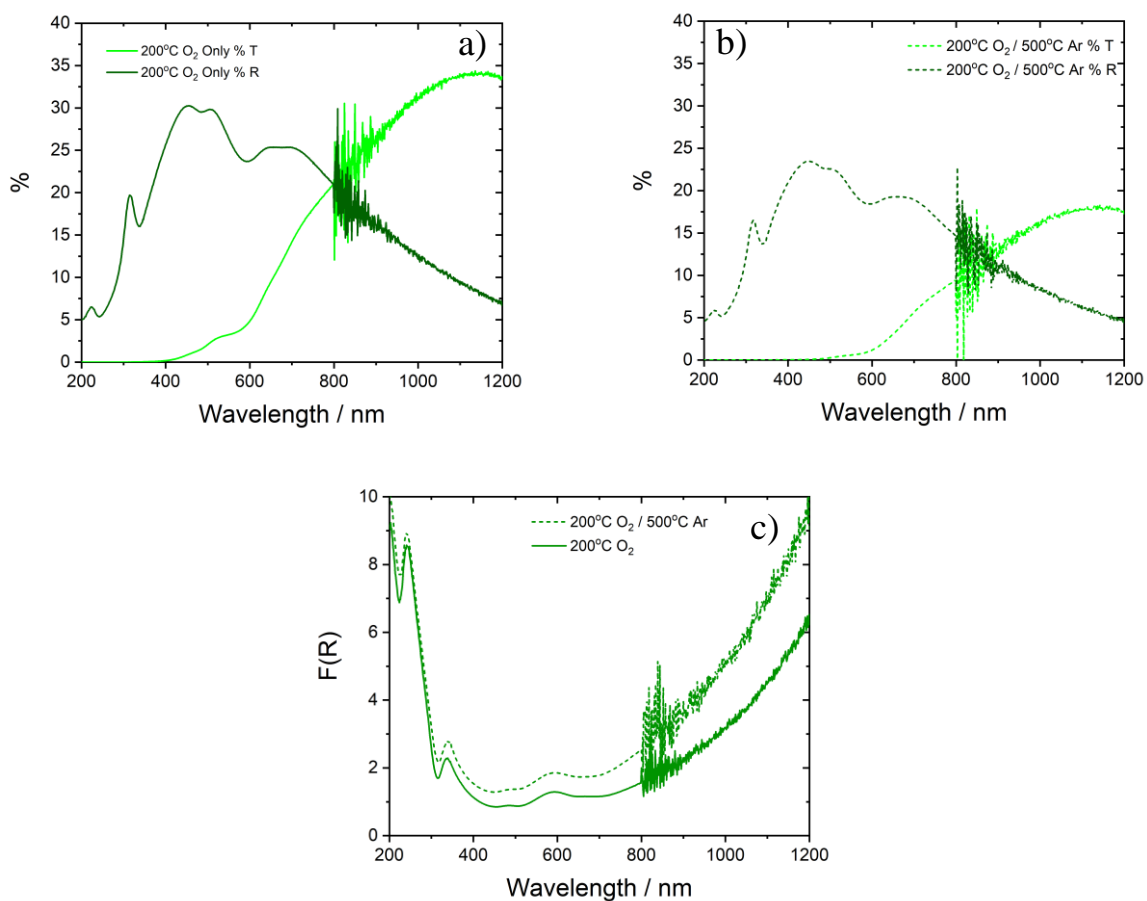


Figure A2.3. a) UV-Vis-NIR transmittance (T) and reflectance (R) data collected for CuGaO_2 films annealed at 200 °C/ O_2 and b) 200 °C/ O_2 followed by 500 °C/ Ar . c) Kubelka-Munk plot calculated from reflectance data.

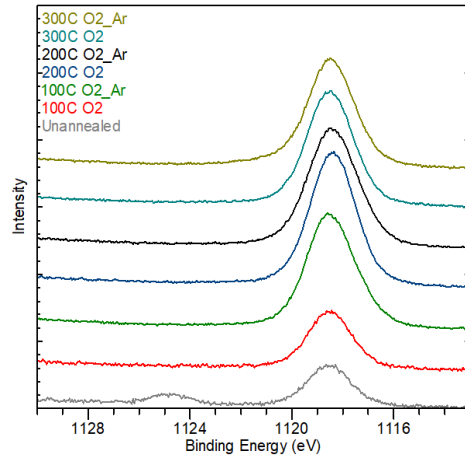


Figure A2.4. XPS of Ga2p_{3/2} peak over all annealing conditions

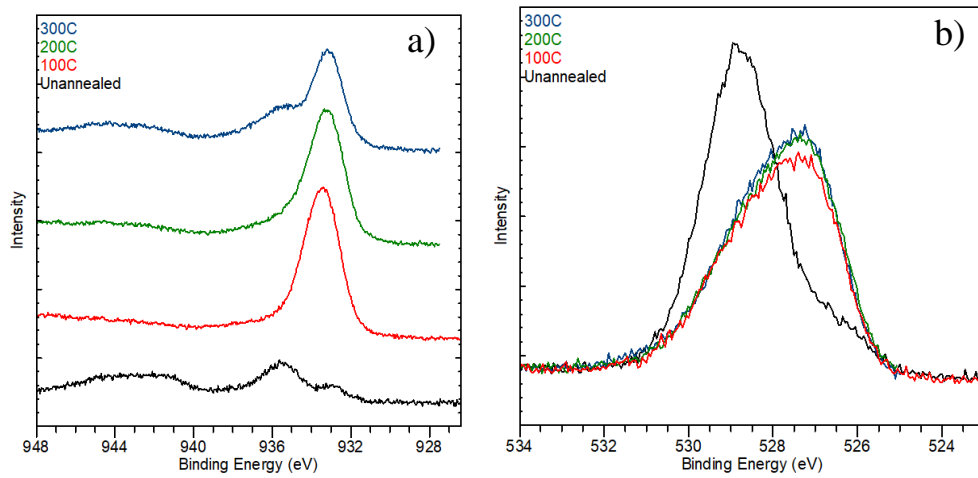


Figure A2.5. XPS of a) Cu 2p_{3/2} and b) O 1s peaks for Ar annealed films

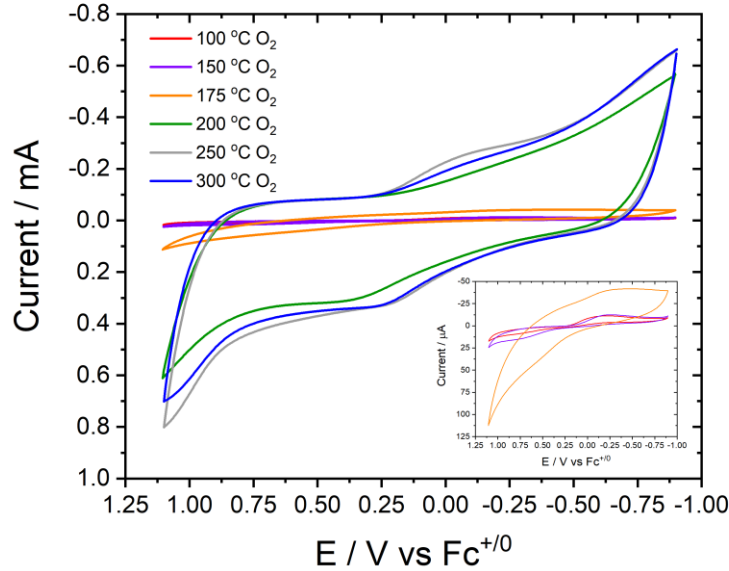


Figure A2.6. CV at all temperatures under O₂

EIS Fitting Analysis

Analysis of EIS data was achieved by fitting with the equivalent circuit model shown in Figure 2.7a and Figures A2.7. Equations for the impedance of particular circuit elements are presented below. All data and fitting constants are presented thereafter as figures and tables.

Resistors

$$Z_R = R$$

Capacitors (Constant Phase Elements)

$$Z_{CPE} = \frac{1}{Q(i\omega)^\beta}$$

Transmission Line

$$Z_{TL} = \left(\frac{R_d R_{film}}{1 + R_{film} C_{film} (i\omega)^\beta} \right)^{1/2} \coth \left[(R_{film} / R_d) (1 + R_{film} C_{film} (i\omega)^\beta)^{1/2} \right]$$

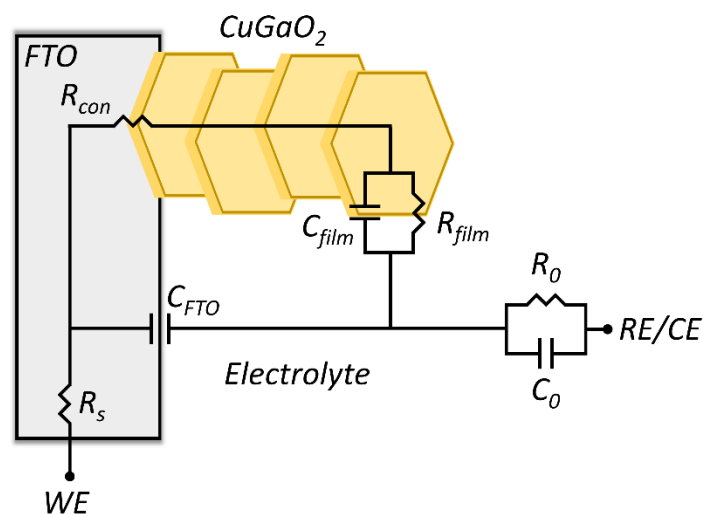


Figure A2.7. Equivalent circuit used to model 100 °C O₂ data.

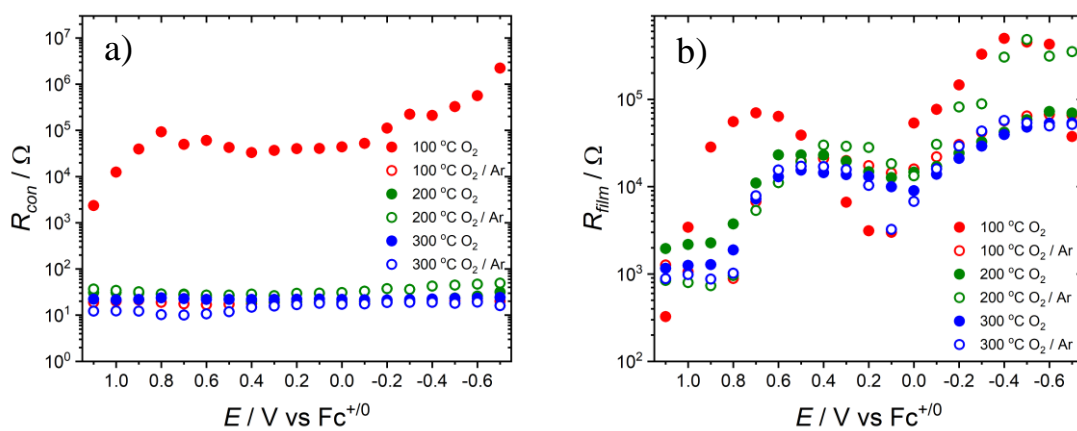


Figure A2.8: a) R_{con} measurements of films at each annealing condition and b) R_{film} measurements for films at each annealing condition.

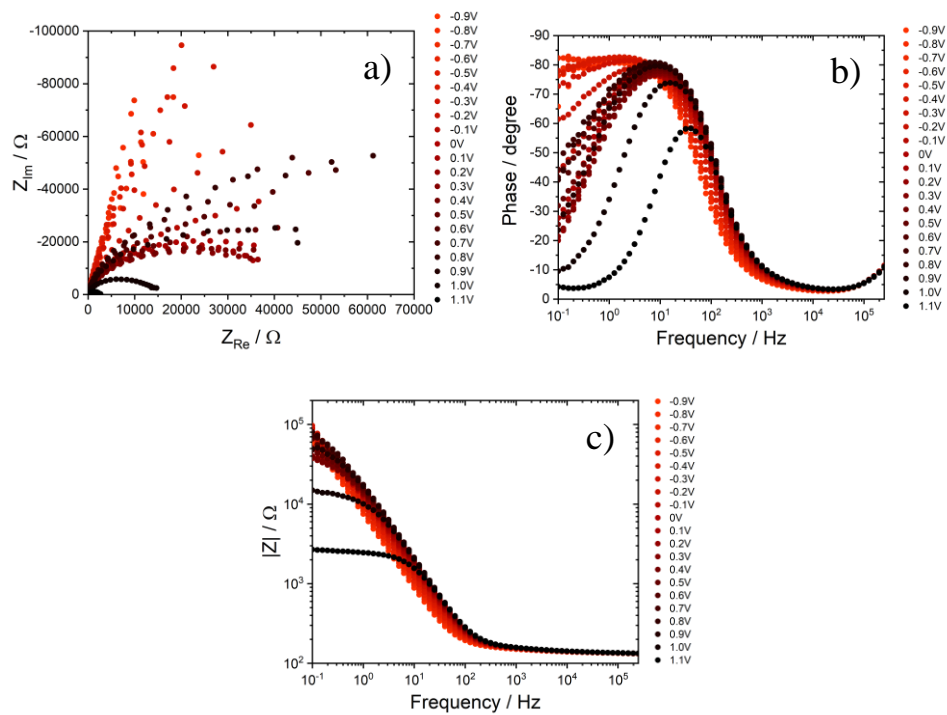


Figure A2.9: EIS data for a CuGaO₂ film annealed at 100 °C under O₂. a) Nyquist, b) Bode – Phase, c) Bode – Z

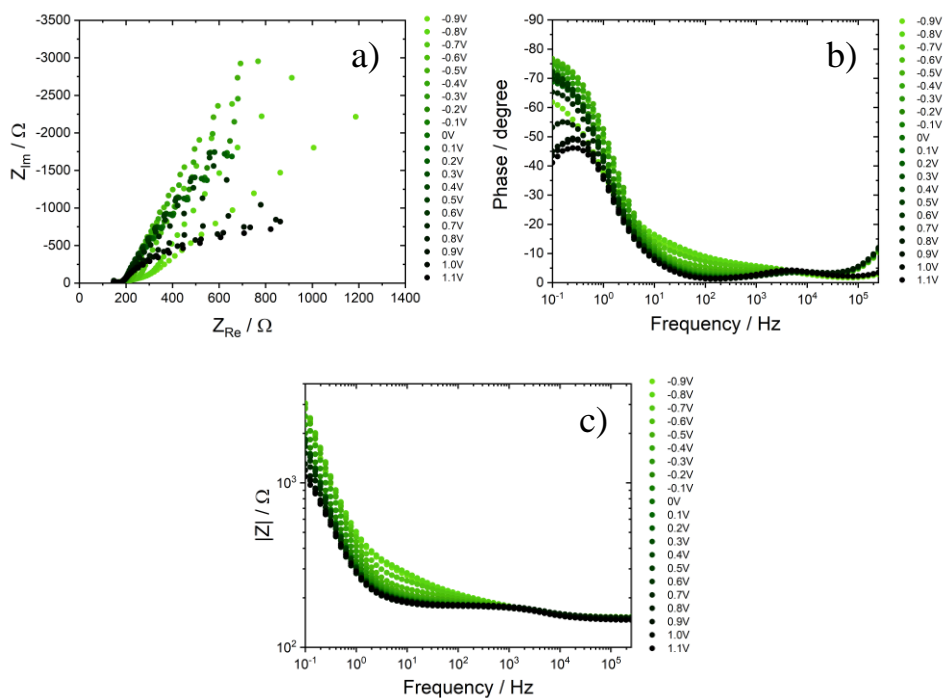


Figure A2.10: EIS data for a CuGaO₂ film annealed at 200 °C under O₂. a) Nyquist, b) Bode – Phase, c) Bode – Z

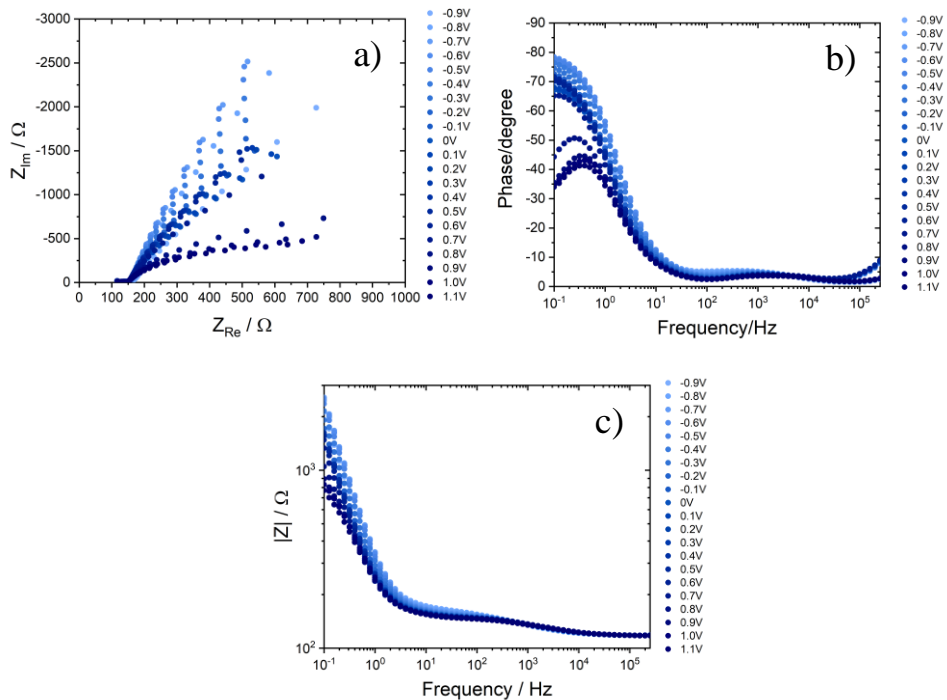


Figure A2.11: EIS data for a CuGaO₂ film annealed at 300 °C under O₂. a) Nyquist, b) Bode – Phase, c) Bode – Z

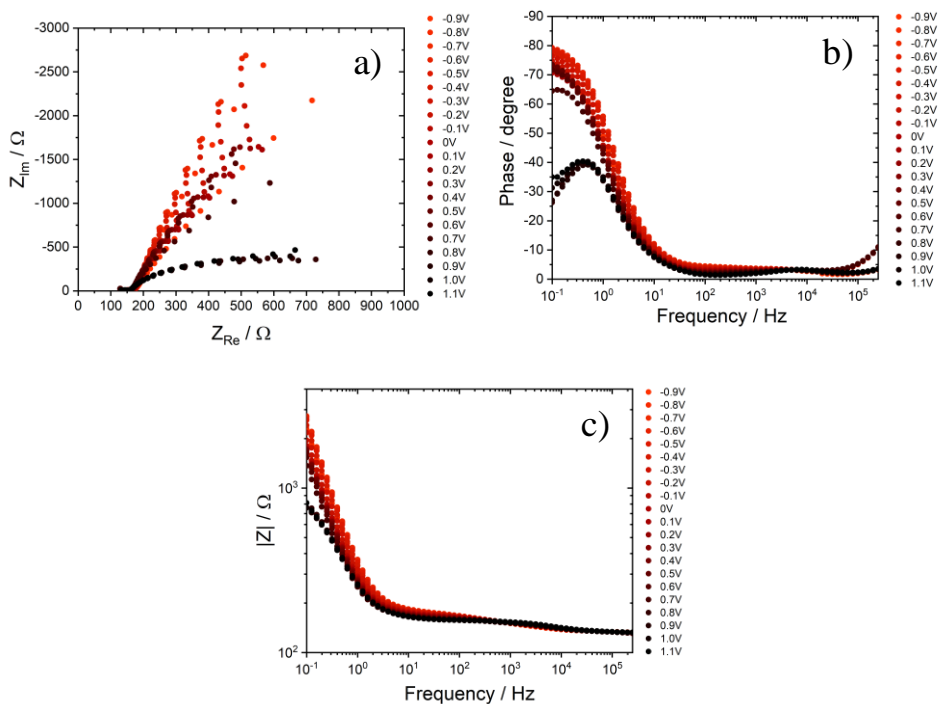


Figure A2.12: EIS data for a CuGaO₂ film annealed at 100 °C under O₂ followed by 500 °C under Ar. a) Nyquist, b) Bode – Phase, c) Bode – Z

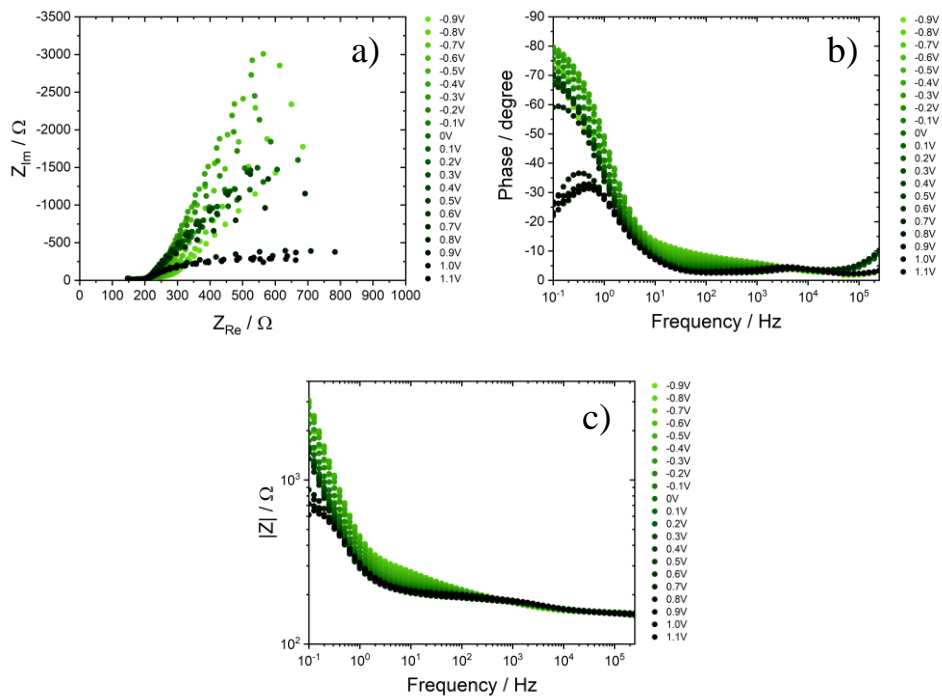


Figure A2.13: EIS data for a CuGaO₂ film annealed at 200 °C under O₂ followed by 500 °C under Ar. a) Nyquist, b) Bode – Phase, c) Bode – Z

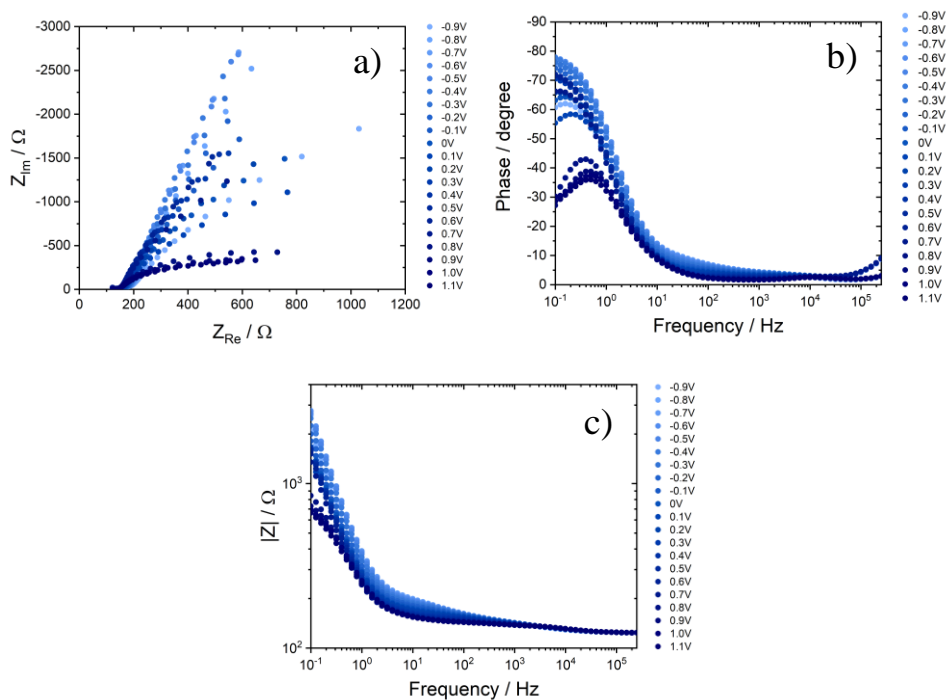


Figure A2.14: EIS data for a CuGaO₂ film annealed at 300 °C under O₂ followed by 500 °C under Ar. a) Nyquist, b) Bode – Phase, c) Bode – Z

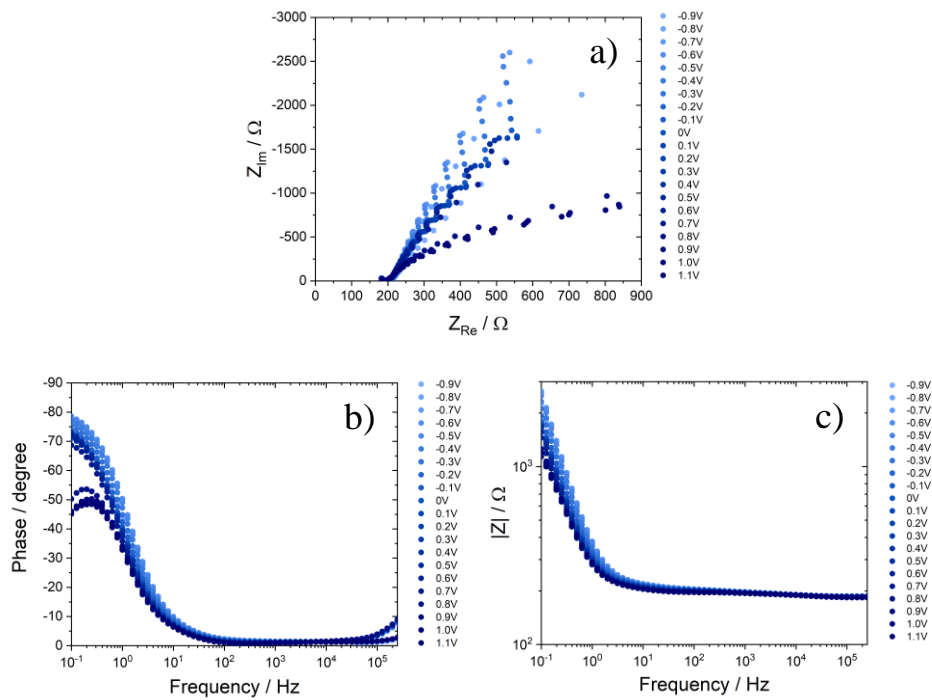


Figure A2.15: EIS data for a CuGaO₂ film annealed at 500 °C under Ar. a) Nyquist, b) Bode – Phase, c) Bode – Z

Table A2.2: Impedance fit for 100°C O₂ Annealed Film^a

Potential	R _s	R ₀	C ₀	β ₀	R _{con}	R _{film}	C _{film}	β _{film}	C _{FTO}	β _{FTO}
-0.9	1.00	129.60	1.03E-09	0.99	2.01E+05	8.45E+03	2.00E-05	0.90	2.41E-05	0.95
-0.8	1.00	129.60	1.03E-09	0.99	1.25E+07	1.55E+04	2.00E-05	0.90	2.23E-05	0.92
-0.7	1.00	129.60	1.03E-09	0.99	2.24E+06	3.74E+04	2.00E-05	1.00	2.09E-05	0.92
-0.6	1.00	129.60	1.03E-09	0.99	5.63E+05	4.26E+05	7.24E-05	1.00	1.95E-05	0.93
-0.5	1.00	129.60	1.03E-09	0.99	3.26E+05	4.51E+05	2.87E-06	1.00	1.65E-05	0.94
-0.4	1.00	129.60	1.03E-09	0.99	2.10E+05	4.98E+05	3.23E-06	1.00	1.46E-05	0.96
-0.3	1.00	129.60	1.03E-09	0.99	2.22E+05	3.27E+05	6.18E-06	1.00	1.47E-05	0.94
-0.2	1.00	129.60	1.03E-09	0.99	1.12E+05	1.46E+05	1.64E-05	1.00	1.51E-05	0.92
-0.1	1.00	129.60	1.03E-09	0.99	5.24E+04	7.67E+04	4.35E-05	0.85	1.42E-05	0.92
0	1.00	129.60	1.03E-09	0.99	4.37E+04	5.36E+04	1.87E-04	0.85	1.34E-05	0.93
0.1	1.00	129.60	1.03E-09	0.99	4.06E+04	3.00E+03	4.50E-04	0.85	1.27E-05	0.93
0.2	1.00	129.60	1.03E-09	0.99	4.03E+04	3.13E+03	2.75E-04	1.00	1.26E-05	0.91
0.3	1.00	129.60	1.03E-09	0.99	3.68E+04	6.64E+03	1.67E-04	1.00	1.22E-05	0.90
0.4	1.00	129.60	1.03E-09	0.99	3.32E+04	2.15E+04	7.15E-05	0.79	1.09E-05	0.92
0.5	1.00	129.60	1.03E-09	0.99	4.27E+04	3.89E+04	5.51E-05	0.80	1.11E-05	0.91
0.6	1.00	129.60	1.03E-09	0.99	6.07E+04	6.38E+04	3.31E-05	1.00	1.06E-05	0.91
0.7	1.00	129.60	1.03E-09	0.99	5.00E+04	7.00E+04	1.06E-05	0.90	8.74E-06	0.95
0.8	1.00	129.60	1.03E-09	0.99	9.33E+04	5.55E+04	3.59E-05	0.78	1.04E-05	0.91
0.9	1.00	129.60	1.03E-09	0.99	3.93E+04	2.83E+04	3.04E-05	0.63	9.05E-06	0.95
1	1.00	129.60	1.03E-09	0.99	1.25E+04	3.42E+03	2.63E-04	0.74	9.33E-06	0.95
1.1	1.00	129.60	1.03E-09	0.99	2.36E+03	3.26E+02	3.89E-03	0.80	1.01E-05	0.94

^aThis data set fit with impedance model shown in Figure A2.7; Units- R_s, R₀, R_{con}, R_{film} (Ω)
C₀, C_{film}, C_{FTO} (F)

Table A2.3: Impedance fit for 100°C O₂ / 500°C Ar Annealed Film^a

Potential	R _s	R ₀	C ₀	β ₀	R _{con}	R _D	R _{film}	C _{film}	β _{film}	C _{FTO}	β _{FTO}
-0.9	2.21	132.30	5.85E-10	0.96	15.92	113.40	1.59E+04	6.83E-04	0.93	2.85E-06	0.98
-0.8	1.77	133.40	2.00E-09	0.95	19.17	84.42	4.28E+04	5.87E-04	0.94	8.15E-06	0.89
-0.7	1.67	133.40	1.94E-09	0.95	20.04	76.55	6.59E+04	5.65E-04	0.95	9.86E-06	0.87
-0.6	1.62	133.40	1.98E-09	0.95	20.02	72.42	6.69E+04	5.73E-04	0.95	9.54E-06	0.87
-0.5	1.10	133.50	1.61E-09	0.96	20.26	69.98	6.43E+04	5.96E-04	0.94	1.04E-05	0.85
-0.4	0.97	133.40	1.55E-09	0.96	20.39	65.26	5.67E+04	6.42E-04	0.94	1.10E-05	0.84
-0.3	0.96	133.40	1.55E-09	0.96	20.08	62.87	4.20E+04	7.10E-04	0.93	1.12E-05	0.84
-0.2	0.96	133.40	1.47E-09	0.97	19.68	61.37	3.04E+04	7.91E-04	0.92	1.05E-05	0.84
-0.1	0.87	133.50	1.44E-09	0.97	19.11	61.45	2.19E+04	8.58E-04	0.92	9.03E-06	0.85
0	0.79	133.50	1.44E-09	0.97	18.82	59.02	1.59E+04	8.92E-04	0.92	9.13E-06	0.85
0.1	0.80	133.40	1.49E-09	0.97	18.9	52.74	1.44E+04	9.04E-04	0.92	8.94E-06	0.84
0.2	0.54	133.50	1.46E-09	0.97	19.3	47.83	1.74E+04	9.05E-04	0.92	9.55E-06	0.83
0.3	1.15	132.60	1.19E-09	0.98	18.63	50.00	1.98E+04	9.09E-04	0.92	7.31E-06	0.85
0.4	0.89	133.20	1.49E-09	0.97	17.57	48.88	2.09E+04	9.27E-04	0.93	5.56E-06	0.88
0.5	0.70	133.30	1.54E-09	0.96	17.18	46.90	1.97E+04	9.58E-04	0.93	5.55E-06	0.88
0.6	0.91	133.10	1.55E-09	0.96	16.87	43.30	1.55E+04	1.02E-03	0.92	4.95E-06	0.89
0.7	0.93	132.90	1.57E-09	0.96	17.57	35.39	6.74E+03	1.12E-03	0.91	6.60E-06	0.86
0.8	0.40	133.20	2.02E-09	0.86	18.99	23.56	8.88E+02	1.20E-03	0.89	1.07E-05	0.81
0.9	0.31	132.90	1.87E-09	0.86	21.34	6.32	8.76E+02	1.27E-03	0.85	1.40E-05	0.78
1	0.54	133.10	1.83E-09	0.87	20.13	0.55	1.06E+03	1.33E-03	0.81	7.22E-06	0.83
1.1	1.50	132.60	1.13E-09	0.91	19.02	3.18	1.27E+03	1.40E-03	0.79	3.49E-06	0.90

^aThis data set fit with impedance model shown in Figure 2.7a; Units- R_s, R₀, R_{con}, R_d, R_{film} (Ω)
C₀, C_{film}, C_{FTO} (F)

Table A2.4: Impedance fit for 200°C O₂ Annealed Film^a

Potential	R _s	R ₀	C ₀	β ₀	R _{con}	R _D	R _{film}	C _{film}	β _{film}	C _{FTO}	β _{FTO}
-0.9	1.00	125.00	3.81E-09	0.90	1.13E+03	3.07E+04	3.36E+04	5.59E-05	1.00	1.78E-05	0.86
-0.8	1.00	125.00	3.81E-09	0.90	7.67E+03	4.84E+04	3.90E+04	6.58E-05	1.00	2.29E-05	0.85
-0.7	1.00	125.00	3.81E-09	0.90	9.70E+03	5.08E+04	3.90E+04	7.73E-05	1.00	2.49E-05	0.84
-0.6	1.00	125.00	3.81E-09	0.90	8.73E+03	4.41E+04	3.52E+04	9.75E-05	1.00	2.87E-05	0.82
-0.5	1.00	125.00	3.81E-09	0.90	6.86E+03	3.47E+04	2.94E+04	1.17E-04	1.00	3.59E-05	0.78
-0.4	1.00	125.00	3.81E-09	0.90	5.34E+03	2.67E+04	2.32E+04	1.40E-04	1.00	4.59E-05	0.75
-0.3	1.00	125.00	3.81E-09	0.90	4.10E+03	2.08E+04	1.77E+04	1.76E-04	1.00	5.65E-05	0.72
-0.2	1.00	125.00	3.81E-09	0.90	3.08E+03	1.53E+04	1.29E+04	2.24E-04	1.00	6.52E-05	0.70
-0.1	1.00	125.00	3.81E-09	0.90	2.15E+03	1.13E+04	9.00E+03	2.99E-04	1.00	6.62E-05	0.70
0	1.00	125.00	3.81E-09	0.90	1.74E+03	8.52E+03	6.21E+03	3.85E-04	1.00	6.62E-05	0.69
0.1	1.00	125.00	3.81E-09	0.90	1.43E+03	6.81E+03	4.73E+03	5.32E-04	1.00	6.05E-05	0.70
0.2	1.00	125.00	3.81E-09	0.90	1.25E+03	5.65E+03	4.02E+03	7.94E-04	1.00	5.70E-05	0.70
0.3	1.00	125.00	3.81E-09	0.90	9.98E+02	4.66E+03	5.81E+03	1.27E-03	0.94	5.01E-05	0.71
0.4	1.00	125.00	3.81E-09	0.90	7.78E+02	2.87E+03	1.14E+04	1.52E-03	0.92	4.07E-05	0.74
0.5	1.00	125.00	3.81E-09	0.90	6.14E+02	1.68E+03	1.13E+04	1.67E-03	0.94	3.16E-05	0.77
0.6	1.00	125.00	2.49E-09	0.90	4.93E+02	1.03E+03	7.37E+03	1.80E-03	0.93	2.36E-05	0.80
0.7	1.00	125.00	1.89E-09	0.90	4.29E+02	6.95E+02	3.17E+03	1.95E-03	0.92	1.90E-05	0.82
0.8	1.00	125.00	1.33E-09	0.90	4.23E+02	6.16E+02	9.61E+02	2.17E-03	1.00	1.79E-05	0.83
0.9	1.00	125.00	1.28E-09	0.90	4.61E+02	6.86E+02	5.71E+02	2.11E-03	1.00	1.76E-05	0.83
1	1.00	125.00	1.28E-09	0.90	5.62E+02	7.67E+02	4.70E+02	2.17E-03	1.00	1.87E-05	0.82
1.1	1.00	125.00	1.28E-09	0.90	6.28E+02	8.57E+02	4.02E+02	2.53E-03	0.96	1.99E-05	0.81

^aThis data set fit with impedance model shown in Figure 2.7a; Units- R_s, R₀, R_{con}, R_d, R_{film} (Ω)
C₀, C_{film}, C_{FTO} (F)

Table A2.5: Impedance fit for 200°C O₂ / 500°C Ar Annealed Film^a

Potential	R _s	R ₀	C ₀	β ₀	R _{con}	R _D	R _{film}	C _{film}	β _{film}	C _{FTO}	β _{FTO}
-0.9	52.71	104.20	1.58E-07	0.61	47.27	283.2	1.48E+04	8.27E-04	0.92	3.55E-05	0.74
-0.8	55.39	101.50	1.48E-08	0.85	47.21	304.1	5.86E+04	6.33E-04	0.93	2.84E-05	0.76
-0.7	49.84	107.00	9.46E-09	0.87	49.02	255	3.50E+05	5.17E-04	0.94	3.13E-05	0.75
-0.6	61.34	95.11	8.14E-09	0.90	46.75	220.7	3.12E+05	4.91E-04	0.95	2.89E-05	0.75
-0.5	50.25	106.30	1.16E-08	0.86	44.81	181.6	4.84E+05	5.08E-04	0.95	2.80E-05	0.75
-0.4	57.92	98.26	8.35E-09	0.90	42.37	149.1	3.04E+05	5.49E-04	0.95	2.30E-05	0.76
-0.3	65.35	92.56	1.96E-08	0.85	36	131.3	8.86E+04	6.18E-04	0.94	1.43E-05	0.81
-0.2	63.43	92.25	7.45E-09	0.91	37.62	111.9	8.14E+04	6.94E-04	0.93	2.73E-05	0.73
-0.1	71.14	84.33	4.47E-09	0.96	33.09	103.8	3.06E+04	8.12E-04	0.91	1.28E-05	0.79
0	66.85	89.32	4.54E-09	0.95	30.95	94.75	1.33E+04	8.99E-04	0.90	1.14E-05	0.80
0.1	71.29	85.58	2.58E-09	0.99	29.82	83.94	1.83E+04	9.80E-04	0.88	1.10E-05	0.80
0.2	62.03	93.92	2.41E-09	0.98	29.58	79.65	2.81E+04	9.93E-04	0.89	1.41E-05	0.76
0.3	67.66	87.73	5.55E-09	0.94	26.3	79.51	2.90E+04	1.03E-03	0.89	8.76E-06	0.81
0.4	71.12	81.68	2.61E-09	1.00	28.41	75.11	2.99E+04	1.05E-03	0.89	1.14E-05	0.76
0.5	70.65	82.28	2.60E-09	1.00	27.27	75.55	1.93E+04	1.07E-03	0.90	8.78E-06	0.78
0.6	71.28	81.70	2.67E-09	1.00	27.03	74.39	1.11E+04	1.09E-03	0.90	7.01E-06	0.80
0.7	70.00	83.14	2.66E-09	1.00	27.55	68.74	5.33E+03	1.16E-03	0.89	6.13E-06	0.82
0.8	71.32	82.82	3.06E-09	0.90	28.85	56.59	9.62E+02	1.22E-03	0.87	7.72E-06	0.81
0.9	72.12	81.96	4.33E-09	0.88	31.94	40.88	7.34E+02	1.27E-03	0.84	1.04E-05	0.78
1	76.26	77.99	4.06E-09	0.89	34.22	33.49	7.97E+02	1.28E-03	0.81	1.07E-05	0.78
1.1	80.24	73.81	5.45E-09	0.88	36.74	29.06	8.42E+02	1.37E-03	0.78	1.26E-05	0.77

^aThis data set fit with impedance model shown in Figure 2.7a; Units- R_s, R₀, R_{con}, R_d, R_{film} (Ω)
C₀, C_{film}, C_{FTO} (F)

Table A2.6: Impedance fit for 300°C O₂ Annealed Film^a

Potential	R _s	R ₀	C ₀	β ₀	R _{con}	R _D	R _{film}	C _{film}	β _{film}	C _{FTO}	β _{FTO}
-0.9	0.02	118.70	4.25E-10	0.96	21.79	124.80	1.28E+04	7.31E-04	0.92	7.67E-06	0.91
-0.8	0.12	119.30	1.83E-09	0.94	25.14	69.40	3.61E+04	6.24E-04	0.93	1.17E-05	0.88
-0.7	0.25	119.10	1.78E-09	0.94	24.12	62.12	5.38E+04	5.99E-04	0.94	1.12E-05	0.88
-0.6	0.38	118.90	1.64E-09	0.95	23.16	54.80	5.31E+04	6.14E-04	0.94	1.01E-05	0.89
-0.5	0.91	118.00	1.25E-09	0.97	23.09	50.25	4.81E+04	6.50E-04	0.93	1.15E-05	0.87
-0.4	1.01	117.80	1.19E-09	0.97	22.45	48.41	3.95E+04	7.13E-04	0.93	1.14E-05	0.86
-0.3	4.10	114.80	1.45E-09	0.96	21.65	48.44	2.91E+04	8.03E-04	0.92	1.03E-05	0.87
-0.2	1.86	117.00	1.23E-09	0.97	21.26	49.14	2.10E+04	9.00E-04	0.91	8.89E-06	0.88
-0.1	4.02	114.90	1.26E-09	0.97	21.47	49.83	1.38E+04	9.69E-04	0.91	8.96E-06	0.87
0	6.42	112.40	1.26E-09	0.98	21.99	46.68	8.97E+03	9.81E-04	0.91	9.65E-06	0.86
0.1	7.34	111.60	1.45E-09	0.97	22.33	41.65	9.98E+03	9.70E-04	0.91	1.08E-05	0.86
0.2	6.24	112.70	1.48E-09	0.97	22.15	39.28	1.31E+04	9.55E-04	0.91	1.15E-05	0.85
0.3	6.06	112.80	1.48E-09	0.97	22.00	39.87	1.37E+04	9.47E-04	0.91	1.12E-05	0.85
0.4	7.28	111.60	1.53E-09	0.97	21.91	39.47	1.45E+04	9.58E-04	0.92	1.10E-05	0.85
0.5	9.13	109.70	1.54E-09	0.97	21.95	39.23	1.54E+04	9.88E-04	0.92	1.10E-05	0.85
0.6	13.48	105.20	1.42E-09	0.98	21.99	39.35	1.30E+04	1.04E-03	0.91	1.09E-05	0.85
0.7	15.56	103.20	8.26E-09	0.82	22.82	34.07	7.25E+03	1.13E-03	0.90	1.84E-05	0.79
0.8	8.74	109.10	6.63E-10	0.94	23.72	31.11	1.88E+03	1.24E-03	0.89	2.14E-05	0.77
0.9	0.40	118.70	4.46E-09	0.80	21.87	21.51	1.28E+03	1.28E-03	0.86	1.21E-05	0.85
1	1.97	116.00	1.18E-09	0.89	21.57	14.07	1.25E+03	1.31E-03	0.82	1.00E-05	0.85
1.1	0.00	117.50	2.98E-10	0.99	22.08	14.21	1.16E+03	1.44E-03	0.81	1.06E-05	0.85

^aThis data set fit with impedance model shown in Figure 2.7a; Units- R_s, R₀, R_{con}, R_d, R_{film} (Ω)
C₀, C_{film}, C_{FTO} (F)

Table A2.7: Impedance fit for 300°C O₂ / 500°C Ar Annealed Film^a

Potential	R _s	R ₀	C ₀	β ₀	R _{con}	R _D	R _{film}	C _{film}	β _{film}	C _{FTO}	β _{FTO}
-0.9	1.47	117.30	3.14E-10	0.98	21.46	125.60	1.28E+04	7.33E-04	0.92	6.67E-06	0.92
-0.8	1.51	124.00	1.54E-09	0.96	17.52	183.90	3.66E+04	5.96E-04	0.93	7.43E-06	0.89
-0.7	1.61	124.00	1.56E-09	0.96	16.01	204.60	5.16E+04	5.64E-04	0.94	4.57E-06	0.93
-0.6	0.75	124.80	1.67E-09	0.95	19.07	156.00	4.95E+04	5.61E-04	0.94	1.04E-05	0.85
-0.5	3.00	123.10	2.35E-09	0.93	17.96	150.60	5.36E+04	5.84E-04	0.94	7.68E-06	0.89
-0.4	4.65	121.20	2.14E-09	0.94	18.94	135.30	5.73E+04	6.21E-04	0.94	1.01E-05	0.86
-0.3	5.28	120.70	2.66E-09	0.92	18.96	123.30	4.34E+04	6.87E-04	0.93	1.15E-05	0.85
-0.2	2.15	123.50	2.04E-09	0.94	18.82	114.10	2.92E+04	7.71E-04	0.92	1.22E-05	0.84
-0.1	1.83	124.00	2.50E-09	0.92	17.54	106.50	1.60E+04	8.51E-04	0.92	1.00E-05	0.85
0	1.24	124.40	2.09E-09	0.94	17.16	91.85	6.76E+03	8.93E-04	0.91	1.09E-05	0.84
0.1	5.96	120.00	2.77E-09	0.92	18.00	75.00	3.24E+03	9.00E-04	0.92	1.00E-05	0.85
0.2	1.77	123.00	1.09E-09	0.98	16.90	60.99	1.03E+04	9.55E-04	0.88	1.00E-05	0.83
0.3	0.10	124.60	1.12E-09	0.98	15.71	66.12	1.57E+04	9.31E-04	0.91	1.01E-05	0.83
0.4	0.56	123.60	8.64E-10	0.99	14.77	63.39	1.70E+04	9.50E-04	0.91	1.00E-05	0.82
0.5	2.79	122.00	1.08E-09	0.98	11.90	62.64	1.72E+04	9.80E-04	0.92	3.08E-06	0.92
0.6	1.94	123.00	1.15E-09	0.98	10.61	60.80	1.55E+04	1.03E-03	0.92	1.84E-06	0.97
0.7	2.50	122.50	1.27E-09	0.97	10.03	55.11	7.88E+03	1.14E-03	0.91	1.41E-06	0.99
0.8	2.45	122.40	1.31E-09	0.89	10.29	45.84	1.02E+03	1.26E-03	0.89	1.74E-06	0.97
0.9	3.54	120.60	5.20E-10	0.95	12.18	25.99	8.72E+02	1.31E-03	0.84	4.47E-06	0.88
1	3.44	121.10	9.74E-10	0.91	12.30	7.66	9.84E+02	1.44E-03	0.76	3.58E-06	0.91
1.1	1.17	123.30	8.27E-10	0.92	12.24	14.20	8.86E+02	1.51E-03	0.77	3.97E-06	0.89

^aThis data set fit with impedance model shown in Figure 2.7a; Units- R_s, R₀, R_{con}, R_d, R_{film} (Ω)
C₀, C_{film}, C_{FTO} (F)

2.7 References

- (1) Wang, J.; Ibarra, V.; Barrera, D.; Xu, L.; Lee, Y.-J.; Hsu, J. W. P. Solution Synthesized P-Type Copper Gallium Oxide Nanoplates as Hole Transport Layer for Organic Photovoltaic Devices. *J. Phys. Chem. Lett.* **2015**, *6*, 1071–1075.
- (2) Renaud, A.; Cario, L.; Deniard, P.; Gautron, E.; Rocquefelte, X.; Pellegrin, Y.; Blart, E.; Odobel, F.; Jobic, S. Impact of Mg Doping on Performances of CuGaO₂ Based P-Type Dye-Sensitized Solar Cells. *J. Phys. Chem. C* **2014**, *118*, 54–59.
- (3) Creissen, C. E.; Warnan, J.; Reisner, E. Solar H₂ Generation in Water with a CuCrO₂ Photocathode Modified with an Organic Dye and Molecular Ni Catalyst. *Chem. Sci.* **2018**, *9*, 1439–1447.
- (4) Odobel, F.; Pellegrin, Y. Recent Advances in the Sensitization of Wide-Band-Gap Nanostructured P-Type Semiconductors. Photovoltaic and Photocatalytic Applications. *J. Phys. Chem. Lett.* **2013**, *4*, 2551–2564.
- (5) Xiong, D.; Xu, Z.; Zeng, X.; Zhang, W.; Chen, W.; Xu, X.; Wang, M.; Cheng, Y.-B. Hydrothermal Synthesis of Ultrasmall CuCrO₂ Nanocrystal Alternatives to NiO Nanoparticles in Efficient P-Type Dye-Sensitized Solar Cells. *J. Mater. Chem.* **2012**, *22*, 24760–24768.
- (6) Renaud, A.; Chavillon, B.; Pleux, L. L.; Pellegrin, Y.; Blart, E.; Boujtita, M.; Pauporté, T.; Cario, L.; Jobic, S.; Odobel, F. CuGaO₂: A Promising Alternative for NiO in P-Type Dye Solar Cells. *J. Mater. Chem.* **2012**, *22*, 14353–14356.
- (7) Yu, M.; Natu, G.; Ji, Z.; Wu, Y. P-Type Dye-Sensitized Solar Cells Based on Delafossite CuGaO₂ Nanoplates with Saturation Photovoltages Exceeding 460 mV. *J. Phys. Chem. Lett.* **2012**, *3*, 1074–1078.
- (8) Srinivasan, R.; Chavillon, B.; Doussier-Brochard, C.; Cario, L.; Paris, M.; Gautron, E.; Deniard, P.; Odobel, F.; Jobic, S. Tuning the Size and Color of the P-Type Wide Band Gap Delafossite Semiconductor CuGaO₂ with Ethylene Glycol Assisted Hydrothermal Synthesis. *J. Mater. Chem.* **2008**, *18*, 5647–5653.
- (9) Kumagai, H.; Sahara, G.; Maeda, K.; Higashi, M.; Abe, R.; Ishitani, O. Hybrid Photocathode Consisting of a CuGaO₂ P-Type Semiconductor and a Ru(II)–Re(I) Supramolecular Photocatalyst: Non-Biased Visible-Light-Driven CO₂ Reduction with Water Oxidation. *Chem. Sci.* **2017**, *8*, 4242–4249.
- (10) Xu, Z.; Xiong, D.; Wang, H.; Zhang, W.; Zeng, X.; Ming, L.; Chen, W.; Xu, X.; Cui, J.; Wang, M. Remarkable Photocurrent of P-Type Dye-Sensitized Solar Cell Achieved by Size Controlled CuGaO₂ Nanoplates. *J. Mater. Chem. A* **2014**, *2*, 2968–2976.
- (11) Zhang, H.; Wang, H.; Chen, W.; Jen, A. K.-Y. CuGaO₂: A Promising Inorganic Hole-Transporting Material for Highly Efficient and Stable Perovskite Solar Cells. *Adv. Mater.* **2017**, *29*, 1604984.
- (12) Xiong, D.; Zhang, W.; Zeng, X.; Xu, Z.; Chen, W.; Cui, J.; Wang, M.; Sun, L.; Cheng, Y.-B. Enhanced Performance of P-Type Dye-Sensitized Solar Cells Based on Ultrasmall Mg-Doped CuCrO₂ Nanocrystals. *ChemSusChem* **2013**, *6*, 1432–1437.

- (13) Wang, J.; Lee, Y.-J.; Hsu, J. W. P. Sub-10 Nm Copper Chromium Oxide Nanocrystals as a Solution Processed P-Type Hole Transport Layer for Organic Photovoltaics. *J. Mater. Chem. C* **2016**, *4*, 3607–3613.
- (14) Yu, M.; I. Draskovic, T.; Wu, Y. Cu(I)-Based Delafossite Compounds as Photocathodes in P-Type Dye-Sensitized Solar Cells. *Phys. Chem. Chem. Phys.* **2014**, *16*, 5026–5033.
- (15) Draskovic, T. I.; Yu, M.; Wu, Y. 2H-CuScO₂ Prepared by Low-Temperature Hydrothermal Methods and Post-Annealing Effects on Optical and Photoelectrochemical Properties. *Inorg. Chem.* **2015**, *54*, 5519–5526.
- (16) Lekse, J. W.; Underwood, M. K.; Lewis, J. P.; Matranga, C. Synthesis, Characterization, Electronic Structure, and Photocatalytic Behavior of CuGaO₂ and CuGa_{1-x}Fe_xO₂ (X = 0.05, 0.10, 0.15, 0.20) Delafossites. *J. Phys. Chem. C* **2012**, *116*, 1865–1872.
- (17) Jang, Y. J.; Park, Y. B.; Kim, H. E.; Choi, Y. H.; Choi, S. H.; Lee, J. S. Oxygen-Intercalated CuFeO₂ Photocathode Fabricated by Hybrid Microwave Annealing for Efficient Solar Hydrogen Production. *Chem. Mater.* **2016**, *28*, 6054–6061.
- (18) Prévot, M. S.; Jeanbourquin, X. A.; Bourée, W. S.; Abdi, F.; Friedrich, D.; van de Krol, R.; Guijarro, N.; Le Formal, F.; Sivula, K. Evaluating Charge Carrier Transport and Surface States in CuFeO₂ Photocathodes. *Chem. Mater.* **2017**, *29*, 4952–4962.
- (19) Gu, J.; Yan, Y.; Krizan, J. W.; Gibson, Q. D.; Detweiler, Z. M.; Cava, R. J.; Bocarsly, A. B. P-Type CuRhO₂ as a Self-Healing Photoelectrode for Water Reduction under Visible Light. *J. Am. Chem. Soc.* **2014**, *136*, 830–833.
- (20) Gu, J.; Wuttig, A.; Krizan, J. W.; Hu, Y.; Detweiler, Z. M.; Cava, R. J.; Bocarsly, A. B. Mg-Doped CuFeO₂ Photocathodes for Photoelectrochemical Reduction of Carbon Dioxide. *J. Phys. Chem. C* **2013**, *117*, 12415–12422.
- (21) Read, C. G.; Park, Y.; Choi, K.-S. Electrochemical Synthesis of P-Type CuFeO₂ Electrodes for Use in a Photoelectrochemical Cell. *J. Phys. Chem. Lett.* **2012**, *3*, 1872–1876.
- (22) Toyoda, K.; Hinogami, R.; Miyata, N.; Aizawa, M. Calculated Descriptors of Catalytic Activity for Water Electrolysis Anode: Application to Delafossite Oxides. *J. Phys. Chem. C* **2015**, *119*, 6495–6501.
- (23) Kawazoe, H.; Yasukawa, M.; Hyodo, H.; Kurita, M.; Yanagi, H.; Hosono, H. P-Type Electrical Conduction in Transparent Thin Films of CuAlO₂. *Nature* **1997**, *389*, 939–942.
- (24) Tate, J.; Ju, H. L.; Moon, J. C.; Zakutayev, A.; Richard, A. P.; Russell, J.; McIntyre, D. H. Origin of P-Type Conduction in Single-Crystal CuAlO₂. *Phys. Rev. B* **2009**, *80*, 165206.
- (25) Herraiz-Cardona, I.; Fabregat-Santiago, F.; Renaud, A.; Julián-López, B.; Odobel, F.; Cario, L.; Jobic, S.; Giménez, S. Hole Conductivity and Acceptor Density of P-Type CuGaO₂ Nanoparticles Determined by Impedance Spectroscopy: The Effect of Mg Doping. *Electrochimica Acta* **2013**, *113*, 570–574.
- (26) Sheets, W. C.; Mugnier, E.; Barnabé, A.; Marks, T. J.; Poepelmeier, K. R. Hydrothermal Synthesis of Delafossite-Type Oxides. *Chem. Mater.* **2006**, *18*, 7–20.

- (27) Yu, M.; Draskovic, T. I.; Wu, Y. Understanding the Crystallization Mechanism of Delafossite CuGaO₂ for Controlled Hydrothermal Synthesis of Nanoparticles and Nanoplates. *Inorg. Chem.* **2014**, *53*, 5845–5851.
- (28) Ueda, K.; Hase, T.; Yanagi, H.; Kawazoe, H.; Hosono, H.; Ohta, H.; Orita, M.; Hirano, M. Epitaxial Growth of Transparent P-Type Conducting CuGaO₂ Thin Films on Sapphire (001) Substrates by Pulsed Laser Deposition. *J. Appl. Phys.* **2001**, *89*, 1790–1793.
- (29) Wang, C.; Li, Q.; Wang, F.; Xia, G.; Liu, R.; Li, D.; Li, N.; Spendelow, J. S.; Wu, G. Morphology-Dependent Performance of CuO Anodes via Facile and Controllable Synthesis for Lithium-Ion Batteries. *ACS Appl. Mater. Interfaces* **2014**, *6*, 1243–1250.
- (30) Chen, K.; Song, S.; Li, K.; Xue, D. Water-Soluble Inorganic Salts with Ultrahigh Specific Capacitance: Crystallization Transformation Investigation of CuCl₂ Electrodes. *CrystEngComm* **2013**, *15*, 10367–10373.
- (31) Lu, Y.; Yan, H.; Qiu, K.; Cheng, J.; Wang, W.; Liu, X.; Tang, C.; Kim, J.-K.; Luo, Y. Hierarchical Porous CuO Nanostructures with Tunable Properties for High Performance Supercapacitors. *RSC Adv.* **2015**, *5*, 10773–10781.
- (32) Bard, A. J.; Faulkner, L. R. *Electrochemical Methods: Fundamentals and Applications*; Wiley: New York, 1980.
- (33) Fabregat-Santiago, F.; Garcia-Belmonte, G.; Bisquert, J.; Zaban, A.; Salvador, P. Decoupling of Transport, Charge Storage, and Interfacial Charge Transfer in the Nanocrystalline TiO₂/Electrolyte System by Impedance Methods. *J. Phys. Chem. B* **2002**, *106*, 334–339.
- (34) Bisquert, J. Theory of the Impedance of Electron Diffusion and Recombination in a Thin Layer. *J. Phys. Chem. B* **2002**, *106*, 325–333.
- (35) Shi, L.; Wang, F.; Wang, Y.; Wang, D.; Zhao, B.; Zhang, L.; Zhao, D.; Shen, D. Photoluminescence and Photocatalytic Properties of Rhombohedral CuGaO₂ Nanoplates. *Sci. Rep.* **2016**, *6*, 21135.
- (36) Flynn, C. J.; McCullough, S. M.; Oh, E.; Li, L.; Mercado, C. C.; Farnum, B. H.; Li, W.; Donley, C. L.; You, W.; Nozik, A. J. Site-Selective Passivation of Defects in NiO Solar Photocathodes by Targeted Atomic Deposition. *ACS Appl. Mater. Interfaces* **2016**, *8*, 4754–4761.
- (37) Meyer, G. J. Molecular Approaches to Solar Energy Conversion with Coordination Compounds Anchored to Semiconductor Surfaces. *Inorg. Chem.* **2005**, *44*, 6852–6864.
- (38) Flynn, C. J.; Oh, E. E.; McCullough, S. M.; Call, R. W.; Donley, C. L.; Lopez, R.; Cahoon, J. F. Hierarchically-Structured NiO Nanoplatelets as Mesoscale P-Type Photocathodes for Dye-Sensitized Solar Cells. *J. Phys. Chem. C* **2014**, *118*, 14177–14184.
- (39) Ingram, B. J.; Harder, B. J.; Hrabe, N. W.; Mason, T. O.; Poepelmeier, K. R. Transport and Defect Mechanisms in Cuprous Delafossites. 2. CuScO₂ and CuYO₂. *Chem. Mater.* **2004**, *16*, 5623–5629.
- (40) Robertson, J.; Clark, S. J. Limits to Doping in Oxides. *Phys. Rev. B* **2011**, *83*, 75205.

- (41) Scanlon, D. O.; Watson, G. W. Conductivity Limits in CuAlO₂ from Screened-Hybrid Density Functional Theory. *J. Phys. Chem. Lett.* **2010**, *1*, 3195–3199.
- (42) Isawa, K.; Yaegashi, Y.; Komatsu, M.; Nagano, M.; Sudo, S.; Karppinen, M.; Yamauchi, H. Synthesis of Delafossite-Derived Phases, RCuO_{2+δ} with R=Y, La, Pr, Nd, Sm, and Eu, and Observation of Spin-Gap-like Behavior. *Phys. Rev. B* **1997**, *56*, 3457–3466.
- (43) Cava, R. J.; Zandbergen, H. W.; Ramirez, A. P.; Takagi, H.; Chen, C. T.; Krajewski, J. J.; Peck, W. F.; Waszczak, J. V.; Meigs, G.; Roth, R. S. LaCuO_{2.5+x} and YCuO_{2.5+x} Delafossites: Materials with Triangular Cu^{2+δ} Planes. *J. Solid State Chem.* **1993**, *104*, 437–452.
- (44) Garlea, O.; Darie, C.; Bougerol, C.; Isnard, O.; Bordet, P. Structure of LaCuO_{2.66}: An Oxidized Delafossite Compound Containing Hole-Doped Kagome Planes of Cu²⁺ Cations. *Solid State Sci.* **2003**, *5*, 1095–1104.
- (45) Ingram, B. J.; González, G. B.; Mason, T. O.; Shahriari, D. Y.; Barnabè, A.; Ko, D.; Poepelmeier, K. R. Transport and Defect Mechanisms in Cuprous Delafossites. 1. Comparison of Hydrothermal and Standard Solid-State Synthesis in CuAlO₂. *Chem. Mater.* **2004**, *16*, 5616–5622.
- (46) Hamberg, I.; Granqvist, C. G. Evaporated Sn-doped In₂O₃ Films: Basic Optical Properties and Applications to Energy-efficient Windows. *J. Appl. Phys.* **1986**, *60*, R123–R160.
- (47) Han, M.; Jiang, K.; Zhang, J.; Yu, W.; Li, Y.; Hu, Z.; Chu, J. Structural, Electronic Band Transition and Optoelectronic Properties of Delafossite CuGa_{1-x}Cr_xO₂ (0 ≤ X ≤ 1) Solid Solution Films Grown by the Sol–gel Method. *J. Mater. Chem.* **2012**, *22*, 18463–18470.
- (48) Kawazoe, H.; Yasukawa, M.; Hyodo, H.; Kurita, M.; Yanagi, H.; Hosono, H. P-Type Electrical Conduction in Transparent Thin Films of CuAlO₂. *Nature* **1997**, *389*, 939–942.
- (49) Pavlishchuk, V. V.; Addison, A. W. Conversion Constants for Redox Potentials Measured versus Different Reference Electrodes in Acetonitrile Solutions at 25°C. *Inorganica Chim. Acta* **2000**, *298*, 97–102.
- (50) Flynn, C. J.; McCullough, S. M.; Li, L.; Donley, C. L.; Kanai, Y.; Cahoon, J. F. Passivation of Nickel Vacancy Defects in Nickel Oxide Solar Cells by Targeted Atomic Deposition of Boron. *J. Phys. Chem. C* **2016**, *120*, 16568–16576.

Chapter 3

Influence of Synthesis pH and Post-Synthetic Annealing on the Hole Density of CuGaO₂ Mesoporous Films

3.1 Introduction

The development of heterojunction solar cell devices, which separate the fundamental processes of light absorption and charge transport to convert sunlight to electricity, have emerged as an attractive alternative to traditional Si-based photovoltaics.¹ This is due to the cheaper and more earth abundant components, such as transition metal oxides, metal chalcogenides, polymers, and small molecules that can be used for light absorption and charge transport. The most studied heterojunction devices include dye-sensitized solar cells (DSSCs), perovskite solar cells (PSCs), quantum dot solar cells (QDSCs), and organic photovoltaics (OPVs). Transition metal oxides, in particular n-type oxides like TiO₂, have been studied significantly as mesoporous films to understand the processes through which electrons are transported to improve efficiencies of heterojunction devices.²⁻⁷ Most semiconductor metal oxides are n-type semiconductors due to their band structure, where the effective mass of electrons is small leading to fast charge transport through the conduction band. Holes must be transported through the valence band, which is usually based in localized oxygen 2p orbitals, leading to a large effective mass of holes.⁸ Late transition metal oxides, such as NiO and Cu₂O, have d orbitals that overlap with the O 2p orbitals, helping to delocalize charge, lower the effective mass of holes, and improve hole transport through the valence band.^{9,10} Like electron transport through n-type oxides, hole transport through p-type oxides will be affected by the types of defects present in the nanocrystals.

Delafossite CuGaO₂ has been a particularly interesting p-type metal oxide for exploration of hole transport. CuGaO₂ is a ternary metal oxide that has arisen as a potential alternative to NiO

as an HTM because of its more favorable band position to typical redox mediators, and its greater transparency to visible light.¹¹ CuGaO₂ has thus far been utilized in many different heterojunction devices including DSSCs^{12,13}, PSCs^{14–16}, OPVs¹⁷, and even as a scaffold for photocatalytic devices.¹⁸ The crystal structure of CuGaO₂ consists of Cu^I atoms linearly coordinated to Ga-O octahedra, giving nanocrystalline CuGaO₂ its typical form of hexagonal plates, due to its anisotropic crystal structure. The hydrothermal synthesis of CuGaO₂ has been previously shown to be affected by synthesis pH, which can alter the nanocrystalline structure.¹⁹ This nanocrystalline structure is almost certainly related to charge transport through nanocrystalline films and needs to be investigated further.

A common component of mesoporous thin film formation is high temperature annealing and this step can have several purposes. Synthesis of metal oxides from hydroxide decomposition can be achieved from high temperature annealing.^{20–23} This step can also sinter particles together to induce better contact between nanoparticles²⁴, as well as create the porous network of the film by the oxidized/pyrolyzed polymer.²⁵ Metal oxide nanocrystals can also have defects intrinsic to their structures, and these defects can be remediated or enhanced by annealing under different environments. Typically, high temperature annealing is done in atmospheres of either air, oxygen, or Ar. For n-type metal oxides, which typically have oxygen vacancy or interstitial metal atom defects, annealing under air or oxygen can remediate those defects.²⁶ p-Type defects consist of metal vacancies and oxygen interstitials, implying that annealing under oxidizing conditions can increase the number of defects in the structure. Under a reducing environment, such as H₂, it is possible these defects could be remediated.

In a previous study we explored CuGaO₂ nanocrystals specifically synthesized at pH 9 and annealed at different temperatures under an O₂ environment. In this study we found that all thin

films studied, regardless of temperature, exhibited high conductivity, consistent with that of a doped metal oxide. While this is practical for some type of heterojunction solar cell designs that require thin HTMs, such as OPVs, the high level of defects could significantly contribute to recombination events, causing loss of photocurrent in devices.^{12,13,27} We assigned these defects as copper vacancies, perhaps due to the pH at which the particles were synthesized. However, this raised the question of how do we control these defects, and can they be tailored for versatility in heterojunction devices?

In this chapter we study the synthesis of CuGaO_2 at pH 5 and 9, which resulted in changes in the morphology of the nanocrystals. These nanocrystals were then subjected to annealing under O_2 , Ar, and H_2 environments to assess the contribution of annealing atmosphere on electrochemical behavior. We find that pH 9 has similar electrochemistry under O_2 and Ar environments, revealing large hole densities and metallic behavior. However, H_2 shows a decrease in hole density introduces some semiconductive behavior in the electrochemistry. pH 5 nanocrystalline films exhibited semiconductive behavior under all annealing conditions, with controllable changes to the chemical capacitance of the films. Cyclic voltammetry (CV) and electrochemical impedance spectroscopy (EIS) were used to understand these changes in chemical capacitance.

3.2 Experimental

3.2.1 *CuGaO₂ Nanocrystal Synthesis* CuGaO_2 was synthesized using a previously reported procedure.²⁸ Briefly, 5 mmol of copper (II) nitrate ($\text{Cu}(\text{NO}_3)_2 \cdot x\text{H}_2\text{O}$, Millipore Sigma, 99.999%) and gallium (III) nitrate ($\text{Ga}(\text{NO}_3)_3 \cdot x\text{H}_2\text{O}$, Millipore Sigma, 99.9%) were dissolved in 15 mL of mill-Q water. Solution was cooled on an ice bath, then 5 mL of ethylene glycol

added, followed by titration of 2.5 M KOH to reach synthesis pH. Particles were synthesized at pH 5 (~5.5 mL of KOH) and pH 9 (~8 mL of KOH). After stirring for 1 hour, solution was transferred to Teflon-lined autoclave (Parr) and heated at 190 °C for 24 hours. Particles were then removed from autoclave and washed with dilute ammonium hydroxide (NH₄OH, stock 28 vol%, BDH) followed by centrifugation, to remove any Cu₂O side product that formed during the synthesis. This was repeated 3 times. Particles were then dried from acetone in a vacuum oven overnight.

3.2.2 Mesoporous Film Preparation CuGaO₂ powder was made into paste by adding CuGaO₂ to pH 1 water. Different paste weights were required for pH 5 and pH 9 CuGaO₂ due to the differences in particle size. For pH 9, a 15 wt% paste was made (typically 0.5 g was added to 3.3 mL of water) and for pH 5 a 25 wt% paste was made (typically 0.5 g was added to 2 mL of water). Poly(ethylene glycol) (PEG, MW 20,000, Millipore Sigma) was used for film porosity, and was added to the mixture at half the weight of the metal oxide added (7.5% for pH 9 and 12.5% for pH 5). The paste was then sonicated using an ultrasonication horn, as well as in a sonicator bath to homogenize the mixture. Paste was constantly stirred on a stir plate until films were made. CuGaO₂ mesoporous films were prepared by doctor blading pastes on to conductive FTO glass (F:SnO₂, 15 Ω/cm², Hartford Glass Inc.). Films were then annealed under O₂ (99.999%, Airgas), Ar (99.999%, Airgas), or H₂/N₂ (5% H₂, Airgas) in a tube furnace (Lindberg M Blue). The annealing was achieved via a 30-minute temperature ramp to 350 °C, maintained at 350 °C for 30 minutes, and then cooled back down to room temperature, all while maintaining flow of the annealing gas (400 cm³/min).

3.2.3 Characterization Powder X-Ray Diffraction (PXRD) was performed to assess particle crystallinity using a Bruker D8 Discover diffractometer (Cu Kα source) with a Vantec 2000 two-

dimensional area detector. UV-Vis-near IR transmittance and reflectance spectra were collected using a Cary 5000 spectrophotometer with an integrating sphere accessory. Reflectance data was converted using Kubelka-Munk equation $F(R) = \frac{(1-R)^2}{2R}$. Scanning electron microscopy (SEM) of the CuGaO₂ powders was performed using a Jeol JSM-7000F field emission scanning electron microscope. Surface area of the films was estimated by dye-loading of P1 dye using a 300 μM solution of the dye in acetonitrile. Films were soaked overnight, then removed from the dye solution and rinsed with acetonitrile to remove unbound dye. Because of the large amount of light scatter from the films due to particle size, dye was de-loaded from the films and measured in solution to estimate dye loading. The dye was de-loaded by soaking the film briefly in 2 mL of 0.1 M KOH in 1:1 MeCN:H₂O. The addition of base caused a color change in the dye, and titration studies were performed to assess the stability of the dye conversion. This titration, and the concentration curve used to calculate the extinction coefficient for the new peak are reported in the appendix of this chapter. The absorbance of the solution was measure using a Cary 8454 spectrophotometer. The surface area of the film was calculated by approximating a spherical footprint of the P1 dye and calculating an area from the number of molecules measured from UV-Vis.

3.2.4 Electrochemical Analysis In order to perform electrochemical experiments, all films were cut in 3.5 x 1 cm² rectangles with exposed CuGaO₂ mesoporous film that was 1 x 1 cm². Cyclic voltammetry (CV) experiments were performed with a Gamry 1010E potentiostat. Data were collected using a three-electrode setup where the working electrode was the CuGaO₂ film on FTO, the counter electrode was Pt mesh, and the reference was an aqueous Ag/AgCl electrode (satd. KCl). All experimenters were performed in acetonitrile (MeCN, BDH) with 0.1 M LiClO₄ (99.99%, Millipore Sigma) electrolyte at a scan rate of 50 mV/s unless otherwise

indicated. All reference potentials were calibrated before and after experiments using ferrocene ($\text{Fc}^{+/0}$). The $E_{1/2}(\text{Fc}^{+/0})$ was consistently measured to be 0.4 V vs Ag/AgCl in MeCN with 0.1 M LiClO_4 . This value was used to adjust all potentials to the ferrocene reference. Electrochemical impedance spectroscopy (EIS) was performed using the same potentiostat and three-electrode cell setup as the CV experiments. Data was collected over the potential range -0.9 to 1.1 V vs $\text{Fc}^{+/0}$, with a frequency range of 15000 – 0.1 Hz with 0.1 V steps and a modulation potential of 10 mV. EIS and CV experiments were also performed in 0.05 M I^-/I_3^- with 0.1 M LiClO_4 as a redox mediator to see if the contribution of defects in the CuGaO_2 films changed their ability to oxidize and reduce a redox active electrolyte.

3.3 Results

CuGaO_2 nanocrystals were synthesized using a hydrothermal preparation method previously reported.^{13,28} Powder XRD was collected for the nanocrystalline powders and films after annealing. The powders show no residual Cu_2O side product that is typically produced in the reaction, which is washed away with NH_4OH after the synthesis. At pH 5 and pH 9 the 3R-phase of CuGaO_2 is synthesized, which is the predominant phase observed for CuGaO_2 . As shown previously, there is a preferred orientation for the nanocrystals in the films compared to the powders because of the anisotropic, plate-like morphology of the nanocrystals. When the nanocrystals are spread as films there is enhancement of the (003) and (006) peaks associated with the (00 l) direction of the nanocrystal (**Figure 3.1**). The ratio of the (006)/(012) peak for pH 5 CuGaO_2 is 2.04 and for pH 9 CuGaO_2 is 1.92, compared to the powder XRD which had a (006)/(012) ratio of 0.49 and 0.5 for pH 5 and pH 9 CuGaO_2 , respectively. This indicates that the preferred orientation for each particle type is similar, but slightly higher for the pH 5 particles.

Annealing conditions did not induce the formation of any other side products, such as Cu^0 metal, CuO , or CuGa_2O_4 (**Figure A3.1**).

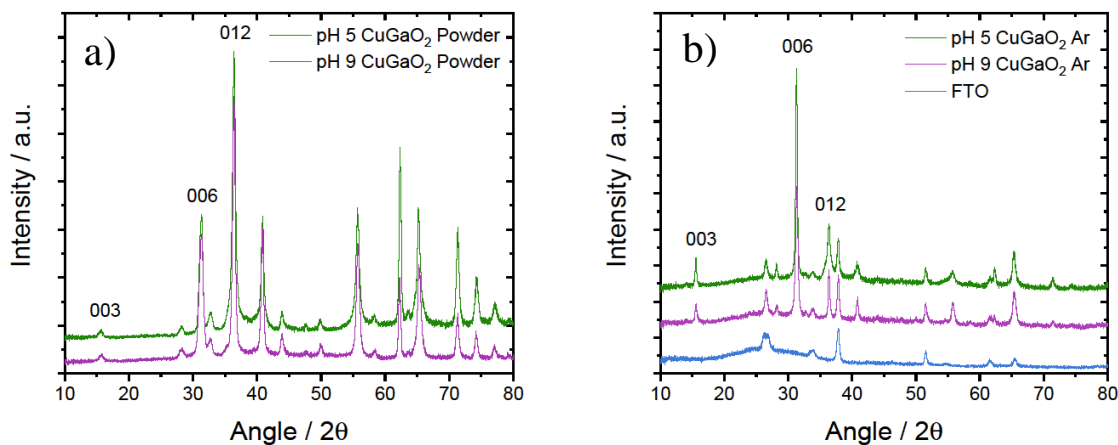


Figure 3.1: Powder XRD of a) pH 5 and pH 9 powders and b) pH 5 and pH 9 nanocrystals cast as mesoporous films.

SEM of the CuGaO_2 powders shows the same general nanocrystalline morphology, which consists of hexagonal plates, for pH 5 and pH 9 particles, but with drastic differences in size (**Figure 3.2**). pH 9 CuGaO_2 consisted of particles that averaged 100-200 nm in width and 40 nm in height, while pH 5 showed very large plates anywhere from 500 nm to 2 μm in width and only 25-50 nm thick. With pH 5 there is also a significant amount of particle breakage, due to the anisotropic nature of the particles. Given the difference in aspect ratio between pH 9 and pH 5 (5 and 40, respectively), the breakage of the pH 5 particles is not surprising. The slightly higher orientation preference for pH 5 is also not surprising given the significantly larger plate size.

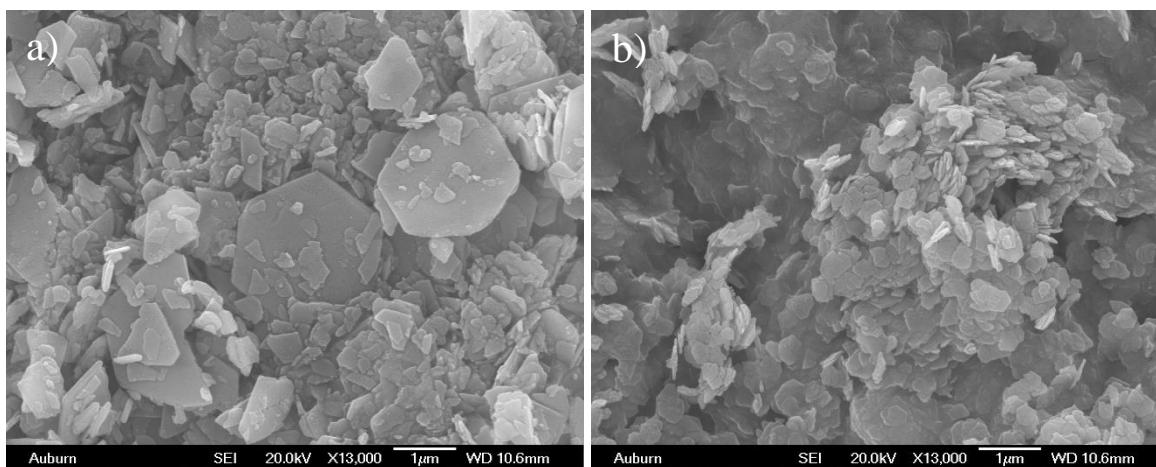


Figure 3.2: SEM of a) pH 5 and b) pH 9 CuGaO₂ Powders

The solids resulting from the synthesis at pH 5 and pH 9 have other optical characteristic differences as well. Firstly, the color of the solid synthesized at pH 5 is yellow/tan in color, and the solid synthesized at pH 9 is gray in color. Since CuGaO₂ is a wide band gap semiconductor it is expected to be yellow/white in color because it should not absorb visible light. The dark color of the pH 9 powder could be related to the copper vacancies that are present in the material, which are discussed in Chapter 2.²⁸ This qualitative results seems to indicate that there are fewer defects in pH 5 that result in optical changes to the particles. The transmittance and reflectance of the films was measured and the reflectance was converted to F(R) using the Kubelka-Munk equation. F(R) plots of the films show some optical features are present for pH 9 that are not for pH 5 (**Figure 3.3**). There are also two features at 590 nm and 492 nm that are specific to pH 9 particles. However, the most notable facet of the data is the significant absorption in the NIR region exhibited by pH 9 particles, and somewhat by pH 5, indicative of a plasmon resonance. The appearance of plasmon resonance bands in the NIR is typically indicative of the concentration of charge carriers (in this case holes) in a material.²⁹ pH 9 O₂ and Ar films show significant absorbance in this region, indicative of a high density of charge carriers in the material. Upon H₂ annealing, the absorbance of the plasmon band decreases significantly,

indicating that H₂ annealing has decreased the hole concentration in the material. The similarity of the O₂ and Ar annealed plasmon also indicates that the hole density is so large that further oxidation does not increase the concentration significantly. The case of pH 5 is interesting because in all cases the absorbance of the plasmon band is significantly lower than that of pH 9. However, the hole concentration does seem to vary with annealing condition, as oxidation of the pH 5 film with O₂ increases the plasmon band, and reduction with H₂ decreases the plasmon band.

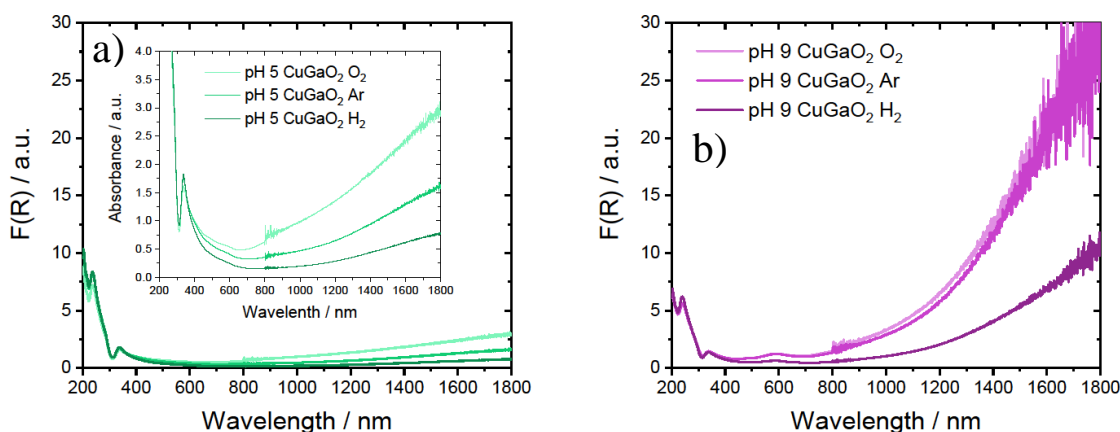


Figure 3.3: Diffuse reflectance spectra of a) pH 5 and b) pH 9 CuGaO₂ films.

Electrochemical studies on pH 5 and pH 9 CuGaO₂ were performed to assess how pH synthesis and annealing affect the electrochemical properties of the films. All electrochemistry was performed with 0.1 M LiClO₄ in acetonitrile. For CVs all scan rates were 50 mV/s unless otherwise indicated. The films were made such that surface areas between pH 5 and pH 9 films would be similar, and this was estimated using dye adsorption studies. This is done by adsorbing a photoactive molecule to the surface of the films and using the extinction coefficient of the dye to estimate surface coverage/surface area of the film. Films were dyed with the P1 dye (4-(Bis-{4-[5-(2,2-dicyano-vinyl)-thiophene-2-yl]-phenyl}-amino)-benzoic acid), a well-studied p-type DSSC dye³⁰, and UV-Vis showed that all films regardless of pH and annealing condition are able

to adsorb molecular dyes at their surfaces. Because of the large particle size, the films scatter a significant amount of light, therefore direct UV-Vis of the films is difficult to assess dye loading. Therefore, following surface attachment, the dye was removed from the surface using 0.1 M KOH in 1:1 MeCN:H₂O and measured by UV-Vis (**Figure A3.2**). A new extinction coefficient was calculated for the dye because of the change in absorbance in basic media, which was found to be $\epsilon = 42,000 \text{ M}^{-1} \text{ cm}^{-1}$. This measurement showed that the pH 5 films on average, absorbed more dye than the pH 9 films (**Table 3.1**) which indicates that they have a higher surface area. For the purpose of film preparation, pH 5 pastes were made more concentrated due to difficulty of making a viscous dispersion at low concentrations. The higher concentration could have influenced the higher absorption, as there are more particles present in the film. Interestingly, pH 5 and 9 both showed that of Ar annealed films adsorbed the least dye and H₂ annealed films adsorbed the most.

Table 3.1: PI Dye Adsorption to CuGaO₂

<i>Film</i>	<i>Absorbance</i>	<i>Conc (uM)</i>	<i>Moles</i>	<i>Molecules</i>	<i>Surface Area (cm²)</i>
<i>pH 5 Ar</i>	0.309	7.34	1.47E-08	8.84E+15	2.79E+02
<i>pH 5 O₂</i>	0.369	8.76	1.75E-08	1.06E+16	3.33E+02
<i>pH 5 H₂</i>	0.392	9.31	1.86E-08	1.12E+16	3.54E+02
<i>pH 9 Ar</i>	0.248	5.89	1.18E-08	7.09E+15	2.24E+02
<i>pH 9 O₂</i>	0.275	6.53	1.31E-08	7.87E+15	2.48E+02
<i>pH 9 H₂</i>	0.331	7.86	1.57E-08	9.47E+15	2.99E+02

The general CV features for pH 9 under all annealing conditions are fairly similar, and consistent with what we previously showed for pH 9 CuGaO₂ under O₂.²⁸ There is a quasi-reversible redox feature around 0.1 V vs. Fc⁺⁰ that we previously assigned to a Cu^{2+/+} redox wave, most likely due to the formation of Cu-OH at the nanocrystal surface, that we identified previously through XPS.²⁸ These types of features have been present in other Cu-based electrodes.^{31,32} There is also a fairly steep increase in current with an onset at very positive

potentials, assigned to an increased density of states in the valence band of the CuGaO₂. What is also present is rather large non-faradaic current, particularly below what should be the valence band minimum, $E < 0.1 \text{ V vs. Fc}^{+/0}$. For pH 9 this was previously attributed to the presence of defects that cause Fermi level pinning, which increases the overall capacitance observed. From CV data it appears that there is no significant change in the electrochemical properties of pH 9 films with annealing.

pH 5 CuGaO₂ CVs show significantly different behavior than what was observed for pH 9 films. Under all annealing conditions the overall capacitance has decreased, particularly at potentials negative of the valence band, assuming a flatband potential of 0.1V vs. Fc⁺⁰. This is a qualitative indication that the Fermi level is unpinned, and the CV behavior is more typical of a semiconductor. The quasi-reversible redox feature is still present for pH 5 films, particularly for O₂ and Ar annealed films, indicating that the surface hydroxides identified for pH 9 CuGaO₂ are potentially affecting pH 5 electrochemistry as well. However, pH 5 H₂ shows a significant decrease in the quasi-reversible oxidation, indicating that reduction of the film under H₂ contributed to passivation of those surface states. The change in the amount of current passed at more positive potentials is interesting as well, where it can be seen that maximum current is achieved in the O₂ annealed case. The Ar annealed case is almost identical to the O₂ CV, except for a decrease in current at more positive potentials. H₂ again shows the most significant change, where current at all potentials has decreased compared to O₂ and Ar annealed films.

If both pH 5 and 9 CuGaO₂ films are scanned at more negative potentials, a sharp peak appears in the CVs around -0.7 V vs. Fc⁺⁰ (**Figure A3.3**). Peaks such as these in thin film electrochemistry typically indicate some monoenergetic defect state. This feature appears 800 mV more negative than the flatband potential, and seems to be unfilled, considering it is not seen

in the CVs shown in **Figure 3.4**. Scanning more negative seems to reduce this state, resulting in the oxidative peak that is seen on the return sweep. This peak appears regardless of annealing condition and changes very little, indicating it is an inherent feature to CuGaO₂.

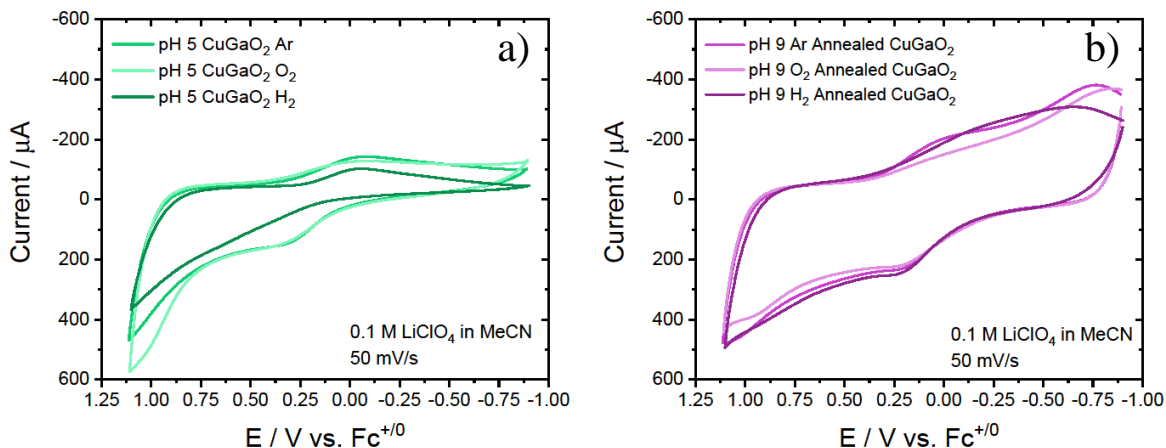


Figure 3.4: CV measurements of a) pH 5 CuGaO₂ films and b) pH 9 CuGaO₂ films annealed under Ar, O₂, and H₂ at 350 °C

This CV data highlights the necessity of using EIS to elucidate more electronic information about these mesoporous films. pH 9 CV's in particular have such a high background capacitance that it is difficult to elucidate the faradaic components in the system. We have limited the possible faradic pathways by using a non redox-active electrolyte, which means only processes related to the film itself should be observed. The capacitance observed in the CVs could be due to several different processes, such as the chemical capacitance (C_{μ}) from the density of valence band and defect states, as well as just the double-layer capacitance, known as the Helmholtz capacitance, at the electrode/solution interface. These processes can be separated with EIS because it is an AC-technique and the capacitances at different interfaces is frequency dependent. This is discussed more significantly in Section 1.3.2 of Chapter 1.

Complete Nyquist, Bode Phase, and Bode Z plots for each film can be found in the appendix of this chapter (**Figures A3.4-A3.6**). Starting with pH 9 CuGaO₂, O₂ annealed films displayed

EIS similar to what was reported in our previous study, where we found the overall film capacitance does not change significantly over the potential range that was probed. However, we now show C_{real} vs. frequency plots, which are a direct measurement of every capacitor present in the electrochemical system (**Figure 3.5**). In the same way that Bode Z plots show the total resistance present in a system, these plots show the capacitance. Any plateau in a C_{real} plot is related to a capacitor in the electrochemical system.³³ The interfaces in our system which are probed are the FTO/CuGaO₂ interface (solid/solid), the FTO/solution interface (solid/solution), and the CuGaO₂/solution interface (solid/solution). The interface of most interest is, of course, the CuGaO₂/solution interface, which will provide information about C_{μ} as well as any defect states related to the valence band. For C_{real} plots of pH 9 CuGaO₂, we see that our conclusions about O₂ annealed films is proven true, where the capacitance measured in the low frequency region does not change as a function of potential, and maintains a high value over the entire potential range. This also seems to be the case for Ar annealed CuGaO₂. H₂ annealed CuGaO₂, however, does show significantly more variability with potential than O₂ or Ar annealed films. All pH 9 CuGaO₂ film conditions give CVs that imply that the Fermi level is pinned in those cases. However, clearly there are changes to the electrochemical properties of pH 9 CuGaO₂ with H₂ annealing. This further emphasizes the difficulty of mesoporous film assessment using only CV and demonstrates the necessity of using EIS for capacitance evaluation.

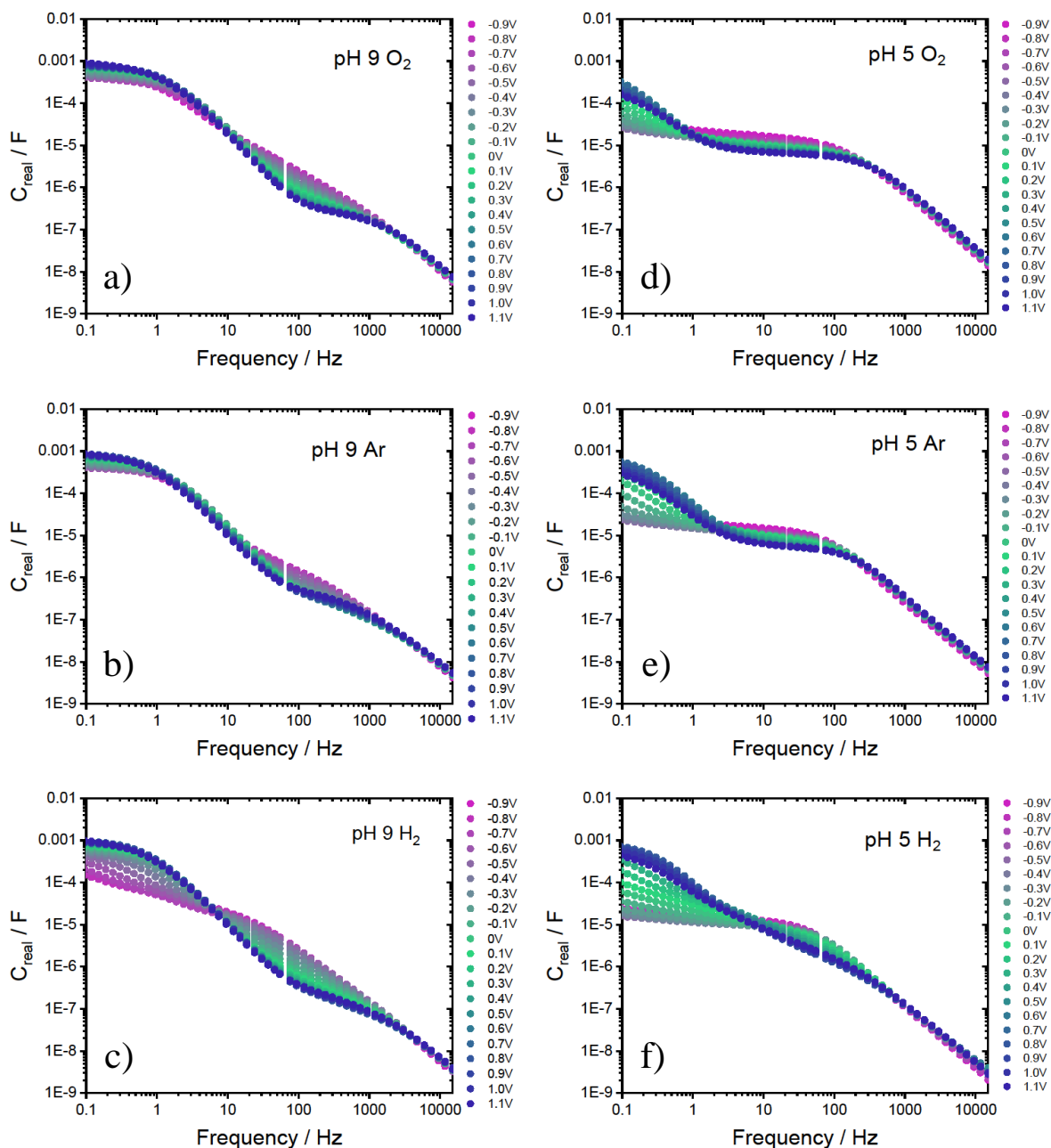


Figure 3.5: C_{real} vs. frequency plots for a) pH 9 CuGaO_2 O_2 , b) pH 9 CuGaO_2 Ar, c) pH 9 CuGaO_2 H_2 , d) pH 5 CuGaO_2 O_2 , e) pH 5 CuGaO_2 Ar, and f) pH 5 CuGaO_2 H_2 .

pH 5 CuGaO_2 shows even more variability with potential under all annealing conditions tested, showing an increase in capacitance with potential in the range of 1 Hz – 0.1 Hz, consistent with observing the density of states in the valence band at the $\text{CuGaO}_2/\text{solution}$ interface. This capacitance also seems to vary with annealing condition, where it can be seen that

the maximum capacitance measured at the most positive potential, 1.1 V vs. $\text{Fc}^{+/0}$, increases in the order $\text{O}_2 < \text{Ar} < \text{H}_2$. What is fascinating about this observed change in capacitance is that the current change observed in the CVs has the exact opposite trend, where more current is produced in the case of O_2 and less in the case of H_2 . This trend of current in the CVs is consistent with changes in the film resistance, which will be discussed next.

The mid-frequency capacitance change should be addressed here as well, although it is currently not fully understood. When EIS is performed on blank FTO glass in the same electrolyte, the capacitance featured in the mid-frequency region (100 Hz – 1 Hz) is very similar to the capacitance observed here for pH 5 O_2 and Ar at all potentials. At negative potentials for pH 5 H_2 the capacitance behavior in this range is similar to that of FTO, but then seems to change as more positive potential is applied. Specifically, the loss of the plateau feature is indicative of two things: 1) the ideality of the interface is changing, which changes the slope of the capacitance or 2) a different interface is now dominating in that frequency range over those potentials. For pH 9 CuGaO_2 the behavior in the mid-frequency region is even more peculiar, starting with an almost indistinguishable capacitance that then flattens to a very small capacitance value ($< 10^{-6}$ F) and also shifts to higher frequency values, between 100 – 1000 Hz. The most negative potential for pH 9 H_2 seems to be similar to the C_{real} data for pH 5 at more mild potentials (-0.2 – 0.2 V), indicating that there is some overlap in the electrochemical behavior of the films.

Lastly, it is worth mentioning that the monoenergetic trap, located around 0.7 V vs. $\text{Fc}^{+/0}$ does not seem to appear in the capacitance plots measured at that potential. This can particularly be seen in the pH 5 cases where the FTO dominates at the more negative potentials. However, this feature shows up significantly in resistance data.

The differences in resistance of the films can also give an indication of their electrochemical behavior. **Figure 3.6** shows an overlay of nyquist plots for pH 5 and 9 films at all annealing conditions at 0V vs $\text{Fc}^{+/0}$. The Nyquist plots for this data are slightly convoluted by the large resistance to charge transfer in our system due to the use of a non-redox active electrolyte. However, the magnitude of resistance does seem to give an indication to the overall conductivity of the film. The Bode Z and Nyquist plots for all films at all potentials show that the total resistance is significantly higher for pH 5 films at potentials below the valence band edge compared to pH 9 films (**Figure A3.4 and A3.6**). In fact, for pH 9 O_2 and Ar films, the total resistance does not change significantly as a function of potential, similar to the capacitance. pH 9 H_2 does have an increase in resistance, particularly at potentials above the band gap, but the resistance is still significantly lower than that measured for all pH 5 films. The larger resistances measured for the pH 5 films is consistent with the lower overall current in pH 5 film CVs, including the even lower current passed by pH 5 H_2 , which had the largest resistance measured for all films (**Figure 3.6**).

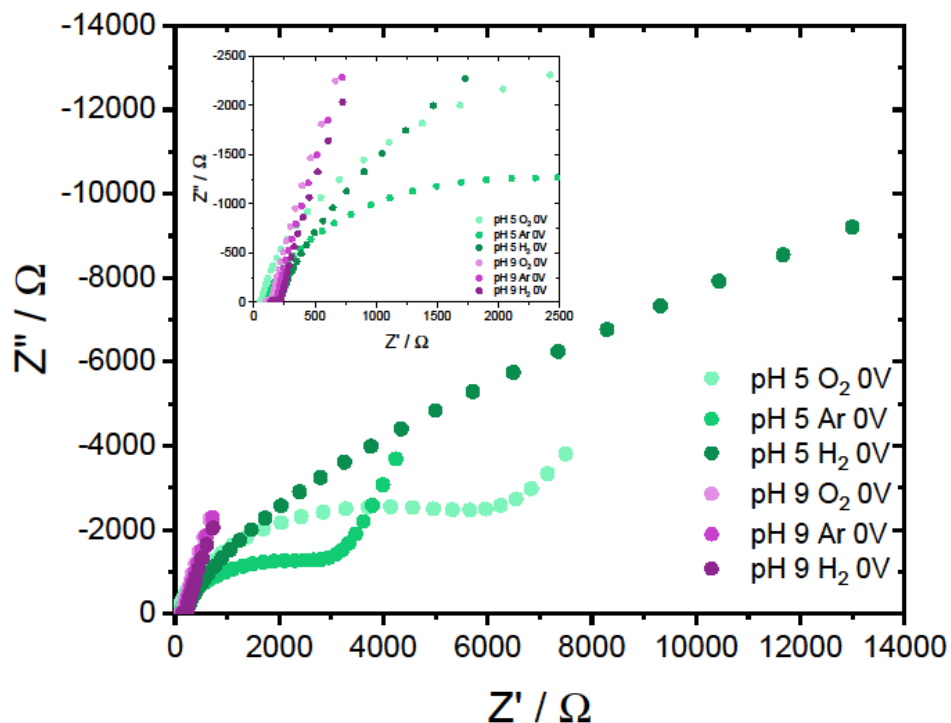


Figure 3.6: Nyquist plots of pH 5 and pH 9 O₂, Ar, and H₂ Annealed films displaying the difference in total resistance between pH 5 and 9 films, as well as showing the variability of the resistance with annealing condition.

Another important resistance component typical to metal oxides mesoporous films is the resistance to charge diffusion through the mesoporous network (R_d) and is related to the overall conductivity and charge density in the film. While this is typically modelled with equivalent circuits, it has a distinct shape in Nyquist plots that can be observed and identified. In both pH 5 and 9 CuGaO₂ films there appears to be a diffusional resistance component observed in the Nyquist plots (**Figure 3.7**). This diffusional feature is certainly different between pH 5 and 9 films and does seem to be affected by annealing condition. **Figure 3.7a** shows that the diffusional resistance can be observed for pH 5 H₂ films between 0.2 – 0.6 V vs Fc⁺⁰, while in the O₂ condition at the same potentials (**Figure 3.7b**) the diffusional feature is no longer present. pH 9 H₂ also shows diffusion resistance, but this feature is observed at potentials significantly

more negative than the potentials where the feature appears for pH 5. Interestingly, pH 9 O₂ also seems to display this feature in the same potential range, albeit at very small resistances.

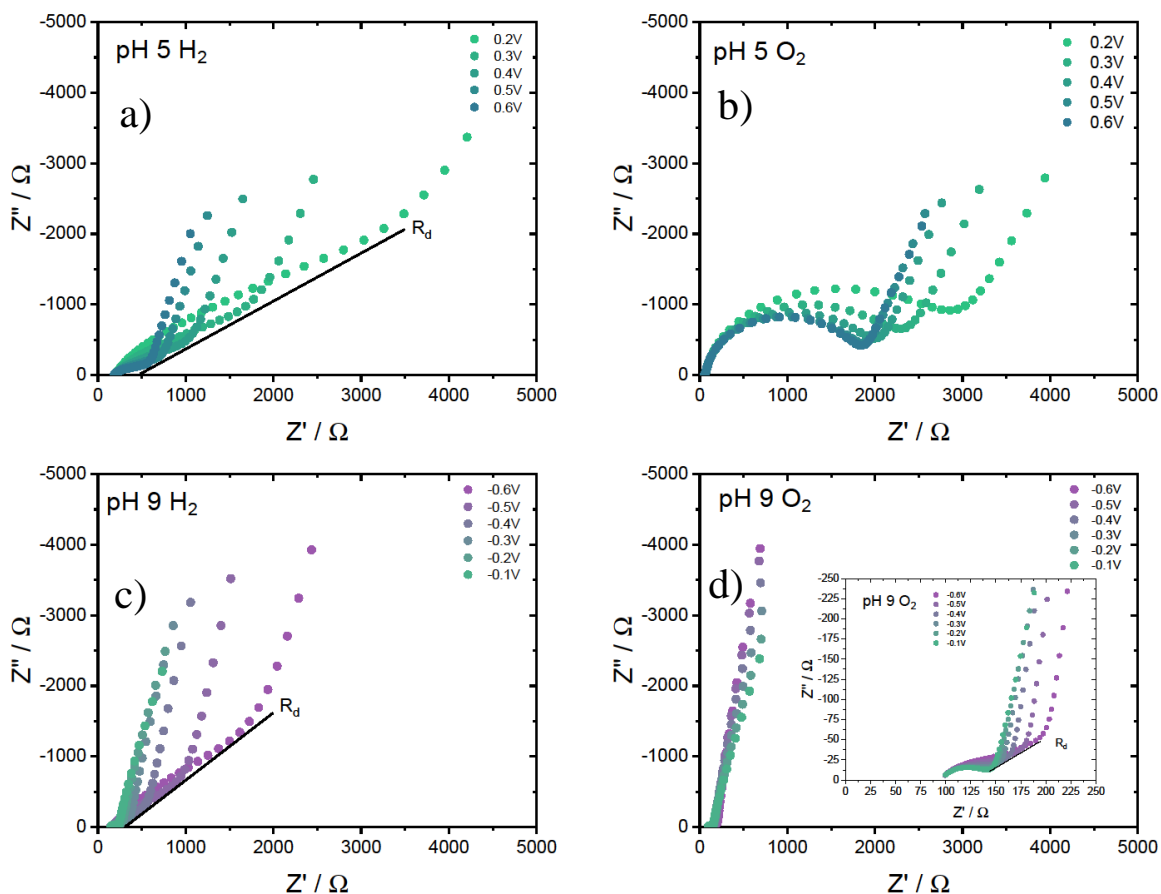


Figure 3.7: Nyquist plots showing the diffusional resistance feature in 0.2 – 0.6 V vs. $Fc^{+/0}$ range for a) pH 5 H₂ and b) pH 5 O₂. The diffusional resistance feature is shown from -0.6 – -0.1 V vs $Fc^{+/0}$ for c) pH 9 H₂ and d) pH 9 O₂.

The use of annealing conditions to control the electrochemical behavior of the films also indicates that the behavior induced by one annealing condition could be “undone” by subsequent annealing under another condition. To test this, films that were annealed under O₂ initially were later annealed under H₂ to see if the initially oxidized films could be reduced. The results of this experiment are shown in the C_{real} vs frequency plots with Nyquist insets in **Figure 3.8**. pH 9

CuGaO₂, which already displays highly oxidized behavior in the Ar annealed case, again shows highly oxidized behavior in the case of initial O₂ annealing. After subsequent H₂ annealing the features consistent with initial H₂ annealing do appear, such as the increase in total resistance at more negative potentials and more variability in the capacitance with potential. However, the effect of H₂ after initial O₂ annealing seems decreased with respect to performing H₂ annealing in the first. pH 5 shows even more reversibility with annealing condition, with the H₂ state after O₂ annealing looking almost identical to initial H₂. The difference in this affect between pH 5 and 9 is most likely related to the initial synthesis and the intrinsic hole density of CuGaO₂ under each condition. The cyclic voltammetry behavior mirrors the results of the impedance where in both pH 5 and 9 films the O₂ annealed films pass more current than the H₂ annealed films. The difference in current is greater for pH 5 films than pH 9. These films were even oxidized back with more O₂ annealing after H₂ annealing, revealing a level of reversibility in this process.

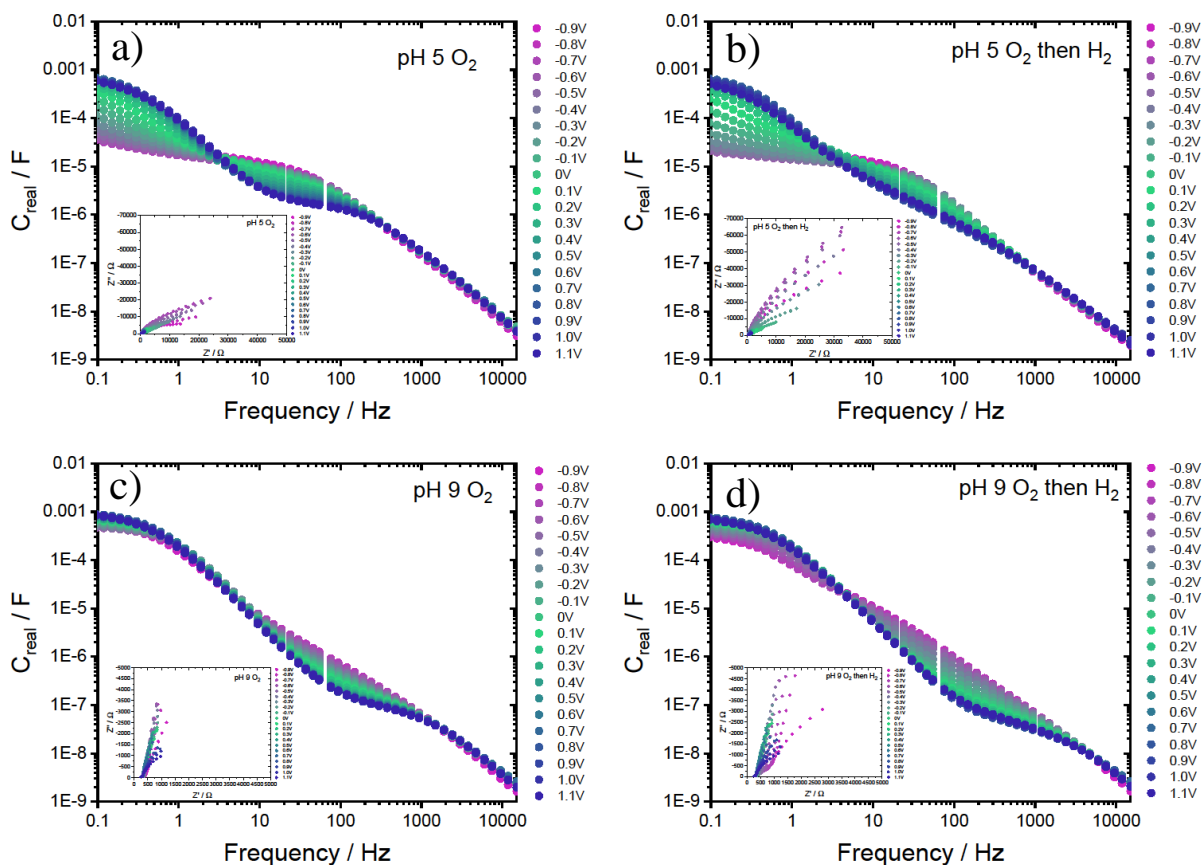


Figure 3.8: C_{real} vs Frequency plots with Nyquist insets for a) pH 5 O_2 b) pH 5 O_2 then H_2 c) pH 9 O_2 and d) pH 9 O_2 then H_2 annealed CuGaO_2 films.

The defect concentration in these materials almost certainly influences the operation of solar cell devices that employ them, therefore acquiring some device relevant measurements can be informative on how modifying the defect chemistry could affect device performance. To this end, CV and EIS of the films was also performed in the presence of I^-/I_3^- , a common redox mediator used in DSSCs. A typical CV for I^-/I_3^- is shown in **Figure A3.7**, where its two redox features ($3\text{I}^- \rightarrow \text{I}_3^- + 2e^-$ ($E_{1/2} = 0.49$ V) and $2\text{I}_3^- \rightarrow 3\text{I}_2 + 2e^-$ ($E_{1/2} = -0.45$) can be observed. CVs of both pH 5 and 9 films with I^-/I_3^- show both oxidation peaks, but do not show any subsequent reduction at the potentials scanned (**Figure 3.9**). This is consistent with having a semiconductor material where only the valence band states are accessible for oxidizing the redox mediator. pH 9

films seem to have larger non-faradaic current at potentials below the I^-/I_3^- oxidation, compared to pH 5 films, but otherwise no reduction of I^-/I_3^- is observed. Since there seems to be a high level of vacancies in pH 9 $CuGaO_2$ films that could contribute to surface defects, the lack of reductive current is particularly interesting. The onset of oxidation of I^-/I_3^- does not seem to shift very much with annealing condition in the case of pH 9, staying around 0.125 V vs. $Fc^{+/0}$, measured at 0.5 mA of current passed. pH 5, however, has an onset of around 0.250 V vs $Fc^{+/0}$ for O_2 and Ar annealed films, that then shifts 80 mV more positive to 0.330 V vs $Fc^{+/0}$ with H_2 annealing. In all cases, the onset of oxidation is more negative with pH 9 films than pH 5 films, indicating a more negative Fermi level position for pH 9 $CuGaO_2$. Overlays of pH 5 and 9 films at the same annealing condition in I^-/I_3^- are shown in **Figure A3.8**.

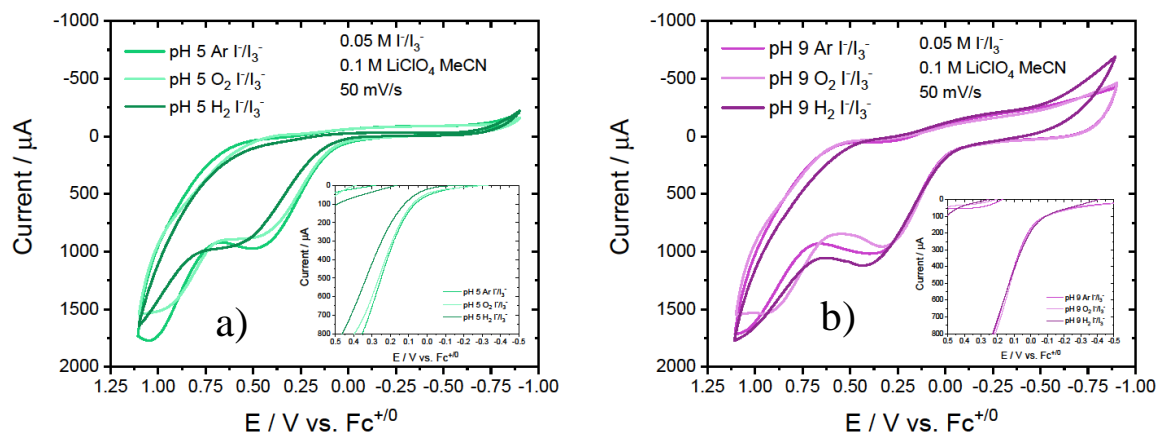


Figure 3.9: CVs of a) pH 5 $CuGaO_2$ and b) pH 9 $CuGaO_2$ film in 0.05 M I^-/I_3^- electrolyte

3.4 Discussion

The hydrothermal synthesis of $CuGaO_2$ is the most typical synthetic method that has been employed for generating $CuGaO_2$ nanocrystals³⁴, as well as for studying their formation. Previously Yu et. al. reported on the crystallization mechanism of $CuGaO_2$ and studied the effect of pH on the resulting particle morphology and size.¹⁹ The pH of the synthesis has a large effect

on the speciation of Cu and Ga hydroxides, and the reactivity of those resulting hydroxides to make the desired delafossite phase. They report the formation of unfavorable gallium phases below pH 4 and the formation of Cu side products above pH 6. Our synthesis of CuGaO₂ at pH 9 seems to produce more Cu₂O than pH 5, consistent with the observation of Yu and coworkers. The Cu₂O produced in the syntheses is removed by washing in dilute base. The investigation of CuGaO₂ synthesis has also involved finding a way to make smaller particles, as this will be beneficial in solar cell device application for optical transparency and dye loading. Most publications on CuGaO₂ using hydrothermal methods have synthesized CuGaO₂ at pH 5 or similar, where it was initially reported the smallest particles were produced.³⁵ It was later found that precursor temperature mattered significantly for particles size, as colder temperatures induced more controlled seeding for particle growth.¹³ This study also used pH's closer to 9 to help induce smaller particles, consistent with our synthesis. Given these differences in particle synthesis and how they relate to device function, it has seemed pertinent to understand the effect of pH on the electrochemical properties of the CuGaO₂ films. Our findings suggest that there is, in fact, a large contribution of the pH of particle synthesis to the conductivity and hole transport properties of the films.

Chapter 2 of this thesis discussed EDS measurements for pH 9 synthesized CuGaO₂ in which the particles were ~4% deficient in copper atoms, giving a calculated hole density of ~10²¹ cm⁻³, on the order of charge density in transparent conducting oxides such as F:SnO₂ (FTO). Elemental analysis on pH 5 CuGaO₂ still needs to be performed, but our diffuse reflectance and electrochemical data suggest that pH 5 synthesized particles do not suffer the same magnitude of hole density as particles synthesized at pH 9. This is not surprising given the observations of Yu, as well as our own, that the amount of Cu₂O side product is higher at pH 9 than at pH 5. It

appears that higher pH's make Cu_2O formation a kinetically favorable product, which consumes copper that can no longer incorporate into the delafossite crystal structure, leaving vacancies. Every vacancy induces the formation of Cu^{2+} to charge balance, creating a hole. The initial spectroscopic and electrochemical differences between pH 5 and pH 9 CuGaO_2 seem to be related to the occurrence of vacancy formation in pH 9 that is not occurring in pH 5 particles.

The other p-type metal oxide defect that is possible is the introduction of interstitial oxygens, which can change the coordination environment of copper atoms from linear to square planar, stabilizing the formation of Cu^{2+} atoms in the crystal structure. Our annealing condition under an O_2 environment can almost certainly induce the formation of interstitial oxygens, but it seems that the influence of this defect is significantly different between pH 5 and 9 films. Our spectroscopic analysis of pH 9 films shows that the background hole density is already so high, seemingly due to the high hole concentration induced by the copper vacancies, that the introduction of oxygen to make interstitial defects has little to no effect. This can be seen by the very small change in the plasmon resonance feature in the UV-Vis data and the capacitance data from EIS. The introduction of H_2 to reduce the film can certainly remediate an interstitial oxygen by reacting to form water, which volatilizes at the high annealing temperatures. However, since we believe the majority of the defects in pH 9 are initially due to copper vacancies, which cannot be simply remediated by annealing, the effect of the reducing environment will be limited. There is a difference in the spectroscopic data for pH 9 after H_2 annealing which means that some number of defects have been remediated, so it can be reasonably assumed that some Cu^{2+} is reduced back to Cu^+ , which can perhaps be stabilized by the formation of a hydride. Further elemental analysis such as EDS and thermogravimetric analysis is needed to confirm this hypothesis.

The spectroscopic data of pH 5 CuGaO₂ indicates that the initial condition of pH 5 has significantly fewer defects than pH 9, which means that O₂ annealing could induce more defects in pH 5. This seems to be the case, as the plasmonic band for pH 5 shifts with annealing condition, specifically increasing with O₂ meaning that the hole concentration is increasing. The affect of O₂ indicates that there is most likely an introduction of interstitial oxygens, changing the conductivity, but it is significantly less than the affect that the copper vacancies are having on the conductivity of pH 9 particles. To estimate the concentration of oxygen atoms introduced in the pH 5 particles requires thermogravimetric analysis under an O₂ environment. The change in hole concentration is also indirectly observed from changes in the diffusion resistance associated with charge transport in the films. At low concentration of holes, the resistance to hole diffusion will be large while at high hole concentration the resistance will be small and/or negligible. Firstly, observation of diffusion resistance in the pH 9 H₂ annealed case is a good indicator that the reduction of some oxidized species contributing to hole density has taken place. The fact that this feature is still mildly present in the O₂ annealed case is surprising, but it is significantly smaller than the feature observed in the H₂ case. pH 5 films, on the other hand, exhibit anticipated behavior of observing the diffusion component clearly in the H₂ case, but not in the O₂ case. It is possible the diffusion feature is being suppressed by the mid-frequency arc in the Nyquist making it difficult to identify. The presence of a diffusion component will become more obvious when fitting the data with equivalent circuit models, as a higher quality fit could require using it. Regardless, there is a clear change in diffusion with annealing and with synthesis pH, highlighting a change in the hole density.

NiO has been significantly studied as a p-type material for DSSCs, and similar conclusions have been drawn about the contribution of Ni vacancies and their effect on the electrochemical

properties of NiO films. Cyclic voltammograms of NiO films commonly display two quasi-reversible redox features associated with oxidation of Ni²⁺ to Ni³⁺ and Ni³⁺ to Ni⁴⁺, and these oxidations are usually stabilized by the presence of surface hydroxides.³⁶ Similar conclusions were formed in chapter 2 based on data from XPS. However, it could be reasonably assumed that annealing with H₂ could remove surface hydroxides by forming water, decreasing the quasi-reversible feature present in the CVs. Indirect evidence that this could be occurring is the increase in the number of dye molecules present in H₂ annealed films, as the removal of surface hydroxides could open an adsorption site for the dye. Regardless of annealing condition, the quasi-reversible feature assigned as Cu^{2+/+} was seen in CVs for pH 5 and 9 films. If XPS shows that the presence of surface hydroxides is less under certain annealing conditions, then another explanation for the presence of the quasi-reversible redox feature could be oxidation/reduction of copper atoms in the valence band of CuGaO₂. It is known that the most positive states in the valence band are based in Cu *d* orbitals, while the rest of the band consists of O *2p* orbitals.¹⁰ The two onsets of oxidative current observed could indicate oxidation of two different components of the band structure. The plausibility of this is further supported by the current increase seen with oxygen annealing at more positive potentials, perhaps due to incorporation of interstitial oxygens that can contribute to valence band oxidation.

It has been shown that the remediation of Ni vacancies using methods like atomic layer deposition to fill in the vacancies with Ni atoms can effectively remove the typical quasi-reversible features from NiO CVs.³⁷ Chemical and thermal reduction of NiO has also been investigated and shows that a decrease in defects can increase the photovoltage produced in NiO based solar devices, related to a change in the Fermi level of the NiO.³⁸ The contribution of these defect states on recombination events in solar cells has been studied significantly as well.³⁹

These studies on NiO reflect the behavior that has been observed in our CuGaO₂ films due to the different types of defects and how synthesis and annealing can change the electrochemistry of the films. However, the assignment of defects in NiO has been strongly affiliated with surface defects, and interestingly a study showed that surface defects in NiO give CV behavior in I⁻/I₃⁻ where both oxidation and reduction processes are observed.³⁹ When the defects are remediated via atomic layer deposition, the reduction feature disappears and only the oxidation of the redox mediator is observed. This contrasts with our data, where both pH 5 and 9 only show oxidative current in I⁻/I₃⁻ electrolyte. It is possible that the defect states for CuGaO₂, particularly in pH 9 particles, are still surface bound, but that their ability to catalyze the reduction is insufficient, as the increase in current below the oxidation onset could be related to poor I⁻/I₃⁻ reduction. Based on these experiments, however, it seems clear that pH 5 particles do not suffer from the same level of defects as pH 9 particles.

Despite the lack of clarity related to the exact nature of the copper vacancy, the higher hole density induced by the copper vacancies can clearly affect how the particles will function in devices from several facets. The I⁻/I₃⁻ electrochemistry experiments show that the difference in hole density has an effect on the open circuit voltage of a device, based on the change in oxidation onset with particle pH. From the perspective of getting the most voltage out of a device, pH 5 H₂ annealed CuGaO₂ would give the largest V_{oc} based on the onset of its oxidation of I⁻/I₃⁻. Photocurrent is also an important parameter of a solar cell measurement, and it is commonly seen that increasing the V_{oc} can result in a decrease in the J_{sc}, which does not necessarily help improve the fill factor of solar cell devices.⁴⁰ No direct measurements were performed to probe how particle synthesis or annealing would affect J_{sc}, but the higher dye loading on pH 5 H₂ films would also certainly contribute to a better J_{sc}. Using only reducing

conditions to make a better solar cell device may not be the conclusive best way, as oxidation of CuGaO₂ and NiO with ozone or O₂ has shown to improve the device function of different types of solar cells.^{17,41}

All of the data shown indicates that pH 5 CuGaO₂ has a lower carrier density than that of pH 9 CuGaO₂, most likely due to the lower concentration of copper vacancies in the delafossite particles. The density of holes in the valence band determines the Fermi-level of a semiconductor based on the equation:

$$3.1) E_F = E_{VB} - k_B T \ln \left(\frac{N_{VB}}{n_h} \right)$$

Where E_F is the Fermi-level energy, E_{VB} is the valence band flat-band potential, k_B is Boltzman's constant, T is temperature, N_{VB} is the density of valence band states and n_h is the number of holes. n_h will also changes as a function of potential applied to the system, given by the relationship:

$$3.2) n_h = n_h^0 + n_h(E)$$

The Fermi level of the films is certainly different for pH 5 and 9 films based on the I^-/I_3^- data, where the oxidation of the redox mediator is significantly more positive for pH 9 films than pH 5 films. However, the behavior of the pH 9 films is more consistent with having a “pinned” Fermi-level, where the density of holes is so high that the Fermi-level has pushed into the valence band of the material, causing band “unpinning”.⁴² This phenomenon is what causes the metallic behavior of our pH 9 CuGaO₂ films, and it is unclear if H₂ annealing is reducing enough to unpin the Fermi level for pH 9 films. pH 5 CuGaO₂, however, seems to behave as a true semiconductor, and the semiconductor/liquid interface is behaving ideally⁴³, indicating the Fermi level position can be controlled by the introduction and removal of defects.

3.5 Conclusion

In this chapter the synthesis of CuGaO_2 nanocrystals and the annealing conditions on their resultant mesoporous films were studied spectroscopically and electrochemically to understand their natural density of hole carriers, and how the introduction/remediation of defects in the nanocrystals could influence that charge carrier density. As discussed previously in chapter 2, there was strong electrochemical evidence and elemental analysis to suggest that pH 9 CuGaO_2 already had a high density of holes in the material induced by copper vacancies. This chapter further supports those findings by showing evidence for remediation of those defects by annealing under a reducing environment. This hypothesis was further supported by the study of particles synthesized at pH 5, which clearly have a naturally lower carrier density than pH 9. pH 5 particles showed more susceptibility to annealing conditions than pH 9 particles, demonstrating that high temperature annealing can be an effective post-synthetic method for altering carrier density.

This work will be further completed by fitting analysis of the impedance data to extract values for the resistance and capacitance at each interface in our system. Finding a physically relevant model that reasonably fits our data will also help us evaluate the more unclear aspects of the impedance data, such as the mid-frequency feature and how it changes with annealing. Elemental analysis is also needed to further characterize the particles and the possible defects present in the material. This will be accomplished using EDS to study the bulk material composition, XPS to study the film surface, and TGA to study the change in mass of the material with the addition of oxygen.

3.6 Appendix

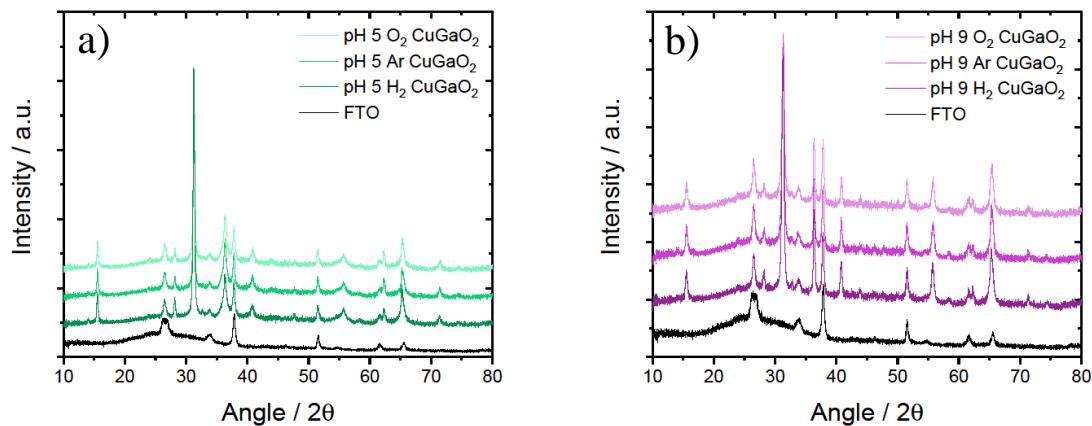


Figure A3.1: Powder XRD of a) pH 5 CuGaO_2 and b) pH 9 CuGaO_2 annealed under O_2 , Ar and H_2 . Annealing shows there is no formation of side products.

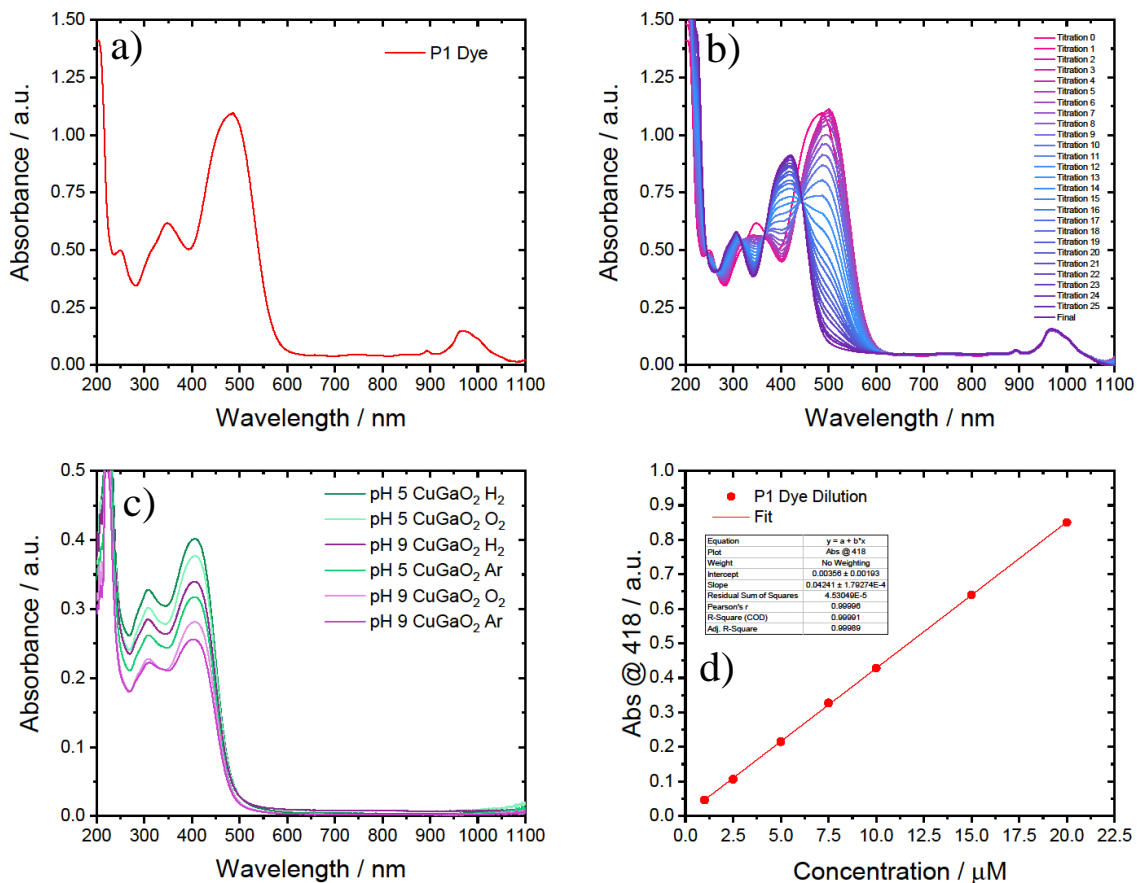


Figure A3.2: a) UV-Vis of P1 dye in 1:1 MeCN: H_2O . b) Titration of P1 dye in 1:1 MeCN: H_2O with 0.1M KOH in 1:1 MeCN: H_2O . c) UV-Vis of P1 dye desorbed from CuGaO_2 films. d) Calibration curve to calculate extinction coefficient of P1 dye in base.

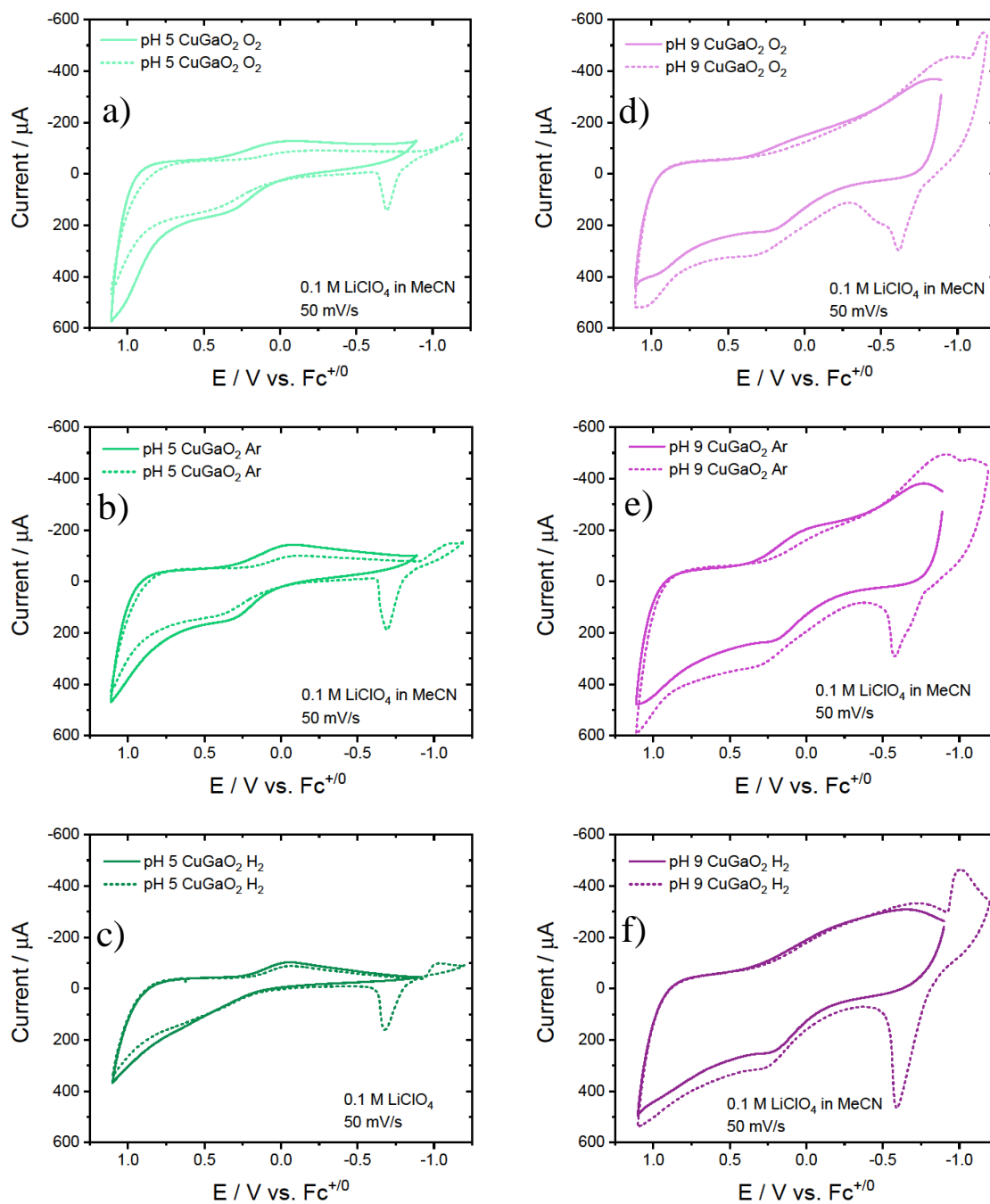


Figure A3.3: pH 5 CuGaO₂ annealed under a) O₂, b) Ar, and c) H₂ displaying the sharp oxidative peak present at more negative potentials. d)-e) show the same data for pH 9 CuGaO₂.

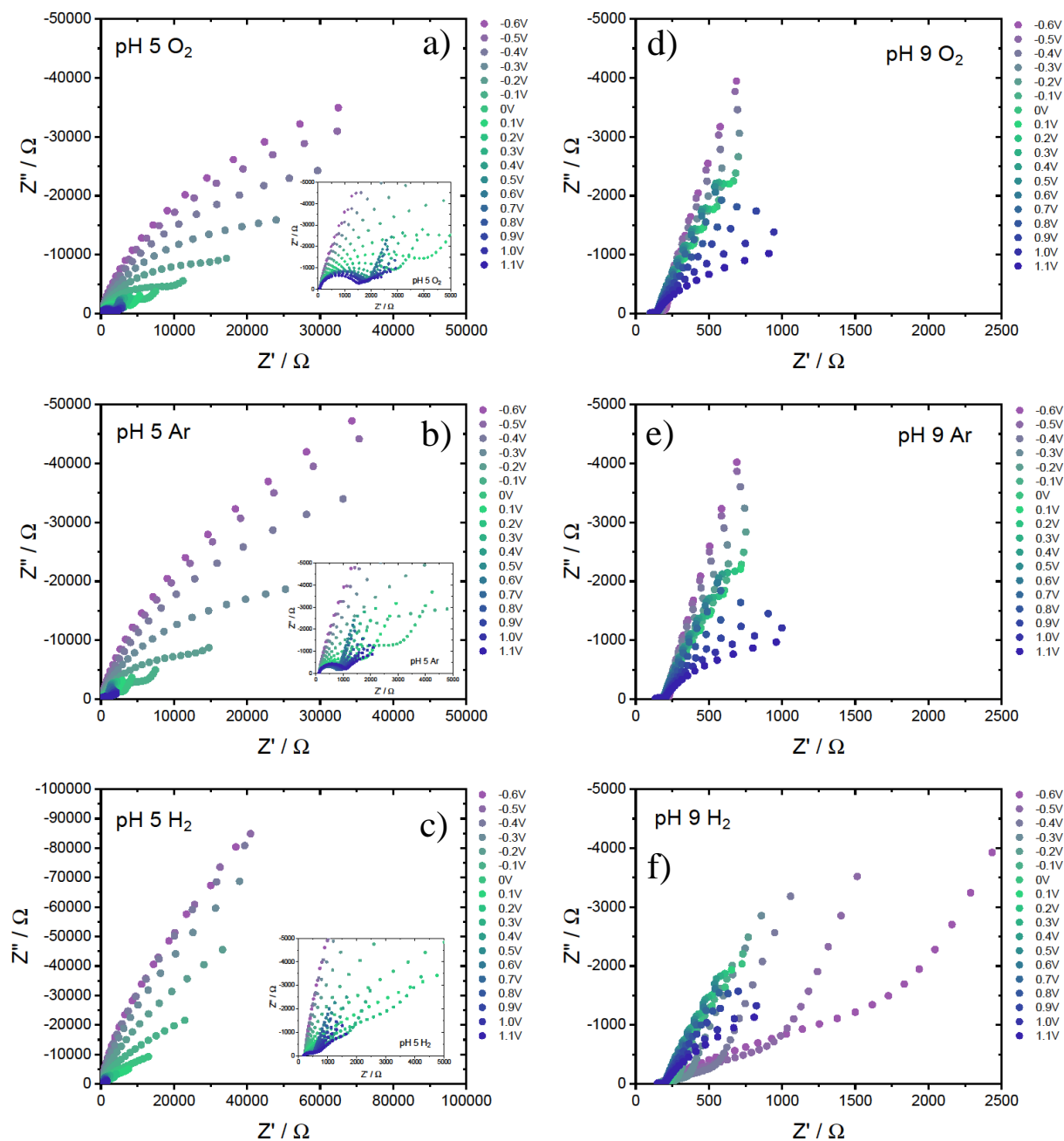


Figure A3.4: Nyquist plots of pH 5 CuGaO₂ O₂, Ar, and H₂ annealed films (a-c)) and pH 9 CuGaO₂ O₂, Ar, and H₂ annealed films (d-f)). Potential -0.9, -0.8, and -0.7 V are excluded from the plots for clarity because the resistance at those potentials is highly influenced by the monoenergetic state at -0.7 V.

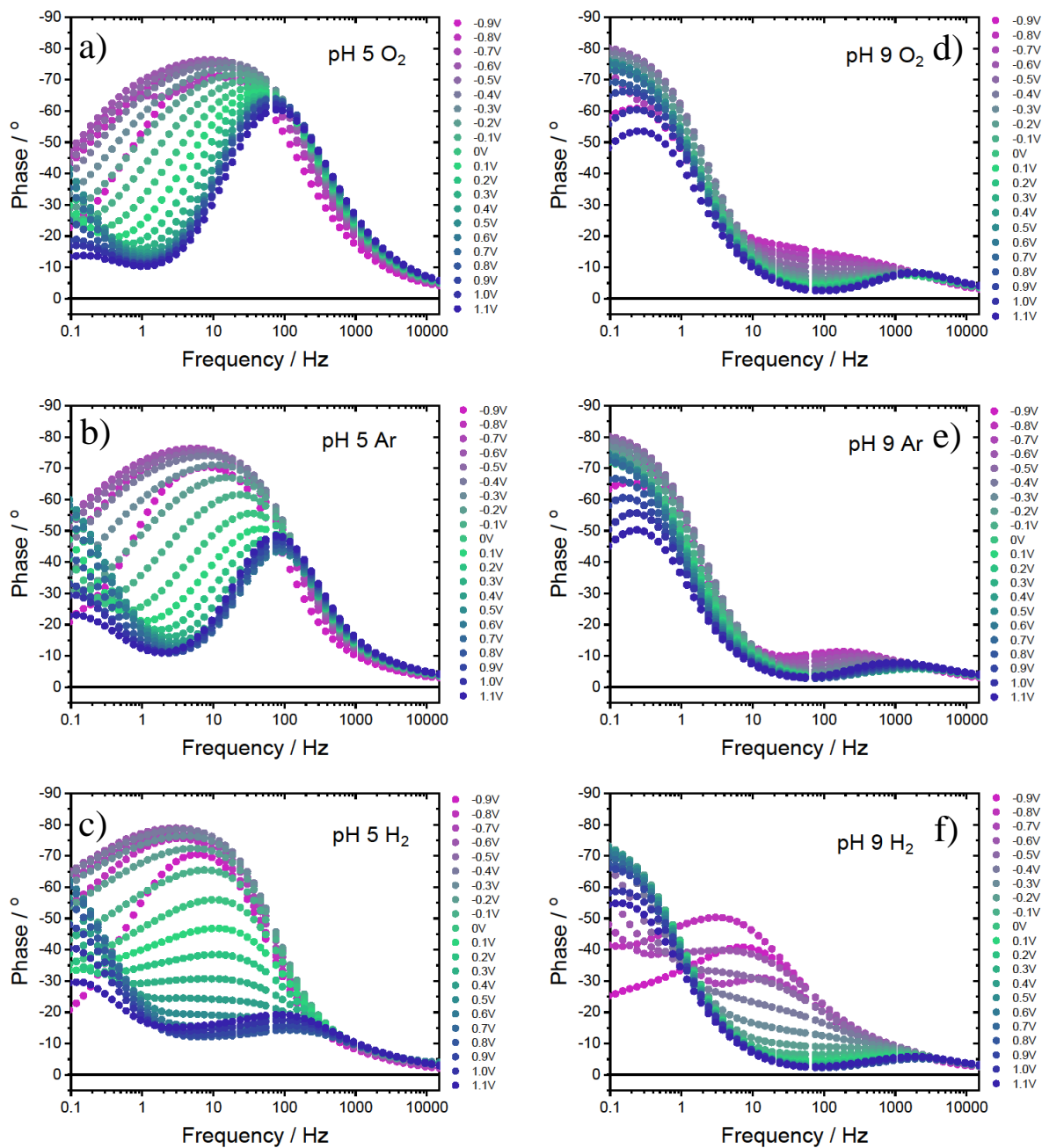


Figure A3.5: Bode phase plots of pH 5 CuGaO₂ O₂, Ar, and H₂ annealed films (a-c)) and pH 9 CuGaO₂ O₂, Ar, and H₂ annealed films (d-f)).

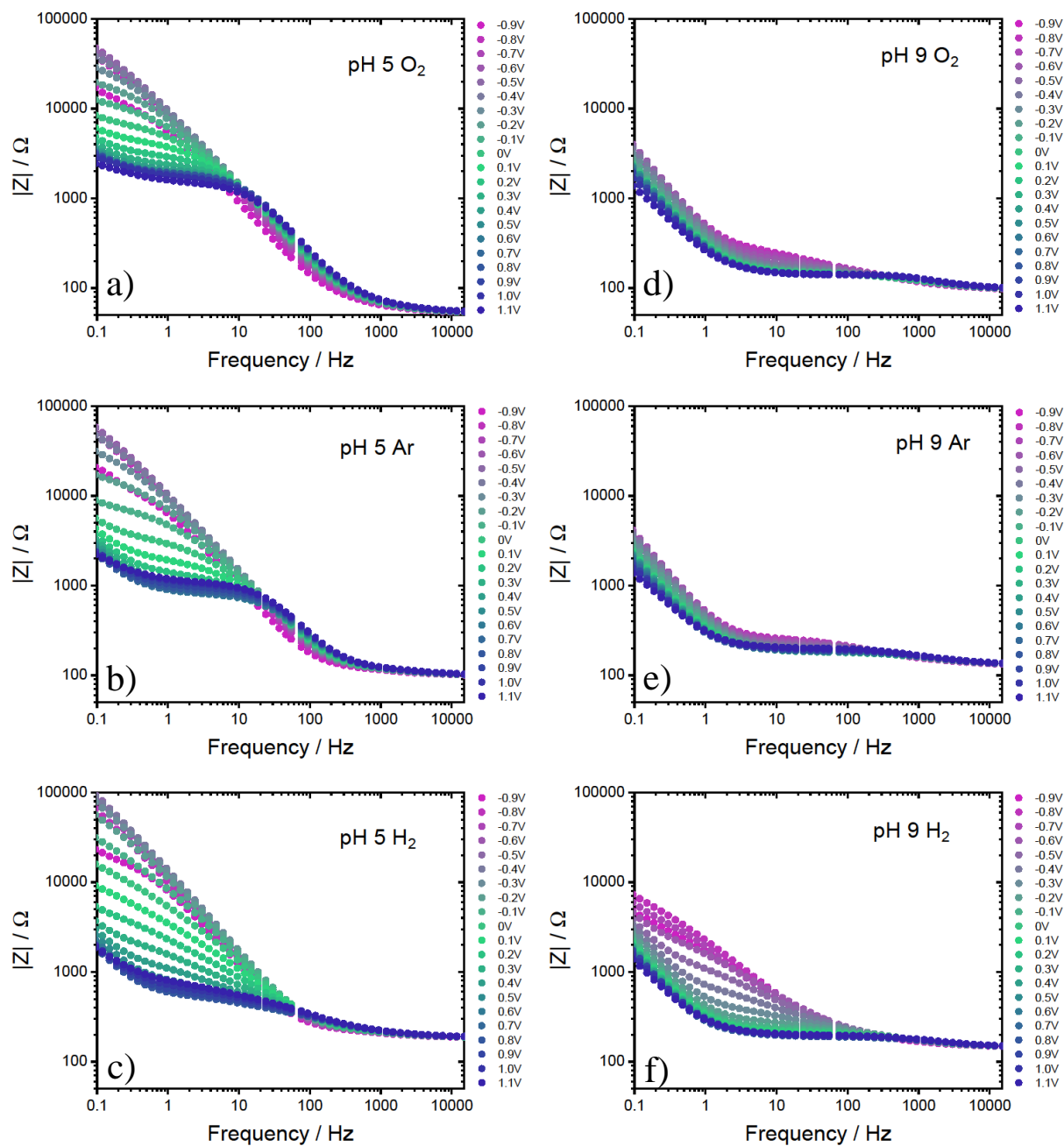


Figure A3.6: Bode phase plots of pH 5 $CuGaO_2$ O_2 , Ar, and H_2 annealed films (a-c)) and pH 9 $CuGaO_2$ O_2 , Ar, and H_2 annealed films (d-f)).

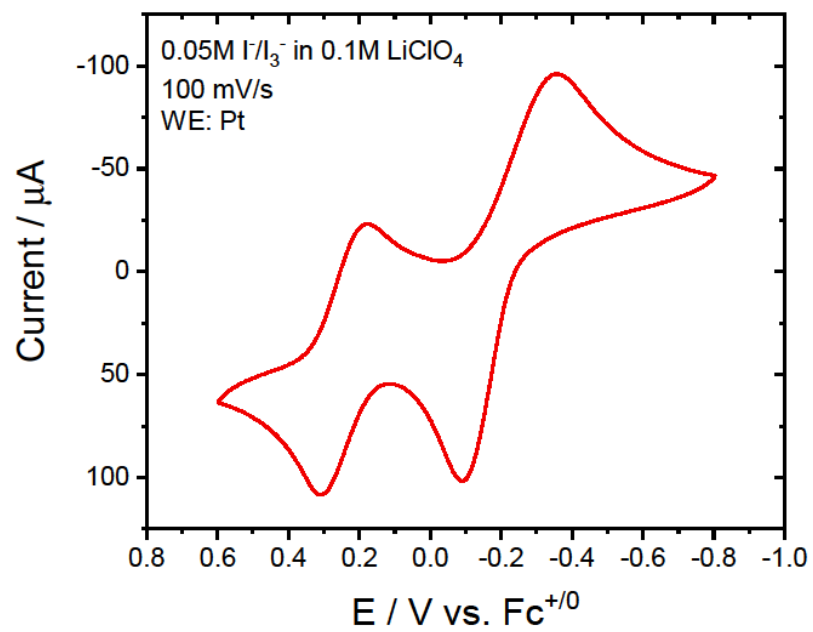


Figure A3.7: CV of I⁻/I₃⁻ redox couple in 0.1 M LiClO₄ in MeCN at 100 mV/s.

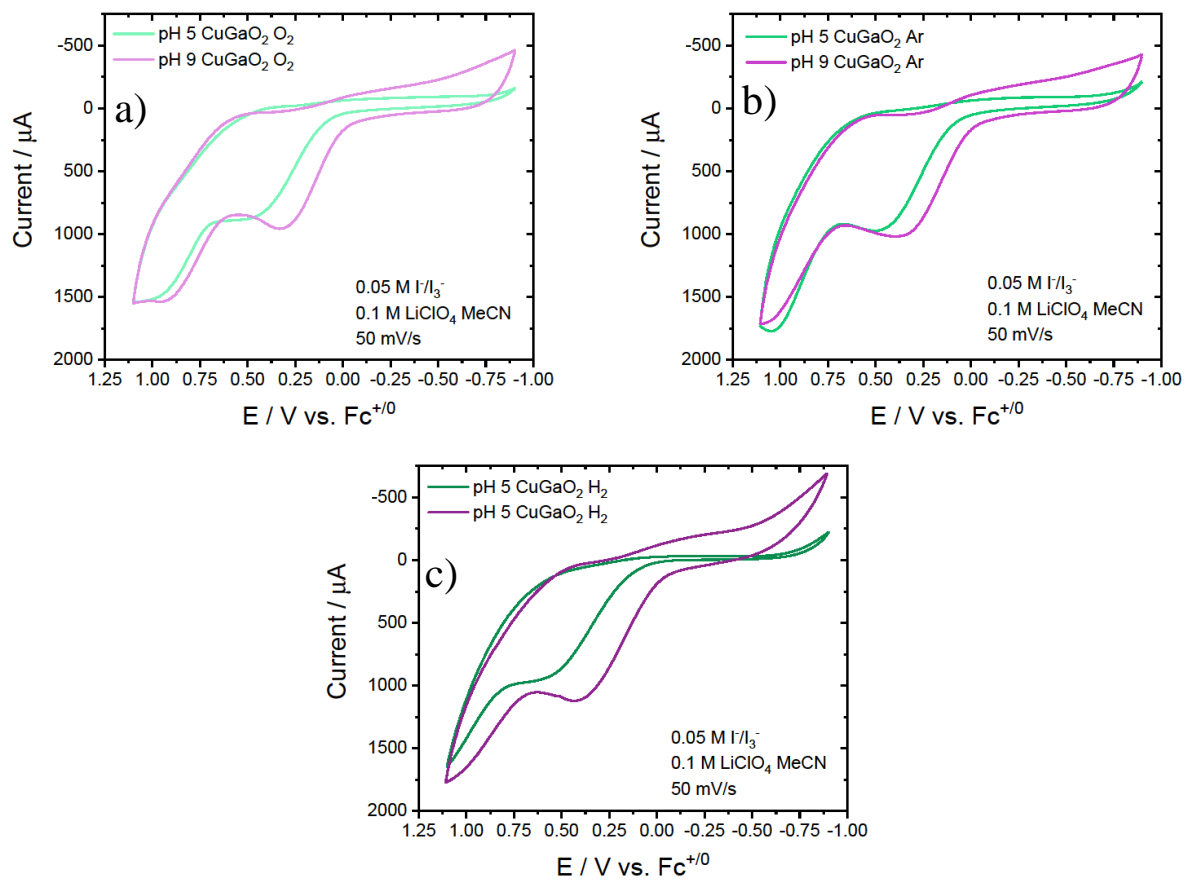


Figure A3.8: Comparison of a) pH 5 and 9 O_2 annealed, b) pH 5 and 9 Ar annealed, and c) pH 5 and 9 H_2 annealed CuGaO_2 in I^-/I_3^- redox mediator.

3.7 References

- (1) O'Regan, B.; Grätzel, M. A Low-Cost, High-Efficiency Solar Cell Based on Dye-Sensitized Colloidal TiO₂ Films. *Nature* **1991**, *353* (6346), 737–740. <https://doi.org/10.1038/353737a0>.
- (2) Mora-Seró, I.; Bisquert, J. Fermi Level of Surface States in TiO₂ Nanoparticles. *Nano Lett.* **2003**, *3* (7), 945–949. <https://doi.org/10.1021/nl0342390>.
- (3) Weibel, A.; Bouchet, R.; Knauth, P. Electrical Properties and Defect Chemistry of Anatase (TiO₂). *Solid State Ion.* **2006**, *177* (3), 229–236. <https://doi.org/10.1016/j.ssi.2005.11.002>.
- (4) Fabregat-Santiago, F.; Barea, E. M.; Bisquert, J.; Mor, G. K.; Shankar, K.; Grimes, C. A. High Carrier Density and Capacitance in TiO₂ Nanotube Arrays Induced by Electrochemical Doping. *J. Am. Chem. Soc.* **2008**, *130* (34), 11312–11316. <https://doi.org/10.1021/ja710899q>.
- (5) Mani, A.; Huisman, C.; Goossens, A.; Schoonman, J. Mott–Schottky Analysis and Impedance Spectroscopy of TiO₂/6T and ZnO/6T Devices. *J. Phys. Chem. B* **2008**, *112* (33), 10086–10091. <https://doi.org/10.1021/jp8013964>.
- (6) Gimenez, S.; Dunn, H. K.; Rodenas, P.; Fabregat-Santiago, F.; Miralles, S. G.; Barea, E. M.; Trevisan, R.; Guerrero, A.; Bisquert, J. Carrier Density and Interfacial Kinetics of Mesoporous TiO₂ in Aqueous Electrolyte Determined by Impedance Spectroscopy. *J. Electroanal. Chem.* **2012**, *668*, 119–125. <https://doi.org/10.1016/j.jelechem.2011.12.019>.
- (7) Bertoluzzi, L.; Herraiz-Cardona, I.; Gottesman, R.; Zaban, A.; Bisquert, J. Relaxation of Electron Carriers in the Density of States of Nanocrystalline TiO₂. *J. Phys. Chem. Lett.* **2014**, *5* (4), 689–694. <https://doi.org/10.1021/jz4027584>.
- (8) Wang, Z.; Nayak, P. K.; Caraveo-Frescas, J. A.; Alshareef, H. N. Recent Developments in P-Type Oxide Semiconductor Materials and Devices. *Adv. Mater.* **2016**, *28* (20), 3831–3892. <https://doi.org/10.1002/adma.201503080>.
- (9) Schuler, T. M.; Ederer, D. L.; Itza-Ortiz, S.; Woods, G. T.; Callcott, T. A.; Woicik, J. C. Character of the Insulating State in NiO: A Mixture of Charge-Transfer and Mott-Hubbard Character. *Phys. Rev. B* **2005**, *71* (11), 115113. <https://doi.org/10.1103/PhysRevB.71.115113>.
- (10) Raebiger, H.; Lany, S.; Zunger, A. Origins of the p -Type Nature and Cation Deficiency in Cu_2O and Related Materials. *Phys. Rev. B* **2007**, *76* (4), 045209. <https://doi.org/10.1103/PhysRevB.76.045209>.
- (11) Renaud, A.; Chavillon, B.; Pleux, L. L.; Pellegrin, Y.; Blart, E.; Boujtita, M.; Pauporté, T.; Cario, L.; Jobic, S.; Odobel, F. CuGaO₂: A Promising Alternative for NiO in p-Type Dye Solar Cells. *J. Mater. Chem.* **2012**, *22* (29), 14353–14356. <https://doi.org/10.1039/C2JM31908J>.
- (12) Renaud, A.; Chavillon, B.; Pleux, L. L.; Pellegrin, Y.; Blart, E.; Boujtita, M.; Pauporté, T.; Cario, L.; Jobic, S.; Odobel, F. CuGaO₂: A Promising Alternative for NiO in p-Type Dye Solar Cells. *J. Mater. Chem.* **2012**, *22* (29), 14353–14356. <https://doi.org/10.1039/C2JM31908J>.

- (13) Xu, Z.; Xiong, D.; Wang, H.; Zhang, W.; Zeng, X.; Ming, L.; Chen, W.; Xu, X.; Cui, J.; Wang, M.; Powar, S.; Bach, U.; Cheng, Y.-B. Remarkable Photocurrent of P-Type Dye-Sensitized Solar Cell Achieved by Size Controlled CuGaO₂ Nanoplates. *J. Mater. Chem. A* **2014**, *2* (9), 2968–2976. <https://doi.org/10.1039/C3TA14072E>.
- (14) Lee, B.; Yun, A. J.; Kim, J.; Gil, B.; Shin, B.; Park, B. Aminosilane-Modified CuGaO₂ Nanoparticles Incorporated with CuSCN as a Hole-Transport Layer for Efficient and Stable Perovskite Solar Cells. *Adv. Mater. Interfaces* **2019**, *6* (22), 1901372. <https://doi.org/10.1002/admi.201901372>.
- (15) Papadas, I. T.; Savva, A.; Ioakeimidis, A.; Eleftheriou, P.; Armatas, G. S.; Choulis, S. A. Employing Surfactant-Assisted Hydrothermal Synthesis to Control CuGaO₂ Nanoparticle Formation and Improved Carrier Selectivity of Perovskite Solar Cells. *Mater. Today Energy* **2018**, *8*, 57–64. <https://doi.org/10.1016/j.mtener.2018.03.003>.
- (16) Zhang, H.; Wang, H.; Chen, W.; Jen, A. K.-Y. CuGaO₂: A Promising Inorganic Hole-Transporting Material for Highly Efficient and Stable Perovskite Solar Cells. *Adv. Mater.* **2017**, *29* (8), 1604984. <https://doi.org/10.1002/adma.201604984>.
- (17) Wang, J.; Ibarra, V.; Barrera, D.; Xu, L.; Lee, Y.-J.; Hsu, J. W. P. Solution Synthesized P-Type Copper Gallium Oxide Nanoplates as Hole Transport Layer for Organic Photovoltaic Devices. *J. Phys. Chem. Lett.* **2015**, *6* (6), 1071–1075. <https://doi.org/10.1021/acs.jpcclett.5b00236>.
- (18) Kumagai, H.; Sahara, G.; Maeda, K.; Higashi, M.; Abe, R.; Ishitani, O. Hybrid Photocathode Consisting of a CuGaO₂ P-Type Semiconductor and a Ru(II)–Re(I) Supramolecular Photocatalyst: Non-Biased Visible-Light-Driven CO₂ Reduction with Water Oxidation. *Chem. Sci.* **2017**, *8* (6), 4242–4249. <https://doi.org/10.1039/C7SC00940B>.
- (19) Yu, M.; Draskovic, T. I.; Wu, Y. Understanding the Crystallization Mechanism of Delafossite CuGaO₂ for Controlled Hydrothermal Synthesis of Nanoparticles and Nanoplates. *Inorg. Chem.* **2014**, *53* (11), 5845–5851. <https://doi.org/10.1021/ic500747x>.
- (20) Yang, P.; Li, L.; Yu, S.; Zheng, H.; Peng, W. The Annealing Temperature and Films Thickness Effect on the Surface Morphology, Preferential Orientation and Dielectric Property of NiO Films. *Appl. Surf. Sci.* **2019**, *493*, 396–403. <https://doi.org/10.1016/j.apsusc.2019.06.223>.
- (21) Purushothaman, K. K.; Muralidharan, G. The Effect of Annealing Temperature on the Electrochromic Properties of Nanostructured NiO Films. *Sol. Energy Mater. Sol. Cells* **2009**, *93* (8), 1195–1201. <https://doi.org/10.1016/j.solmat.2008.12.029>.
- (22) Brisse, R.; Faddoul, R.; Bourgeteau, T.; Tondelier, D.; Leroy, J.; Campidelli, S.; Berthelot, T.; Geffroy, B.; Jousselme, B. Inkjet Printing NiO-Based p-Type Dye-Sensitized Solar Cells. *ACS Appl. Mater. Interfaces* **2017**, *9* (3), 2369–2377. <https://doi.org/10.1021/acsami.6b12912>.
- (23) Koebel, M. M.; Nadargi, D. Y.; Jimenez-Cadena, G.; Romanyuk, Y. E. Transparent, Conducting ATO Thin Films by Epoxide-Initiated Sol–Gel Chemistry: A Highly Versatile Route to Mixed-Metal Oxide Films. *ACS Appl. Mater. Interfaces* **2012**, *4* (5), 2464–2473. <https://doi.org/10.1021/am300143z>.

- (24) Wang, Z.; Demopoulos, G. P. Nanoscale Photo-Absorbing Kesterite Grown on Anatase Mesoscopic Films by Sequential Binary Chalcogenide Solution Deposition-Exchange, Annealing, and Etching. *Cryst. Growth Des.* **2016**, *16* (7), 3618–3630. <https://doi.org/10.1021/acs.cgd.6b00033>.
- (25) Innocenzi, P.; Malfatti, L. Mesoporous Thin Films: Properties and Applications. *Chem. Soc. Rev.* **2013**, *42* (9), 4198–4216. <https://doi.org/10.1039/C3CS35377J>.
- (26) Ho, Y.-C.; Hoque, M. N. F.; Stoneham, E.; Warzywoda, J.; Dallas, T.; Fan, Z. Reduction of Oxygen Vacancy Related Traps in TiO₂ and the Impacts on Hybrid Perovskite Solar Cells. *J. Phys. Chem. C* **2017**, *121* (43), 23939–23946. <https://doi.org/10.1021/acs.jpcc.7b08384>.
- (27) Renaud, A.; Cario, L.; Deniard, P.; Gautron, E.; Rocquefelte, X.; Pellegrin, Y.; Blart, E.; Odobel, F.; Jobic, S. Impact of Mg Doping on Performances of CuGaO₂ Based P-Type Dye-Sensitized Solar Cells. *J. Phys. Chem. C* **2014**, *118* (1), 54–59. <https://doi.org/10.1021/jp407233k>.
- (28) Bredar, A. R. C.; Blanchet, M. D.; Comes, R. B.; Farnum, B. H. Evidence and Influence of Copper Vacancies in P-Type CuGaO₂ Mesoporous Films. *ACS Appl. Energy Mater.* **2019**, *2* (1), 19–28. <https://doi.org/10.1021/acsaem.8b01558>.
- (29) Farnum, B. H.; Morseth, Z. A.; Brennaman, M. K.; Papanikolas, J. M.; Meyer, T. J. Application of Degenerately Doped Metal Oxides in the Study of Photoinduced Interfacial Electron Transfer. *J. Phys. Chem. B* **2015**, *119* (24), 7698–7711. <https://doi.org/10.1021/jp512624u>.
- (30) Qin, P.; Zhu, H.; Edvinsson, T.; Boschloo, G.; Hagfeldt, A.; Sun, L. Design of an Organic Chromophore for P-Type Dye-Sensitized Solar Cells. *J. Am. Chem. Soc.* **2008**, *130* (27), 8570–8571. <https://doi.org/10.1021/ja8001474>.
- (31) Lu, Y.; Yan, H.; Qiu, K.; Cheng, J.; Wang, W.; Liu, X.; Tang, C.; Kim, J.-K.; Luo, Y. Hierarchical Porous CuO Nanostructures with Tunable Properties for High Performance Supercapacitors. *RSC Adv.* **2015**, *5* (14), 10773–10781. <https://doi.org/10.1039/C4RA16924G>.
- (32) Wang, C.; Li, Q.; Wang, F.; Xia, G.; Liu, R.; Li, D.; Li, N.; Spendelow, J. S.; Wu, G. Morphology-Dependent Performance of CuO Anodes via Facile and Controllable Synthesis for Lithium-Ion Batteries. *ACS Appl. Mater. Interfaces* **2014**, *6* (2), 1243–1250. <https://doi.org/10.1021/am405061c>.
- (33) Bredar, A. R. C.; Chown, A. L.; Burton, A. R.; Farnum, B. H. Electrochemical Impedance Spectroscopy of Metal Oxide Electrodes for Energy Applications. *ACS Appl. Energy Mater.* **2020**, *3* (1), 66–98. <https://doi.org/10.1021/acsaem.9b01965>.
- (34) Sheets, W. C.; Mugnier, E.; Barnabé, A.; Marks, T. J.; Poepelmeier, K. R. Hydrothermal Synthesis of Delafossite-Type Oxides. *Chem. Mater.* **2006**, *18* (1), 7–20. <https://doi.org/10.1021/cm051791c>.
- (35) Srinivasan, R.; Chavillon, B.; Doussier-Brochard, C.; Cario, L.; Paris, M.; Gautron, E.; Deniard, P.; Odobel, F.; Jobic, S. Tuning the Size and Color of the P-Type Wide Band Gap Delafossite Semiconductor CuGaO₂ with Ethylene Glycol Assisted Hydrothermal Synthesis. *J. Mater. Chem.* **2008**, *18* (46), 5647–5653. <https://doi.org/10.1039/B810064K>.

- (36) Boschloo, G.; Hagfeldt, A. Spectroelectrochemistry of Nanostructured NiO. *J. Phys. Chem. B* **2001**, *105* (15), 3039–3044. <https://doi.org/10.1021/jp003499s>.
- (37) Flynn, C. J.; McCullough, S. M.; Li, L.; Donley, C. L.; Kanai, Y.; Cahoon, J. F. Passivation of Nickel Vacancy Defects in Nickel Oxide Solar Cells by Targeted Atomic Deposition of Boron. *J. Phys. Chem. C* **2016**, *120* (30), 16568–16576. <https://doi.org/10.1021/acs.jpcc.6b06593>.
- (38) D'Amario, L.; Jiang, R.; Cappel, U. B.; Gibson, E. A.; Boschloo, G.; Rensmo, H.; Sun, L.; Hammarström, L.; Tian, H. Chemical and Physical Reduction of High Valence Ni States in Mesoporous NiO Film for Solar Cell Application. *ACS Appl. Mater. Interfaces* **2017**, *9* (39), 33470–33477. <https://doi.org/10.1021/acsami.7b01532>.
- (39) Tian, L.; Tyburski, R.; Wen, C.; Sun, R.; Abdellah, M.; Huang, J.; D'Amario, L.; Boschloo, G.; Hammarström, L.; Tian, H. Understanding the Role of Surface States on Mesoporous NiO Films. *J. Am. Chem. Soc.* **2020**. <https://doi.org/10.1021/jacs.0c08886>.
- (40) D'Amario, L.; Jiang, R.; Cappel, U. B.; Gibson, E. A.; Boschloo, G.; Rensmo, H.; Sun, L.; Hammarström, L.; Tian, H. Chemical and Physical Reduction of High Valence Ni States in Mesoporous NiO Film for Solar Cell Application. *ACS Appl. Mater. Interfaces* **2017**, *9* (39), 33470–33477. <https://doi.org/10.1021/acsami.7b01532>.
- (41) Zhao, X.; Chen, J.; Park, N.-G. Importance of Oxygen Partial Pressure in Annealing NiO Film for High Efficiency Inverted Perovskite Solar Cells. *Sol. RRL* **2019**, *3* (4), 1800339. <https://doi.org/10.1002/solr.201800339>.
- (42) Bard, A. J.; Bocarsly, A. B.; Fan, F. R. F.; Walton, E. G.; Wrighton, M. S. The Concept of Fermi Level Pinning at Semiconductor/Liquid Junctions. Consequences for Energy Conversion Efficiency and Selection of Useful Solution Redox Couples in Solar Devices. *J. Am. Chem. Soc.* **1980**, *102* (11), 3671–3677. <https://doi.org/10.1021/ja00531a001>.
- (43) Bisquert, J.; Cendula, P.; Bertoluzzi, L.; Gimenez, S. Energy Diagram of Semiconductor/Electrolyte Junctions. *J. Phys. Chem. Lett.* **2014**, *5* (1), 205–207. <https://doi.org/10.1021/jz402703d>.

Chapter 4

Epitaxially Grown Spinel MnFe_2O_4 and Its Ability to Perform the Oxygen Reduction Reaction

4.1 Introduction

The use of alkaline fuel cells in our changing energy economy relies heavily on Pt as an oxygen reduction catalyst, which is costly for widespread use of this technology.¹ The exploration of new materials that are cheaper and more abundant is important for the availability of this technology. The catalysis of the oxygen reduction reaction (ORR) is complicated by its sluggish kinetics, which result from the need for O_2 to adsorb to the surface of the catalyst, break the $\text{O}=\text{O}$ (498 kJ mol^{-1}), then desorb from the surface, which usually involves several different peroxide or hydroxide intermediates.² There are two pathways for ORR and in alkaline conditions known as the 4-electron and 2x2- electron pathways. These reactions were discussed in Section 1.1.3 of Chapter 1. The 4-electron pathway is thermodynamically more favorable, due to the more efficient conversion of O_2 and the avoidance of peroxide side products, which can be detrimental to other components of fuel cells.³ The challenge of finding alternative catalysts to Pt lie in materials that not only have similar overpotentials, but also have similar selectivity for the 4-electron pathway.

Spinel oxide materials have the chemical formula AB_2O_4 , where the A cation is typically in the 2+ oxidation state and occupies tetrahedral sites in the structure and the B cation is typically in the 3+ oxidation state and occupies octahedral sites. This arrangement of A_{tet} and B_{oct} is referred to as a normal spinel. Depending on the identity of the metal cations, the A metal may also occupy octahedral sites, forcing the B metal to occupy tetrahedral sites. The arrangement is referred to as an inverse spinel where the degree of inversion is maximized when all A metals

occupy octahedral sites. In addition, distortions of the lattice can result from Jahn-Teller effects based on metal site occupancy.

The attractiveness of spinel materials for catalyzing ORR stems from having two metal cations in the spinel structure, which allows for versatility and tunability of the reactivity of these materials depending on the identity of the cations. Many of the elements on the periodic table can be incorporated into the spinel structure giving a large library of materials to explore.⁴ In terms of low cost and abundance, the first row transition metals have been heavily explored as nanomaterials for ORR, and almost all of the first row transition metal spinels show some propensity towards ORR, with some even demonstrating onset potentials that are competitive with Pt.⁵ The ability of these materials to perform ORR lies in the oxidation state promiscuity and the occupation of different coordination sites within the spinel structure. Co, Fe, and Mn for example all have at least two different thermodynamically possible oxidation states that can be utilized when catalyzing the ORR reaction, which is important for charge balance and electron transfer when performing catalysis.⁶ For example, Fe has known oxidation states of 2+, 3+, and 4+ which means reduction of Fe sites in spinel structures introduces excess electrons that can be used to reduce O₂. Studies have also showed that the occupation of octahedral or tetrahedral sites for different cations will change the catalyst ability to perform ORR.^{7,8}

The exploration of almost all ORR catalysts has typically been done with nanocrystalline materials on a carbon support. The carbon support seems important to enhancing the conductivity and stability of the metal oxide catalyst, but also seems to perform ORR as well, albeit less efficiently.^{2,9,10} The complexities of this system make it difficult to understand the contribution of just the spinel metal oxide to the ORR capabilities of the surface and its true catalytic activity. Understanding the intrinsic thermodynamics and kinetics of the ORR reaction

on spinel metal oxide surfaces is important to understanding the mechanism of ORR with spinel metal oxides. Surface studies of metal oxides for ORR have been achieved in the literature by studying epitaxially grown films.^{11–15} In these studies, a complex oxide thin film is grown on a conductive substrate, which can then be made into an electrode to study the electrochemical properties of the materials. Notably, most ORR studies on epitaxially grown materials have been done on noble metals or perovskite oxides. This most likely stems from the availability of substrates on which to grow epitaxial films. Because the substrate needs to be conductive, either a metal substrate, such as gold, platinum, or palladium, or a doped metal oxide must be used. The lattice parameters of the substrate material will influence the epitaxial growth of the desired material, so understanding how this influences growth is important to the resulting functionality of the catalyst. Of the doped oxide substrates the most common is niobium doped-strontium titanate (Nb:SrTiO₃, Nb:STO) which has the perovskite crystal structure, and has been used for studying epitaxial perovskite oxides for ORR. To our knowledge, there are no examples in the literature of epitaxially grown spinel films that have been studied for ORR.

This chapter describes the study of ORR on epitaxially grown MnFe₂O₄, which has been studied significantly as nanocrystals for ORR catalysis.^{5,16–19} The epitaxial films studied were prepared using molecular beam epitaxy (MBE), a common epitaxial growth method which was discussed more in Section 1.3.3 of Chapter 1. MnFe₂O₄ has been grown epitaxially using MBE previously²⁰, but not specifically for the study of ORR catalysis. Once grown, the films were made into electrodes using a rotating disk electrode (RDE) mount, shown in **Figure 4.1**. This is the first study to our knowledge of MnFe₂O₄ grown on a perovskite substrate and provides insight into the specific mechanism through which MnFe₂O₄ catalyzes ORR. This study is also

beneficial as we continue to research heterojunction epitaxial films, by combining spinel and perovskite materials, as potential bifunction catalysts for OER and ORR.

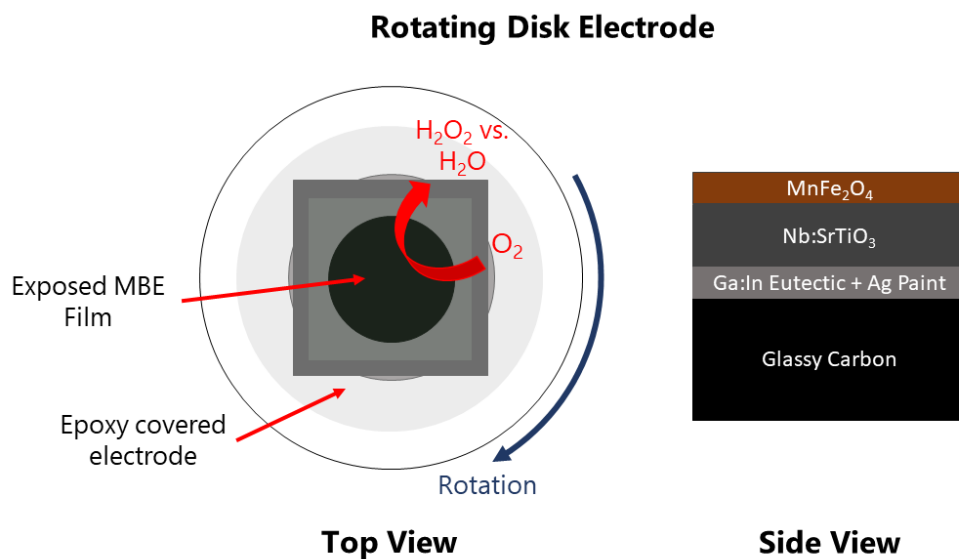


Figure 4.1: Diagram of electrode used to study MnFe_2O_4 epitaxial films for ORR catalysis.

4.2 Experimental

4.2.1 Synthesis of MnFe_2O_4 Films MnFe_2O_4 films were grown on either (001)-oriented or (111)-oriented niobium-doped SrTiO_3 , ($\text{Nb}:\text{STO}$, 0.7 wt%) conductive cubic perovskite substrates using molecular beam epitaxy (MBE) (Mantis Deposition). Substrates were sonicated in acetone and isopropyl alcohol for 5 minutes each before being loaded into the MBE chamber. Mn and Fe metals were deposited concurrently during growth and effusion cells were kept at constant temperature, with deposition rates calibrated using a quartz-crystal microbalance pre-growth. The sample stage was heated to a constant temperature using an infrared ceramic heating source and measured via a thermocouple on the stage, which causes an overestimation of $\sim 50\text{-}100$ °C relative to the substrate surface temperature. Samples were grown at 525 °C setpoints and subsequently cooled to ambient temperatures over ~ 30 minutes. O_2 gas was introduced into the chamber and maintained at $\sim 7.0 \times 10^{-6}$ Torr during film growth and cooling.

4.2.2 Characterization of $MnFe_2O_4$ Films Reflection high-energy electron diffraction (RHEED), a technique sensitive to the first few atomic layers of a film surface, was used to monitor the growth process. After growth, samples were analyzed using x-ray photoelectron spectroscopy (XPS, PHI 5400 refurbished by RBD Instruments). The XPS system was connected to the MBE chamber by vacuum transfer line to prevent atmospheric contamination. A monochromatic Al $K\alpha$ x-ray source, an electron pass energy of 35.75 eV and a scanning step size of 0.05 eV was used for all samples. The conductivity of the Nb:STO substrates negated the need for an electron emission neutralizer for sample charge compensation. All spectra were shifted accordingly to place their O 1s metallic oxygen bond peaks at 530.0 eV binding energy. O 1s spectra for samples before atmosphere exposure were fit with one metal-oxygen peak. Spectra for samples after exposure were fit with two peaks, one for metallic oxygen and one at higher binding energy representing all atmospheric contamination effects (**Figure A4.2**). Atomic force microscopy (AFM) was used to acquire images of film topography, and were acquired using a Park XE7 AFM in non-contact mode.

4.2.3 Electrocatalytic studies of $MnFe_2O_4$ Films Electrodes were constructed from $MnFe_2O_4$ films by mounting films on RDE tips with a glassy-carbon-disk working electrode (Pine Research, 5 mm diameter) as the contact material, shown in **Figure 4.1**. The electrode was constructed using Ga:In eutectic (99.99%, sigma Aldrich) and silver paint (Ted Pella). A drop of Ga:In eutectic was placed in the middle of the glassy carbon electrode to make the electrical contact to the backside of the Nb:STO. Before the film was placed, a “moat” of Ag paint was placed around the eutectic. The Ag paint is used as a conductive adhesive, so the film sticks to the glassy carbon surface. The eutectic is there to further improve the contact. The film is placed on the eutectic and paint and allowed to dry for 30 minutes. Once the film cannot be moved with

gentle pressure an inert epoxy (Loctite D-609) is used to cover the film, making sure any exposed glassy carbon, eutectic, and Ag paint are covered so they do not interfere with electrochemical measurements. The epoxy is placed such that the edge of the Nb:STO substrate is covered as well, leaving only exposed MnFe_2O_4 film. The epoxy is left to dry at room temperature for at least 24 hours before submersion in electrolyte. The area of the exposed film was measured using ImageJ software.

All electrochemical measurements were performed in 0.1M KOH as the electrolyte. A Hg/HgO reference electrode was used and checked against ferricyanide for every experiment for accurate conversion to RHE, which all potentials are reported against. All CVs and RDE experiments were performed using a WaveDriver 20 bipotentiostat (Pine Research) with an MSR rotator (Pine Research). All EIS experiments were performed using a Gamry 1010E potentiostat. For non-catalysis electrochemistry N_2 (UHP 99.999%, Airgas) was purged into the solution for at least 30 minutes. For ORR measurements O_2 (UHP 99.999%, Airgas) was purged into the solution for at least 30 minutes. Pt/C (20 wt%, Fuel Cell Store) was purchased to perform standard experiments to assess our electrochemical setup.

4.3 Results

MnFe_2O_4 spinel was successfully grown on Nb:STO substrates. The films were grown on 10 mm x 10 mm substrates, then subsequently diced into 5 mm x 5 mm pieces so that different methods characterization could be performed. For the purpose of this chapter, experiments were performed on three different spinel films: MnFe_2O_4 grown on (001) Nb:STO at ~5 nm thickness, on (001) at ~20 nm thickness, and on (111) Nb:STO at ~5 nm thickness. These thicknesses are estimated based on growth time of the films, but still need verification via XRD. Initial

determination of the growth success was done by in situ RHEED analysis, which can determine the crystallinity and surface morphology of the material based on the scattering of electrons from the film surface. **Figure 4.2a** and **4.2b** show RHEED analysis of MnFe_2O_4 5 nm (001) and 5 nm (111) films. MnFe_2O_4 grown on (001)-oriented Nb:STO show that films form (001)-oriented spinel structures with island-like surface quality, while MnFe_2O_4 grown on (111)-oriented Nb:STO forms a (111)-oriented spinel structure with both island and planar-like surface quality. This is indicated by the spotted pattern for MnFe_2O_4 grown on the (001) film, as opposed to the lines with some spots for the film grown on the (111) surface. The RHEED pattern for films grown on the (001) substrates is the same regardless of thickness with the RHEED for 20 nm MnFe_2O_4 on (001) Nb:STO is shown in **Figure A4.1**. For all films used in this study, the RHEED patterns obtained during growth monitoring showed little change, indicating that the orientations are uniform throughout the films, and indicates their single crystalline quality. AFM analysis, shown in **Figure 4.2c** and **4.2d**, further verifies RHEED results, as the root mean square roughness for the (001) films is greater at 3.2 nm, compared to 1.0 nm for the (111) film. AFM for 20 nm MnFe_2O_4 on (001) can be found in the appendix (**Figure A4.1**).

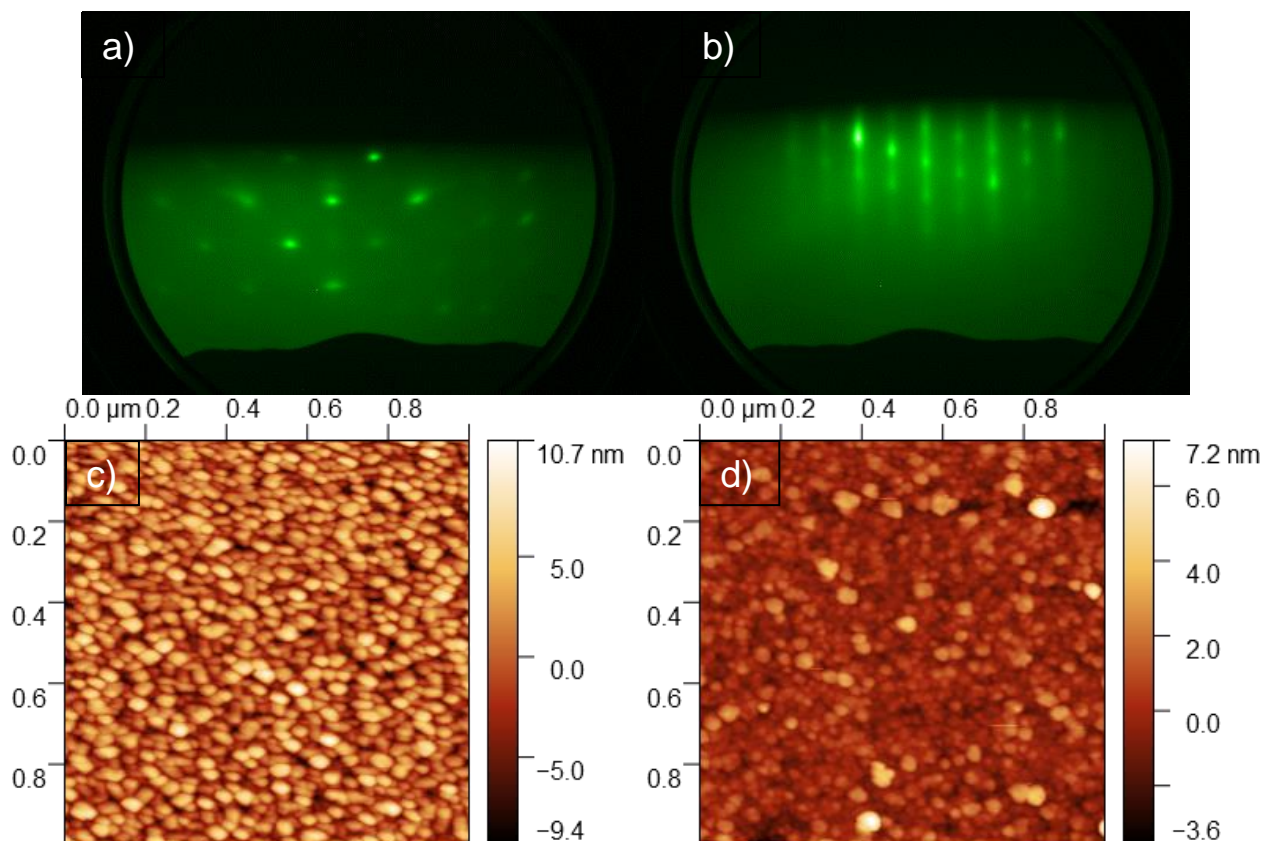


Figure 4.2: a)-b) RHEED and c)-d) AFM analysis of MnFe_2O_4 films grown on (001) and (111) substrates.

XPS analysis of the films was performed to characterize the composition of the films, including stoichiometry and metal oxidation states to further confirm the synthesis of a spinel. XPS data for Mn 2p, and Fe 2p are shown in **Figure 4.3**, with stoichiometry results found in **Table 4.1**. The percentages shown in **Table 4.1** are based on total metal content excluding oxygen. It should be noted that all spectra in XPS are normalized, so the absolute peak intensity is unrelated to stoichiometry. The Mn-Fe stoichiometry for samples still under vacuum was determined by comparing areas of the Mn 2p and Fe 2p regions after implementing Shirley background subtraction and sensitivity factors of 2.42 and 2.686, respectively. Reliable stoichiometry determination from XPS is difficult without MnFe_2O_4 standards, and atomic concentration determined from XPS here should be considered as a high-Mn bound and low-Fe

bound. A perfect MnFe_2O_4 spinel composition should be 33.3% Mn^{2+} and 66.7% Fe^{3+} . Both (001) samples and the (111) sample under vacuum show very similar spectral features, indicating that the oxidation states of the Mn and Fe are consistent across the films. The Mn $2p_{3/2}$, located around 641 eV has a satellite peak around 647 eV, which indicates a Mn^{2+} oxidation state²¹. Fe $2p_{1/2}$, positioned around 726 eV, has a satellite peak (733 eV) that indicates that Fe is in a 3+ oxidation state.²² The stoichiometry of the films under vacuum does vary from film to film, with both 5 nm films showing a Mn excess, and the 20 nm film showing Mn deficiency. These films were also characterized using EDS to obtain stoichiometry for comparison (**Table A4.1**) and shows similar stoichiometric values, but with higher at% of Fe.

Table 4.1: Stoichiometry from XPS

XPS	Mn/Fe at%	Mn at%	Fe at%
5 nm (001) Vacuum	0.619	38.2	61.8
5 nm (111) Vacuum	0.517	34.1	65.9
20 nm (001) Vacuum	0.449	31.0	69.0
20 nm (001) Air Exposed	0.393	28.2	71.8
20 nm (001) Post-Catalysis 1	0.312	23.8	76.2
20 nm (001) Post-Catalysis 2	0.331	24.8	75.2

For 20 nm MnFe_2O_4 (001) films the XPS spectra were compared for three conditions: under vacuum immediately following synthesis, exposed to air, and after catalysis. Due to changes in the spectra shape, particularly the $2p_{1/2}$ regions for both Mn and Fe, stoichiometry for post-catalysis samples could not be reliably determined from the entire Mn and Fe 2p regions as was done for the samples under vacuum. Instead the ratio of the areas for the Mn $2p_{3/2}$ and Fe $2p_{3/2}$ regions were used, and the vacuum calculation was used as a reference of known stoichiometry (fitting example found **Figure A4.4**). All of the air exposed and post catalysis samples showed a

significantly higher Mn deficiency, or a higher Fe content, similar to what is seen in the stoichiometric calculations from EDS. For the post-catalysis samples the Mn deficiency could be due to removal of Mn from the film due to etching during catalysis, although equal etching of both Mn and Fe would be expected. The films analyzed post-catalysis were both mounted on the RDE tip with different amounts of epoxy coverage to test how this affected film stability. Post-catalysis film 1 had only minimal epoxy coverage, leaving some Nb:STO substrate exposed, while post-catalysis film 2 was covered such that only the MnFe_2O_4 film was exposed. It was found that post-catalysis film 1 now had peaks related to Sr and Ti appearing in the XPS spectra, which can be seen in the C 1s region (**Figure A4.5**), indicating etching of the film surface. The peaks were not present in the vacuum sample nor used film 2. This result indicates that the MBE film is susceptible to etching at the junction of the film and the substrate.

In post-catalysis analysis it was also important to determine if the oxidation state of the Mn or Fe changed due to electrochemical cycling or degradation. Mn 3s spectra are comprised of two peaks, and the binding energy separation between them can be used to determine Mn valence.²³ In these spectra, large Fe 3s peaks overlap with the higher binding energy Mn 3s peak, making definite oxidation state determination from Mn 3s unreliable for MnFe_2O_4 . However, trends in separation would indicate a change in oxidation state for samples where catalysis was performed. Specifically, if there was a decrease in peak separation between samples this would indicate a change in oxidation state from Mn^{2+} to Mn^{3+} . However, samples showed an increase in Mn 3s peak separation after catalysis was performed, indicating the oxidation state remains Mn^{2+} (**Figure A4.3**).

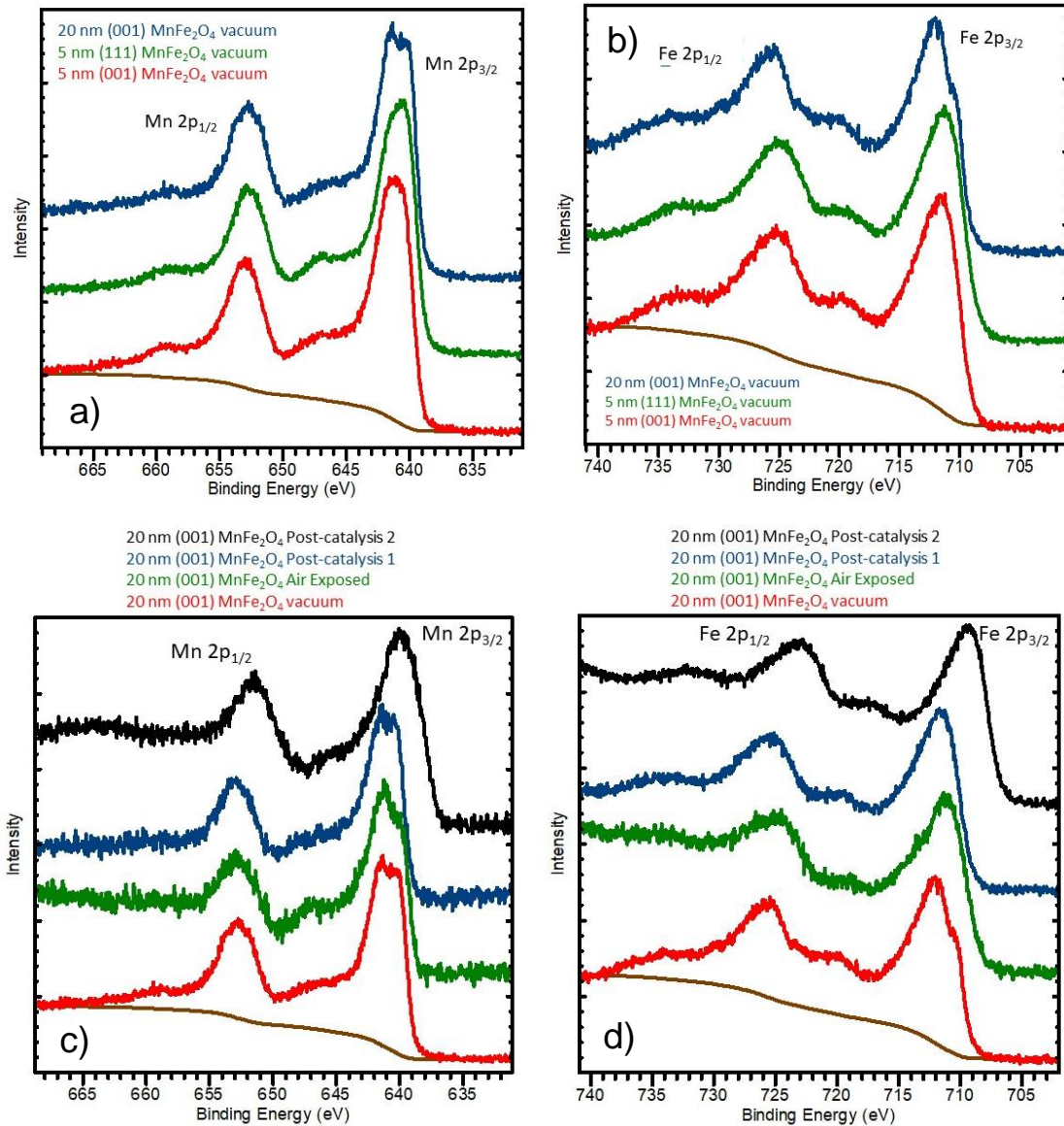


Figure 4.3: XPS of a) Mn 2p region and b) Fe 2p region for 20 nm (001), 5 nm (001), and 5 nm (001). c) XPS of c) Mn 2p region and d) Fe 2p region of 20 nm (001) MnFe₂O₄ after air exposure and catalysis.

The electrode design of the films was important in several ways. First, a good electrical contact needed to be made to the Nb:STO substrate in order to be able to properly study the MnFe₂O₄ film. The materials used to make the electrical contact has been used previously for similar studies on perovskite films for ORR. Second, the film needed to be covered such that the underlying GC disk, conductive silver paint, or Ga:In eutectic were not exposed as they could

significantly influence the resulting electrochemistry. For this reason, an electrically and chemically inert epoxy was used to coat the edges of the film. As mentioned above, covering any exposed substrate was found to be very important to the electrochemical stability of the films. **Figure A4.6** shows cycling of the film with the Nb:STO edge exposed and it can be seen that in only 20 cycles there is a significant reduction of the current and the electrochemical features present in the CV, consistent with the XPS spectra showing peaks related to the underlying substrate. Knowing the film surface area is extremely important for analyzing catalytic measurements of films, and the use of epoxy to coat the electrode reduces the area of the film exposed for electrochemistry. ImageJ software was used to estimate the surface area of the film exposed.

Before the films were exposed to oxygen for ORR testing, CVs of the films were measured under N_2 to understand their basic electrochemical features related to $MnFe_2O_4$. The electrochemical experiments were performed on the exact films that were characterized and discussed above. We note that these films were a commodity, and films could only be studied once in solution before the electrochemical features changed significantly. Therefore, significantly oxidizing and reducing potentials were avoided to prevent degradation of the films. Studies of bare Nb:STO were performed as well, and indicate that there is no contribution from the substrate on the electrochemical features observed (**Figure A4.7**).

Figure 4.4a shows CVs for $MnFe_2O_4$ on the 5 nm (111), 5 nm (001), and 20 nm (001) films. Despite their different surface roughness and thickness the CVs are very similar. There are 2 quasi-reversible redox features at 0.96 V and 0.62 V vs RHE. These quasi-reversible features have been observed in CVs of $MnFe_2O_4$ nanocrystals on carbon black, and their position is consistent with what we have observed in our films.^{16,24} Both features have previously been

assigned to the oxidation and reduction of Mn sites in MnFe_2O_4 nanocrystals, as the redox potentials for Fe are more negative.^{16,25,26} Comparing the 5 nm thick films, it was observed that the (001) film passed more current than the (111) film, even after the CVs were normalized for area. This is consistent with the (001) films having a larger surface roughness, as measured from AFM, compared to the (111) film.

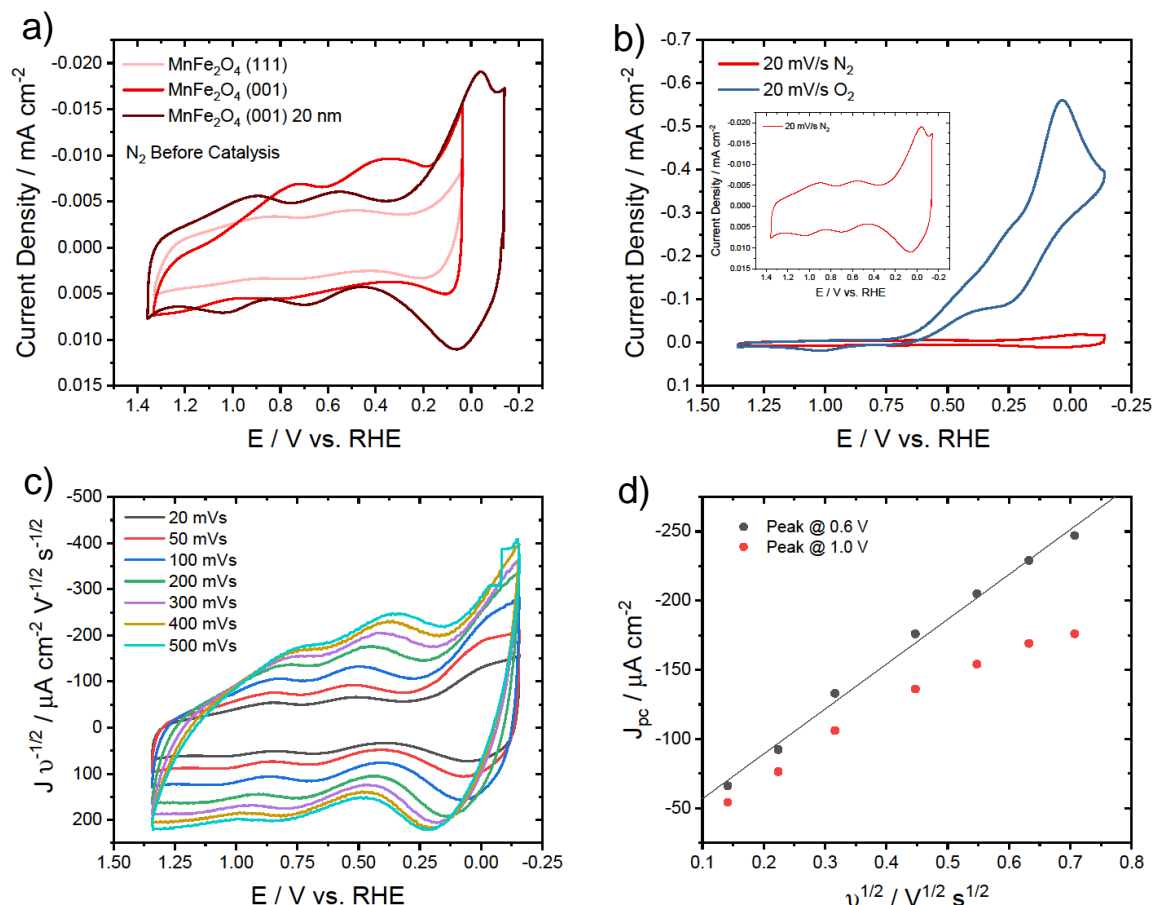


Figure 4.4: a) CVs comparing MnFe_2O_4 films grown on (001) and (111) substrates. b) CV of 20 nm (001) MnFeO_2 under O_2 and N_2 before RDE experiments. c) CVs of MnFe_2O_4 at 20, 50, 100, 200, 300, 400, and 500 mV/s scan rates, and normalized to the square root of the scan rate. d) Peak currents for the cathodic peaks vs the square root of the scan rate showing a linear relationship.

When probed under different scan rates these features show linear dependence on the square root of the scan rate, consistent with electron transfer involving a diffusion event. **Figures 4.4c** and **4.4d** show the CVs normalized to the square root of the scan rate, and the linear dependence

of the cathodic peak current with $v^{1/2}$, respectively. The cathodic peak at 1.0 V vs RHE does not have the same linear dependence as the peak at 0.6 V, but this appears to be because the potentials were not scanned positive enough to fully resolve the wave. Given the dependence on diffusion with respect to the redox features, it is most likely that they are related to Mn site oxidation and reduction stabilized by the formation of surface hydroxides. The distinction of two separate Mn redox features could be contributed to the proclivity of Mn to occupy both tetrahedral and octahedral sites in the MnFe_2O_4 structure.²⁷

Figure 4.4b shows CVs of the (001) 20 nm MnFe_2O_4 film saturated with O_2 , compared to the CV under N_2 . Under O_2 the film shows a significant increase in current, indicative of their catalytic reactivity towards O_2 . This increase appears to start concurrently with the second manganese feature, although a true peak for O_2 reduction is not observed until 0.03 V vs RHE. This increase in O_2 also occurs for the 5 nm (001) and (111) film, but the CVs were not initially scanned negative under O_2 to resolve the wave (**Figure A4.8**). CVs under N_2 after catalysis studies were scanned more negative and show two redox features in the range that O_2 reduction appears to be occurring (**Figure A4.9**). These features are most likely related to oxidation and reduction of iron sites in the MnFe_2O_4 structure. Either the exposure to the alkaline conditions of the electrolyte, or the process of performing ORR is changing the film surface in some way. In particular, the CV for 20 nm (001) looks significantly different, as a sharp peak arises that is present both under N_2 and O_2 . After completion of these experiments, the 20 nm (001) film was removed from solution for repeat electrochemical analysis. As shown in **Figure A4.10**, the film was significantly less catalytic in the secondary electrochemical experiment than it was upon initial catalysis.

For a true understanding of the catalytic abilities of MnFe_2O_4 films, RDE experiments were performed. Under O_2 saturation, rotation of the films allows for separation of electron transfer controlled and diffusion limited processes, particularly for reactions like O_2 reduction, which have inherently slow kinetics for electron transfer. Both (001) films and (111) 5 nm MnFe_2O_4 films were studied at varying rotation rates to perform a Koutecky-Levich analysis, shown in **Figure 4.5**. We note that proper Koutecky-Levich analysis requires smooth hydrodynamic flow of the electrolyte over the electrode surface for extraction of proper data.²⁸ We believe that the data do not deviate significantly from the proper flow required for analysis, given the quality of the data we obtain, but we note that there is more noise in our rotation data than is typically seen for perfectly flat surfaces. In order to have comparable numbers to other literature reports of MnFe_2O_4 ORR catalysis, 20 mV/s was used as the scan rate for all rotations. RDE experiments show that the current increases with increasing rotation rate, as expected. At all rotation rates it is apparent that diffusion limited current is being achieved. From the polarization curve at 1600 RPM, the maximum current for 5 nm (001), 20 nm (001), and 5 nm (111) films are -5.2 mA/cm^2 , -5.3 mA/cm^2 and -5.3 mA/cm^2 , respectively, showing that all films pass the same current at the same rotation rate. The $E_{1/2}$ of the main reduction wave, defined at half the maximum current, is 0 V for 5 nm (111), slightly more negative at -0.02 V for 5 nm (001), and 0.042 V for 20 nm (001) MnFe_2O_4 . The E_{onset} for any chemical process must be defined at a specific amount of current passed. Typically, the ORR literature has defined this current as $10 \mu\text{A/cm}^2$, which would result in $E_{\text{onset}} = 0.77 \text{ V}$, 0.74 V , and 0.68 V for 20 nm (001), 5 nm (001), and 5 nm (111) films respectively. However, that onset is not consistent with the large increase in current observed for the large take off for ORR. The onset of the large wave was measured where $500 \mu\text{A/cm}^2$ of

current were passed, giving $E_{\text{onset}} = 0.22$ V for 20 nm (001), 0.12 V for 5 nm (001), and 0.15 V for 5 nm (111) MnFe_2O_4 films.

RDE data was then converted to Koutecky-Levich plots, by plotting the inverse of current density (J^{-1}) vs. the square root of angular frequency of rotation ($\omega^{1/2}$), to yield a linear relationship. At large overpotentials, the kinetic limitations of the system should be minimized, giving intercepts that are close to zero. At lower overpotentials, larger intercepts are yielded because there is a greater kinetic limitation to performing the electron transfer reaction. The slope of the line should be the same at every potential if the reaction is only dictated by diffusion of O_2 to the electrode surface followed by electron transfer. This slope can be used to solve for the number of electrons transferred based on the Koutecky-Levich equation (**Equation 4.1**). Here, n is the number of electrons transferred at the electrode surface, F is Faraday's constant ($96,486 \text{ C mol}^{-1}$), C_0 is the saturation concentration of O_2 in 0.1 M KOH at 1 atm of O_2 pressure ($1.26 \times 10^{-6} \text{ mol cm}^{-3}$), D_0 is the diffusion coefficient of O_2 in 0.1 M KOH ($1.93 \times 10^{-5} \text{ cm}^2 \text{ s}^{-1}$), ν is the kinematic viscosity of the 0.1 M KOH electrolyte ($1.09 \times 10^{-2} \text{ cm}^2 \text{ s}^{-1}$), and ω is the rotation rate in rad s^{-1} .

$$4.1) J_L = 0.62nFC_0(D_0)^{2/3}\nu^{-1/6}\omega^{1/2}$$

Figure 4.5d-f show Koutecky-Levich plots for 20 nm (001), 5 nm (001), and 5 nm (111) MnFe_2O_4 films. Polarization curves for the 20 nm (001) and 5 nm (111) film were scanned more negative than for the (001) film, but the Koutecky-Levich plots were made from the same data range for both films. Over the same potential range, it can be seen that the plots are similar, but the 20 nm (001) and 5 nm (111) films have better linearity at smaller overpotentials compared to the 5 nm (001) film. The 20 nm (001) film shows the smallest change in current with potential, consistent with having a sharper onset for ORR. The slopes of the Koutecky-Levich plots were

measure at -0.25 V vs RHE and are 2338, 2068, and 2228 $\text{A}^{-1} \text{cm}^2 \text{S}^{1/2} \text{rad}^{-1/2}$ for 20 nm (001), 5 nm (001) and 5 nm (111) respectively. Using the literature values for C_0 , D_0 , and v that were listed above, the electron transfer number was calculated from the slope of the Koutecky-Levich plots of each film. Electron transfer numbers are shown in **Table 4.2**. All films showed electron numbers close to 4, which strongly indicates a preference for the direct 4-electron reduction pathway for O_2 as opposed to the 2 x 2 electron pathway that produces H_2O_2 as a byproduct.

Table 4.2: Electron transfer (n), exchange current density, and rate constants (k) for MnFe_2O_4 film ORR

Film	n value	Exchange current density	Rate constant
20 nm (001)	3.71	2.95×10^{-8}	6.54×10^{-8}
5 nm (001)	4.2	7.98×10^{-11}	1.56×10^{-10}
5 nm (111)	3.9	1.03×10^{-10}	2.17×10^{-10}

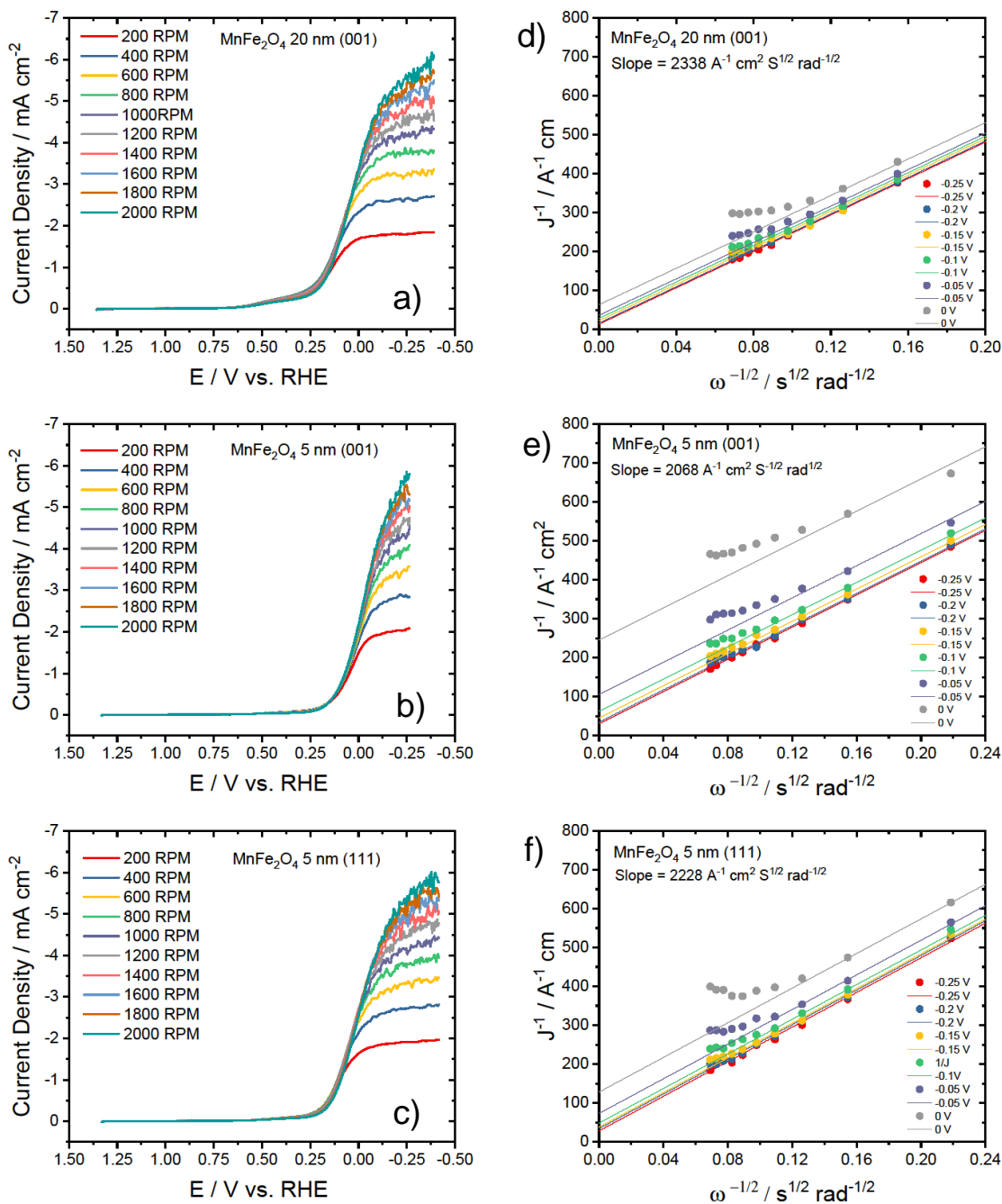


Figure 4.5: Polarization curves at different rotation rates for a) 20 nm (001), b) 5 nm (001), and c) 5 nm (111) MnFe_2O_4 in 0.1M KOH saturated with O_2 . Koutecky-Levich plots for d) 20 nm (001) e) 5 nm (001), and f) 5 nm (111) MnFe_2O_4 films.

To better understand the reaction rate for O_2 reduction at the MnFe_2O_4 surface Tafel analysis was performed. Tafel analysis is used to understand how a reaction rate is dependent on the overpotential applied to the system and is measured in the regime dominated by the kinetics for

electron transfer of a chemical reaction. From these plots, a Tafel slope can be measured as well as an exchange current density. The Tafel slope is a measure of how the overpotential will change the reaction rate and is determined by the rate limiting step in a reaction mechanism.²⁹ The exchange current density is that which occurs at zero overpotential, which can be used to extract a rate constant for an electrochemical process.²⁹

The Tafel plots for the MBE films studied were formed by plotting the overpotential applied (potential applied vs RHE – 1.23 V) vs log of the current density (**Figure 4.6**), which was done using the polarization curve at 1600 rpm. Two possible kinetic regions are observed in the Tafel plots: -0.58 to -0.7 V, and -1.0 to -1.2 V overpotential range, which corresponds to 0.65 to 0.53 V vs RHE and 0.23 to 0 V vs RHE. This is concurrent with where we see rises in current in the RDE polarization plots, and these regions overlay fairly well at all rotation rates (**Figure A4.12**). Tafel slopes were calculated for both kinetic regions and are listed in the plots. The first kinetic region occurs in the range of the Mn redox waves and is most likely related to catalysis at these sites. The Tafel slope for this region is small for the 20 nm (001) MnFe₂O₄, and largest for the 5 nm (001). The second kinetic region, most likely related to Fe-mediated ORR catalysis, has the smallest Tafel slopes for both 5 nm films, and the largest for the 20 nm (001) film.

The extrapolation of the Tafel slopes to zero overpotential yields the exchange current densities, which can be used to calculate a rate constant using **Equation 4.2**, where n is calculated from the slope of the Koutecky-Levich plots, F is Faraday's constant, and C_0 is the saturation concentration of O₂ in 0.1 M KOH. Rate constants were only calculated for the Tafel slope measured at more negative overpotentials, as this region clearly leads to a diffusion limited regime in which the calculated electron transfer number is more confident. The exchange current

densities and the resulting rate constants are listed in **Table 4.2**. The largest rate constant is measured for the 20 nm (001) and the smallest for the 5 nm (001) film.

$$4.2) J_k = nFkC_0$$

All Koutecky-Levich and Tafel analysis was performed with purchased Pt/C in the same electrolyte to have a comparison for the data. The data for these studies are shown in **Figure A4.11**. Notably, the calculated electron transfer number calculated for Pt/C is ~ 5 , the Tafel slope calculated was 86 mV/dec, and the exchange current density was 4.9×10^{-9} . These numbers do deviate from other literature reports of Pt/C, but were calculated using the same methods used for our MBE films.

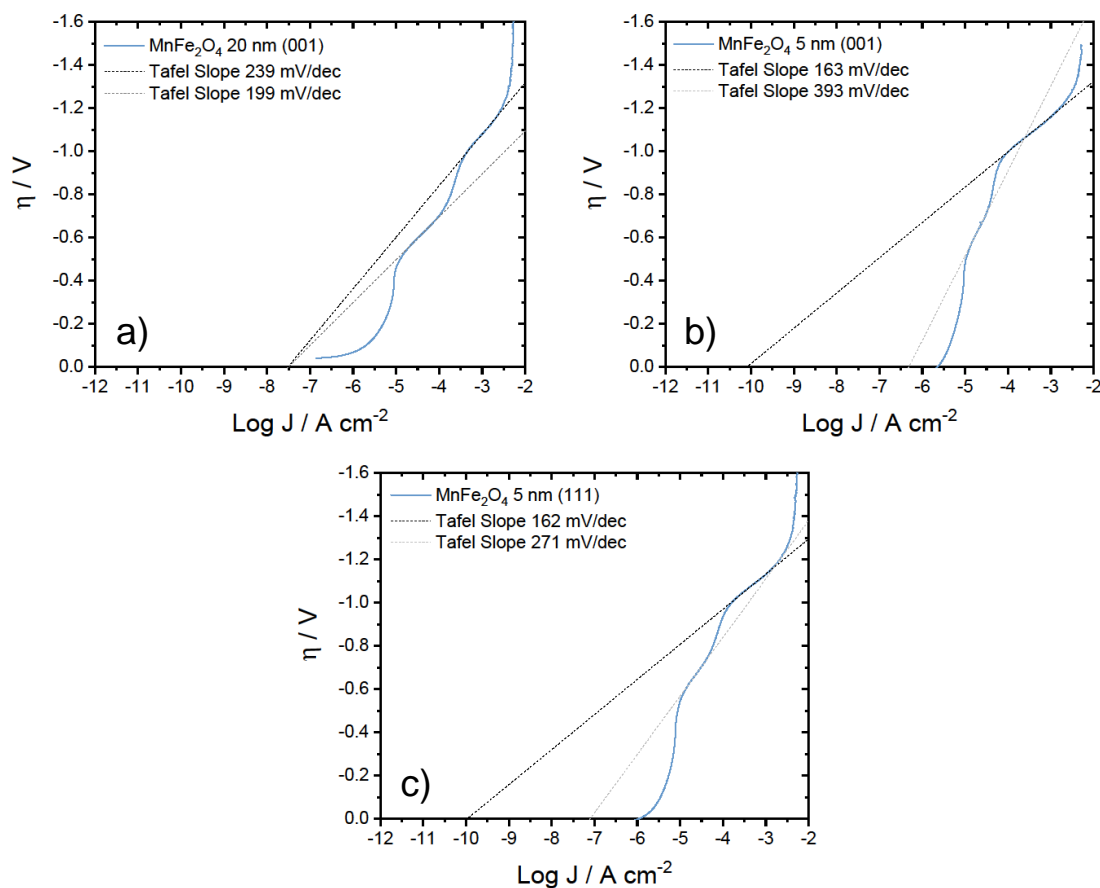


Figure 4.5: Tafel plots of a) 20 nm (001), b) 5 nm (001), and c) 5 nm (111) MnFe₂O₄. The Tafel plots were produced using the polarization plots for RDE at 1600 RPM.

4.4 Discussion

The study of ORR on epitaxial films, such as noble metals and perovskites, has been achieved in the literature^{12–14,26,30,31}, but this is the first report of epitaxial grown MnFe_2O_4 studied for ORR. Previous reports of ORR catalysis studies on noble metal films, which were placed directly in the electrode configuration like a normal glassy carbon or Pt disk electrode, have been reported.^{11–13} This could not be done with our MBE films, therefore modification of the RDE method was necessary, and was done using conductive contacts that have been used for other electrode designs.^{14,32} This allows for true rotational studies of these films, which is important for ORR characterization.

The growth of MnFe_2O_4 spinels with MBE has been previously reported^{20,33}, as well as MBE growth of Fe_3O_4 on a perovskite substrate, where Moyer et. al. observe similar surface growth patterns, such as island growth, for those spinel films.³⁴ This is most likely due to the surface energy of spinel structures, where the (111) surface has been found to be the lowest energy surface.³⁵ On (001) MgAl_2O_4 substrates the films are planar and 2D, indicating that lattice mismatch between the perovskite substrate and the spinel film forces the island growth to occur, most likely to reduce lattice strain. The island growth could induce some faceting, where the islands consist of (111) or (110) facets. To gain insight into the composition of the films, scanning tunneling electron microscopy will be performed, as well as XRD which can help identify crystal facets and give film thicknesses for the films that were studied. This is important for further characterizing how the films perform ORR catalysis.

In several studies of ORR, investigation of faceting has been performed to understand which crystal faces will perform the best.^{36–40} The active site for a catalyst depends significantly on the coordination environment of the metal cation and exposure of that active site, which can have

different confirmation depending on the exposed crystal facet. It has been found that the (111) facet of spinels are more active than (001)³⁷, and we expected this to reflect in our studies of the single crystalline films. However, the superiority of the (111) facet is inconclusive in our study. The difference in onset potential at 500 $\mu\text{A}/\text{cm}^2$ between the 5 nm films is only 30 mV, while the 20 nm (001) film has an onset 100 mV more positive than both films. This indicates that there is a thickness dependence on the onset potential for these MBE films. This is most likely due to exposure of more active sites that can catalyze ORR, consistent with the (001) films having a higher roughness factor, which translates to a higher surface area. Comparing the 5 nm films, the data seems to indicate that the 111 film could be slightly more catalytically active, but the difference is marginal.

The better onset potential for the 20 nm (001) film does not translate to a higher electron transfer number. The 20 nm (001) film had the lowest electron transfer number of 3.7, while the 5 nm (001) had the highest electron transfer number of 4.2. While electron transfer numbers under 4 could indicate a mixture of the 4-electron and 2 x 2- electron pathways, a number greater than 4 is more unusual. Numbers greater than 4 have been reported in the literature for Pt/C⁴¹, and this is most likely due to error in the measurement. Regardless, these films have high selectivity for the 4-electron pathway, which limits the formation of H₂O₂. Peroxide can be detrimental to fuel cell performance, so catalysts that limit its formation are preferable. The slightly larger electron transfer numbers could be related to film thickness, where charge transport through the 20 nm film could be more challenging, limiting the electron transfer number. The effect of thickness on perovskite epitaxial films has been investigated and it was found that films that are too thin are limited in their ORR activity.¹⁴ Our findings are somewhat

similar in terms of onset potentials, but the selectivity for the 4-electron pathway does not seem to be limited by thickness.

In most studies of spinel ORR it has been found that there is a trend in the occupation of octahedral sites in the spinel structure and the activity of the ORR catalyst.^{5,24,42} This is related to the oxidation state of the metal, as well as e_g orbital occupancy, where it has been found for Mn that it shows better ORR activity in its high spin, 3+ oxidation state, because its subsequent reduction to Mn^{2+} is favorable.⁴² Spinels are particularly interesting case study for this phenomena, because the structure and occupation of ions in tetrahedral or octahedral sites can vary significantly due the ability of the structures to invert. In a study of the identity of the 3+ cation and its contribution to catalysis, Co-based and Mn-based spinels were found to have a normal spinel structure, with Mn spinels having a tetragonal distortion due to Jahn-Teller effects of the 3+ cation in the octahedral site.⁵ Fe-based spinels, however, have a higher tendency to form the inverse spinel, which gives ferrite spinels the unique property of having two different metals on octahedral sites.⁵ While the identity of the A-site cation, which can affect the degree of inversion, has been studied for ORR catalysis in ferrite spinels, there is no consensus on which ferrite spinel actually performs the best. One study found that $CoFe_2O_4$ is the best ferrite catalyst⁵, while another gives the title to $MnFe_2O_4$.¹⁶ This could be due to difference in synthesis methods and catalyst preparation, which further highlights the need for more detailed study of pure spinel materials. Interestingly between these two materials, $CoFe_2O_4$ has a fully inverse spinel structure, which has been found to be important for its catalytic ability⁷, while $MnFe_2O_4$ should only be about 20% inverted.²⁷

Most nanocrystalline studies of $MnFe_2O_4$ characterize it as fully inverse, based on its XRD pattern. The synthesis of the $MnFe_2O_4$ nanocrystals could certainly influence the degree of

inversion. In a study of MnFe_2O_4 nanorods it was found using Mossbauer spectroscopy that the degree of inversion was around 70% as opposed to the expected 20%.⁴³ It was proposed that the significantly higher inversion could be due to Mn^{2+} reducing Fe^{3+} to Fe^{2+} , thus increasing the concentration of Mn^{3+} which strongly prefers octahedral sites. This has also been measured for MnFe_2O_4 nanocrystals used for ORR, using XPS.⁸ The defect tolerance in nanocrystalline materials is significantly higher than that of single crystalline materials, and different synthesis methods could influence the redox potentials of the metal cations and how they incorporate into the spinel structure. With MBE growth, most defects are going to be the result of lattice mismatch between the substrate and the resulting film. There is little evidence of Mn^{3+} from XPS measurements for our films, even in samples after catalysis was performed, so it is unlikely that there is a higher degree of inversion than one would expect for MnFe_2O_4 . Analysis of the films with STEM and XRD can help characterize this further.

From this ORR study of MnFe_2O_4 it seems that there is a high selectivity for direct reduction of O_2 to OH^- , based on the obtained electron transfer numbers. This has been observed for MnFe_2O_4 in several studies, albeit with some differences.^{5,16,24} The significant difference for our study lies in the large overpotential, which measured at the $E_{1/2}$ is 0.8 – 1.0 V more negative than the what has previously been reported for MnFe_2O_4 . The overpotential should depend on the number of active sites available and the ability for O_2 to interact with those active sites. For MnFe_2O_4 it seems that the Mn cations have greater ability to catalyze ORR, as it has been seen that pure Fe_3O_4 spinel is a significantly worse ORR catalyst.^{5,16} As seen in our CVs of the films, we clearly have redox features that are consistent with Mn reduction and oxidation, as well as an increase in current that seems to be related to the activity of those features. However, there does not seem to be enough Mn active sites available on the film, as diffusion limited current isn't

reached until potentials 0.5 V more negative than where the Mn redox features occur. This is most likely related to Fe-mediated catalysis dominating at the more negative overpotentials, where Fe redox chemistry can occur. This could imply that in MnFe_2O_4 spinel nanocrystals the structure of the spinel is more flexible, to allow for higher Mn occupation of octahedral sites, as well as more promiscuity of the Mn valence. In fact, it has been found for MnFe_2O_4 nanocrystals Mn deficiency or excess will change the distribution of Mn^{2+} and Mn^{3+} cations, essentially doping the material with more Mn.²⁴ This seems important for improved onset potentials for ORR catalysis. To explore this further with MBE, comparing the MnFe_2O_4 films with pure Fe_3O_4 and pure Mn_3O_4 could provide insight.

The other component of nanocrystalline catalysts that we cannot account for in our study with MBE films is the contribution of the high surface area conductive carbon that is typically added to catalysts mixtures. This has been found to be very necessary to achieve better overpotentials for many different catalysts, including noble metal catalysts or metal oxides.^{9,10,44-46} In a study of Co_3O_4 by Liang et. al., it is very clear that the addition of carbon is necessary for Co_3O_4 to be an effective catalyst.⁴⁷ There even seems to be a dependence on the type of carbon material used, such as graphene or carbon nanotubes¹⁶, and even the dopant level in the carbon material.⁴⁸ Another common component is the Nafion, an ionic polymer for proton transport, that has an effect on the activity and rate constants associated with catalysis.^{49,50} To study the fundamental properties of specific materials for ORR catalysis, single crystalline materials on a conductive substrate can be achieved, and highlights explanations of ORR catalysis with spinel nanocrystals where the nanocrystal may be only a small component of the catalytic behavior observed in the system.

4.5 Conclusions and Future Work

Here we have shown the successful study of MnFe_2O_4 films grown via MBE for ORR catalysis. This is the first study of a spinel MBE film investigated for ORR catalysis and we find that the RDE setup is a suitable method for mechanistically analyzing the catalytic ability of these films. Because the films cannot be reused, the study of the films is somewhat limited. However further understanding of MnFe_2O_4 can be achieved with nanocrystalline studies, as these are more relevant to fuel cell applications. The insight provided from MnFe_2O_4 MBE will inform how MnFe_2O_4 nanocrystals perform and what could be the predominant mechanism. The study of other spinels using MBE films should also be done, to see if trends observed for nanocrystals spinels is consistent with what is observed for a true single crystalline material. This will also contribute to furthering this work towards heterojunction composite films, which consist of a perovskite matrix with spinel pillars, that can act as a bifunctional catalyst for ORR and OER.

4.6 Appendix

EDS	110920_2		110920_1		111319_3	
	Mn	Fe	Mn	Fe	Mn	Fe
1	29.38	70.62	8.04	91.96	29.93	70.07
2	40.13	59.87	34.86	65.14	28.56	72.3
3	31.82	68.18	22.39	77.61	27.7	71.44
4	33.93	66.07	38.56	61.44	29.44	70.56
Avg	33.815	66.185	31.93667	68.06333	28.9075	71.0925

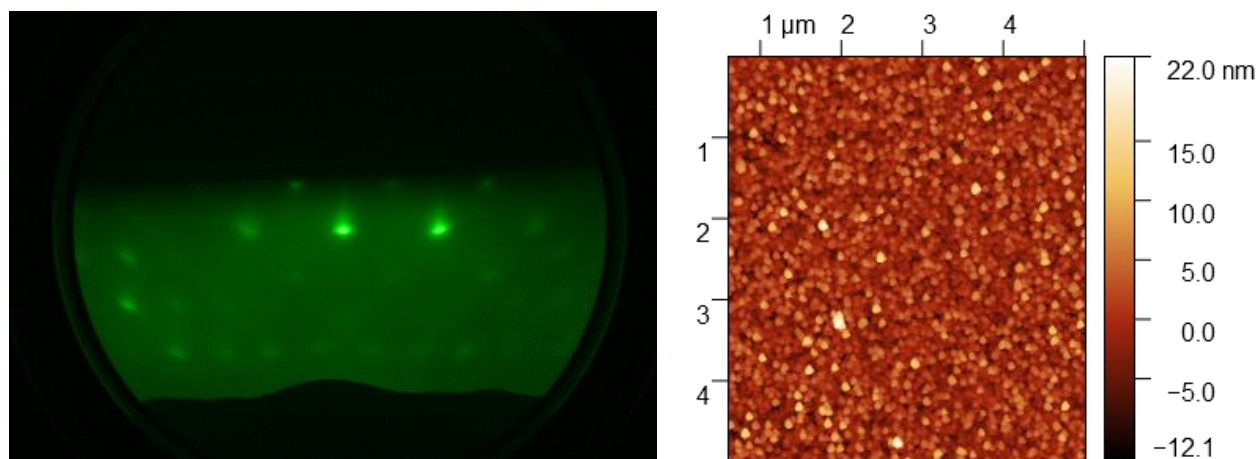


Figure A4.1: RHEED and AFM of 20 nm (001) MnFe_2O_4

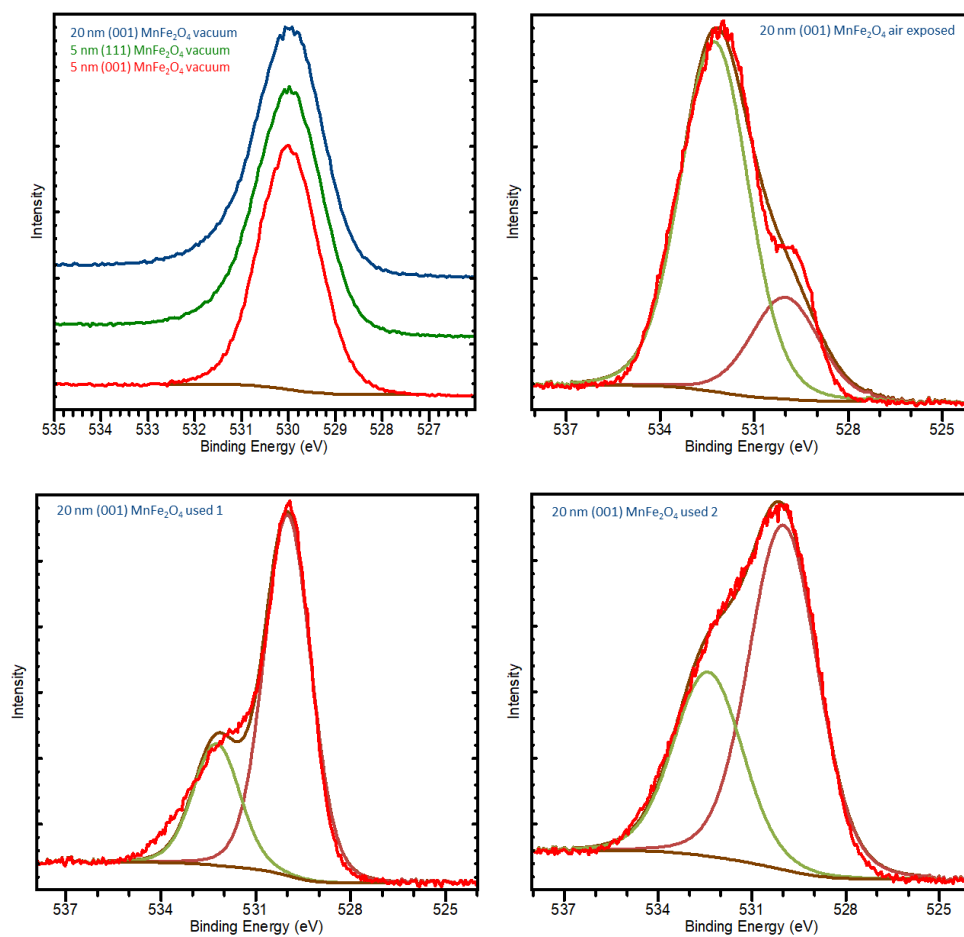


Figure A4.2: O 1s XPS region

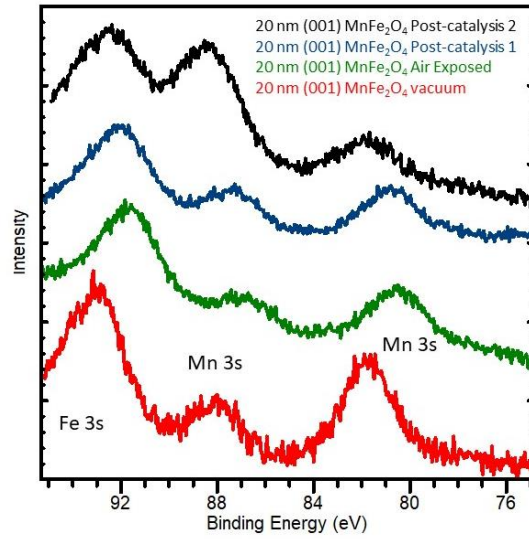


Figure A4.3: Mn 3s XPS for 20 nm (001) MnFe₂O₄ under vacuum, after air exposure, and post catalysis

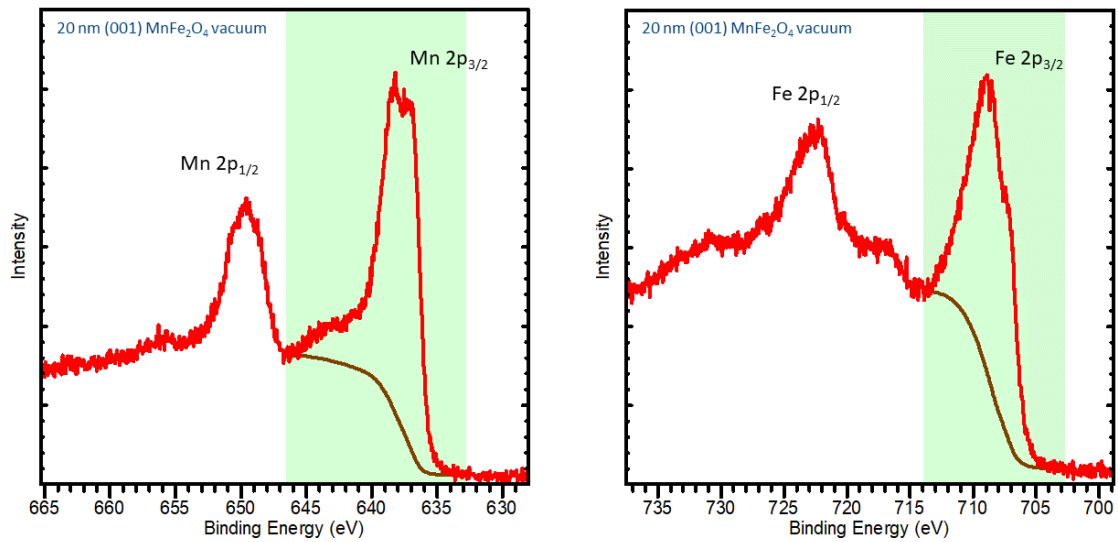


Figure A4.4: Fitting example of Mn and Fe 2p regions for stoichiometric determination

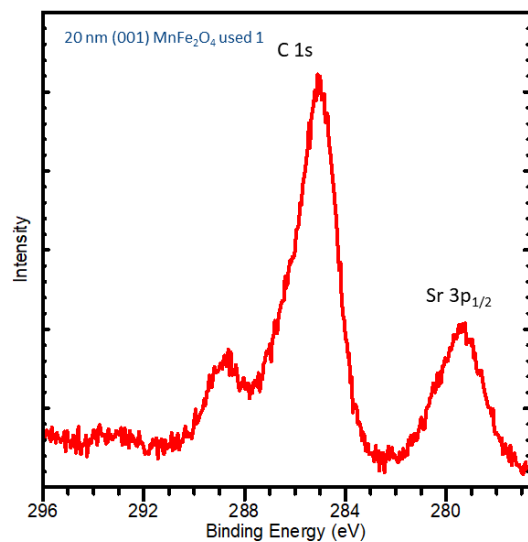


Figure A4.5: C1s XPS for 20 nm (001) comparing vacuum and used film 1 showing exposed Sr

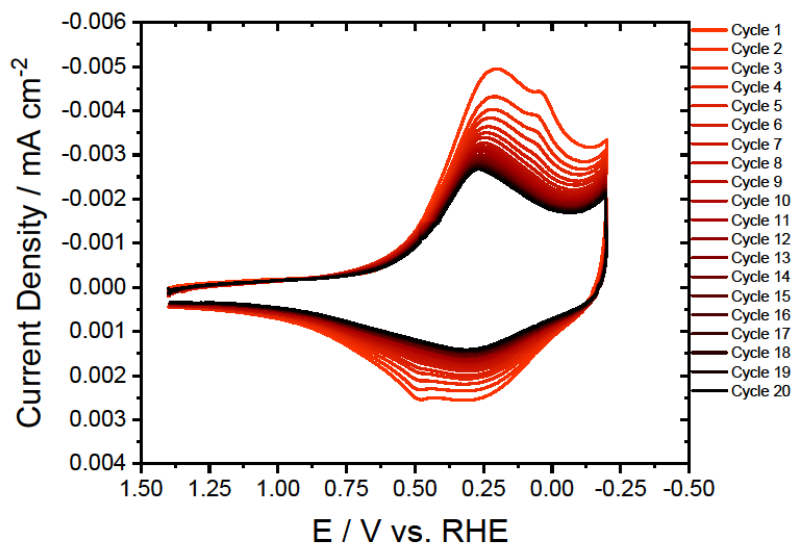


Figure A4.6: Electrochemical cycling of 20 nm (001) with substrate exposed, showing film degradation.

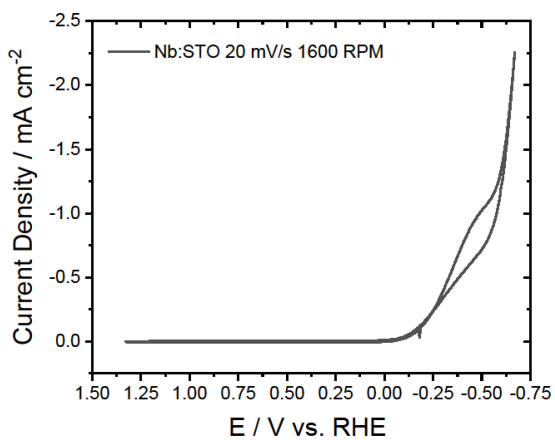
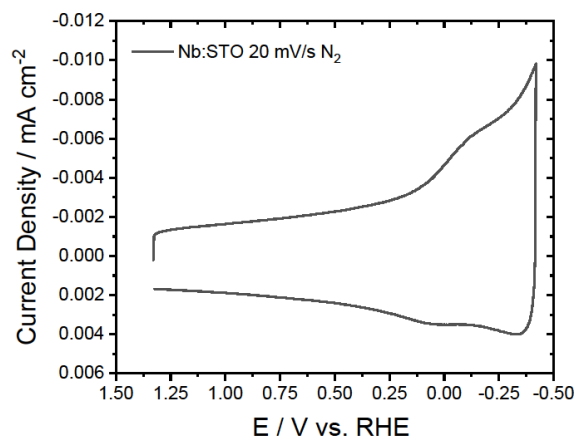


Figure A4.7: CV and RDE of Nb:STO

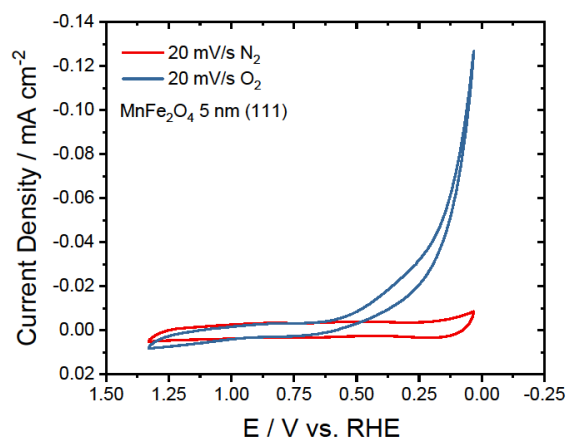
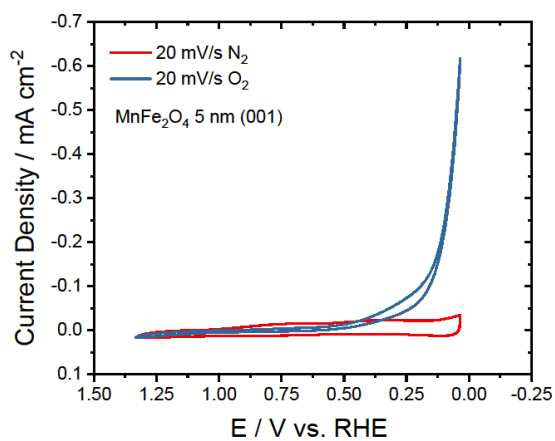


Figure A4.8: CV of 5 nm (001) and (111) films before catalysis experiments comparing N₂ and O₂

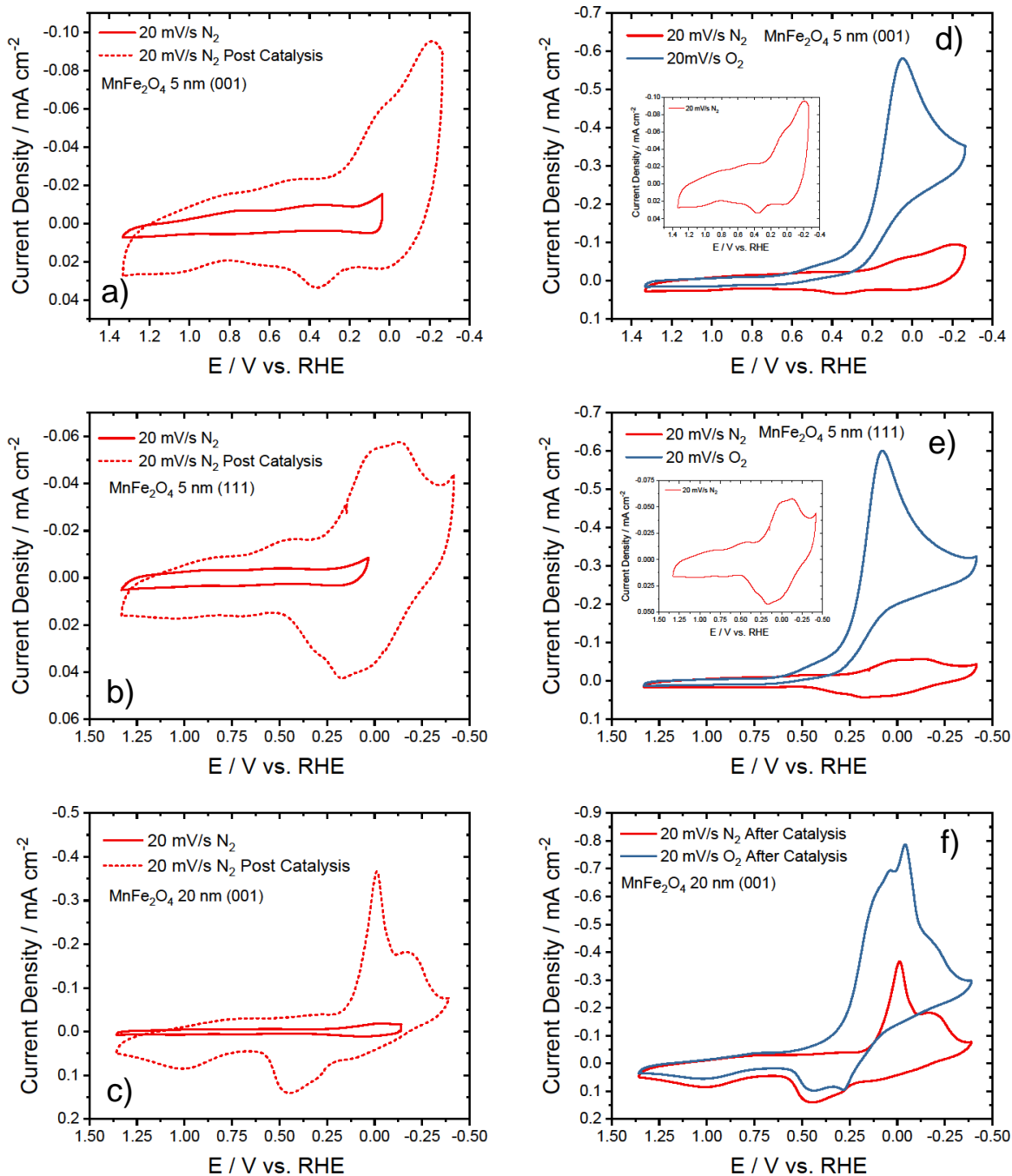


Figure A4.9: N_2 before and after catalysis CV comparison for a) 5 nm (001), b) 5 nm (111), and c) 20 nm (001) films. N_2 and O_2 after catalysis CV comparison for d) 5 nm (001), e) 5 nm (111), and f) 20 nm (001) films.

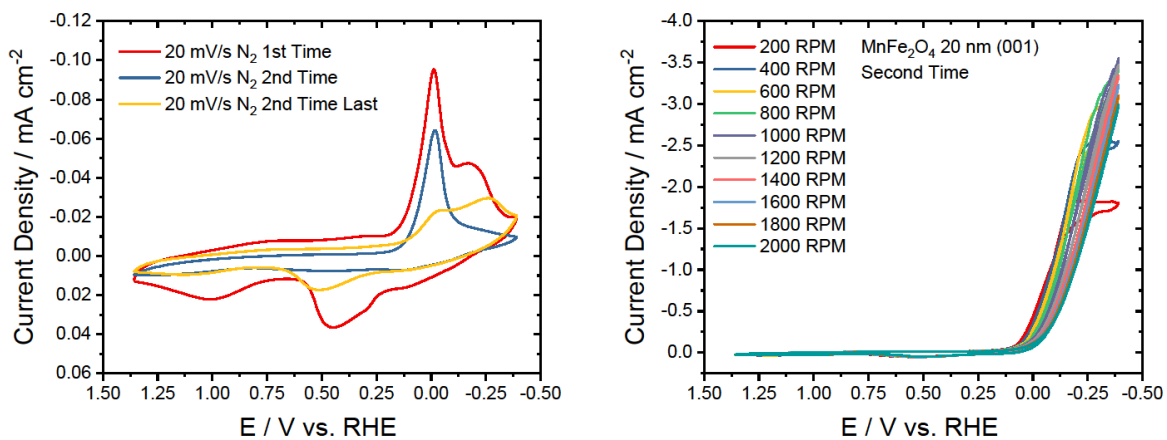


Figure A4.10: CV and RDE of 20 nm (001) of follow-up catalytic studies

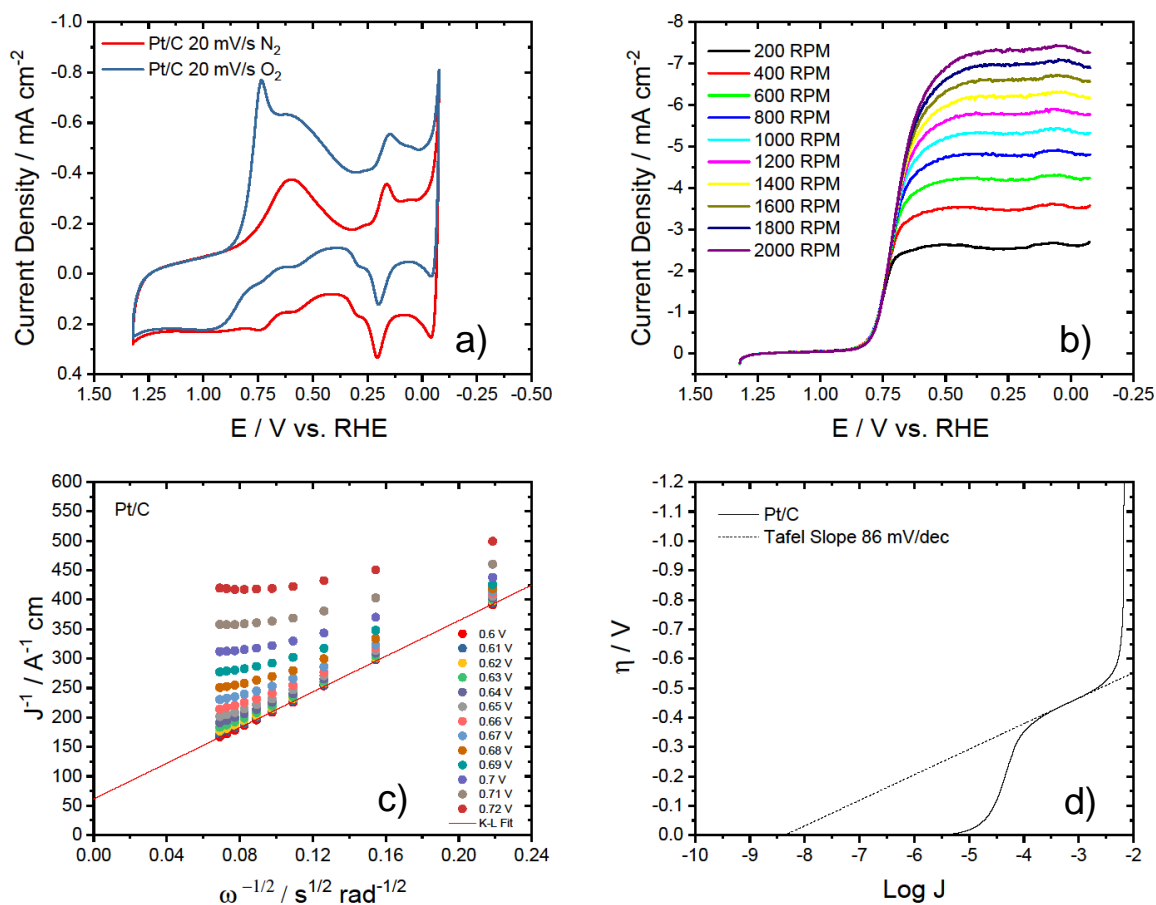


Figure A4.11: a) CV, b) RDE, c) K-L, and d) Tafel Plot of Pt/C

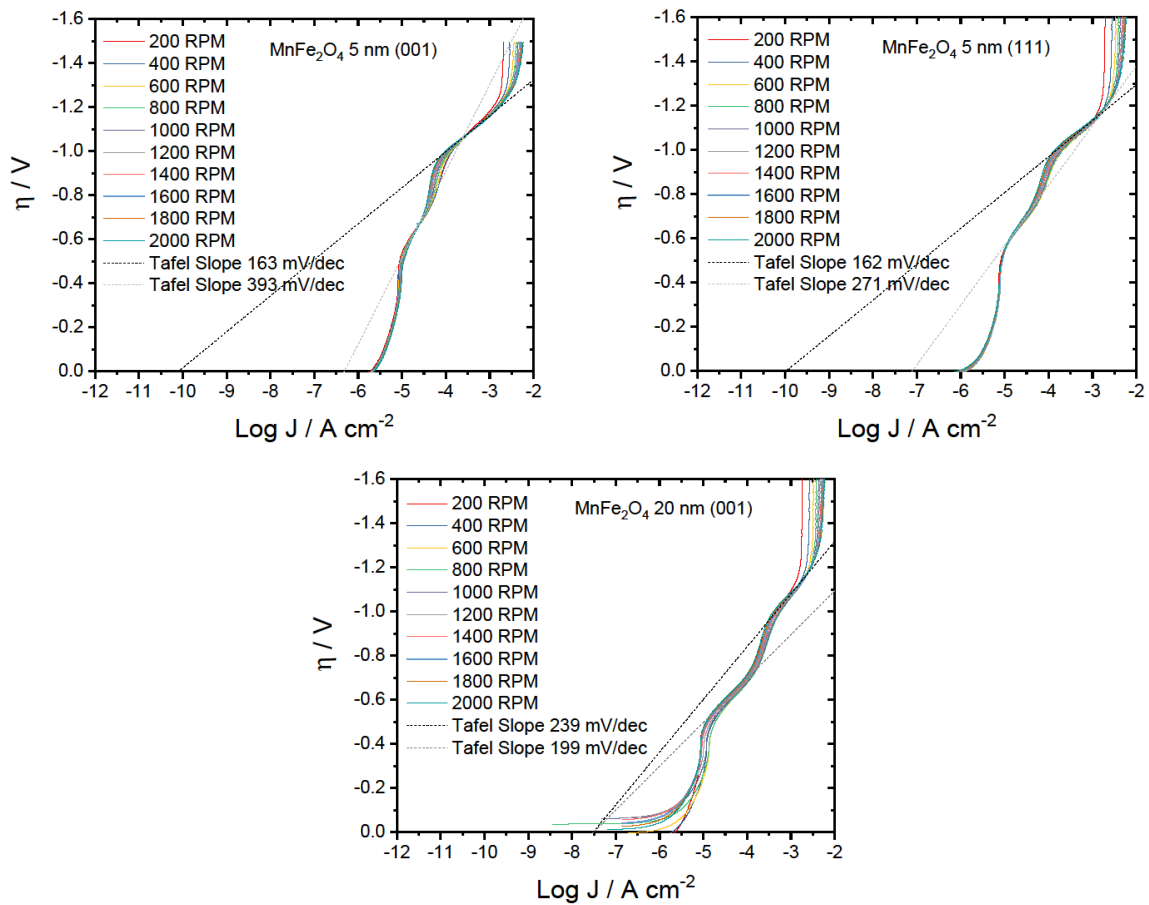


Figure A4.12: Tafel plots at all RPMs

4.7 References

- (1) Gasteiger, H. A.; Marković, N. M. Just a Dream—or Future Reality? *Science* **2009**, *324* (5923), 48–49. <https://doi.org/10.1126/science.1172083>.
- (2) Ma, R.; Lin, G.; Zhou, Y.; Liu, Q.; Zhang, T.; Shan, G.; Yang, M.; Wang, J. A Review of Oxygen Reduction Mechanisms for Metal-Free Carbon-Based Electrocatalysts. *Npj Comput. Mater.* **2019**, *5* (1), 1–15. <https://doi.org/10.1038/s41524-019-0210-3>.
- (3) Cheng, F.; Chen, J. Metal–Air Batteries: From Oxygen Reduction Electrochemistry to Cathode Catalysts. *Chem. Soc. Rev.* **2012**, *41* (6), 2172–2192. <https://doi.org/10.1039/C1CS15228A>.
- (4) Zhao, Q.; Yan, Z.; Chen, C.; Chen, J. Spinels: Controlled Preparation, Oxygen Reduction/Evolution Reaction Application, and Beyond. *Chem. Rev.* **2017**, *117* (15), 10121–10211. <https://doi.org/10.1021/acs.chemrev.7b00051>.
- (5) Yang, Y.; Xiong, Y.; Holtz, M. E.; Feng, X.; Zeng, R.; Chen, G.; DiSalvo, F. J.; Muller, D. A.; Abruña, H. D. Octahedral Spinel Electrocatalysts for Alkaline Fuel Cells. *Proc. Natl. Acad. Sci.* **2019**, *116* (49), 24425–24432. <https://doi.org/10.1073/pnas.1906570116>.
- (6) Vielstich, W.; Lamm, A.; Gasteiger, H. Handbook of Fuel Cells. Fundamentals, Technology, Applications. **2003**.
- (7) Wu, G.; Wang, J.; Ding, W.; Nie, Y.; Li, L.; Qi, X.; Chen, S.; Wei, Z. A Strategy to Promote the Electrocatalytic Activity of Spinels for Oxygen Reduction by Structure Reversal. *Angew. Chem. Int. Ed.* **2016**, *55* (4), 1340–1344. <https://doi.org/10.1002/anie.201508809>.
- (8) Zhou, Y.; Xi, S.; Wang, J.; Sun, S.; Wei, C.; Feng, Z.; Du, Y.; Xu, Z. J. Revealing the Dominant Chemistry for Oxygen Reduction Reaction on Small Oxide Nanoparticles. *ACS Catal.* **2018**, *8* (1), 673–677. <https://doi.org/10.1021/acscatal.7b03864>.
- (9) Poux, T.; Napolskiy, F. S.; Dintzer, T.; Kéranguéven, G.; Istomin, S. Ya.; Tsirlina, G. A.; Antipov, E. V.; Savinova, E. R. Dual Role of Carbon in the Catalytic Layers of Perovskite/Carbon Composites for the Electrocatalytic Oxygen Reduction Reaction. *Catal. Today* **2012**, *189* (1), 83–92. <https://doi.org/10.1016/j.cattod.2012.04.046>.
- (10) Kim, J. H.; Cheon, J. Y.; Shin, T. J.; Park, J. Y.; Joo, S. H. Effect of Surface Oxygen Functionalization of Carbon Support on the Activity and Durability of Pt/C Catalysts for the Oxygen Reduction Reaction. *Carbon* **2016**, *101*, 449–457. <https://doi.org/10.1016/j.carbon.2016.02.014>.
- (11) Markovic, N. M.; Gasteiger, H. A.; Ross, P. N. Oxygen Reduction on Platinum Low-Index Single-Crystal Surfaces in Sulfuric Acid Solution: Rotating Ring-Pt(Hkl) Disk Studies. *J. Phys. Chem.* **1995**, *99* (11), 3411–3415. <https://doi.org/10.1021/j100011a001>.
- (12) Climent, V.; Marković, N. M.; Ross, P. N. Kinetics of Oxygen Reduction on an Epitaxial Film of Palladium on Pt(111). *J. Phys. Chem. B* **2000**, *104* (14), 3116–3120. <https://doi.org/10.1021/jp993480t>.

- (13) Blizanac, B. B.; Ross, P. N.; Marković, N. M. Oxygen Reduction on Silver Low-Index Single-Crystal Surfaces in Alkaline Solution: Rotating Ring DiskAg(Hkl) Studies. *J. Phys. Chem. B* **2006**, *110* (10), 4735–4741. <https://doi.org/10.1021/jp056050d>.
- (14) May, K. J.; Fenning, D. P.; Ming, T.; Hong, W. T.; Lee, D.; Stoerzinger, K. A.; Biegalski, M. D.; Kolpak, A. M.; Shao-Horn, Y. Thickness-Dependent Photoelectrochemical Water Splitting on Ultrathin LaFeO₃ Films Grown on Nb:SrTiO₃. *J. Phys. Chem. Lett.* **2015**, *6* (6), 977–985. <https://doi.org/10.1021/acs.jpcclett.5b00169>.
- (15) Lee, D.; Jacobs, R.; Jee, Y.; Seo, A.; Sohn, C.; Ievlev, A. V.; Ovchinnikova, O. S.; Huang, K.; Morgan, D.; Lee, H. N. Stretching Epitaxial La_{0.6}Sr_{0.4}CoO_{3-δ} for Fast Oxygen Reduction. *J. Phys. Chem. C* **2017**, *121* (46), 25651–25658. <https://doi.org/10.1021/acs.jpcc.7b06374>.
- (16) Zhu, H.; Zhang, S.; Huang, Y.-X.; Wu, L.; Sun, S. Monodisperse MxFe₃-XO₄ (M = Fe, Cu, Co, Mn) Nanoparticles and Their Electrocatalysis for Oxygen Reduction Reaction. *Nano Lett.* **2013**, *13* (6), 2947–2951. <https://doi.org/10.1021/nl401325u>.
- (17) Li, Z.; Gao, K.; Han, G.; Wang, R.; Li, H.; Zhao, X. S.; Guo, P. Solvothermal Synthesis of MnFe₂O₄ Colloidal Nanocrystal Assemblies and Their Magnetic and Electrocatalytic Properties. *New J. Chem.* **2014**, *39* (1), 361–368. <https://doi.org/10.1039/C4NJ01466A>.
- (18) Wei, C.; Feng, Z.; Baisariyev, M.; Yu, L.; Zeng, L.; Wu, T.; Zhao, H.; Huang, Y.; Bedzyk, M. J.; Sritharan, T.; Xu, Z. J. Valence Change Ability and Geometrical Occupation of Substitution Cations Determine the Pseudocapacitance of Spinel Ferrite XFe₂O₄ (X = Mn, Co, Ni, Fe). *Chem. Mater.* **2016**, *28* (12), 4129–4133. <https://doi.org/10.1021/acs.chemmater.6b00713>.
- (19) Khilari, S.; Pradhan, D. MnFe₂O₄@nitrogen-Doped Reduced Graphene Oxide Nanohybrid: An Efficient Bifunctional Electrocatalyst for Anodic Hydrazine Oxidation and Cathodic Oxygen Reduction. *Catal. Sci. Technol.* **2017**, *7* (24), 5920–5931. <https://doi.org/10.1039/C7CY01844D>.
- (20) Matzen, S.; Moussy, J.-B.; Mattana, R.; Bouzehouane, K.; Deranlot, C.; Petroff, F.; Cezar, J. C.; Arrio, M.-A.; Sainctavit, Ph.; Gatel, C.; Warot-Fonrose, B.; Zheng, Y. Epitaxial Growth and Ferrimagnetic Behavior of MnFe₂O₄(111) Ultrathin Layers for Room-Temperature Spin Filtering. *Phys. Rev. B* **2011**, *83* (18), 184402. <https://doi.org/10.1103/PhysRevB.83.184402>.
- (21) Biesinger, M. C.; Payne, B. P.; Grosvenor, A. P.; Lau, L. W. M.; Gerson, A. R.; Smart, R. St. C. Resolving Surface Chemical States in XPS Analysis of First Row Transition Metals, Oxides and Hydroxides: Cr, Mn, Fe, Co and Ni. *Appl. Surf. Sci.* **2011**, *257* (7), 2717–2730. <https://doi.org/10.1016/j.apsusc.2010.10.051>.
- (22) Yamashita, T.; Hayes, P. Analysis of XPS Spectra of Fe²⁺ and Fe³⁺ Ions in Oxide Materials. *Appl. Surf. Sci.* **2008**, *254* (8), 2441–2449. <https://doi.org/10.1016/j.apsusc.2007.09.063>.
- (23) Cerrato, J. M.; Hochella, M. F.; Knocke, W. R.; Dietrich, A. M.; Cromer, T. F. Use of XPS to Identify the Oxidation State of Mn in Solid Surfaces of Filtration Media Oxide Samples from Drinking Water Treatment Plants. *Environ. Sci. Technol.* **2010**, *44* (15), 5881–5886. <https://doi.org/10.1021/es100547q>.

- (24) Zhou, Y.; Xi, S.; Wang, J.; Sun, S.; Wei, C.; Feng, Z.; Du, Y.; Xu, Z. J. Revealing the Dominant Chemistry for Oxygen Reduction Reaction on Small Oxide Nanoparticles. *ACS Catal.* **2018**, *8* (1), 673–677. <https://doi.org/10.1021/acscatal.7b03864>.
- (25) Sander, M.; Hofstetter, T. B.; Gorski, C. A. Electrochemical Analyses of Redox-Active Iron Minerals: A Review of Nonmediated and Mediated Approaches. *Environ. Sci. Technol.* **2015**, *49* (10), 5862–5878. <https://doi.org/10.1021/acs.est.5b00006>.
- (26) Stoerzinger, K. A.; Lü, W.; Li, C.; Ariando; Venkatesan, T.; Shao-Horn, Y. Highly Active Epitaxial $\text{La}(1-x)\text{SrxMnO}_3$ Surfaces for the Oxygen Reduction Reaction: Role of Charge Transfer. *J. Phys. Chem. Lett.* **2015**, *6* (8), 1435–1440. <https://doi.org/10.1021/acs.jpcclett.5b00439>.
- (27) West, A. R. *Solid State Chemistry and Its Applications*; John Wiley & Sons, 2014.
- (28) Treimer, S.; Tang, A.; Johnson, D. C. A Consideration of the Application of Koutecký-Levich Plots in the Diagnoses of Charge-Transfer Mechanisms at Rotated Disk Electrodes. *Electroanalysis* **2002**, *14* (3), 165–171. [https://doi.org/10.1002/1521-4109\(200202\)14:3<165::AID-ELAN165>3.0.CO;2-6](https://doi.org/10.1002/1521-4109(200202)14:3<165::AID-ELAN165>3.0.CO;2-6).
- (29) Holewinski, A.; Linic, S. Elementary Mechanisms in Electrocatalysis: Revisiting the ORR Tafel Slope. *J. Electrochem. Soc.* **2012**, *159* (11), H864. <https://doi.org/10.1149/2.022211jes>.
- (30) Temmel, S. E.; Fabbri, E.; Pergolesi, D.; Lippert, T.; Schmidt, T. J. Investigating the Role of Strain toward the Oxygen Reduction Activity on Model Thin Film Pt Catalysts. *ACS Catal.* **2016**, *6* (11), 7566–7576. <https://doi.org/10.1021/acscatal.6b01836>.
- (31) Lee, D.; Jacobs, R.; Jee, Y.; Seo, A.; Sohn, C.; Ievlev, A. V.; Ovchinnikova, O. S.; Huang, K.; Morgan, D.; Lee, H. N. Stretching Epitaxial $\text{La}_{0.6}\text{Sr}_{0.4}\text{CoO}_{3-\delta}$ for Fast Oxygen Reduction. *J. Phys. Chem. C* **2017**, *121* (46), 25651–25658. <https://doi.org/10.1021/acs.jpcc.7b06374>.
- (32) Stoerzinger, K. A.; Lü, W.; Li, C.; Ariando; Venkatesan, T.; Shao-Horn, Y. Highly Active Epitaxial $\text{La}(1-x)\text{SrxMnO}_3$ Surfaces for the Oxygen Reduction Reaction: Role of Charge Transfer. *J. Phys. Chem. Lett.* **2015**, *6* (8), 1435–1440. <https://doi.org/10.1021/acs.jpcclett.5b00439>.
- (33) Bachelet, R.; Coux, P. de; Warot-Fonrose, B.; Skumryev, V.; Niu, G.; Vilquin, B.; Saint-Girons, G.; Sánchez, F. Functional Spinel Oxide Heterostructures on Silicon. *CrystEngComm* **2014**, *16* (47), 10741–10745. <https://doi.org/10.1039/C4CE01817F>.
- (34) Moyer, J. A.; Gao, R.; Schiffer, P.; Martin, L. W. Epitaxial Growth of Highly-Crystalline Spinel Ferrite Thin Films on Perovskite Substrates for All-Oxide Devices. *Sci. Rep.* **2015**, *5* (1), 10363. <https://doi.org/10.1038/srep10363>.
- (35) Mishra, R. K.; Thomas, G. Surface Energy of Spinel. *J. Appl. Phys.* **1977**, *48* (11), 4576–4580. <https://doi.org/10.1063/1.323486>.
- (36) Buvat, G.; Eslamibidgoli, M. J.; Youssef, A. H.; Garbarino, S.; Ruediger, A.; Eikerling, M.; Guay, D. Effect of IrO_6 Octahedron Distortion on the OER Activity at (100) IrO_2 Thin Film. *ACS Catal.* **2020**, *10* (1), 806–817. <https://doi.org/10.1021/acscatal.9b04347>.

- (37) Zheng, Y.; Gao, R.; Zheng, L.; Sun, L.; Hu, Z.; Liu, X. Ultrathin Co₃O₄ Nanosheets with Edge-Enriched {111} Planes as Efficient Catalysts for Lithium–Oxygen Batteries. *ACS Catal.* **2019**, *9* (5), 3773–3782. <https://doi.org/10.1021/acscatal.8b05182>.
- (38) Poulain, R.; Klein, A.; Proost, J. Electrocatalytic Properties of (100)-, (110)-, and (111)-Oriented NiO Thin Films toward the Oxygen Evolution Reaction. *J. Phys. Chem. C* **2018**, *122* (39), 22252–22263. <https://doi.org/10.1021/acs.jpcc.8b05790>.
- (39) Maiyalagan, T.; Chemelewski, K. R.; Manthiram, A. Role of the Morphology and Surface Planes on the Catalytic Activity of Spinel LiMn_{1.5}Ni_{0.5}O₄ for Oxygen Evolution Reaction. *ACS Catal.* **2014**, *4* (2), 421–425. <https://doi.org/10.1021/cs400981d>.
- (40) Min, X.; Chen, Y.; Kanan, M. W. Alkaline O₂ Reduction on Oxide-Derived Au: High Activity and 4e[−] Selectivity without (100) Facets. *Phys. Chem. Chem. Phys.* **2014**, *16* (27), 13601–13604. <https://doi.org/10.1039/C4CP01337A>.
- (41) Ozenler, S.; Sahin, N.; Akaydin, B.; Ovecoglu, L.; Genc, A.; Léger, J.-M.; Napporn, T. W.; Kadirgan, F. Comparison of the ORR Activity of Carbon Supported PtCo/C and PtSnCo/C Electrocatalysts for PEM Fuel Cells. *ECS Trans.* **2011**, *41* (1), 1031. <https://doi.org/10.1149/1.3635635>.
- (42) Wei, C.; Feng, Z.; Scherer, G. G.; Barber, J.; Shao-Horn, Y.; Xu, Z. J. Cations in Octahedral Sites: A Descriptor for Oxygen Electrocatalysis on Transition-Metal Spinels. *Adv. Mater.* **2017**, *29* (23), 1606800. <https://doi.org/10.1002/adma.201606800>.
- (43) Hou, X.; Feng, J.; Xu, X.; Zhang, M. Synthesis and Characterizations of Spinel MnFe₂O₄ Nanorod by Seed–Hydrothermal Route. *J. Alloys Compd.* **2010**, *491* (1), 258–263. <https://doi.org/10.1016/j.jallcom.2009.10.029>.
- (44) Zhao, S.; Guo, T.; Fan, J.; Wang, L.; Han, M.; Wang, J.; Wu, Y.; Chen, Y. Versatile Synthesis of Ultrafine Ternary Spinel Oxides/Carbon Nanohybrids toward the Oxygen Reduction Reaction. *Energy Fuels* **2020**, *34* (7), 9069–9075. <https://doi.org/10.1021/acs.energyfuels.0c01901>.
- (45) Wu, X.; Niu, Y.; Feng, B.; Yu, Y.; Huang, X.; Zhong, C.; Hu, W.; Li, C. M. Mesoporous Hollow Nitrogen-Doped Carbon Nanospheres with Embedded MnFe₂O₄/Fe Hybrid Nanoparticles as Efficient Bifunctional Oxygen Electrocatalysts in Alkaline Media. *ACS Appl. Mater. Interfaces* **2018**, *10* (24), 20440–20447. <https://doi.org/10.1021/acsami.8b04012>.
- (46) Celorrio, V.; Dann, E.; Calvillo, L.; Morgan, D. J.; Hall, S. R.; Fermin, D. J. Oxygen Reduction at Carbon-Supported Lanthanides: The Role of the B-Site. *ChemElectroChem* **2016**, *3* (2), 283–291. <https://doi.org/10.1002/celec.201500440>.
- (47) Liang, Y.; Li, Y.; Wang, H.; Zhou, J.; Wang, J.; Regier, T.; Dai, H. Co₃O₄ Nanocrystals on Graphene as a Synergistic Catalyst for Oxygen Reduction Reaction. *Nat. Mater.* **2011**, *10* (10), 780–786. <https://doi.org/10.1038/nmat3087>.
- (48) Wang, L.; Sofer, Z.; Pumera, M. Will Any Crap We Put into Graphene Increase Its Electrocatalytic Effect? *ACS Nano* **2020**, *14* (1), 21–25. <https://doi.org/10.1021/acsnano.9b00184>.

- (49) Kocha, S. S.; Zack, J. W.; Alia, S. M.; Neyerlin, K. C.; Pivovar, B. S. Influence of Ink Composition on the Electrochemical Properties of Pt/C Electrocatalysts. *ECS Trans.* **2013**, *50* (2), 1475. <https://doi.org/10.1149/05002.1475ecst>.
- (50) Chen, Y.; Zhong, Q.; Li, G.; Tian, T.; Tan, J.; Pan, M. Electrochemical Study of Temperature and Nafion Effects on Interface Property for Oxygen Reduction Reaction. *Ionics* **2018**, *24* (12), 3905–3914. <https://doi.org/10.1007/s11581-018-2533-3>.

Chapter 5

Group 13 Lewis Acid Catalyzed Synthesis of Cu₂O Nanocrystals via Hydroxide Transmetallation

5.1 Introduction

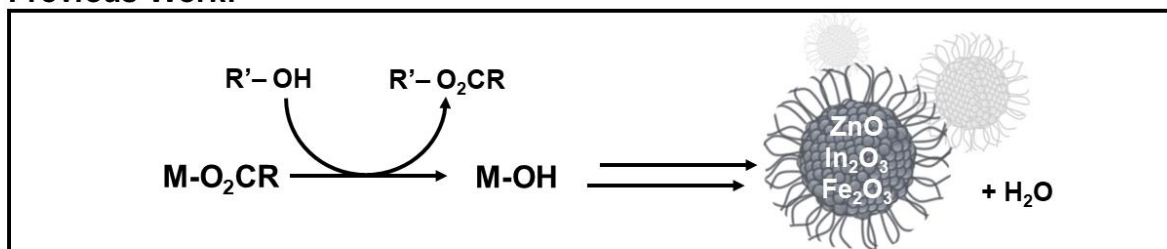
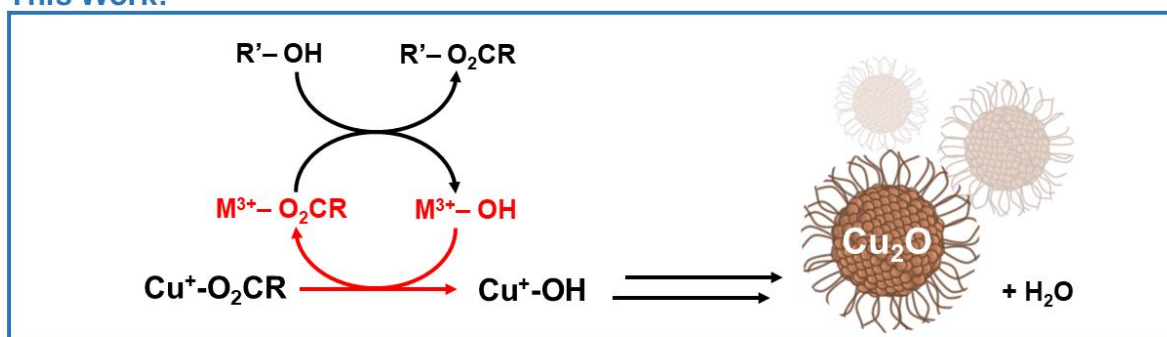
The colloidal synthesis of nanocrystalline solids is a highly active area of research given that many nanocrystalline materials have unique properties for applications in optical, photochemical/photocatalytic, and electrochemical/electrocatalytic fields.^{1,2} The synthetic methods developed for these materials often involve a high level of control on the composition, morphology, and size of the nanocrystals (NCs) generated.^{2,3} The most investigated methods have been based on heat-up or hot-injection procedures which are typically done in organic solvents toward the synthesis of metal chalcogenide semiconductors.^{4,5} Each method operates under similar principles where the reaction of precursor molecules with a solvent and a surfactant leads to a nucleation event followed by NC growth, as described by the LaMer mechanism⁶, although more recently the theory of NC growth has been expanded due to the complexities of the precursors and reaction environments.⁷

The hot-injection method relies on a fast injection of precursor molecules into the reaction solution and requires rapid reactivity of the precursor to ensure a single nucleation event. However, the scale-up of the synthesis is challenging because of its reliance on uniform mixing to achieve a single nucleation event and homogeneous cooling of the reaction to separate nucleation and growth. The heat-up synthesis method does not suffer from these setbacks because all reaction components are present upon heating of the reaction, simplifying issues with scale-up. However, secondary nucleation events are more likely to occur because of sustained monomer generation, which can overlap the growth and nucleation stages of the reaction,

broadening nanocrystal size. The heat-up synthesis also requires careful tailoring of precursor reactivity, particularly with respect to formation of ternary and quaternary NCs.

More recently, a continuous-injection method has been developed for metal oxide NCs and has shown great promise for controlled generation of a wide variety of materials.⁸ While both the hot-injection and continuous-injection methods introduce precursor molecules to a pre-heated reaction solution, the continuous-injection is performed with a slower, controlled injection rate such that addition of the entire precursor volume can take multiple minutes to achieve. Instead of rapid nucleation and growth observed during fast hot-injection, the continuous-injection method allows for a layer-by-layer growth of NCs and fine control of size, morphology, and doping.⁸⁻¹²

For the synthesis of metal oxides, the reaction proceeds via metal-catalyzed esterification of long-chain carboxylic acids with long-chain alcohols to produce the corresponding ester and metal hydroxide (M-OH) monomers (**Scheme 5.1**, top). Most commonly, the acid and alcohol of choice are oleic acid (HO_2CR , $\text{R} = \text{R}' = \text{C}_{17}\text{H}_{33}$) and oleyl alcohol (HOR' , $\text{R}' = \text{C}_{18}\text{H}_{35}$). M-OH monomers then condense to form metal oxide NCs with water as a byproduct. The successful synthesis of nanocrystals using the continuous-injection method relies on the ability of the precursor metal to catalyze the esterification reaction to form M-OH in addition to the proclivity of M-OH monomers to undergo condensation to form a metal oxide. A wide variety of metal oxide NCs have been synthesized with this method, including In_2O_3 , CoO , Mn_3O_4 , Fe_2O_3 , and ZnO .^{8,13-15} The doping of In_2O_3 with different metals (*e.g.* $\text{Sn}:\text{In}_2\text{O}_3$) and the generation of core-shell NCs have established the versatility of this method.^{8-10,16}

Previous Work:**This Work:**

Scheme 5.1: Reaction schemes for metal oxide NC synthesis. (top) Metal oleate (M-O₂CR) catalyzed esterification produces metal hydroxide (M-OH) monomers which undergo condensation to form metal oxide NCs. (bottom) Synthesis of Cu₂O NCs is achieved through an alternative catalytic route in which esterification by a group 13 metal cation results in transmetalation of hydroxide ligands from M³⁺-OH to produce Cu⁺-OH monomers.

Despite the wide range of accessible materials, Ito *et. al.* previously found that NCs consisting of antimony, copper, and silver could not be produced using the continuous-injection method.⁸ This is seemingly due to the inability of these metals to catalyze the necessary esterification reaction to form M-OH monomers. This indicates that more research is needed to understand the different catalytic rates of metals toward esterification and the types of NCs they generate.

Here, we report the direct synthesis of Cu₂O NCs smaller than 100 nm using the continuous-injection method. The key to our approach is the presence of catalytic amounts (1-15 mol%) of Al³⁺, Ga³⁺, or In³⁺ cations. The introduction of cations and inorganic complexes to tune reactivity is not unusual in the metal chalcogenide literature¹⁷⁻¹⁹, but typically the addition of these species changes resultant nanoparticle morphology and not necessarily precursor reactivity. We find that

addition of these metals to our system allows for efficient esterification catalysis to produce M^{3+} -OH species. The hydroxide ligand is then transmetallated from M^{3+} -OH to form Cu^+ -OH monomers (**Scheme 5.1**, bottom), thus bypassing the copper-catalyzed esterification route which is found to be much slower than M^{3+} -catalysis. These Cu^+ -OH monomers then quickly condense to form Cu_2O NCs.

Spectroscopic data (UV-visible and FTIR) collected during and following the injection process provide detailed information about the formation of oleyl oleate ester and the consumption of the copper oleate (Cu^{2+} - O_2CR) precursor over time. These studies point to a new mechanism for metal oxide synthesis in which the generation of a metal oxide NC is not limited by the inherent reactivity of the parent metal (*i.e.* Cu) toward esterification to produce M-OH monomers. Instead, the monomers can be generated by transmetallation from a secondary M^{3+} -OH species produced from esterification catalyzed by a group 13 metal cation. These studies also highlight the competitive and independent reactivity of two metal cations in the same solution and are therefore important for the synthesis of more complex ternary metal oxide NCs.

5.2 Experimental

5.2.1 Materials Oleic acid (technical grade, 90%), and oleyl alcohol (technical grade, 80-85%) were purchased from Alfa Aesar and used as received. Copper (II) acetate ($Cu(OAc)_2$, 98%), indium (III) acetylacetonate ($In(acac)_3$, 99.99%), aluminum (III) acetylacetonate ($Al(acac)_3$, 99.99%), gallium (III) acetylacetonate ($Ga(acac)_3$, 99.99%) were purchased from Sigma-Aldrich and used as received. To monitor the nitrogen (99.999%, Airgas) flow rate, a Cole-Parmer flow meter (model PMR1-010270) was utilized. A syringe pump from New Era Pump Systems, Inc (Model NE-4000) was used to control injection rate.

5.2.2 General Synthesis of Copper(I) Oxide Nanocrystals To synthesize Cu₂O NCs, Cu(OAc)₂ (2.45 mmol) and 0, 1, 5, 10, or 15 mol% of Al(acac)₃, Ga(acac)₃, or In(acac)₃ was placed in a 25 mL 3-neck round bottom flask with 5 mL of oleic acid to result in a 0.49 M [Cu(OAc)₂] mixture. This flask was then capped with three rubber septa and the mixture was heated to 150 °C under nitrogen flow with constant stirring for thirty minutes to produce copper oleate precursor (Cu²⁺-O₂CR) and the corresponding M³⁺-O₂CR catalyst. This step also facilitates the removal of any acetic acid or acetylacetone through evaporation. In a separate 100 mL 3-neck round bottom flask, 25 mL of oleyl alcohol was heated to 200 °C while nitrogen was flowed over the solvent. The precursor solution was allowed to cool to 90 °C before 4 mL of the solution (equivalent to 1.96 mmol of Cu²⁺-O₂CR) was then drawn into a 10 mL syringe and injected into the oleyl alcohol at a rate of 0.35 mL min⁻¹ using a syringe pump. The reaction flask was constantly stirred during and after injection and the solution was held at 200 °C for 5 minutes after the injection was completed. The flask was then removed from heat and slowly cooled to room temperature.

The reaction mixture was centrifuged at 7500 rpm for 10 minutes to separate the solid product and supernatant. The supernatant was collected for further spectroscopic analysis. The solid was washed using 15 mL of hexanes and sonicated using an ultra-sonication horn (Branson 150) for resuspension. An equal volume of acetone was added to precipitate particles in solution. This was followed by centrifugation at 7500 rpm for 5 minutes. The washing and centrifugation steps were repeated 3 times. The resulting solid was dried from acetone in a vacuum oven for characterization. Solid isolation and washing were performed under ambient conditions.

5.2.3 Characterization of Copper(I) Oxide Nanocrystals and Post-Reaction Solutions Solid state materials resulting from the synthesis were characterized using multiple techniques. Powder

X-ray diffraction (PXRD, Rigaku SmartLab, Cu K α) was used to assess phase and crystallinity of the synthesized materials. Diffractograms were collected and compared to a Cu₂O standard (PDF #01-078-2076). Scanning electron microscopy (SEM, Hitachi S-4700 Field Emission Microscopy) and transmission electron microscopy (TEM, Thermofisher Talos F200X, lacey carbon on gold TEM grid) were used to assess particle size and morphology. Energy Dispersive Spectroscopy (EDS, Super-X EDS attached to TEM) was used to determine elemental composition. SEM, TEM, and EDS were performed at the Chapel Hill Analytical and Nanofabrication Laboratory.

The post-reaction solution (*i.e.* supernatant from initial centrifugation) was characterized to understand the extent of reactivity with each M³⁺ catalyst using attenuated total reflectance Fourier transform infrared (ATR-FTIR) spectroscopy (Nicolet iS-50 with built-in ATR) and UV-visible absorbance spectroscopy (Agilent Cary 5000, thin path length (0.2 cm) glass cuvette). For ATR-FTIR measurements, a liquid drop of post-reaction solution was placed directly on diamond ATR crystal.

5.2.4 Time Dependent Copper(I) Oxide Synthesis For kinetic analysis of the Cu₂O synthesis, the reaction was performed as described above, but with small aliquots (100-200 μ L) removed from the reaction approximately every thirty seconds during the injection period, and every minute after the conclusion of the injection period. These aliquots were analyzed via ATR-FTIR by directly adding liquid drops of each aliquot on the ATR crystal. UV-visible absorbance measurements for the aliquots were collected by diluting 100 μ L of aliquot with 900 μ L of oleyl alcohol.

5.3 Results and Discussion

5.3.1 Cu₂O Synthesis Cu₂O nanocrystals were synthesized by a continuous-injection procedure. Cu(OAc)₂ and the appropriate M(acac)₃ salt were first combined in oleic acid (HO₂CR, R= C₁₇H₃₃) and heated at 150 °C for a minimum of 30 minutes to generate Cu²⁺-O₂CR and M³⁺-O₂CR species. The amount of Cu²⁺-O₂CR, also referred to as the precursor, used for each experiment was constant at 1.96 mmol. The concentration of M³⁺-O₂CR catalysts, also referred to as M³⁺, were varied based on mol% of the precursor. 4 mL of the prepared precursor/catalyst solution was then injected at a controlled rate of 0.35 mL/min into oleyl alcohol at 200 °C. After completion of the injection, the temperature was held at 200 °C for 5 minutes to allow for the reaction of any remaining precursor before the flask was removed from the hot plate and allowed to slowly cool to room temperature. Solid products were isolated from the final solution following multiple washing/extraction steps.

Figure 5.1a shows PXRD data collected for solid products resulting from 10 mol% Al³⁺, Ga³⁺, and In³⁺, compared with 0 mol% catalyst. PXRD data for all catalyst conditions are shown in **Figure A5.1**. For Ga³⁺ and In³⁺ reactions, Cu₂O is the exclusive product with no evidence of side products such as CuO or M₂O₃. For some reaction conditions, Cu⁰ was produced as a minor product. Conditions which favored the production of Cu⁰ included elevated temperatures (>215 °C, **Figure A5.2**), slow injection rates, and extended times following injection at which the reaction remained at high temperature. We also note that Cu⁰ was produced for >5 mol% Al³⁺ (**Figure A5.1**). The Cu₂O observed when Cu⁰ metal was present was green in color, as opposed to the yellow/orange solid produced when no Cu⁰ was present. The green colored solid has been attributed to a Cu⁰ core with a Cu₂O shell.²⁰

The fact that Cu_2O is observed instead of CuO indicates that oleyl alcohol acts as a sufficient reductant for the conversion from Cu^{2+} to Cu^+ during the reaction. Evidence for alcohol reduction of copper has previously been reported in the literature.²¹ Given that CuO is not produced in any detectable quantity, we also believe that copper reduction occurs prior to nanocrystal formation such that Cu_2O is formed directly from Cu^+ -OH monomers. In fact, if the reaction temperature was held below 200 °C, no solid formation occurred and the reaction solution stayed green in color, indicating that Cu^{2+} was never reduced. Attempts to use a Cu^+ precursor (*i.e.* $\text{Cu}(\text{OAc})$) as a starting material were unsuccessful, as the exchange of acetate and oleate ligands oxidized Cu^+ to Cu^{2+} with the resulting precursor solution having the same absorbance spectrum and color as Cu^{2+} - O_2CR (**Figure A5.3**).

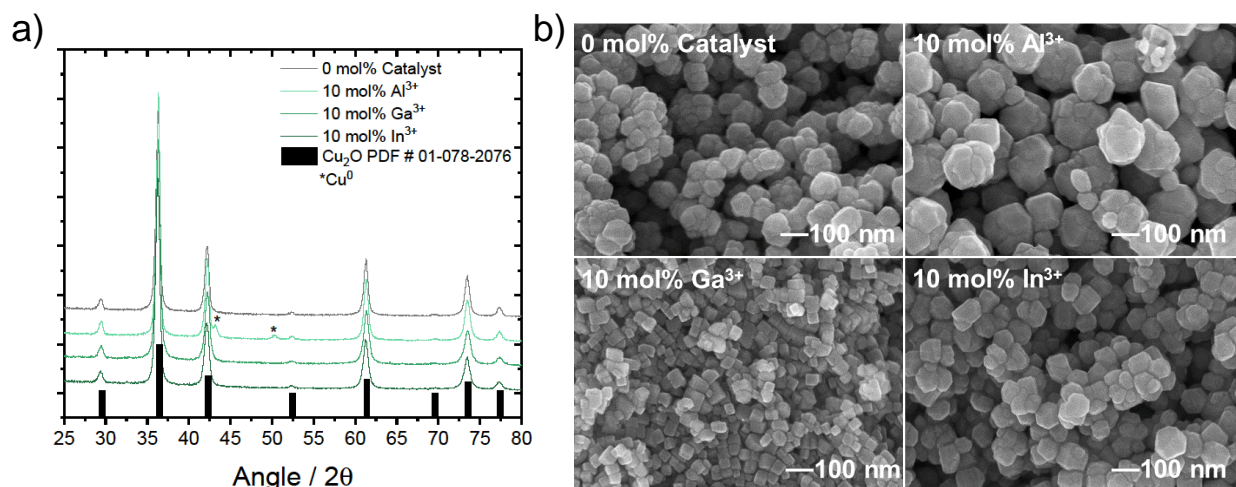


Figure 5.1: a) PXRD data collected for Cu_2O NCs synthesized by continuous-injection of Cu^{2+} - O_2CR as a function of 0 mol% and 10 mol% Al^{3+} , Ga^{3+} , or In^{3+} catalyst loading at 200 °C under N_2 . A standard diffraction pattern for Cu_2O (PDF# 01-078-2076) is shown for comparison. b) SEM images of Cu_2O NCs synthesized in the absence (0 mol%) and presence of 10 mol% M^{3+} catalysts.

In terms of M^{3+} oxide side products, we note that the synthesis of In_2O_3 has been heavily explored with the continuous-injection method.^{8-11,16,22} However, the low concentrations of In^{3+}

used in these studies does not yield In_2O_3 product. For example, control experiments using only $\text{M}^{3+}\text{-O}_2\text{CR}$ up to 0.30 mmol (equivalent to 15 mol% catalyst loading) showed no solid formation for any of the group 13 metal cations. However, injection of $\text{In}^{3+}\text{-O}_2\text{CR}$ and $\text{Ga}^{3+}\text{-O}_2\text{CR}$ at 2 mmol (equivalent to 100 mol% catalysts loading) did yield nanocrystalline In_2O_3 and $\gamma\text{-Ga}_2\text{O}_3$ (**Figure A5.4**). Similar experiments for Al^{3+} at 100 mol% were unsuccessful, as the precursor solidified in the syringe at high concentrations, making it impossible to inject.

SEM images of NCs produced with 0 mol% catalyst and 10 mol% Al^{3+} , Ga^{3+} , or In^{3+} are shown in **Figure 5.1b**. SEM images for 1, 5, and 15 mol% catalysts are shown in **Figure A5.5**. NC sizes for different mol% are given in **Table 5.1** and **Figure A5.6**. With no catalysts present, Cu_2O NCs were found to be roughly spherical with minor faceting and an average size of 129 ± 27 nm. NC agglomeration was also observed and believed to be due to weak coordination of oleate ligands to the Cu_2O surface. This observation was consistent across all reaction conditions. As a function of M^{3+} catalyst, clear differences in the size and morphology of Cu_2O NCs were observed. In general, the size of NCs was found to increase in the order $\text{Ga}^{3+} < \text{In}^{3+} < \text{Al}^{3+}$. Cu_2O produced from Ga^{3+} also exhibited a distinct cubic morphology while NCs resulting from In^{3+} and Al^{3+} were more spherical in shape, similar to those produced in the absence of M^{3+} cations. The change in the morphology with the addition of Ga^{3+} specifically points to a unique change in the kinetics of Cu_2O formation discussed further below. For all M^{3+} cations, no significant trends were observed between NC size and mol% catalyst. TEM images for all reaction conditions are shown in **Figure A5.7-A5.15**. EDS performed in combination with TEM revealed no evidence for In, Ga, or Al atoms within Cu_2O NCs. This result indicates that M^{3+} cations are not doped into Cu_2O nor do they form seed particles from which Cu_2O grows.

Table 5.1: Cu₂O NC sizes (nm)

No Catalyst		0 mol%			
Cu ²⁺ -O ₂ CR		129 ± 27			
With Catalyst	1 mol%	5 mol%	10 mol%	15 mol%	
Al ³⁺	169 ± 30	96 ± 15	191 ± 22	168 ± 43	
Ga ³⁺	62 ± 11	64 ± 13	58 ± 13	72 ± 16	
In ³⁺	111 ± 19	117 ± 17	90 ± 17	85 ± 14	

Despite the noted changes in Cu₂O NC size and morphology with M³⁺ cations, it is not apparent from PXRD or microscopy data that these metals are acting catalytically for Cu₂O formation. However, UV-visible absorbance and FTIR spectroscopy provide compelling evidence for this assignment and offer new insights into possible mechanisms for metal oxide formation. **Figure 5.2** shows UV-visible absorbance spectra obtained from post-reaction solutions for each catalyst. These spectra show a peak at 695 nm consistent with the Cu²⁺-O₂CR precursor. The 0 mol% condition resulted in post-reaction solutions which are deep green in color due to the strong peak at 695 nm. As catalysts were introduced, the intensity of the green color diminished as the peak decreased, finally resulting in a yellow amber color as the peak completely disappeared.

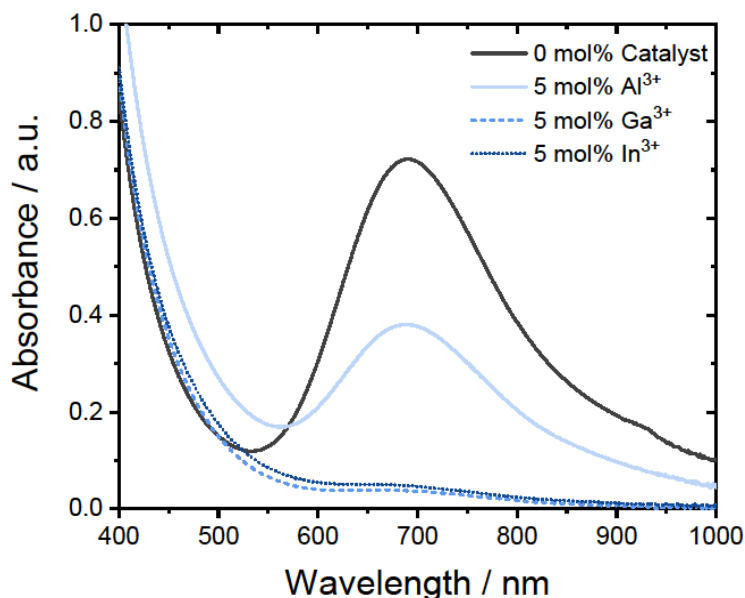


Figure 5.2: UV-visible absorbance spectra of post-reaction solutions obtained from continuous-injection of Cu^{2+} - O_2CR with 0 mol% and 5 mol% Al^{3+} , Ga^{3+} , or In^{3+} at 200 °C under N_2 . The peak at 695 nm is indicative of unreacted Cu^{2+} - O_2CR precursor remaining in solution. Absorbance was corrected for oleyl alcohol.

The magnitude of the 695 nm peak in the post-reaction solution can be used to measure reaction efficiency with the equation $\eta_{\text{rxn}} = 1 - [\text{Cu}^{2+}]_{\text{unreacted}}/[\text{Cu}^{2+}]_{\text{total}}$. The concentration of unreacted precursor was calculated for these solutions based on the extinction coefficient of the 695 nm peak (**Figure A5.16**). In the case of 0 mol% catalyst, $[\text{Cu}^{2+}]_{\text{unreacted}} = 17$ mM, resulting in $\eta_{\text{rxn}} = 76\%$ based on a $[\text{Cu}^{2+}]_{\text{total}} = 68$ mM present in the oleyl alcohol/oleic acid solution after injection. Upon addition of 5 mol% Al^{3+} , Ga^{3+} , or In^{3+} , $[\text{Cu}^{2+}]_{\text{unreacted}}$ decreased to 8.2, 4.4, and 5.9 mM, corresponding to $\eta_{\text{rxn}} = 86, 99,$ and 98% , respectively. In the case of Al^{3+} , the 695 nm peak remained present for all mol% catalyst conditions, indicating incomplete reactivity. $[\text{Cu}^{2+}]_{\text{unreacted}}$ was never less than 7 mM with the addition of up to 15 mol% Al^{3+} , resulting in a maximum $\eta_{\text{rxn}} = 90\%$. (**Figure A5.17**) With Ga^{3+} or In^{3+} , η_{rxn} achieved $>98\%$ for ≥ 5 mol% catalyst loading.

Figure 5.3 shows a summary of FTIR spectra collected for post-reaction solutions as a function of mol% catalyst. Previous literature reports have used FTIR to evaluate the esterification reaction using peaks consistent with free oleic acid (1710 cm^{-1}), oleyl oleate ester (1738 cm^{-1}) and oleyl alcohol (3300 cm^{-1}).⁸ **Figure 5.3** clearly shows the presence of these species in addition to $\text{Cu}^{2+}\text{-O}_2\text{CR}$, identified by the C=O stretch of the bound oleic acid at 1620 cm^{-1} , and an unknown solvent peak at 1660 cm^{-1} likely due to impurity (notably, this peak was constant as a function of reaction conditions, indicating no reactivity in the esterification cycle). Based on FTIR data, all M^{3+} catalysts showed greater reactivity than $\text{Cu}^{2+}\text{-O}_2\text{CR}$ for the conversion of oleic acid to oleyl oleate ester. Consistent with data from UV-visible absorbance, Al^{3+} showed little variation in ester formation as a function of mol% and incomplete consumption of $\text{Cu}^{2+}\text{-O}_2\text{CR}$ (**Figure A5.18**). Ga^{3+} and In^{3+} both showed significant consumption of the oleic acid peak and the $\text{Cu}^{2+}\text{-O}_2\text{CR}$ precursor in addition to formation of the ester peak.

Notably, these data were collected using an ATR-FTIR instrument, and while this is normally not a quantitative method, the low vapor pressure and high viscosity of the oleyl alcohol solvent allowed for a consistent sample volume to be obtained on top of the ATR crystal. Although we do not know the exact path length for the evanescent wave, Beer-Lambert plots of oleic acid (1710 cm^{-1}) and $\text{Cu}^{2+}\text{-O}_2\text{CR}$ (1620 cm^{-1}) (**Figure A5.19-A5.20**) were found to be linear over the absorbance range shown in **Figure 5.3** and allowed for apparent extinction coefficients of $\epsilon_{\text{app}} = 0.16\text{ M}^{-1}$ and 0.56 M^{-1} to be estimated for each peak, respectively. In a separate experiment, the apparent extinction coefficient for oleyl oleate ester at 1738 cm^{-1} was determined to be $\epsilon_{\text{app}} = 0.20\text{ M}^{-1}$ by converting 100% of oleic acid molecules to oleyl oleate ester by heating to $230\text{ }^\circ\text{C}$ in the presence of excess oleyl alcohol and no metal catalysts (**Figure A5.21**). These values allow

for a reliable estimation of the concentrations of reactants and products for the esterification reaction which are discussed further below with respect to time-dependent FTIR experiments.

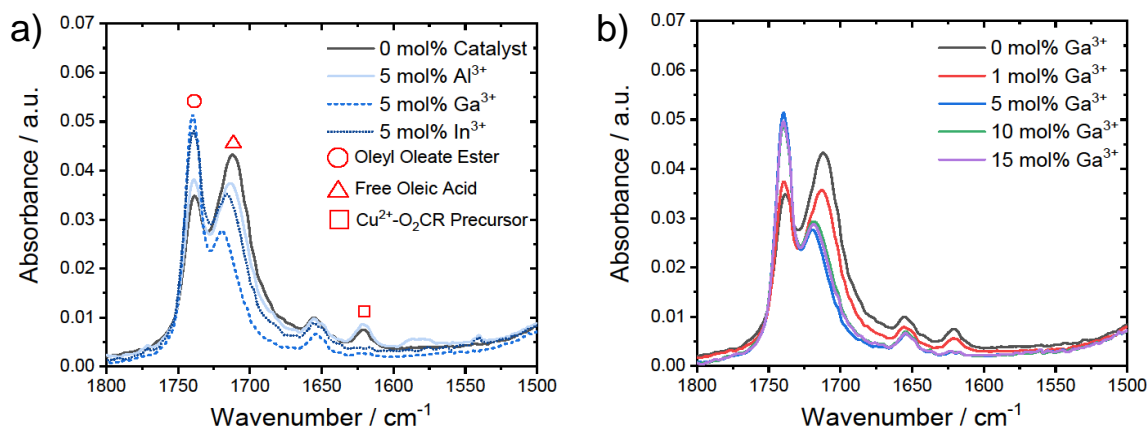


Figure 5.3: a) FTIR absorbance spectra in the C=O region of post-reaction solutions obtained from continuous-injection of $\text{Cu}^{2+}\text{-O}_2\text{CR}$ with 0 mol% and 5 mol% Al^{3+} , Ga^{3+} , or In^{3+} at 200 °C under N_2 . b) Similar data comparing 0-15 mol% Ga^{3+} catalyst loading conditions.

5.3.2 Time-Dependent Experiments The decrease in unreacted Cu^{2+} ions observed by UV-visible absorbance spectroscopy coupled with the enhanced production of oleyl oleate ester observed by FTIR points to a catalytic mechanism for the formation of Cu_2O in the presence of group 13 metals. To gain more insight, we performed time dependent experiments where 100-200 μL aliquots were removed from the reaction solution over a 17-minute time window. These aliquots were then analyzed by FTIR and UV-visible absorbance spectroscopy to observe the consumption of oleic acid and $\text{Cu}^{2+}\text{-O}_2\text{CR}$ precursor while watching the evolution of oleyl oleate ester over time. **Figure 5.4** shows FTIR data for the reaction performed with 5 mol% Ga^{3+} . Similar data are shown in **Figure A5.22** for 0 mol% catalyst, 1 mol% Ga^{3+} , 10 mol% Ga^{3+} , 5 mol% Al^{3+} , and 5 mol% In^{3+} reactions. Note that data are plotted as ΔAbs with respect to the initial spectrum at 0 min, which represents an aliquot removed from the oleyl alcohol solution just before injection began. Over the course of 17 min, these data collectively show the

consumption of oleyl alcohol (3300 cm^{-1}) concomitant with the growth of oleyl oleate ester (1738 cm^{-1}). Peaks associated with free oleic acid (1710 cm^{-1}) and $\text{Cu}^{2+}\text{-O}_2\text{CR}$ precursor (1620 cm^{-1}) were found to increase initially as these species were injected into solution, but eventually decayed over time as the esterification reaction and consumption of $\text{Cu}^{2+}\text{-O}_2\text{CR}$ progressed.

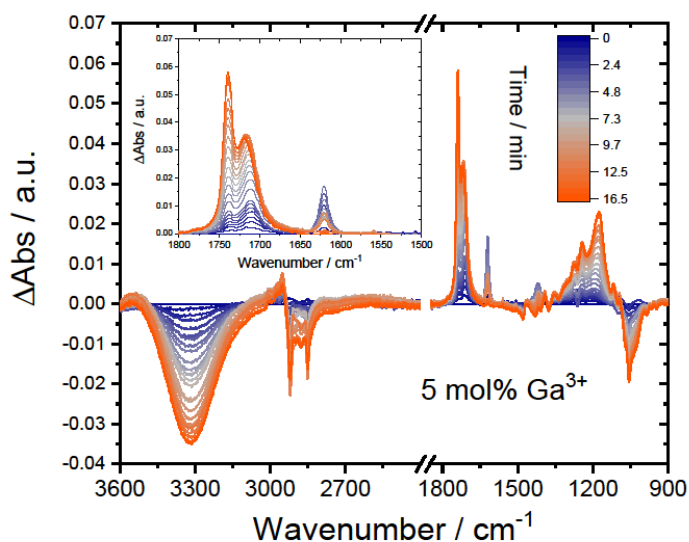


Figure 5.4: FTIR ΔAbs spectra collected for aliquots of reaction solution removed as a function of time during continuous-injection of $\text{Cu}^{2+}\text{-O}_2\text{CR}$ with 5 mol% Ga^{3+} at $200\text{ }^\circ\text{C}$ under N_2 .

By analyzing changes in these peaks with respect to time we can see several trends that occur with each catalyst and mol%. **Figure 5.5a-b** show the $\text{Cu}^{2+}\text{-O}_2\text{CR}$ precursor peak intensity at 1620 cm^{-1} as a function of time for different mol% Ga^{3+} and comparing 5 mol% for each group 13 metal. The rate for the initial buildup of precursor is consistent across all experiments due to the controlled injection rate of 0.35 mL/min , which is completed at the 11.5 min mark based on an injection volume of 4 mL . A 0 mol% catalyst injection performed at $25\text{ }^\circ\text{C}$ is shown for comparison to highlight the rate of precursor growth and maximum concentration of precursor obtained in the absence of esterification or NC formation. Note that the measured maximum concentration of 75 mM represents a 10% increase from the expected concentration of 68 mM .

This was a result of decreased volume from the ~25 aliquots removed from solution during the experiment. Across all reaction conditions, buildup of the precursor is shown to reach a critical limit before being consumed. The time point where consumption begins is consistent with where product formation is observed visually in the experiment as the solution changes from green to yellow. This was also confirmed by UV-visible absorbance spectroscopy by the peak observed at 490 nm, consistent with Cu₂O (**Figure A5.23**).²³ This time point was found to decrease from 9.2 min for 0 mol% Ga³⁺ to 5.5, 4.6, and 4.3 min for 1, 5, and 10 mol% Ga³⁺, respectively. Among the group 13 metals, this time point was found to decrease in the order Al³⁺ (8.9 min) < In³⁺ (4.9 min) < Ga³⁺ (4.6 min) for the 5 mol% condition.

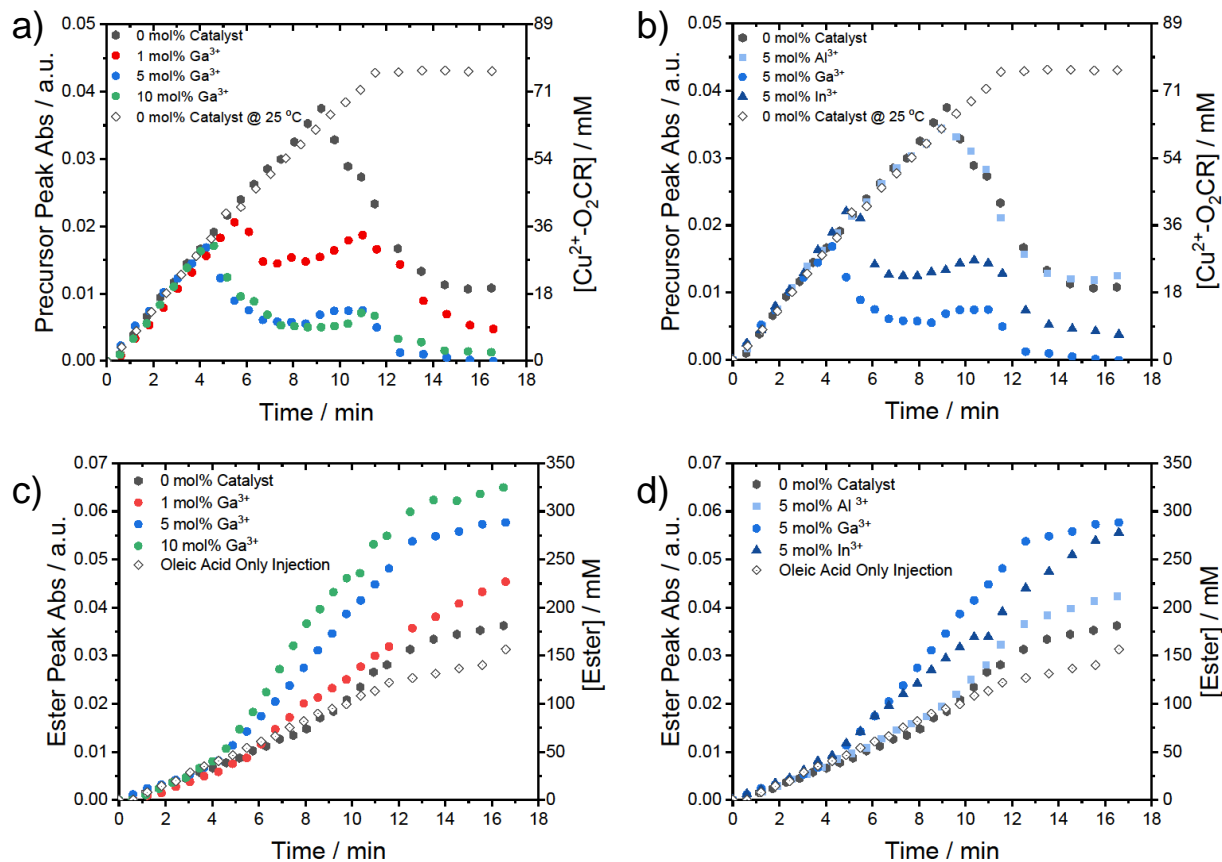
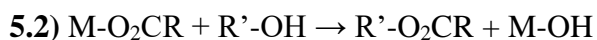
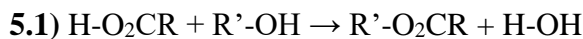


Figure 5.5: a-b) Precursor peak absorbance at 1620 cm⁻¹ obtained from time-dependent FTIR measurements comparing 0-10 mol% Ga³⁺ and different group 13 cations at 5 mol%. c-d) Ester peak absorbance at 1738 cm⁻¹ obtained from time-dependent FTIR measurements comparing 0-10 mol% Ga³⁺ and different group 13 cations at 5 mol%. Precursor and ester concentrations were calculated from apparent extinction coefficients obtained from **Figures A5.19-A5.21**.

In the cases of Ga³⁺ and In³⁺, the precursor peak intensity reached steady-state around 7 min before rising again around 8-9 min and eventually decaying to lower values after 11 min. We believe this observation reflects the balance in rates between addition of the precursor/catalyst via injection and consumption via NC formation. Following the first decrease in precursor concentration, the rate of NC formation likely decreased with time and was equal to the injection rate around the 7 min mark. The rise in precursor around 8-9 min was therefore due to the rate of precursor consumption dropping below the rate of the injection, thus a net addition of precursor

was observed. When the injection was completed around 11 min, the precursor concentration decreased again because the rate of consumption was uncontested.

Figure 5.5c-d show time dependent FTIR data for the oleyl oleate ester peak intensity at 1738 cm^{-1} . Clear changes in the rate of ester formation are observed as a function of mol% Ga^{3+} and the nature of the group 13 metal. In all cases, the linear increase in Abs_{1738} between 0-4 min was due to background esterification as shown for the injection of oleic acid into oleyl alcohol at 200 $^{\circ}\text{C}$ in the absence of any metal (**Equation 5.1**, $\text{R} = \text{C}_{17}\text{H}_{33}$, $\text{R}' = \text{C}_{18}\text{H}_{35}$). The apparent rate for this background process was estimated to be 11 mM min^{-1} based on the linear slope from 0-11 min. The apparent zero-order nature of ester growth is likely due to the excess concentration of oleyl alcohol and the constant replenishment of oleic acid due to the slow injection rate. The total concentration of ester produced by **Equation 5.1** over the 17 min time window was found to be $[\text{Ester}]_{\text{final}} = 94 \text{ mM}$, equivalent to 24% conversion of injected oleic acid.



As the precursor/catalyst solution was injected, metal catalyzed esterification became an additional pathway for ester production (**Equation 5.2**), as indicated by the changes in rate observed at 10, 6, 4, and 4 min for 0, 1, 5, and 10 mol% Ga^{3+} , respectively. These time points were also found to coincide with the sharp decrease in the precursor peak, indicating that consumption of the precursor was triggered by metal catalysis. Furthermore, control experiments performed with 5 mol% Ga^{3+} in the absence of $\text{Cu}^{2+}\text{-O}_2\text{CR}$ exhibited the same rate for ester formation and total ester produced as when $\text{Cu}^{2+}\text{-O}_2\text{CR}$ was present (**Figure A5.24**), indicating

that esterification is dominated by Ga^{3+} catalysis. The rates for metal catalyzed esterification were also found to be zero-order and were estimated to be 24, 20, 28, and 38 mM min^{-1} for 0, 1, 5, and 10 mol% Ga^{3+} based on the linear portion of ester growth immediately following the onset of metal catalysis. The $[\text{Ester}]_{\text{final}}$ produced also increased with mol% Ga^{3+} from 125 mM for 0 mol% to 183, 260, and 307 mM for 1, 5, and 10 mol%, respectively. These data indicate a clear dependence on $[\text{Ga}^{3+}]$ for the esterification reaction.

A comparison of group 13 metals at 5 mol% loading revealed that Al^{3+} catalyzed the esterification reaction only slightly better than $\text{Cu}^{2+}\text{-O}_2\text{CR}$ on its own, with a rate of 27 mM min^{-1} and $[\text{Ester}]_{\text{final}} = 163$ mM (**Table 5.2**). The $[\text{Ester}]_{\text{final}}$ produced for Ga^{3+} (260 mM) and In^{3+} (247 mM) were much larger, but with comparable rates of 28 and 21 mM min^{-1} , respectively.

Turnover numbers (TON) for each catalyst were estimated by the equation $\text{TON} = [\text{Ester}]_{\text{cat}}/[\text{Cat}]$, where $[\text{Ester}]_{\text{cat}} (= [\text{Ester}]_{\text{final}} - [\text{Ester}]_{\text{final}(\text{oleic acid})})$ is the concentration of ester produced by each catalyst and $[\text{Cat}]$ is the total concentration of each metal ion in the reaction solution following injection. For example, at the 5 mol% condition, $[\text{Cu}^{2+}] = 75$ mM and $[\text{M}^{3+}] = 3.8$ mM. Resulting TON's showed that Ga^{3+} was the best group 13 catalyst with 44 ester molecules produced for every Ga^{3+} cation while Cu^{2+} achieved only 0.4 turnovers. Furthermore, TON was found to decrease with higher mol% for the Ga^{3+} series, showing that while the ester formation rate increased with more Ga^{3+} , not all cations were catalytically active. This will be discussed in detail further below.

Table 5.2: Comparison of M³⁺ Esterification Catalysis

Reaction Condition	$\eta_{\text{rxn}}^{\text{a}}$ (%)	Ester Rate ^b (mM min ⁻¹)	[Ester] _{final} ^c (mM)	[Ester] _{cat} ^d (mM)	TON ^e
Oleic acid only	-	11	94	-	-
Cu ²⁺ -O ₂ CR	76	24	125	31	0.4
1 mol% Ga ³⁺	94	20	183	89	119
5 mol% Ga ³⁺	99	28	260	166	44
10 mol% Ga ³⁺	99	38	307	213	28
5 mol% Al ³⁺	86	27	163	69	18
5 mol% In ³⁺	98	21	247	153	41

^a $\eta_{\text{rxn}} = 1 - [\text{Cu}^{2+}]_{\text{unreacted}}/[\text{Cu}^{2+}]_{\text{total}}$; ^bEstimated by the linear slope for growth of 1738 cm⁻¹ FTIR peak; ^c $[\text{Ester}]_{\text{final}} = (\text{Abs}_{\text{final}}(1738 \text{ cm}^{-1}) - \epsilon_{\text{app,acid}}[\text{Acid}]_{\text{total}})/(\epsilon_{\text{app,ester}} - \epsilon_{\text{app,acid}})$ where $\epsilon_{\text{app,acid}} = 0.04 \text{ M}^{-1}$, $\epsilon_{\text{app,ester}} = 0.20 \text{ M}^{-1}$, and $[\text{Acid}]_{\text{total}} = 393 \text{ mM}$; ^d $[\text{Ester}]_{\text{cat}} = [\text{Ester}]_{\text{final}} - [\text{Ester}]_{\text{final(oleic acid)}}$; ^eTON = $[\text{Ester}]_{\text{cat}}/[\text{Cat}]$.

5.3.3 Catalytic Mechanism Based on the established mechanism of M-OH condensation to yield metal oxide NCs, we can reason that every copper ion present within Cu₂O must have existed as a Cu⁺-OH monomer. The generation of these monomers could arise through copper catalyzed esterification like that shown in **Equation 5.2** or, as we propose here, transmetallation with M³⁺-OH species. Unfortunately, we were unable to identify a unique FTIR absorbance resulting from the M³⁺-OH bond, therefore we use the ester peak as an indirect measure of M³⁺-OH formation. The large [Ester]_{cat} observed for Ga³⁺ and In³⁺ indicate that Ga³⁺-OH and In³⁺-OH are produced in high quantities. Based on **Equation 5.2**, the total moles of M³⁺-OH produced over the lifetime of the reaction should be equal to the total moles of ester produced by the catalyst. Many of these M³⁺-OH species are converted back to M³⁺-O₂CR by reacting with oleic acid (**Equation 5.3**) whereby the catalyst is regenerated and may proceed through another cycle.

However, in the presence of $\text{Cu}^+\text{-O}_2\text{CR}$, the transmetallation reaction shown in **Equation 5.4** could equally regenerate the $\text{M}^{3+}\text{-O}_2\text{CR}$ catalyst while also producing $\text{Cu}^+\text{-OH}$. Here, we indicate $\text{Cu}^+\text{-O}_2\text{CR}$ because the reaction does not proceed unless reduction of Cu^{2+} to Cu^+ occurs. Therefore, we believe that the $\text{Cu}^{2+}\text{-O}_2\text{CR}$ precursor is first reduced to $\text{Cu}^+\text{-O}_2\text{CR}$ prior to transmetallation of the -OH ligand.

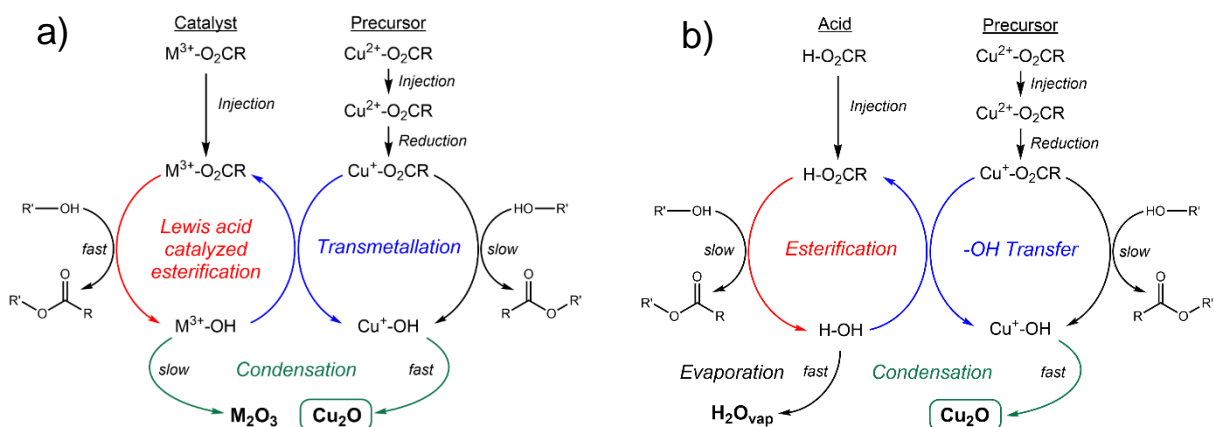


It is important to note that **Equations 5.3-5.4** are the same reaction with the only difference being the nature of the cation bound to the $\text{-O}_2\text{CR}$ ligand, H^+ vs Cu^+ . This comparison highlights the competition that exists between protons and metal cations for -OH ligands during the catalytic cycle. Control experiments which showed 5 mol% Ga^{3+} produced the same amount of ester with or without copper ions present suggest that their inclusion supplants $\text{H-O}_2\text{CR}$ as a reactant with $\text{Ga}^{3+}\text{-OH}$.

While $\text{M}^{3+}\text{-OH}$ species are suitable donors for -OH ligands, H_2O (H-OH) produced through background esterification or $\text{Cu}^+\text{-OH}$ condensation could also deliver -OH ligands and bypass the copper catalyzed esterification route (**Equation 5.5**). In fact, it is known that if H_2O is not efficiently removed from solution during the synthesis of In_2O_3 , then uncontrolled NC growth is observed through ligand exchange of $\text{In}^{3+}\text{-O}_2\text{CR}$ and H_2O to generate $\text{In}^{3+}\text{-OH}$ species.⁸ From **Table 5.2**, it is apparent that a significant amount of $\text{Cu}^+\text{-OH}$ must be generated by ligand exchange between $\text{Cu}^+\text{-O}_2\text{CR}$ and H_2O . This is evident by the fact that $\text{TON} = 0.4$ but $\eta_{\text{rxn}} = 76\%$

for the 0 mol% condition. This means that, on average, only 40% of the copper ions go through one esterification cycle to produce $\text{Cu}^+\text{-OH}$, yet 76% of copper ions are consumed to produce Cu_2O . Notably, the reaction is designed to sweep H_2O from the reaction flask due the elevated temperature (200 °C) and continuous flow of N_2 over the solution surface. Based on **Equation 5.5**, it could even be possible that the copper precursor does not catalyze esterification at all, and instead, the late onset for precursor consumption could be related to a slow buildup of H_2O in solution until a critical concentration is reached.

Scheme 5.2 provides two catalytic cycles to summarize our proposed reactions, with and without M^{3+} catalysts. In the presence of these catalysts, $\text{M}^{3+}\text{-O}_2\text{CR}$ is able to catalyze the formation of oleyl oleate ester ($\text{R}'\text{-O}_2\text{CR}$) in the presence of oleyl alcohol ($\text{R}'\text{-OH}$) to produce $\text{M}^{3+}\text{-OH}$ species. Likewise, $\text{Cu}^+\text{-O}_2\text{CR}$ is able to catalyze the esterification reaction to produce $\text{Cu}^+\text{-OH}$. Given that copper catalysis is observed to be less efficient than M^{3+} catalysis, we believe that most, if not all, $\text{Cu}^+\text{-OH}$ species are generated through transmetallation of -OH from $\text{M}^{3+}\text{-OH}$ to $\text{Cu}^+\text{-O}_2\text{CR}$, defined by the central path. Once $\text{Cu}^+\text{-OH}$ species are formed, rapid condensation occurs to produce Cu_2O NCs. Importantly, the condensation of $\text{M}^{3+}\text{-OH}$ species is in direct competition with transmetallation and therefore the low concentration of M^{3+} catalysts is critical in preventing condensation and achieving the -OH transfer step. In the absence of M^{3+} catalysts, a mirrored reaction cycle can be shown in which oleic acid ($\text{H-O}_2\text{CR}$) replaces the $\text{M}^{3+}\text{-O}_2\text{CR}$ species and undergoes esterification to yield oleyl oleate ester and water (H-OH) as products. Similar to the M^{3+} cycle, water may transfer the -OH ligand to $\text{Cu}^+\text{-O}_2\text{CR}$ to generate $\text{Cu}^+\text{-OH}$ and trigger Cu_2O formation. However, unlike the M^{3+} cycle, the -OH transfer reaction is in competition with the removal of water from the solution by vaporization.



Scheme 5.2: a) Proposed catalytic cycle for M^{3+} catalyzed esterification to ultimately produce Cu_2O NCs through a $-OH$ transmetalation step. b) Proposed catalytic cycle for the synthesis of Cu_2O NCs in the absence of M^{3+} catalysts.

5.3.4 Insights into Group 13 Catalysts Lewis acid catalyzed esterification is a well-studied reaction in the field of organic synthesis.^{24–26} The established mechanism involves activation of the organic acid by coordination of the carbonyl group to the Lewis acidic cation, thus making the carbonyl carbon more susceptible to nucleophilic attack by an alcohol.²⁷ Therefore, the coordination environment around the metal as well its Lewis acidity play key roles in determining reactivity. Here, we have exchanged acetylacetonate ligands for oleate ligands with each group 13 metal to generate active catalysts. This was performed at elevated temperatures under inert gas; however, it is difficult to know the extent to which the ligand exchange reaction has been performed. This is especially important in the case of Al^{3+} . Among the group 13 metals, Al^{3+} is the strongest Lewis acid and would be expected to be the best catalysts for esterification.²⁸ However, here we observe it as the worst catalyst, barely better than the copper precursor. We believe this is due to incomplete exchange of the acetylacetonate ligands during preparation of the catalyst, which would result in catalytically inactive Al^{3+} cations. Indeed, Al^{3+} is the hardest acid and most oxophilic among the group and would therefore be expected to strongly resist ligand exchange from the chelated acetylacetonate environment.

Further evidence that incomplete preparation of the Al^{3+} precursor could be responsible for its lack of catalysis can be found by comparing the esterification rates for each catalyst with the reaction time in which metal catalysis begins. For all metals, including copper, the esterification rate was found to be within the range of 20-30 mM min^{-1} . However, Al^{3+} catalysis did not begin until 8.9 min for the 5 mol% condition compared to 4.6 min for Ga^{3+} and 4.9 min for In^{3+} . The slow reaction time onset could be the result of a low concentration of catalytically active Al^{3+} cations in the precursor solution which would need to build up in the reaction solution before the metal catalyzed esterification rate could be observed. This hypothesis is also predicated on the idea that a small amount of catalyst could maintain a high esterification rate.

Although we do not have mol% dependent data for Al^{3+} , we do have such data in the case of Ga^{3+} . Here, the esterification rate was found to increase with mol% catalyst; however, the TON decreased due to the fact that $[\text{Ester}]_{\text{final}}$ did not increase at the same rate as mol%. This observation suggests that only a small fraction of Ga^{3+} cations are driving the esterification reaction. Control experiments performed in which 100 mol% Ga^{3+} was present in the absence of $\text{Cu}^{2+}\text{-O}_2\text{CR}$, the esterification rate was found to be 23 mM min^{-1} and $[\text{Ester}]_{\text{final}} = 270 \text{ mM}$. This equates to a TON of 2.3. The low TON is the result of $[\text{Ester}]_{\text{final}}$ being roughly equal to that observed for 5-10 mol% Ga^{3+} while the amount of catalyst was 10-20 times larger. One obvious reason for this is that a significant fraction of $\text{Ga}^{3+}\text{-OH}$ species produced from each esterification cycle may undergo condensation with other $\text{Ga}^{3+}\text{-OH}$ species to produce $\gamma\text{-Ga}_2\text{O}_3$. The condensation reaction would thus remove Ga^{3+} from the catalytic cycle and result in a lower amount of active catalysts. The same analysis can be performed with the 100 mol% In^{3+} condition in the absence of $\text{Cu}^{2+}\text{-O}_2\text{CR}$, resulting in an esterification rate of 19 mM min^{-1} , $[\text{Ester}]_{\text{final}} = 287 \text{ mM}$, and $\text{TON} = 2.6$.

The decrease in TON when going from 1 to 10 mol% Ga^{3+} may also be explained by competitive condensation which does not result in solid formation. Group 13 metals in aqueous solution are known to hydrolyze water to form $\mu\text{-OH}$ clusters.²⁹⁻³¹ When carboxylate ligands (*e.g.* acetate) are present, these clusters can also contain bridged carboxylates. In the case of Ga^{3+} and In^{3+} , oligomer chains of acetate ligands and metal cations have even been observed. It is therefore possible that $\mu\text{-OH}$ and $\mu\text{-O}$ coordinated Ga^{3+} clusters could result from condensation as the mol% is increased. This would thus lower the concentration of active Ga^{3+} cations for esterification. Notably, nucleation theory requires a critical concentration of monomers to be present in solution before nucleation may begin.⁴ Below this threshold, the coalescence of monomers into larger clusters is thought to occur but that such structures are unstable and dissolve back into monomer units. Given the established literature of group 13 clusters with $\mu\text{-OH}$ and $\mu\text{-O}$ ligands, we believe these species may be long lived during the catalytic cycle. In fact, the formation of trinuclear $\mu\text{-O}$ clusters in the synthesis of Fe_2O_3 with the continuous-injection method have been observed and used to explain the continuous growth of NCs.¹²

Based on the metrics presented for esterification catalysis, In^{3+} appears to be comparable with Ga^{3+} , however, a clear distinction is made between the morphology and size of the resulting Cu_2O NCs. In the case of In^{3+} , NCs with diameters ≥ 85 nm were produced for all mol% conditions with spherical morphologies and a small degree of faceting. In the case of Ga^{3+} , resulting NCs were notably smaller (≤ 72 nm) and displayed a distinct cubic morphology across all mol% conditions. We believe the origin for this result must be related to the inherent reactivity of each metal towards esterification and transmetallation. **Figure 5.6** shows FTIR ΔAbs spectra in the $\text{C}=\text{O}$ region for 100 mol% Ga^{3+} and In^{3+} injections in the absence of $\text{Cu}^{2+}\text{-O}_2\text{CR}$. While both metals catalyze esterification equally well, there is a notable difference in the

observed absorbance features in the range of $1650 - 1500 \text{ cm}^{-1}$. This region displays peaks associated with the C=O bond of the M^{3+} bound oleate ligand. Interestingly, when the Ga^{3+} - O_2CR was injected into oleyl alcohol at $200 \text{ }^\circ\text{C}$, the precursor peak at 1563 cm^{-1} never grew in substantially during the reaction. In contrast, the In^{3+} - O_2CR peak grew in markedly during the injection period before decaying away upon condensation to form In_2O_3 . Despite the Ga^{3+} - O_2CR peak not being significantly present during the catalytic reaction, nanocrystalline Ga_2O_3 was still produced (**Figure A5.4**).

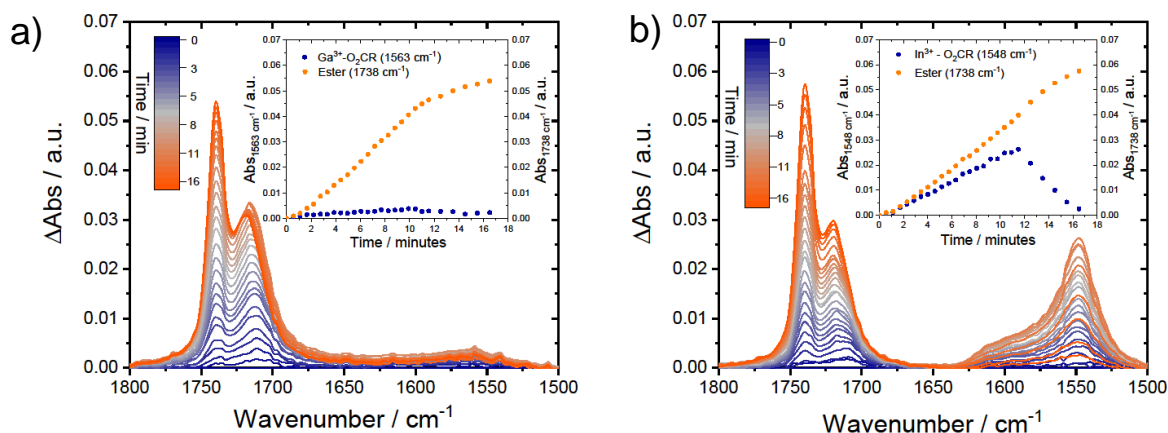


Figure 5.6: FTIR ΔAbs spectra for continuous-injection of 100 mol% a) Ga^{3+} - O_2CR and b) In^{3+} - O_2CR into oleyl alcohol at $200 \text{ }^\circ\text{C}$ under N_2 . Insets for each figure show the precursor peak absorbance for M^{3+} - O_2CR and oleyl oleate ester measured over the course of the reaction.

The absence of a precursor peak in the case of Ga^{3+} may be related to its ability to undergo condensation reactions to form μ -OH clusters. As discussed above, the mol% dependence for Ga^{3+} suggests that only a small fraction of Ga^{3+} cations are needed to maintain high levels of esterification. Indeed, the esterification rate and $[\text{Ester}]_{\text{final}}$ observed for 100 mol% Ga^{3+} were on par with those observed for 1-5 mol% Ga^{3+} . The propensity to form clusters may also be linked

to the kinetics for transmetallation between Ga^{3+} and Cu^+ , as transmetallation would necessarily involve the formation of a bimetallic $\mu\text{-OH}$ complex to facilitate -OH ligand transfer.

In the case of In^{3+} , the persistence of the $\text{In}^{3+}\text{-O}_2\text{CR}$ peak could indicate slower reactivity toward condensation than Ga^{3+} . Fortunately, In_2O_3 synthesis and In^{3+} reactivity has been studied heavily by the Hutchison group^{8,9,16,22} where one particular study focused on the impact of temperature and injection rate on $\text{In}^{3+}\text{-O}_2\text{CR}$ precursor reactivity and the resulting morphology of In_2O_3 nanocrystals.³² They show that at lower temperatures and/or fast injection rates the $\text{In}^{3+}\text{-OH}$ monomers are slower to react, causing branched nanocrystals to form, as opposed to at high temperatures and slower injection rates where spherical particles are observed. Our reaction conditions produced branched nanocrystals (**Figure S25**), which Plummer *et al.* state is related to long-lived $\text{In}^{3+}\text{-OH}$ monomers in solution. Such long lifetimes would imply slow kinetics for condensation and thus transmetallation to Cu^+ .

Further evidence for the hypothesis of faster transmetallation kinetics for Ga^{3+} than In^{3+} can be found in the comparison of the 5 mol% catalyst data shown in **Figure 5.5**. In the case of Ga^{3+} , the time points at which the $\text{Cu}^{2+}\text{-O}_2\text{CR}$ precursor peak decreased, associated with Cu_2O NC formation, and the onset for M^{3+} catalyzed esterification occurred were found to be identical at 4.3 min. In the case of In^{3+} , however, the decrease in the precursor peak (5.5 min) occurred 1.4 min after the onset of esterification (4.9 min). This lag in precursor consumption is a clear indication of transmetallation limited formation of $\text{Cu}^+\text{-OH}$ monomers needed for Cu_2O formation. The rapid transmetallation of -OH ligands from $\text{Ga}^{3+}\text{-OH}$ is therefore believed to be a significant factor in producing the cubic morphology observed for Cu_2O NCs.

5.3.5 Relevance to Metal Oxide Synthesis Many Cu_2O syntheses exist in the literature that give a variety of sizes and morphologies.³³⁻⁴⁵ Early synthesis of small Cu_2O nanocrystals was

achieved by oxidizing Cu^0 nanoparticles to Cu_2O in air.⁴⁶ This was characterized by a shift in color from metallic red to green. The green color of oxidized Cu^0 nanoparticles has been attributed to a Cu^0 core that remains buried beneath a Cu_2O shell.²⁰ Interestingly, Cu_2O that is synthesized directly (*i.e.* from Cu^+ -OH monomers) is yellow/orange in color.^{20,38,47} In most cases, our synthesis produced Cu_2O exclusively and through a direct route, but in the case of high temperature or with > 5 mol% Al^{3+} we produced Cu^0 nanocrystals, a small fraction of which turn green after oxidation in air, consistent with the literature.

Other syntheses which produced Cu_2O directly produce particles that are several hundred nanometers to microns in size and show impressive control over particle morphology.^{37,40,45,48–52} The morphological change observed here with the addition of Ga^{3+} is consistent with the formation of nanocubes. In the literature, fast reactivity of precursors has been attributed with the cubic morphology whereas slower reactivity has resulted in octahedral NCs.⁴⁰ Only a few synthetic methods have been shown to produce small colloidal Cu_2O NCs.^{20,23,38,47} These colloidal particles are capped with a variety of ligands including phosphate, amines, and carboxylates. The use of oleic acid in the continuous-injection method is necessary for the esterification reaction, but we also believe that amines or thiols could better cap the Cu_2O NCs, preventing agglomeration and resulting in smaller particle size.^{53,54}

We note that a recent report by Kim *et al.* described the effect of nonincorporative cations such as Na^+ and K^+ on the synthesis of In_2O_3 NCs where size and shape were effectively tuned.¹¹ These results were explained based on the concentration of free and bound oleate ligands, affected by $[\text{Na}^+]$ and $[\text{K}^+]$, and their influence of surface capping. In the present case, Ga^{3+} may exhibit similar effects to result in the nanocubic morphology of Cu_2O ; however, we also believe that the rates of esterification by Ga^{3+} - O_2CR and transmetallation by Ga^{3+} -OH play significant

roles to determine morphology. To the best of our knowledge, this is the first report of a transmetallation mechanism for metal oxide synthesis. The observation of this mechanism in the present system relies on the competitive nature of metal catalyzed esterification and M-OH condensation reactions. Cu^+ appears to catalyze esterification slowly but undergo rapid condensation when Cu^+ -OH monomers are formed. Ga^{3+} and In^{3+} possess fast catalysis for esterification while their condensation reactions can be inhibited through low mol% loadings. This sets up a reaction scheme where Cu^+ is able to bypass the esterification route and accept -OH ligands from M^{3+} -OH through transmetallation. This type of mechanism could unlock the ability to use metal cations which are not prone to catalyzing the esterification reaction on their own. Although the esterification method has been shown for a number of metals, some have shown resistance to this reactivity, including copper, silver, and antimony.⁸ Furthermore, the inclusion of catalytic amounts of Ga^{3+} or In^{3+} into precursor solutions with other metals which are able to catalyze the esterification reaction (*i.e.* Fe, Co, Mn) may produce new reactivity through a more rapid production of -OH ligands in solution.

The possibility of transmetallation between two metal centers during the synthesis of metal oxides could also open the door to the preparation of new ternary oxide materials. For this to be achieved, the production $\text{M}_1\text{-OH}$ and $\text{M}_2\text{-OH}$ species would need to occur on the same timeframe and kinetics for cross condensation (*i.e.* $\text{M}_1\text{-OH} + \text{M}_2\text{-OH} \rightarrow \text{M}_1\text{-O-M}_2 + \text{H}_2\text{O}$) would need to be faster than the formation of their respective binary oxides. The transmetallation step could even serve as a “buffer” to balance the rates of $\text{M}_1\text{-OH}$ and $\text{M}_2\text{-OH}$ production by transferring -OH ligands to the metal with a slower esterification rate. Indeed, the synthesis of some ternary oxide materials have already been reported in the literature using the continuous-injection method. However, these examples have centered on the synthesis of doped In_2O_3 ^{9,16,22} where the dopant

metal occupies the same coordination environment and atomic position as In^{3+} . It is possible that transmetallation between metals plays a role in the synthetic mechanism for these materials but has not yet been identified. It remains to be seen if the continuous-injection method can be used to produce ternary oxide materials where each metal occupies a unique coordination environment. Notably, the formation of ternary oxides does not occur for the present reaction conditions. Even in the case of 1:1 $\text{Cu}^{1+}:\text{M}^{3+}$ (the ratio for delafossite)⁵⁵⁻⁵⁷ or 1:2 $\text{Cu}^{2+}:\text{M}^{3+}$ (the ratio for spinel)⁵⁸, Cu_2O is always the major product. This speaks to a kinetic mismatch between the formation of $\text{Cu}^+\text{-OH}$ and $\text{M}^{3+}\text{-OH}$ species during the reaction.

5.4 Conclusion

Here we have shown a unique synthetic route for producing Cu_2O NCs by the addition of group 13 Lewis acid catalysts to a continuous-injection methodology. The inclusion of these catalysts are found to enhance the reaction efficiency of copper ions toward inclusion in Cu_2O NCs and result in higher production of $\text{M}^{3+}\text{-OH}$ species through esterification catalysis. Detailed time-dependent spectroscopic analysis reveals a unique transmetallation step between $\text{M}^{3+}\text{-OH}$ species and $\text{Cu}^+\text{-O}_2\text{CR}$ to generate $\text{Cu}^+\text{-OH}$ monomers. This step allows Cu^+ to bypass the typical esterification route for generation of $\text{Cu}^+\text{-OH}$ and results in rapid condensation to form Cu_2O NCs. Of the group 13 metals, we find that Ga^{3+} exhibits our “goldilocks” reactivity, resulting in the smallest NCs and a distinctive cubic morphology. The use of Lewis acids in this reaction scheme could allow for a greater versatility in binary and ternary metal oxide formation. Further investigation of different metal-oleates and their reactivity with the continuous-injection method could allow for new syntheses to be developed for a wide variety of metal oxides.

5.6 Appendix

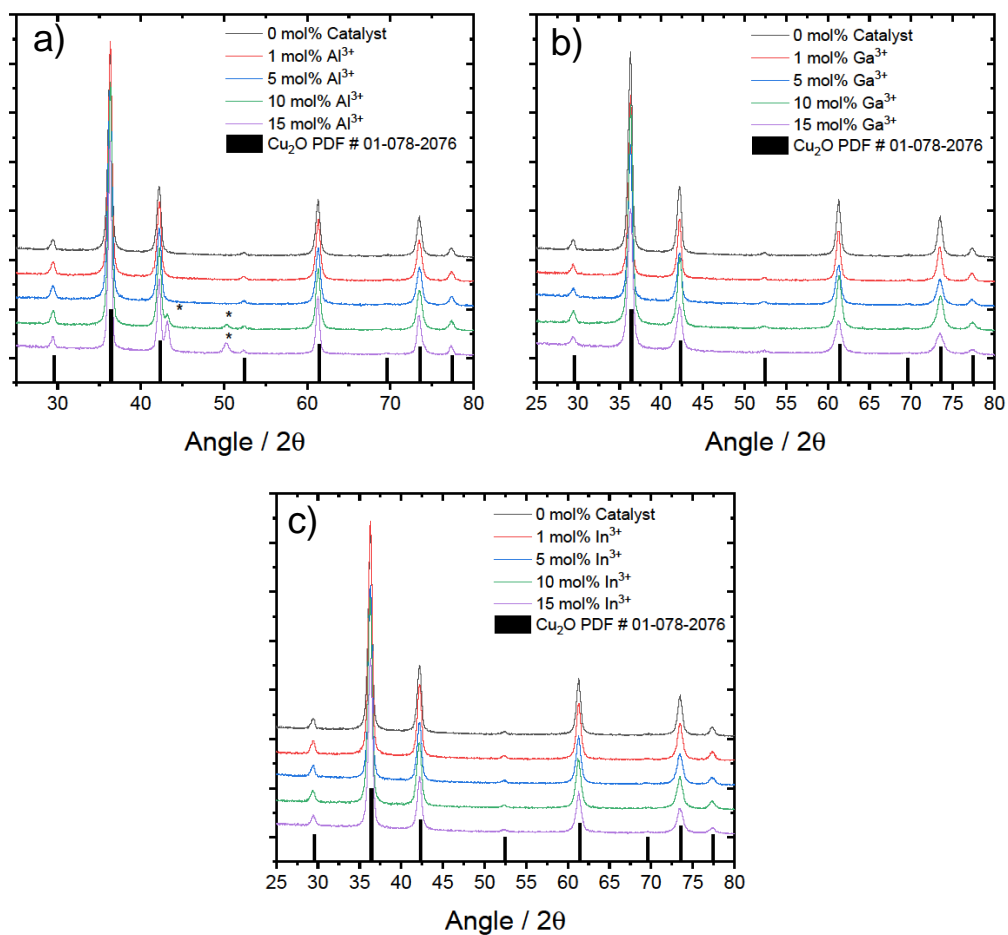


Figure A5.1: PXRD of a) Al^{3+} , b) Ga^{3+} , and c) In^{3+} catalyzed Cu_2O . Asterisks (*) in Al^{3+} data refer to peaks associated with Cu^0 .

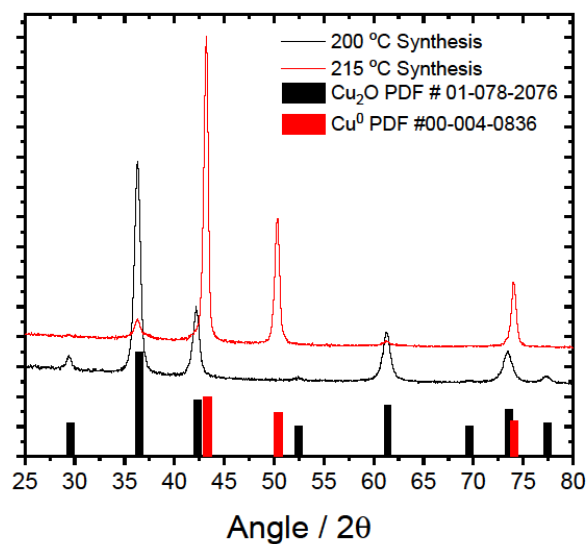


Figure A5.2: PXRD of reaction products at 200 °C and 215 °C.

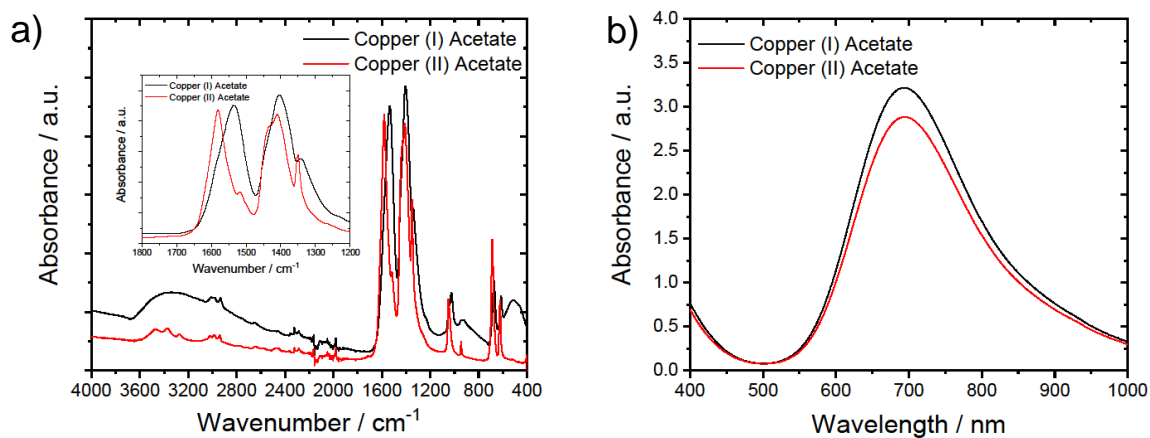


Figure A5.3: a) FTIR of copper (I) acetate and copper (II) acetate solids. b) UV-Vis of precursors synthesized from the exchange of copper (I) acetate and copper (II) acetate with oleic acid. Both solutions were made at 68 mM by dilution with oleyl alcohol.

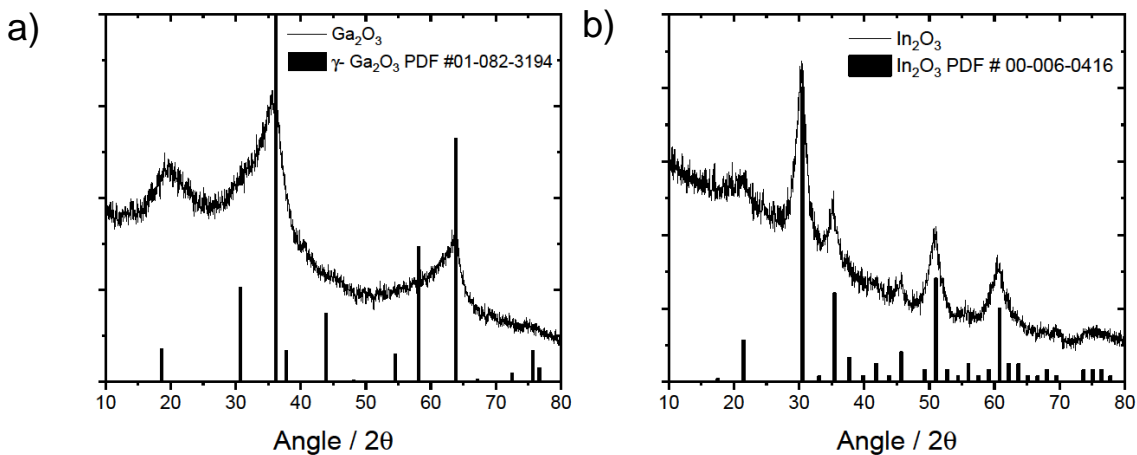


Figure A5.4: PXRD of a) γ - Ga_2O_3 and b) In_2O_3 synthesized via continuous-injection of 2 mmol of M^{3+} - O_2CR into oleyl alcohol at 200 °C under N_2 .

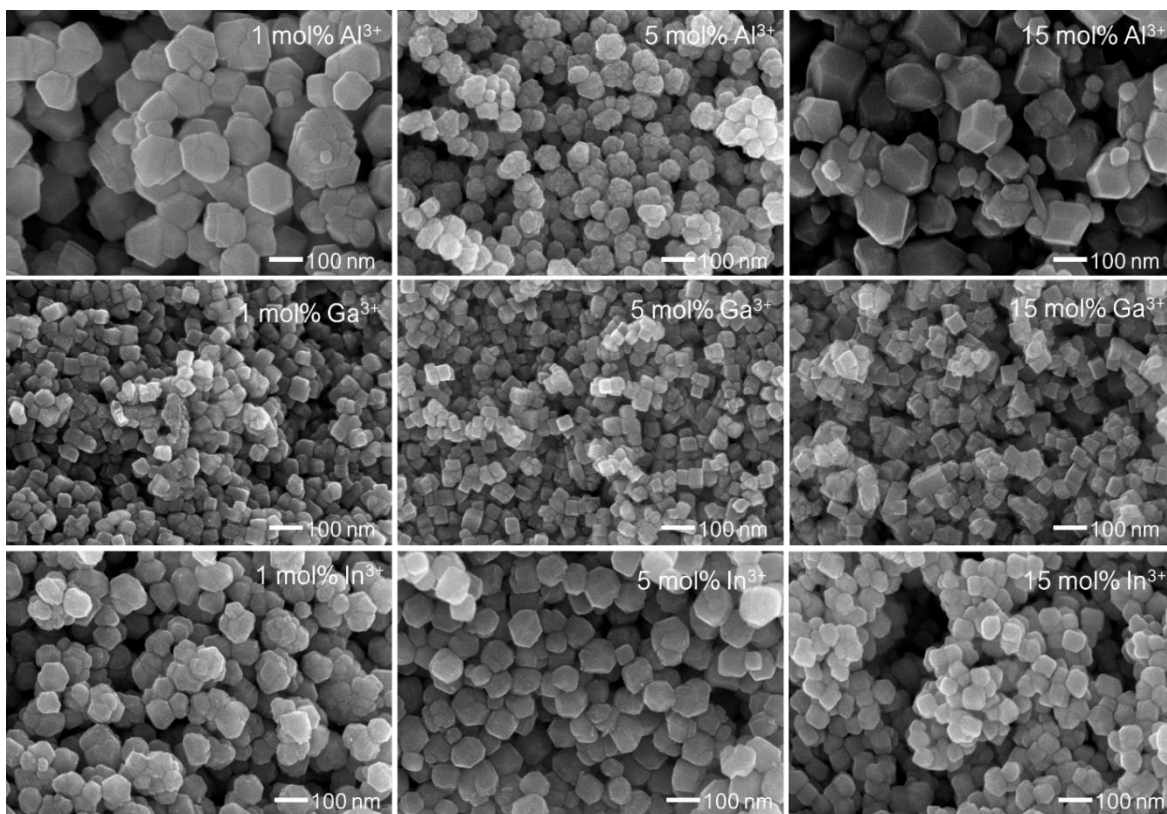


Figure A5.5: SEM of Cu_2O nanocrystals synthesized with 1, 5, and 15 mol% Al^{3+} , Ga^{3+} , and In^{3+} catalysts.

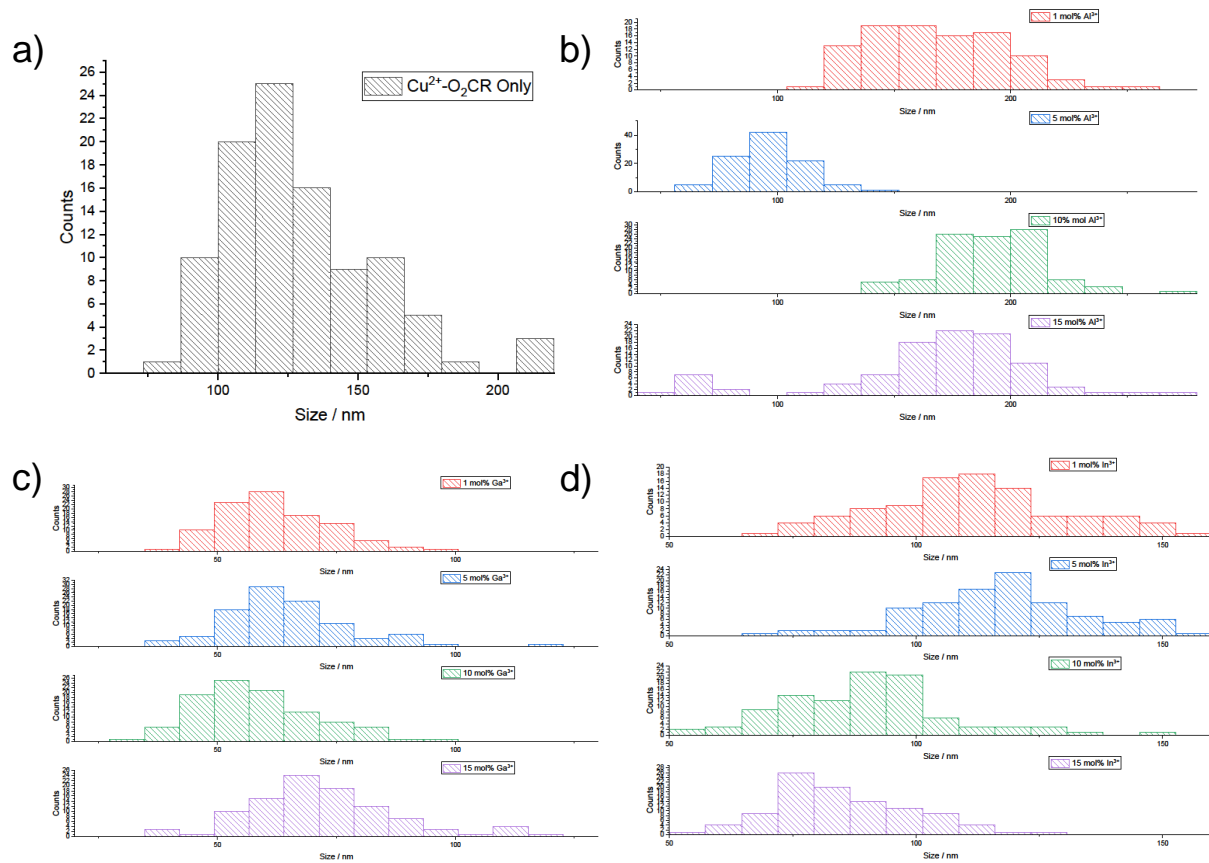


Figure A5.6: Histograms for a) Cu²⁺-O₂CR only injection, b) 1-15 mol% Al³⁺, c) 1-15 mol% Ga³⁺, and d) 1-15 mol% In³⁺. Size analysis was performed from SEM images.

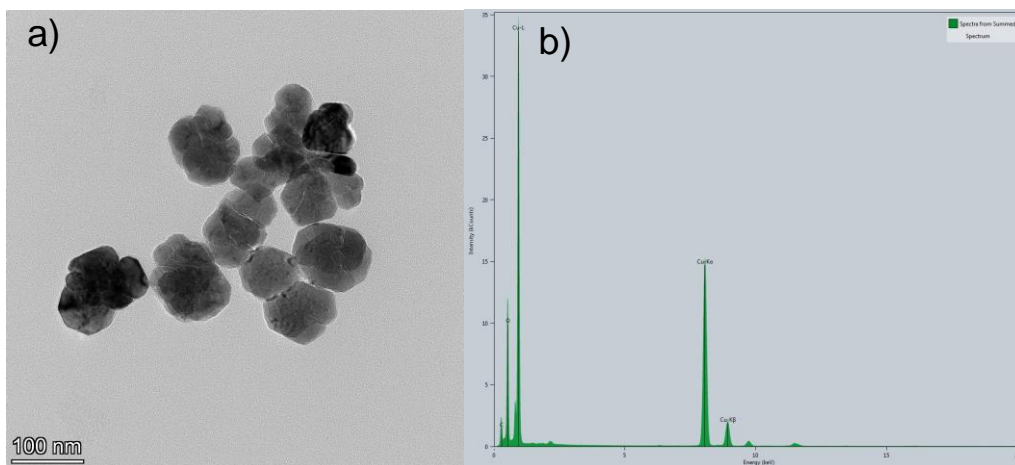


Figure A5.7: a) TEM and b) EDS of Cu^{2+} reaction with 0 mol% catalyst. Unlabeled peaks near 2, 9, and 12 keV are due to Au (TEM grid).

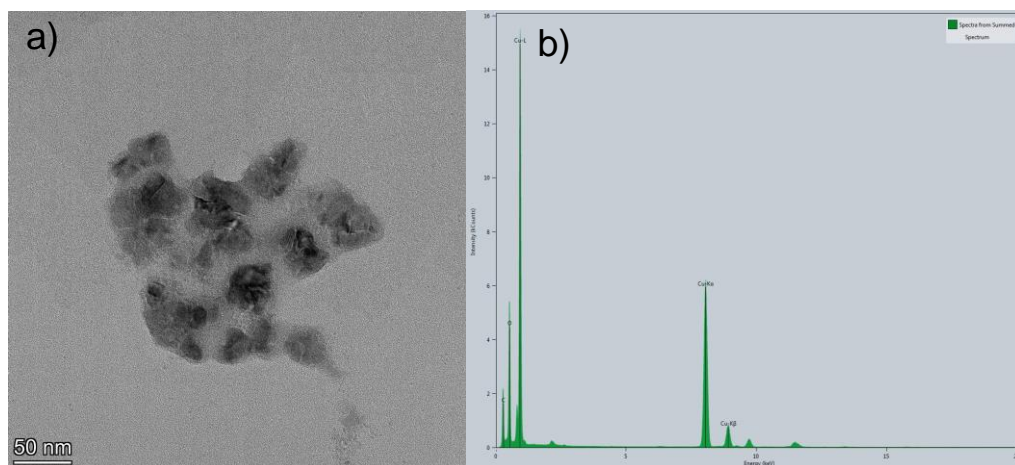


Figure A5.8: a) TEM and b) EDS of Cu^{2+} reaction with 1 mol% Ga^{3+} catalyst. Unlabeled peaks near 2, 9, and 12 keV are due to Au (TEM grid).

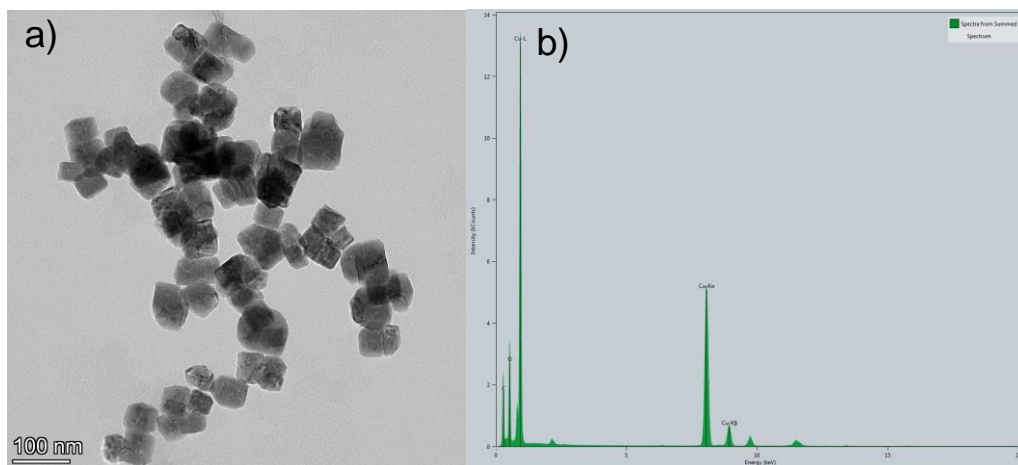


Figure A5.9: a) TEM and b) EDS of Cu^{2+} reaction with 5 mol% Ga^{3+} catalyst. Unlabeled peaks near 2, 9, and 12 keV are due to Au (TEM grid).

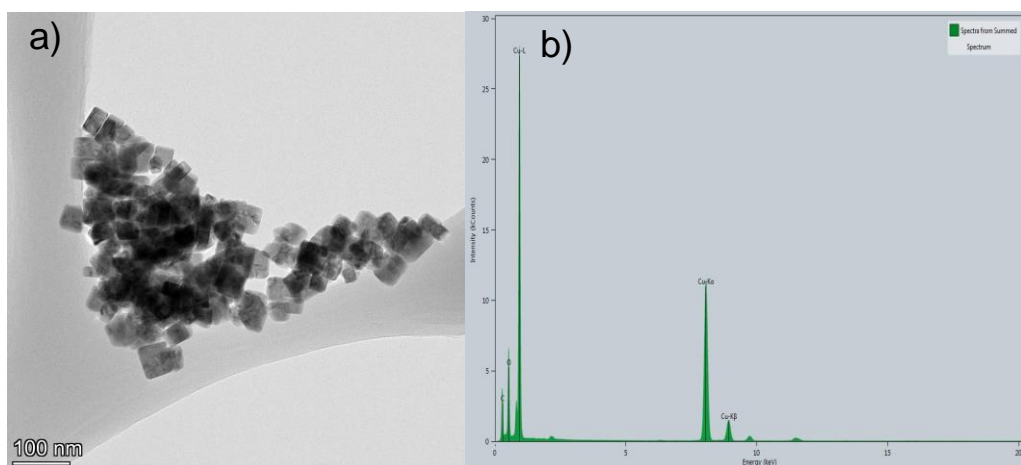


Figure A5.10: a) TEM and b) EDS of Cu^{2+} reaction with 10 mol% Ga^{3+} catalyst. Unlabeled peaks near 2, 9, and 12 keV are due to Au (TEM grid).

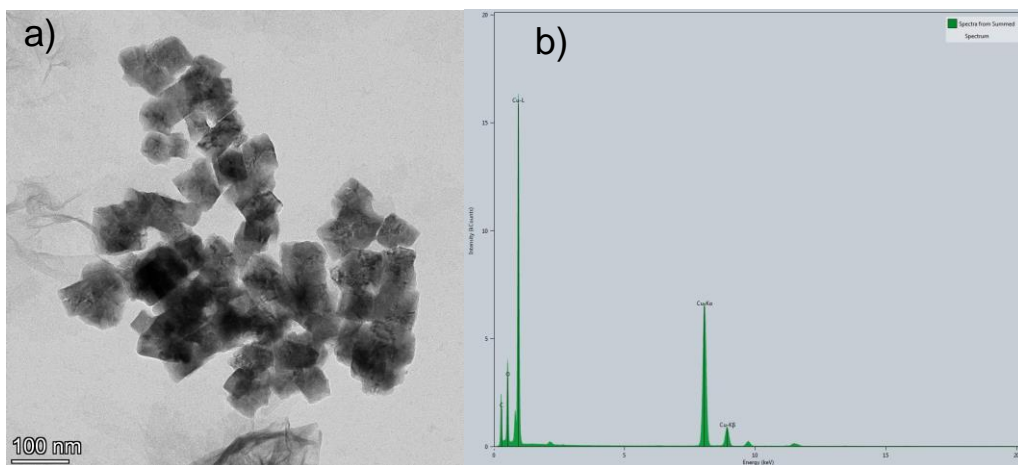


Figure A5.11: a) TEM and b) EDS of Cu^{2+} reaction with 15 mol% Ga^{3+} catalyst. Unlabeled peaks near 2, 9, and 12 keV are due to Au (TEM grid).

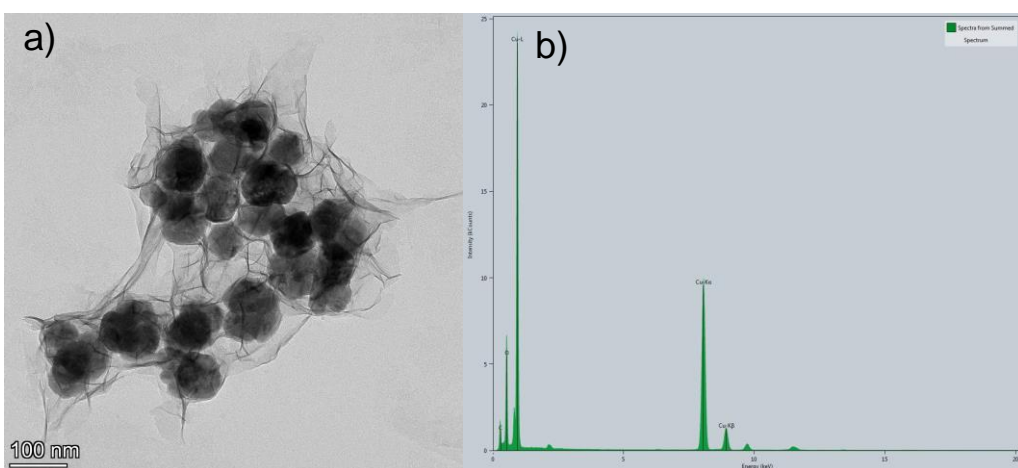


Figure A5.12: a) TEM and b) EDS of Cu^{2+} reaction with 1 mol% In^{3+} catalyst. Unlabeled peaks near 2, 9, and 12 keV are due to Au (TEM grid).

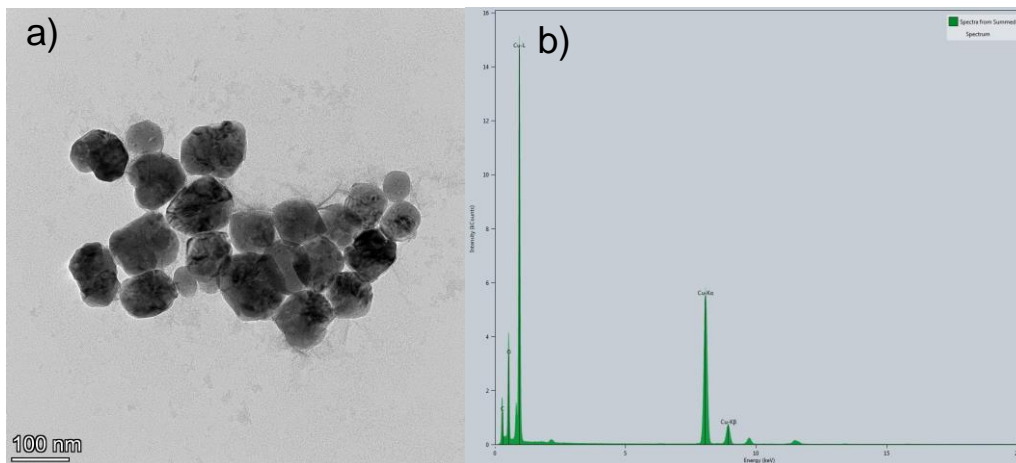


Figure A5.13: a) TEM and b) EDS of Cu^{2+} reaction with 5 mol% In^{3+} catalyst. Unlabeled peaks near 2, 9, and 12 keV are due to Au (TEM grid).

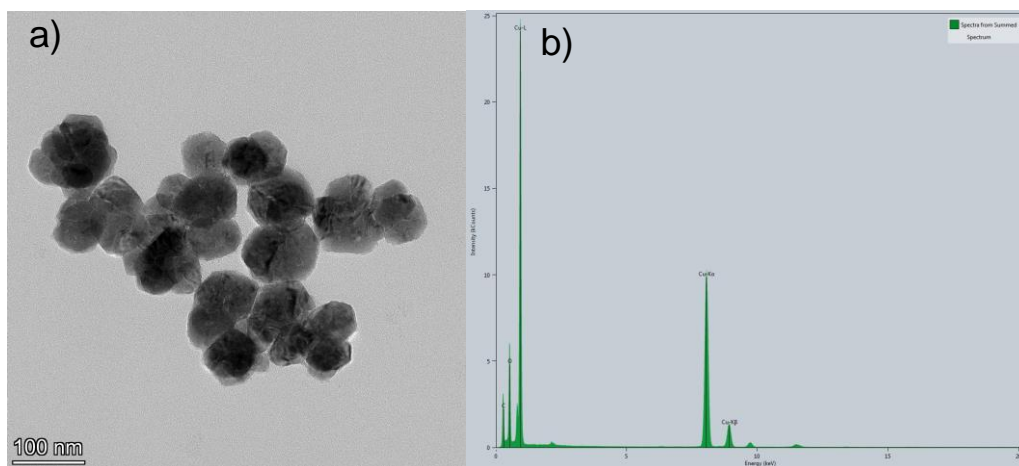


Figure A5.14: a) TEM and b) EDS of Cu^{2+} reaction with 10 mol% In^{3+} catalyst. Unlabeled peaks near 2, 9, and 12 keV are due to Au (TEM grid).

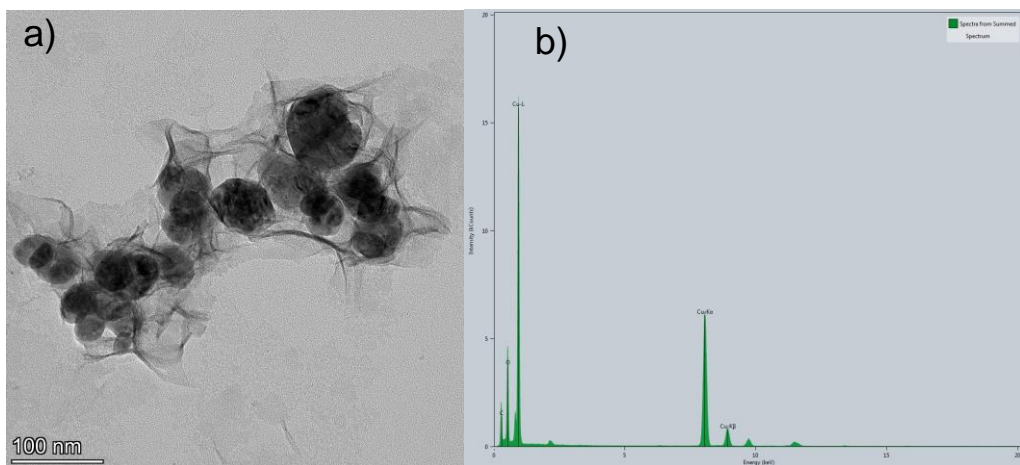


Figure A5.15: a) TEM and b) EDS of Cu^{2+} reaction with 15 mol% In^{3+} catalyst. Unlabeled peaks near 2, 9, and 12 keV are due to Au (TEM grid).

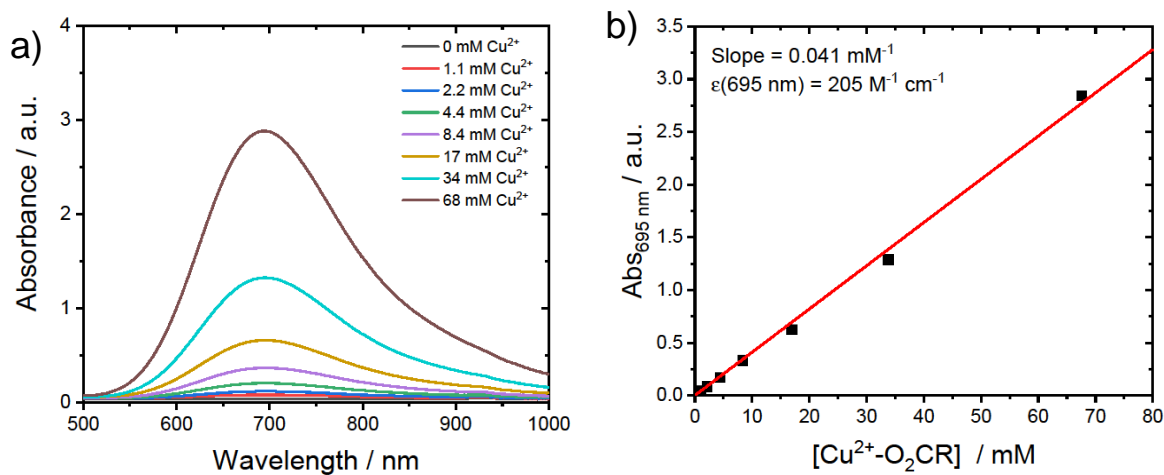


Figure A5.16: a) UV-visible absorbance spectra of $\text{Cu}^{2+}\text{-O}_2\text{CR}$ precursor in oleyl alcohol at controlled concentrations collected in a 0.2 cm path length cuvette. b) Beer-Lambert plot for peak absorbance at 695 nm. Measured slope of 0.041 mM^{-1} results in a calculated $\epsilon(695 \text{ nm}) = 205 \text{ M}^{-1} \text{ cm}^{-1}$.

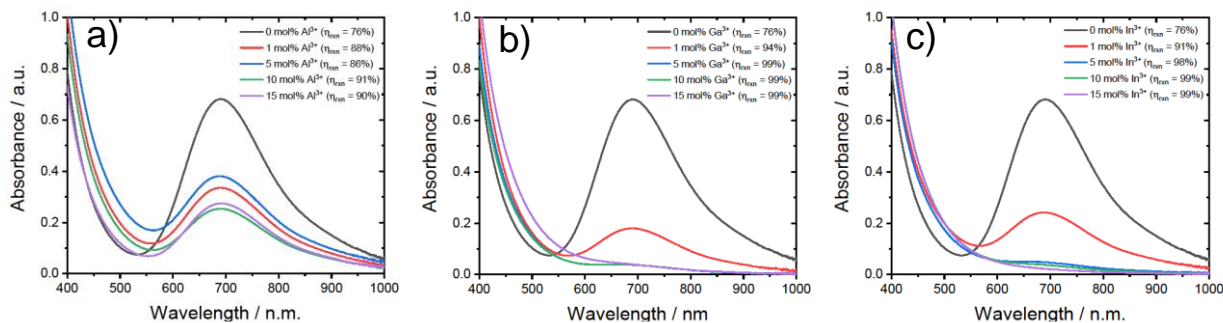


Figure A5.17: UV-visible absorbance spectra of post-reaction solutions for a) Al^{3+} , b) Ga^{3+} , and c) In^{3+} catalysts (0.2 cm path length). The peak at 695 nm is indicative of unreacted Cu^{2+} - O_2CR precursor remaining in solution. Absorbance was corrected for oleyl alcohol with the reaction efficiency indicated in the legend ($\eta_{\text{rxn}} = 1 - [\text{Cu}^{2+}]_{\text{unreacted}}/[\text{Cu}^{2+}]_{\text{total}}$). $[\text{Cu}^{2+}]$ concentration calculated using $\epsilon_{695} = 205 \text{ M}^{-1} \text{ cm}^{-1}$ determined in **Figure A5.16**. $[\text{Cu}^{2+}]_{\text{total}} = 68 \text{ mM}$.

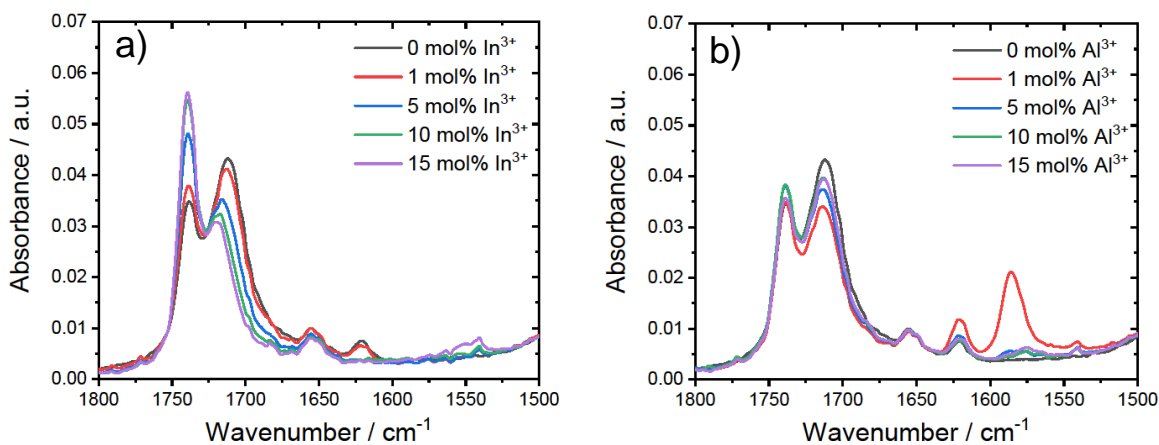


Figure A5.18: FTIR absorbance spectra of post-reaction solutions of a) In^{3+} and b) Al^{3+} catalyzed Cu_2O synthesis.

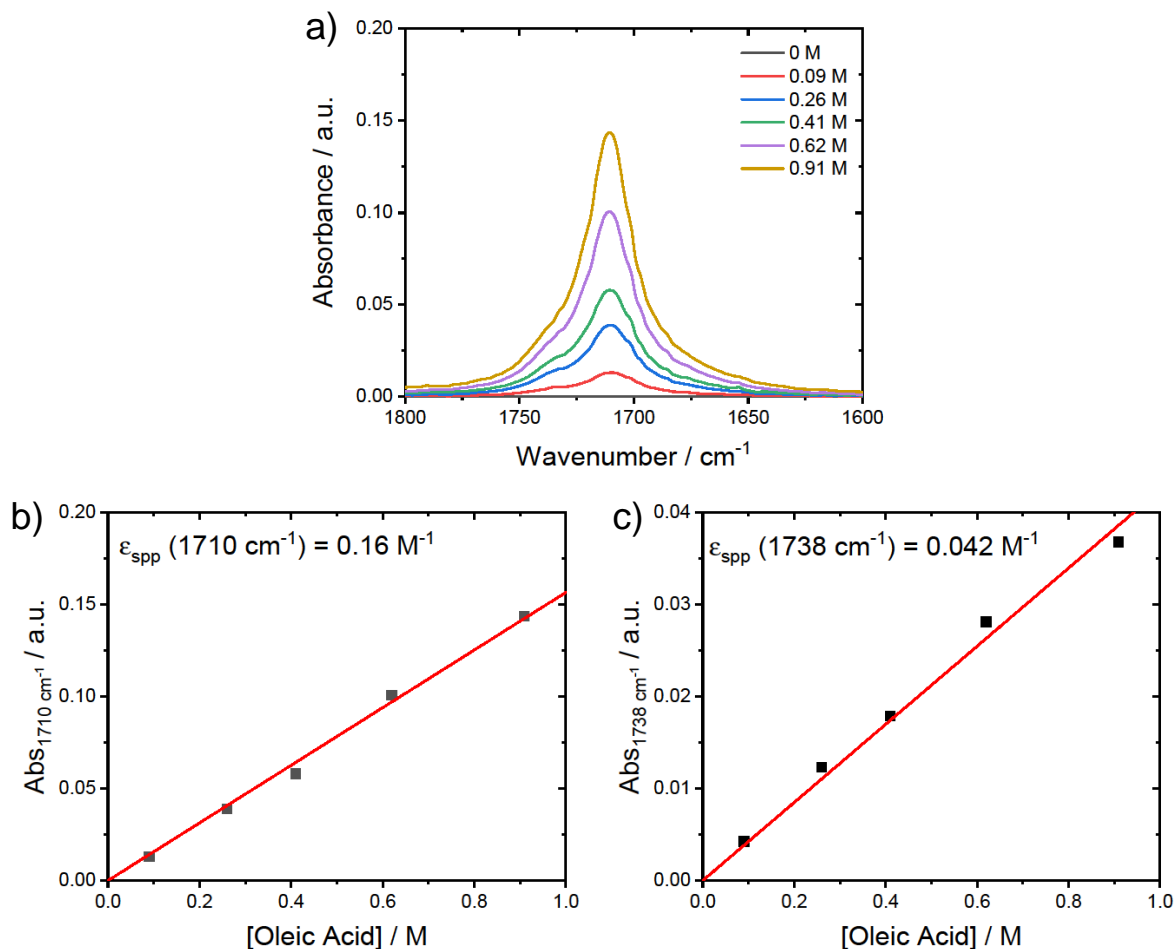


Figure A5.19: a) FTIR absorbance spectra of oleic acid dissolved in oleyl alcohol at controlled concentrations. Spectra are background corrected for oleyl alcohol. (b-c) Beer-Lambert plots for absorbance at 1710 and 1738 cm⁻¹ with slopes of 0.16 and 0.04 M⁻¹, respectively. Despite not knowing the path length associated with the ATR-FTIR measurement, the linearity in these plots indicates a constant path length across different samples. Therefore, the slopes were used directly as apparent extinction coefficients for oleic acid in oleyl alcohol such that $\epsilon_{\text{app}}(1710 \text{ cm}^{-1}) = 0.16 \text{ M}^{-1}$ and $\epsilon_{\text{app}}(1738 \text{ cm}^{-1}) = 0.04 \text{ M}^{-1}$.

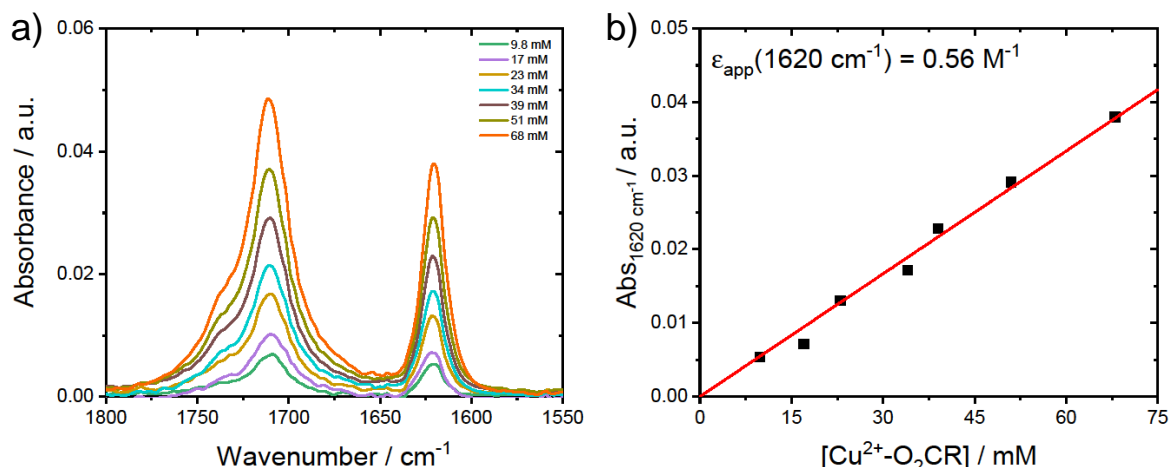


Figure A5.20: a) FTIR absorbance spectra of $\text{Cu}^{2+}\text{-O}_2\text{CR}$ dissolved in oleyl alcohol at controlled concentrations. Spectra are background corrected for oleyl alcohol. b) Beer-Lambert plot for absorbance at 1620 cm^{-1} with a slope of $5.6 \times 10^{-4}\text{ mM}^{-1}$. Despite not knowing the path length associated with the ATR-FTIR measurement, the linearity in these plots indicates a constant path length across different samples. Therefore, the slope was used directly as an apparent extinction coefficients for $\text{Cu}^{2+}\text{-O}_2\text{CR}$ in oleyl alcohol such that $\epsilon_{\text{app}}(1620\text{ cm}^{-1}) = 0.56\text{ M}^{-1}$.

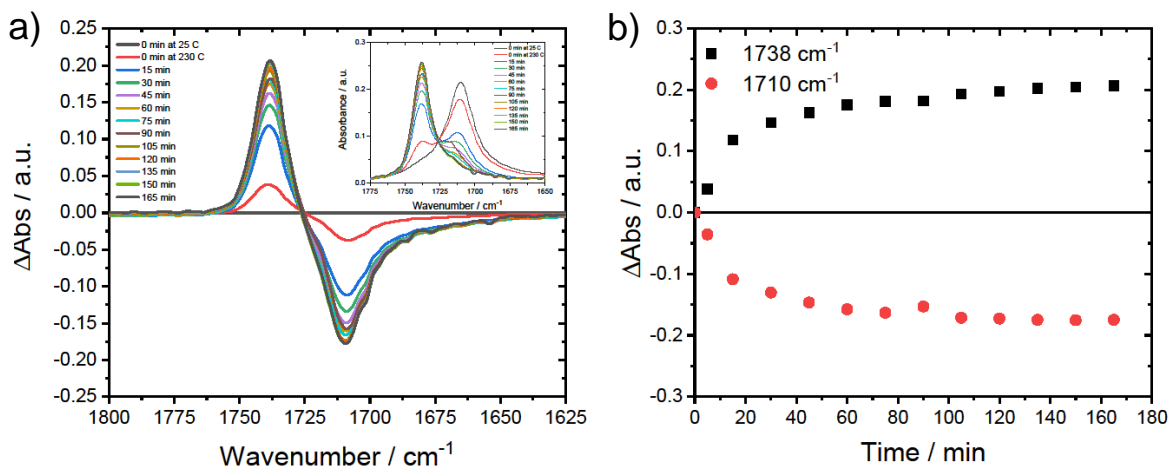


Figure A5.21: a) FTIR ΔAbs spectra of oleic acid dissolved in oleyl alcohol and heated to $230\text{ }^\circ\text{C}$. Time dependent spectra were generated by removing small aliquots from solution over the course of the reaction. ΔAbs data were generated by subtracting all spectra from the initial 0 min at $25\text{ }^\circ\text{C}$ condition. Inset shows raw absorbance data. b) ΔAbs at 1710 and 1738 cm^{-1} plotted versus time of reaction. The final time point at 165 min , representing complete conversion from acid to ester, was used to calculate apparent extinction coefficients for oleyl oleate ester based on the equation $\Delta\text{Abs}(\tilde{\nu}) = \Delta\epsilon(\tilde{\nu})[\text{Ester}]$ where $[\text{Ester}] = 1.27\text{ M}$ and $\Delta\epsilon(\tilde{\nu}) = \epsilon_{\text{ester}}(\tilde{\nu}) - \epsilon_{\text{acid}}(\tilde{\nu})$. Resulting values were $\epsilon_{\text{app}}(1710\text{ cm}^{-1}) = 0.018\text{ M}^{-1}$ and $\epsilon_{\text{app}}(1738\text{ cm}^{-1}) = 0.20\text{ M}^{-1}$.

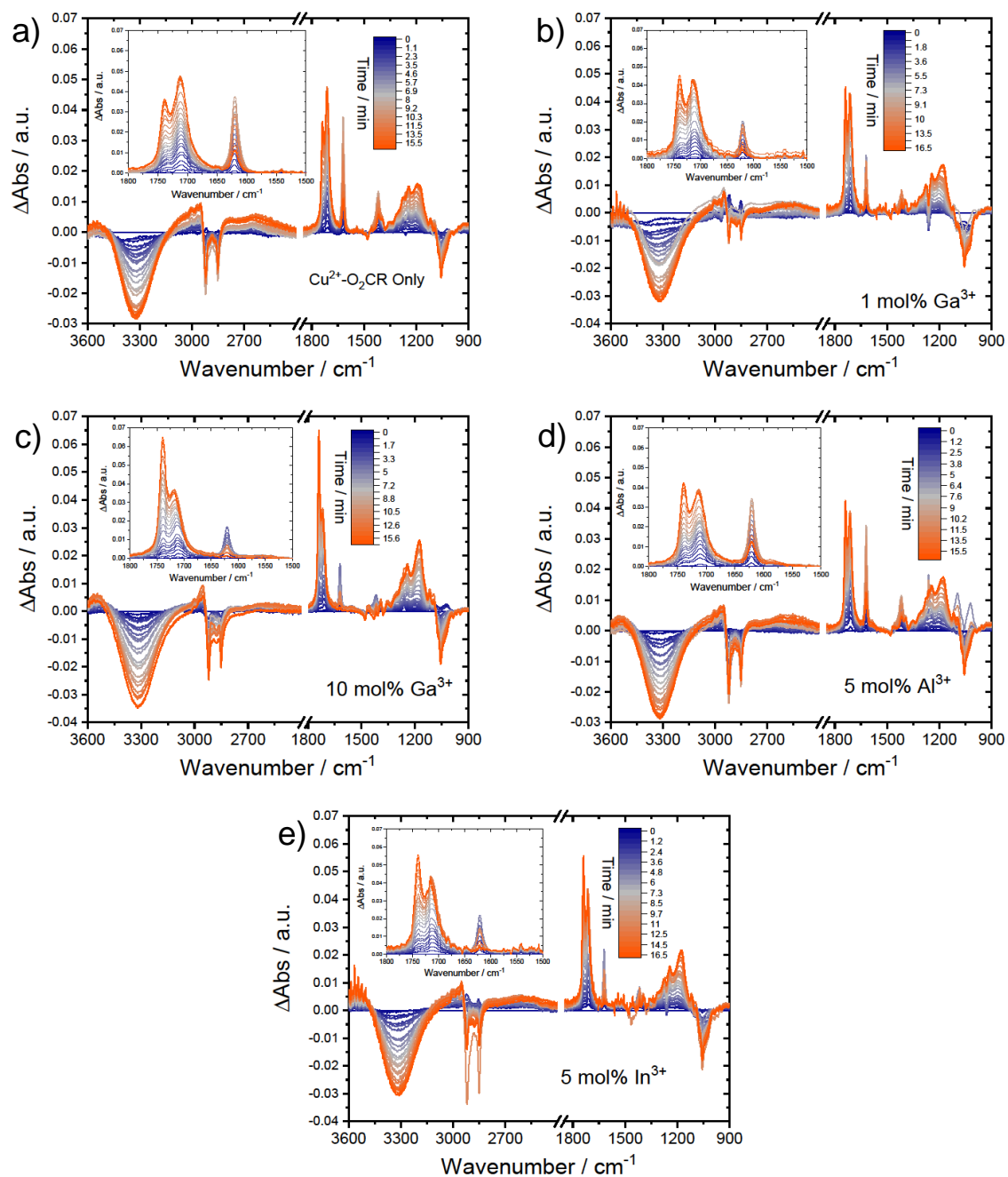


Figure A5.22: Time-dependent FTIR Δ Abs spectra for a) Cu^{2+} - O_2CR only injection, b) 1 mol% Ga^{3+} , 10 mol% Ga^{3+} , 5 mol% Al^{3+} , and 5 mol% In^{3+} catalyzed reactions. Δ Abs spectra generated by subtracting the initial spectrum at $t = 0$ min.

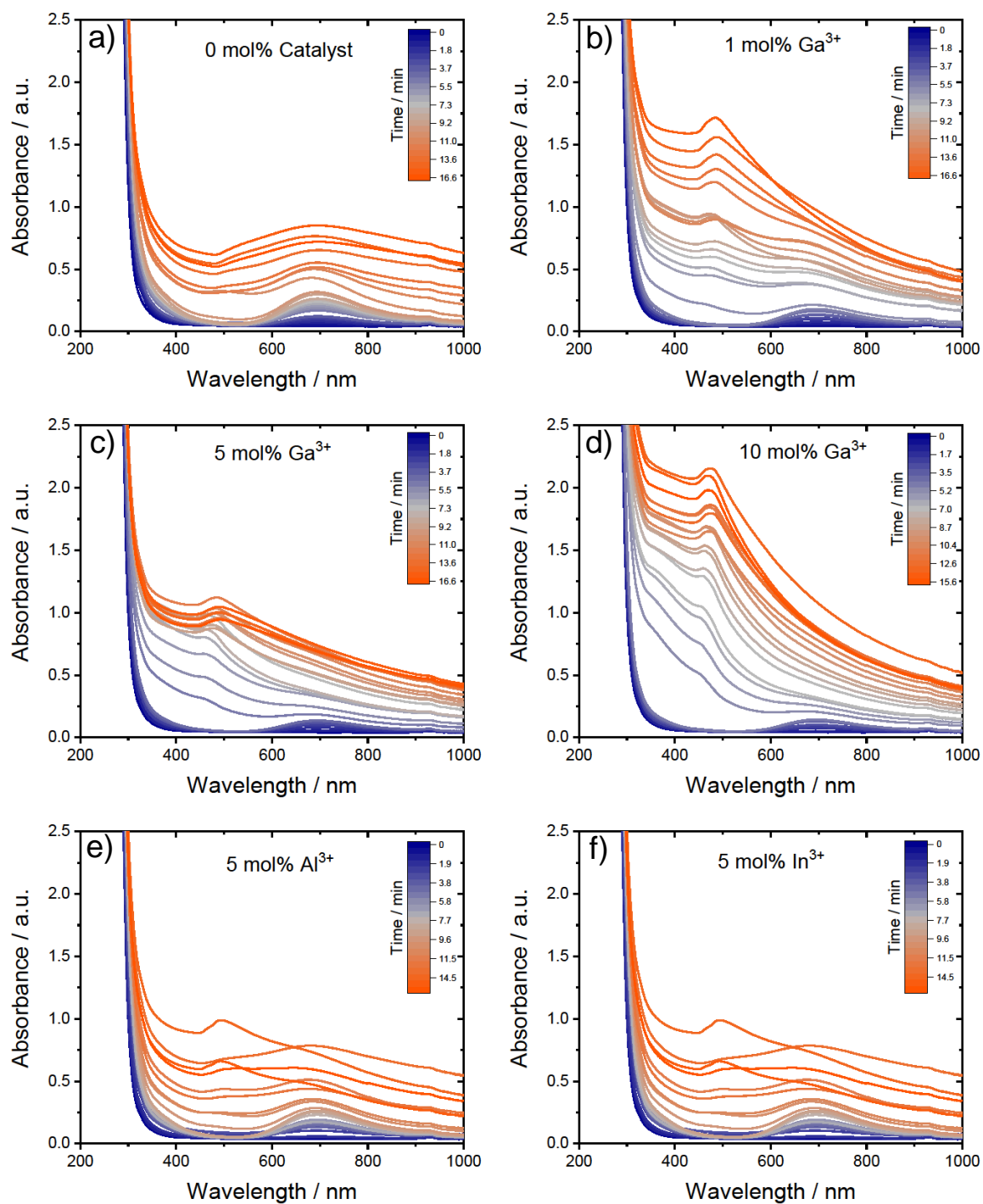


Figure A5.23: Time-dependent UV-visible absorbance spectra for a-d) 0-10 mol% Ga³⁺, e) 5 mol% Al³⁺ and f) 5 mol% In³⁺ catalyzed reactions.

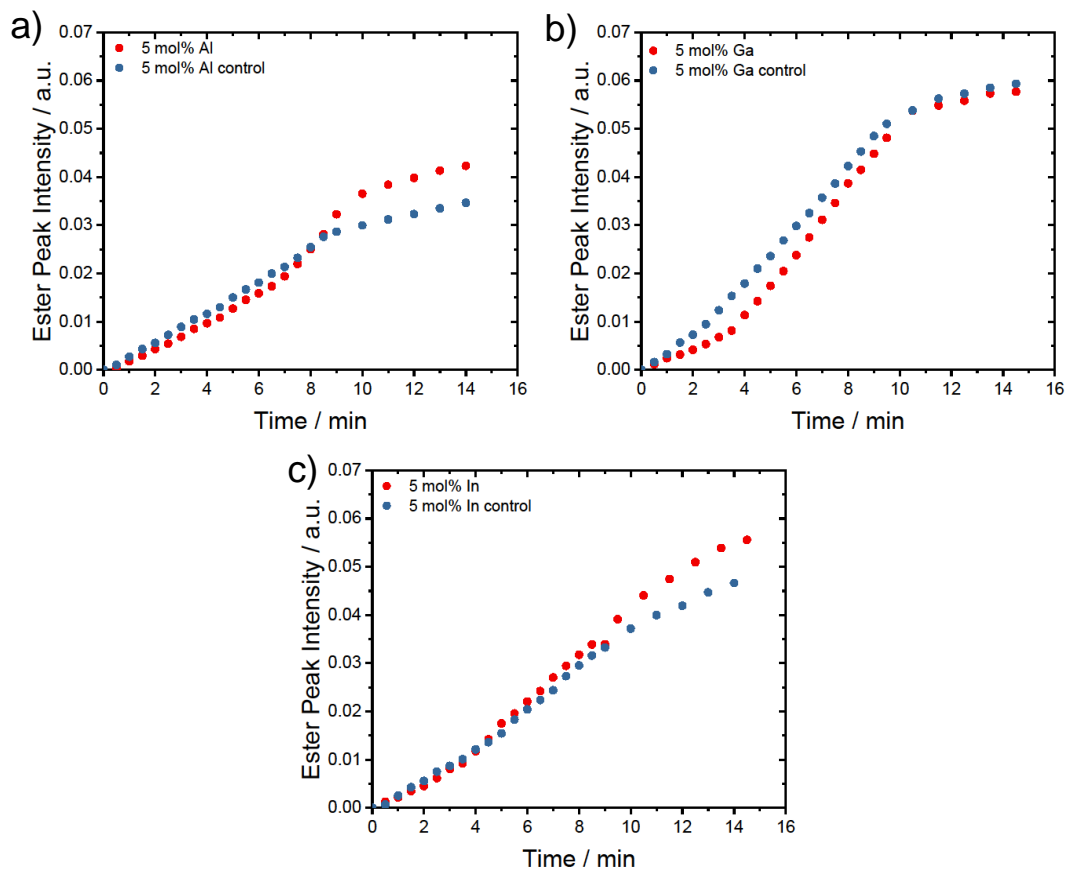


Figure A5.24: Comparison of FTIR ester peak absorbance at 1738 cm^{-1} measured over time for 5 mol% a) Al^{3+} , b) Ga^{3+} , and c) In^{3+} with and without (*i.e.* control) the presence of Cu^{2+} - O_2CR precursor.

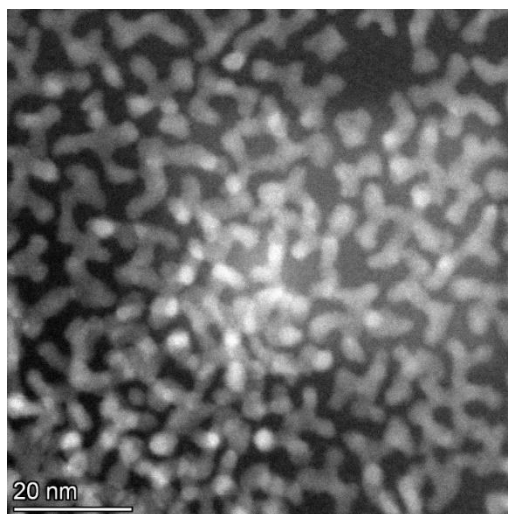


Figure A5.25: TEM HAADF image of In_2O_3 nanocrystals produced with 100 mol% injection of In^{3+} - O_2CR into oleyl alcohol at $200\text{ }^\circ\text{C}$.

5.6 References

- (1) Cargnello, M. Colloidal Nanocrystals as Building Blocks for Well-Defined Heterogeneous Catalysts. *Chem. Mater.* **2019**, *31* (3), 576–596. <https://doi.org/10.1021/acs.chemmater.8b04533>.
- (2) Yin, Y.; Alivisatos, A. P. Colloidal Nanocrystal Synthesis and the Organic–Inorganic Interface. *Nature* **2005**, *437* (7059), 664–670. <https://doi.org/10.1038/nature04165>.
- (3) E. Cloud, J.; S. Yoder, T.; K. Harvey, N.; Snow, K.; Yang, Y. A Simple and Generic Approach for Synthesizing Colloidal Metal and Metal Oxide Nanocrystals. *Nanoscale* **2013**, *5* (16), 7368–7378. <https://doi.org/10.1039/C3NR02404K>.
- (4) van Embden, J.; Chesman, A. S. R.; Jasieniak, J. J. The Heat-Up Synthesis of Colloidal Nanocrystals. *Chem. Mater.* **2015**, *27* (7), 2246–2285. <https://doi.org/10.1021/cm5028964>.
- (5) Agrawal, A.; Cho, S. H.; Zandi, O.; Ghosh, S.; Johns, R. W.; Milliron, D. J. Localized Surface Plasmon Resonance in Semiconductor Nanocrystals. *Chem. Rev.* **2018**, *118* (6), 3121–3207. <https://doi.org/10.1021/acs.chemrev.7b00613>.
- (6) LaMer, V. K.; Dinegar, R. H. Theory, Production and Mechanism of Formation of Monodispersed Hydrosols. *J. Am. Chem. Soc.* **1950**, *72* (11), 4847–4854. <https://doi.org/10.1021/ja01167a001>.
- (7) Wall, M. A.; Cossairt, B. M.; Liu, J. T. C. Reaction-Driven Nucleation Theory. *J. Phys. Chem. C* **2018**, *122* (17), 9671–9679. <https://doi.org/10.1021/acs.jpcc.8b01368>.
- (8) Ito, D.; Yokoyama, S.; Zaikova, T.; Masuko, K.; Hutchison, J. E. Synthesis of Ligand-Stabilized Metal Oxide Nanocrystals and Epitaxial Core/Shell Nanocrystals via a Lower-Temperature Esterification Process. *ACS Nano* **2014**, *8* (1), 64–75. <https://doi.org/10.1021/nn401888h>.
- (9) Jansons, A. W.; Hutchison, J. E. Continuous Growth of Metal Oxide Nanocrystals: Enhanced Control of Nanocrystal Size and Radial Dopant Distribution. *ACS Nano* **2016**, *10* (7), 6942–6951. <https://doi.org/10.1021/acs.nano.6b02796>.
- (10) Jansons, A. W.; Plummer, L. K.; Hutchison, J. E. Living Nanocrystals. *Chem. Mater.* **2017**, *29* (13), 5415–5425. <https://doi.org/10.1021/acs.chemmater.7b00899>.
- (11) Kim, K.; Reimnitz, L. C.; Cho, S. H.; Noh, J.; Dong, Z.; Gibbs, S. L.; Korgel, B. A.; Milliron, D. J. Effect of Nonincorporative Cations on the Size and Shape of Indium Oxide Nanocrystals. *Chem. Mater.* **2020**, *32* (21), 9347–9354. <https://doi.org/10.1021/acs.chemmater.0c03281>.
- (12) Chang, H.; Kim, B. H.; Jeong, H. Y.; Moon, J. H.; Park, M.; Shin, K.; Chae, S. I.; Lee, J.; Kang, T.; Choi, B. K.; Yang, J.; Bootharaju, M. S.; Song, H.; An, S. H.; Park, K. M.; Oh, J. Y.; Lee, H.; Kim, M. S.; Park, J.; Hyeon, T. Molecular-Level Understanding of Continuous Growth from Iron-Oxo Clusters to Iron Oxide Nanoparticles. *J. Am. Chem. Soc.* **2019**, *141* (17), 7037–7045. <https://doi.org/10.1021/jacs.9b01670>.

- (13) Plummer, L. K.; Hutchison, J. E. Understanding the Effects of Iron Precursor Ligation and Oxidation State Leads to Improved Synthetic Control for Spinel Iron Oxide Nanocrystals. *Inorg. Chem.* **2020**, *59* (20), 15074–15087. <https://doi.org/10.1021/acs.inorgchem.0c02040>.
- (14) Cooper, S. R.; Plummer, L. K.; Cosby, A. G.; Lenox, P.; Jander, A.; Dhagat, P.; Hutchison, J. E. Insights into the Magnetic Properties of Sub-10 Nm Iron Oxide Nanocrystals through the Use of a Continuous Growth Synthesis. *Chem. Mater.* **2018**, *30* (17), 6053–6062. <https://doi.org/10.1021/acs.chemmater.8b02389>.
- (15) Wainer, P.; Kendall, O.; Lamb, A.; Barrow, S. J.; Tricoli, A.; Gómez, D. E.; van Embden, J.; Della Gaspera, E. Continuous Growth Synthesis of Zinc Oxide Nanocrystals with Tunable Size and Doping. *Chem. Mater.* **2019**, *31* (23), 9604–9613. <https://doi.org/10.1021/acs.chemmater.9b02655>.
- (16) Jansons, A. W.; Koskela, K. M.; Crockett, B. M.; Hutchison, J. E. Transition Metal-Doped Metal Oxide Nanocrystals: Efficient Substitutional Doping through a Continuous Growth Process. *Chem. Mater.* **2017**, *29* (19), 8167–8176. <https://doi.org/10.1021/acs.chemmater.7b02176>.
- (17) Li, X.; Shen, H.; Niu, J.; Li, S.; Zhang, Y.; Wang, H.; Li, L. S. Columnar Self-Assembly of Cu₂S Hexagonal Nanoplates Induced by Tin(IV)–X Complex as Inorganic Surface Ligand. *J. Am. Chem. Soc.* **2010**, *132* (37), 12778–12779. <https://doi.org/10.1021/ja103955s>.
- (18) Yi, L.; Gao, M. From Ultrathin Two-Dimensional Djurleite Nanosheets to One-Dimensional Nanorods Comprised of Djurleite Nanoplates: Synthesis, Characterization, and Formation Mechanism. *Cryst. Growth Des.* **2011**, *11* (4), 1109–1116. <https://doi.org/10.1021/cg101322s>.
- (19) Machani, T.; Rossi, D. P.; Golden, B. J.; Jones, E. C.; Lotfipour, M.; Plass, K. E. Synthesis of Monoclinic and Tetragonal Chalcocite Nanoparticles by Iron-Induced Stabilization. *Chem. Mater.* **2011**, *23* (24), 5491–5495. <https://doi.org/10.1021/cm2022196>.
- (20) Pike, S. D.; White, E. R.; Regoutz, A.; Sammy, N.; Payne, D. J.; Williams, C. K.; Shaffer, M. S. P. Reversible Redox Cycling of Well-Defined, Ultrasmall Cu/Cu₂O Nanoparticles. *ACS Nano* **2017**, *11* (3), 2714–2723. <https://doi.org/10.1021/acs.nano.6b07694>.
- (21) Singhal, A.; Pai, M. R.; Rao, R.; Pillai, K. T.; Lieberwirth, I.; Tyagi, A. K. Copper(I) Oxide Nanocrystals – One Step Synthesis, Characterization, Formation Mechanism, and Photocatalytic Properties. *Eur. J. Inorg. Chem.* **2013**, *2013* (14), 2640–2651. <https://doi.org/10.1002/ejic.201201382>.
- (22) Crockett, B. M.; Jansons, A. W.; Koskela, K. M.; Sharps, M. C.; Johnson, D. W.; Hutchison, J. E. Influence of Nanocrystal Size on the Optoelectronic Properties of Thin, Solution-Cast Sn-Doped In₂O₃ Films. *Chem. Mater.* **2019**, *31* (9), 3370–3380. <https://doi.org/10.1021/acs.chemmater.9b00538>.
- (23) Tariq, M.; Koch, M. D.; Andrews, J. W.; Knowles, K. E. Correlation between Surface Chemistry and Optical Properties in Colloidal Cu₂O Nanoparticles. *J. Phys. Chem. C* **2020**, *124* (8), 4810–4819. <https://doi.org/10.1021/acs.jpcc.9b10753>.
- (24) Mamidi, N.; Manna, D. Zn(OTf)₂-Promoted Chemoselective Esterification of Hydroxyl Group Bearing Carboxylic Acids. *J. Org. Chem.* **2013**, *78* (6), 2386–2396. <https://doi.org/10.1021/jo302502r>.

- (25) Hou, X.; Qi, Y.; Qiao, X.; Wang, G.; Qin, Z.; Wang, J. Lewis Acid-Catalyzed Transesterification and Esterification of High Free Fatty Acid Oil in Subcritical Methanol. *Korean J. Chem. Eng.* **2007**, *24* (2), 311–313. <https://doi.org/10.1007/s11814-007-5052-x>.
- (26) Maki, T.; Ishihara, K.; Yamamoto, H. N-Alkyl-4-Boronopyridinium Halides versus Boric Acid as Catalysts for the Esterification of α -Hydroxycarboxylic Acids. *Org. Lett.* **2005**, *7* (22), 5047–5050. <https://doi.org/10.1021/ol052061d>.
- (27) Ishihara, K.; Nakayama, M.; Ohara, S.; Yamamoto, H. Direct Ester Condensation from a 1:1 Mixture of Carboxylic Acids and Alcohols Catalyzed by Hafnium(IV) or Zirconium(IV) Salts. *Tetrahedron* **2002**, *58* (41), 8179–8188. [https://doi.org/10.1016/S0040-4020\(02\)00966-3](https://doi.org/10.1016/S0040-4020(02)00966-3).
- (28) Bentley, J. N.; Elgadi, S. A.; Gaffen, J. R.; Demay-Drouhard, P.; Baumgartner, T.; Caputo, C. B. Fluorescent Lewis Adducts: A Practical Guide to Relative Lewis Acidity. *Organometallics* **2020**. <https://doi.org/10.1021/acs.organomet.0c00389>.
- (29) Kamunde-Devonish, M. K.; Fast, D. B.; Mensinger, Z. L.; Gatlin, J. T.; Zakharov, L. N.; Dolgos, M. R.; Johnson, D. W. Synthesis and Solid-State Structural Characterization of a Series of Aqueous Heterometallic Tridecameric Group 13 Clusters. *Inorg. Chem.* **2015**, *54* (8), 3913–3920. <https://doi.org/10.1021/acs.inorgchem.5b00097>.
- (30) Mensinger, Z. L.; Zakharov, L. N.; Johnson, D. W. Synthesis and Crystallization of Infinite Indium and Gallium Acetate 1D Chain Structures and Concomitant Ethyl Acetate Hydrolysis. *Inorg. Chem.* **2009**, *48* (8), 3505–3507. <https://doi.org/10.1021/ic9000945>.
- (31) Clausén, M.; Öhman, L.-O.; Kubicki, J. D.; Persson, P. Characterisation of Gallium(III)-Acetate Complexes in Aqueous Solution: A Potentiometric, EXAFS, IR and Molecular Orbital Modelling Study. *J. Chem. Soc. Dalton Trans.* **2002**, No. 12, 2559–2564. <https://doi.org/10.1039/B111408E>.
- (32) Plummer, L. K.; Crockett, B. M.; Pennel, M. L.; Jansons, A. W.; Koskela, K. M.; Hutchison, J. E. Influence of Monomer Flux and Temperature on Morphology of Indium Oxide Nanocrystals during a Continuous Growth Synthesis. *Chem. Mater.* **2019**, *31* (18), 7638–7649. <https://doi.org/10.1021/acs.chemmater.9b02467>.
- (33) Thoka, S.; Lee, A.-T.; Huang, M. H. Scalable Synthesis of Size-Tunable Small Cu₂O Nanocubes and Octahedra for Facet-Dependent Optical Characterization and Pseudomorphic Conversion to Cu Nanocrystals. *ACS Sustain. Chem. Eng.* **2019**, *7* (12), 10467–10476. <https://doi.org/10.1021/acssuschemeng.9b00844>.
- (34) Mukherjee, I.; Das, S. K.; Jena, B. K.; Saha, R.; Chatterjee, S. Dissimilitude Behaviour of Cu₂O Nano-Octahedra and Nano-Cubes towards Photo- and Electrocatalytic Activities. *New J. Chem.* **2018**, *42* (5), 3692–3702. <https://doi.org/10.1039/C7NJ04474G>.
- (35) Zhang, X.; Zhang, Y.; Huang, H.; Cai, J.; Ding, K.; Lin, S. Electrochemical Fabrication of Shape-Controlled Cu₂O with Spheres, Octahedrons and Truncated Octahedrons and Their Electrocatalysis for ORR. *New J. Chem.* **2017**, *42* (1), 458–464. <https://doi.org/10.1039/C7NJ04200K>.
- (36) Wang, Q.; Kuang, Q.; Wang, K.; Wang, X.; Xie, Z. A Surfactant Free Synthesis and Formation Mechanism of Hollow Cu₂O Nanocubes Using Cl⁻ Ions as the Morphology Regulator. *RSC Adv.* **2015**, *5* (75), 61421–61425. <https://doi.org/10.1039/C5RA08988C>.

- (37) Susman, M. D.; Feldman, Y.; Vaskevich, A.; Rubinstein, I. Chemical Deposition of Cu₂O Nanocrystals with Precise Morphology Control. *ACS Nano* **2014**, *8* (1), 162–174. <https://doi.org/10.1021/nn405891g>.
- (38) Paoletta, A.; Brescia, R.; Prato, M.; Povia, M.; Marras, S.; De Trizio, L.; Falqui, A.; Manna, L.; George, C. Colloidal Synthesis of Cuprite (Cu₂O) Octahedral Nanocrystals and Their Electrochemical Lithiation. *ACS Appl. Mater. Interfaces* **2013**, *5* (7), 2745–2751. <https://doi.org/10.1021/am4004073>.
- (39) Li, Q.; Xu, P.; Zhang, B.; Tsai, H.; Zheng, S.; Wu, G.; Wang, H.-L. Structure-Dependent Electrocatalytic Properties of Cu₂O Nanocrystals for Oxygen Reduction Reaction. *J. Phys. Chem. C* **2013**, *117* (27), 13872–13878. <https://doi.org/10.1021/jp403655y>.
- (40) Huang, W.-C.; Lyu, L.-M.; Yang, Y.-C.; Huang, M. H. Synthesis of Cu₂O Nanocrystals from Cubic to Rhombic Dodecahedral Structures and Their Comparative Photocatalytic Activity. *J. Am. Chem. Soc.* **2012**, *134* (2), 1261–1267. <https://doi.org/10.1021/ja209662v>.
- (41) Hua, Q.; Shang, D.; Zhang, W.; Chen, K.; Chang, S.; Ma, Y.; Jiang, Z.; Yang, J.; Huang, W. Morphological Evolution of Cu₂O Nanocrystals in an Acid Solution: Stability of Different Crystal Planes. *Langmuir* **2011**, *27* (2), 665–671. <https://doi.org/10.1021/la104475s>.
- (42) Yao, K. X.; Yin, X. M.; Wang, T. H.; Zeng, H. C. Synthesis, Self-Assembly, Disassembly, and Reassembly of Two Types of Cu₂O Nanocrystals Unifaceted with {001} or {110} Planes. *J. Am. Chem. Soc.* **2010**, *132* (17), 6131–6144. <https://doi.org/10.1021/ja100151f>.
- (43) Sun, S.; Zhou, F.; Wang, L.; Song, X.; Yang, Z. Template-Free Synthesis of Well-Defined Truncated Edge Polyhedral Cu₂O Architectures. *Cryst. Growth Des.* **2010**, *10* (2), 541–547. <https://doi.org/10.1021/cg900756u>.
- (44) Sui, Y.; Fu, W.; Yang, H.; Zeng, Y.; Zhang, Y.; Zhao, Q.; Li, Y.; Zhou, X.; Leng, Y.; Li, M.; Zou, G. Low Temperature Synthesis of Cu₂O Crystals: Shape Evolution and Growth Mechanism. *Cryst. Growth Des.* **2010**, *10* (1), 99–108. <https://doi.org/10.1021/cg900437x>.
- (45) Kuo, C.-H.; Huang, M. H. Morphologically Controlled Synthesis of Cu₂O Nanocrystals and Their Properties. *Nano Today* **2010**, *5* (2), 106–116. <https://doi.org/10.1016/j.nantod.2010.02.001>.
- (46) Yin, M.; Wu, C.-K.; Lou, Y.; Burda, C.; Koberstein, J. T.; Zhu, Y.; O'Brien, S. Copper Oxide Nanocrystals. *J. Am. Chem. Soc.* **2005**, *127* (26), 9506–9511. <https://doi.org/10.1021/ja050006u>.
- (47) Yuan, X.; Yuan, H.; Ye, L.; Hu, J.; Xu, Y.; Li, P. Ultrasmall Cu₂O Nanocrystals: Facile Synthesis, Controllable Assembly and Photocatalytic Properties. *RSC Adv.* **2015**, *5* (53), 42855–42860. <https://doi.org/10.1039/C5RA06141E>.
- (48) Nikam, A. V.; Arulkashmir, A.; Krishnamoorthy, K.; Kulkarni, A. A.; Prasad, B. L. V. PH-Dependent Single-Step Rapid Synthesis of CuO and Cu₂O Nanoparticles from the Same Precursor. *Cryst. Growth Des.* **2014**, *14* (9), 4329–4334. <https://doi.org/10.1021/cg500394p>.

- (49) Shi, H.; Yu, K.; Sun, F.; Zhu, Z. Controllable Synthesis of Novel Cu₂O Micro/Nano-Crystals and Their Photoluminescence, Photocatalytic and Field Emission Properties. *CrystEngComm* **2011**, *14* (1), 278–285. <https://doi.org/10.1039/C1CE05868A>.
- (50) Zhang, Y.; Deng, B.; Zhang, T.; Gao, D.; Xu, A.-W. Shape Effects of Cu₂O Polyhedral Microcrystals on Photocatalytic Activity. *J. Phys. Chem. C* **2010**, *114* (11), 5073–5079. <https://doi.org/10.1021/jp9110037>.
- (51) Luo, Y.; Li, S.; Ren, Q.; Liu, J.; Xing, L.; Wang, Y.; Yu, Y.; Jia, Z.; Li, J. Facile Synthesis of Flowerlike Cu₂O Nanoarchitectures by a Solution Phase Route. *Cryst. Growth Des.* **2007**, *7* (1), 87–92. <https://doi.org/10.1021/cg060491k>.
- (52) Kuo, C.-H.; Huang, M. H. Facile Synthesis of Cu₂O Nanocrystals with Systematic Shape Evolution from Cubic to Octahedral Structures. *J. Phys. Chem. C* **2008**, *112* (47), 18355–18360. <https://doi.org/10.1021/jp8060027>.
- (53) Kauffman, D. R.; Ohodnicki, P. R.; Kail, B. W.; Matranga, C. Selective Electrocatalytic Activity of Ligand Stabilized Copper Oxide Nanoparticles. *J. Phys. Chem. Lett.* **2011**, *2* (16), 2038–2043. <https://doi.org/10.1021/jz200850y>.
- (54) Oliva-Puigdomènech, A.; De Roo, J.; Kuhs, J.; Detavernier, C.; Martins, J. C.; Hens, Z. Ligand Binding to Copper Nanocrystals: Amines and Carboxylic Acids and the Role of Surface Oxides. *Chem. Mater.* **2019**, *31* (6), 2058–2067. <https://doi.org/10.1021/acs.chemmater.8b05107>.
- (55) Pamplin, B. R.; Kiyosawa, T.; Masumoto, K. Ternary Chalcopyrite Compounds. *Prog. Cryst. Growth Charact.* **1979**, *1* (4), 331–387. [https://doi.org/10.1016/0146-3535\(79\)90002-9](https://doi.org/10.1016/0146-3535(79)90002-9).
- (56) Kawazoe, H.; Yasukawa, M.; Hyodo, H.; Kurita, M.; Yanagi, H.; Hosono, H. P-Type Electrical Conduction in Transparent Thin Films of CuAlO₂. *Nature* **1997**, *389* (6654), 939–942. <https://doi.org/10.1038/40087>.
- (57) Omata, T.; Nagatani, H.; Suzuki, I.; Kita, M.; Yanagi, H.; Ohashi, N. Wurtzite CuGaO₂: A New Direct and Narrow Band Gap Oxide Semiconductor Applicable as a Solar Cell Absorber. *J. Am. Chem. Soc.* **2014**, *136* (9), 3378–3381. <https://doi.org/10.1021/ja501614n>.
- (58) Conrad, F.; Massue, C.; Kühn, S.; Kunkes, E.; Girgsdies, F.; Kasatkin, I.; Zhang, B.; Friedrich, M.; Luo, Y.; Armbrüster, M.; R. Patzke, G.; Behrens, M. Microwave-Hydrothermal Synthesis and Characterization of Nanostructured Copper Substituted ZnM₂O₄ (M = Al, Ga) Spinel as Precursors for Thermally Stable Cu Catalysts. *Nanoscale* **2012**, *4* (6), 2018–2028. <https://doi.org/10.1039/C2NR11804A>.